University of Stellenbosch

Design Aspects and Optimisation of an Axial Field Permanent Magnet Machine with an Ironless Stator

Rong-Jie Wang

Dissertation presented for the degree of

Doctor of Philosophy in Electrical Engineering at

the University of Stellenbosch

Supervisor:

Prof. M.J. Kamper, University of Stellenbosch

March 2003

Declaration

I, the undersigned, hereby declare that the work contained in this dissertation is my own original work and has not previously in its entirety or in part been submitted at any university for a degree.

Abstract

The advent of new high energy product permanent magnet materials has opened great opportunities for novel electrical machine topologies with advantageous features such as high efficiency and high power/weight ratio. Amongst others, axial field permanent magnet (AFPM) machines with ironless stators are increasingly being used in power generation applications. Because of the absence of the core losses, a generator with this type of design can operate at a substantially high efficiency. Besides, the high compactness and disc-shaped profile make this type of machine particularly suitable for compact integrated power generation systems. Due to construction problems, the generator application of this type of machine has been limited to quite a low power range. There is a need to investigate the performance capability of this type of AFPM machine in the upper medium power level.

The focus of this thesis is on the design optimisation of the air-cooled AFPM generator with an ironless stator. A design approach that directly incorporates the finite element field solution in a multi-dimensional optimisation procedure is developed and applied to the design optimisation of a 300 kW (at unity power factor) AFPM generator. To enable an overall design optimisation of the machine, different design aspects, such as the cooling capacity, the mechanical strength and eddy loss, are also studied in this research.

To enable the free movement of the rotor mesh with respect to the stator mesh, the air-gap element originally proposed by Razek et. al. is derived for Cartesian coordinate systems. For minimising the large computation overhead associated with this macro element, a number of existing time-saving schemes have been utilised together with the derived Cartesian air-gap element. The developed finite element time-step model is applied to calculating the steady-state performance of the AFPM machine.

Since the flux distribution in an AFPM machine is three dimensional by nature, calculating the eddy current loss by merely using a simple analytical method may be subject to a significant error. To overcome this problem, the two dimensional finite element field modelling is introduced to perform accurate field analysis. To exploit the full advantages of the two-dimensional finite element modelling, a multi-layer approach is proposed, which takes into

account the variation of the air-gap flux density in the conductors with regard to their relative positions in the air-gap. To account for the radial variation of the field, a multi-slice finite element modelling scheme is devised.

The thermal analysis is an important aspect of the design optimisation of AFPM machines. From a design point of view, it is preferable to have a simple but effective method for cooling analysis and design, which can easily be adapted to a wide range of AFPM machines. In this thesis a thermofluid model of the AFPM machine is developed. The fluid flow model is needed for calculating the air flow rate, which is then used to find the convective heat transfer coefficients. These are important parameters in the subsequent thermal calculations.

Experimental investigations have been carried out to verify each of the above-mentioned models/methods. With these models implemented, the design optimisation of an air-cooled ironless stator 300 kW (at unity power factor) AFPM generator is carried out. The performance measurements done on the fabricated prototype are compared in this thesis with predicted results. The study shows that the proposed design approach can be applied with success to optimise the design of the AFPM machine. The advantages of high power density, high efficiency, no cogging torque and good voltage regulation make this type of AFPM machine very suitable for power generator applications. The optimum steady-state performance of the AFPM machine shows that this machine with an ironless stator is an excellent candidate for high speed power generator applications, even in the upper medium power level. The good cooling capacity of this type of machine holds the promise of its being a self-cooled generator at high power ratings.

Opsomming

Die uitvinding van nuwe hoë energiedigtheid permanent magneet materiale het groot geleenthede vir nuwe elektriese masjien topologië laat ontstaan met voordelige eienskappe soos hoë benuttingsgraad en hoë drywing/gewig verhouding. Onder andere word die aksiaalveld permanente magneet (AVPM) masjiene met kernlose stators toenemend gebruik vir elektriese generator toepassings. As gevolg van die afwesigheid van kernverliese kan 'n generator met hierdie tipe ontwerp teen 'n aansienlik hoë benuttingsgraad werk. Daarbenewens maak die hoë kompaktheid en skyfvorm-profiel die masjien in besonder geskik vir die ontwikkeling van kompak geïntegreerde drywing generator stelsels. As gevolg van konstruksie probleme is die toepassing van hierdie tipe masjien as generator beperk tot redelik lae drywingsgebiede. Dit is nodig om die werkverrigtingsvermoë van hierdie tipe AVPM masjien in die boonste medium drywingsgebied te ondersoek.

Die fokus van hierdie tesis is op die ontwerp-optimering van 'n lugverkoelde AVPM generator met 'n kernlose stator. 'n Ontwerpsbenadering wat die eindige element veldoplossing in 'n multi-dimensionele optimeringsprosedure insluit, is ontwikkel en toegepas op die ontwerpsoptimering van 'n 300 kW (by eenheidsarbeidsfaktor) AVPM generator. Om 'n globale ontwerpsoptimering van die masjien te kan doen is verskillende ontwerpsaspekte soos die verkoelingskapasiteit, meganiese sterkte en werwelverliese ook in hierdie navorsing bestudeer.

Om die vrye beweging van die rotormaas ten opsigte van die statormaas te verseker is die lugspleet-element, soos oorspronklik deur Razek et al voorgestel, afgelei vir Cartesiaanse koördinaat stelsels. Om die lang berekeningstyd geassosieer met hierdie makro-element te minimaliseer is 'n aantal bestaande tydbesparende metodes saam met die ontwikkelde Cartesiaanse lugspleet-element gebruik. Die ontwikkelde eindige element tydstapmodel is toegepas om die bestendige werkverrigting van die AVPM masjien te bereken.

Aangesien die vloedverspreiding in 'n AVPM masjien van nature drie-dimensioneel is, kan die berekening van die werwelstroomverliese tot aansienlike foute lei as eenvoudige analitiese metodes gebruik word. Om hierdie probleem te oorkom is twee-dimensionele eindige element modellering gebruik om akkurate veld-analise te doen. Om die volle voordele van die twee-

dimensionele eindige element modellering te eksploiteer is 'n multi-laag benadering voorgestel wat die variasie van die lugspleetvloeddigtheid in die geleiers met betrekking tot hulle relatiewe lugspleetposisies in ag neem. Om voorsiening te maak vir die radiale variasie van die veld, is 'n multi-skyf eindige element modelleringstegniek ontwikkel.

Die termiese analise is 'n belangrike aspek van die ontwerpsoptimering van AVPM masjiene. Vanuit 'n ontwerpsoogpunt is dit verkieslik om 'n eenvoudige maar tog effektiewe metode van verkoelingsanalise en -ontwerp te hê wat maklik toegepas kan word op 'n wye reeks van AVPM masjiene. In hierdie tesis word 'n termovloeimodel van die AVPM masjien ontwikkel. Hierdie vloeimodel is nodig vir die berekening van die lugvloeitempo, wat op sy beurt weer nodig is om die konveksie hitte-oordrag koëffisiënte te bepaal. Hierdie is belangrike parameters in die opvolgende termiese berekeninge.

Eksperimentele ondersoek is uitgevoer om elkeen van die bogenoemde modelle en metodes te verifieer. Nadat hierdie modelle geïmplimenteer is, is die ontwerpsoptimering van 'n 300 kW (by eenheidsarbeidsfaktor) lugverkoelde kernlose stator AVPM generator uitgevoer. Die werkverrigtingmetings gedoen op 'n vervaardigde prototipe masjien, word in hierdie tesis vergelyk met voorspelde resultate. Daar word getoon dat die voorgestelde ontwerpsbenadering met sukses toegepas kan word om die ontwerp van die AVPM masjien te optimeer. Die voordele van hoë drywingsdigtheid, hoë benuttingsgraad, geen vertandingsdraaimomente en goeie spanningsregulasie maak hierdie masjien baie aantreklik vir generator toepassings. Die optimum bestendige werkverrigting van die AVPM masjien toon dat hierdie masjien met 'n kernlose stator 'n goeie kandidaat is vir hoë spoed generator toepassings, selfs in die boonste medium drywingsgebied. Die goeie verkoelingskapasiteit van hierdie tipe masjien hou die belofte in van'n selfverkoelde generator by hoë drywing aanslae.

Acknowledgements

The author is greatly indebted to Prof. M.J. Kamper, for sharing his expertise and for his guidance throughout the research and his efforts to ensure the availability of financial resources for this research.

He wishes to express his gratitude to Dr. T.J. Flack of the Engineering Department, Cambridge University, U.K., Dr. H. Mohellebi of the University of Mouloud MAMMERI, Algeria, Dr. J.D. Buys of the Department of Mathematics, Stellenbosch University, and Prof. M. Feliachi of the CRTT, Bd de l'Université, France for the useful discussion and the help with verifying the Cartesian Air-Gap Element (CAGE).

He is grateful to Mr. R.T. Dobson of the Department of Mechanical Engineering for his guidance regarding the thermofluid analysis and his interests in the project.

He wishes to thank Mr. K. van der Westhuizen of the Department of Mechanical Engineering for his help with the mechanical strength analysis.

My gratitude also to Prof. S.G. McLaren and his wife Gwen McLaren for proof-reading my thesis and constant encouragements.

He would like to thank the staff members of the Departmental Workshop, Electrical Machines Laboratory, and the Centre for Mechanical Services, especially to Mr. J. Blom, Mr. J. Weerdenburg, Mr. P. Petzer, Mr. A. Swart, Mr. P. Fick, and Mr. A. Dale for their assistance in building and testing the experimental machines.

Many thanks to the University of Stellenbosch (US) and Ecocrete Ltd. for the financial assistance to the project.

To my wife, my parents
and my grandmother in memory

Contents

List of Figures

List of Tables

List of Symbols

Symbols

A	cross-section area of a flow path (m^2), magnetic vector potential (Wb/m)
A_c	cross-section area of a coil (m^2)
A_{con}	cross-section area of a conductor (m^2)
A_{cu}	active copper area of one side of a coil (m^2)
B	flux density (T)
B_{m1}	amplitude of first harmonic of main flux density (T)
B_g	air-gap flux density (T)
B_r	remanent magnetic flux density of the permanent magnet (T)
C_{mo}	moment coefficient
c_p	specific heat at constant pressure (J/kg K)
D	diameter of round ducts (m)
D_h	hydraulic diameter (m)
D_o	outer diameter of electric machine (m)
D_t	the total outer diameter of the machine (m)
E_d, E_q	steady-state values of the $d-$ and $q-$axis induced EMF components (V)
E_{ph}	r.m.s. value of fundamental phase EMF (V)
F	friction force (N), energy functional
F_{12}	shape factor of two surfaces involved in radiation
f	friction factor, frequency (Hz)
G	gap ratio, $\frac{s}{r_o}$
g	gravitational acceleration (m/s^2), ratio of l_g/r_o
Gr	Grashof number
H	magnetic field strength (A/m)
H_c	coercive force of permanent magnet (A/m)
h	local heat transfer coefficient (W/m^2 K)
i_{abc}	instantaneous currents of phases a, b and c (A)
I_d, I_q	steady-state values of $d-$ and $q-$axis stator current components (A)
I_{ph}	phase current of the machine (A)
I_s	space phasor of stator current (A$\angle$rad.)

i	enthalpy (J/kg)
J	current density (A/m^2)
J_{rms}	r.m.s. current density (A/m^2)
k	thermal conductivity (W/m K), pole-arc to pole-pitch ratio
K_ϕ	ratio of electrical loading on rotor $K_\phi = 0$ for AFPMs
K_e	EMF factor combining winding distribution factor and k_p ratio
K_i	current waveform factor
K_l	ratio of D_o/L_e
K_p	pole width to pole pitch ratio
$[K_p]$	Park's transformation
K_r	machine diameter ratio D_i/D_o
k_f	filling factor
k_i	loss coefficient
k_p	electrical power waveform factor
k_r	machine radius ratio r_i/r_o
k_s	slip factor
k_{w1}	winding distribution factor
L, l	length of the flow path, active length of a coil (m^2)
L_d, L_q	$d-$ and $q-$axis synchronous inductances (H)
L_e	end-winding inductance per phase (μH)
l_e	total end-winding length of a coil (m)
L_{es}	effective stack length of the machine (m)
l_g	air-gap length (m)
l_{ip}	inter-pole gap length (m)
l_m	permanent magnet height (m)
l_s	length of a single-turn coil (m)
m	number of phases
m_1	number of phases for each stator
M_o	momentum (N $\cdot$ s)
$\dot{m}$	mass flow rate (kg/s)
n	machine rotation speed (r.p.m.)
n_a	number of parallel circuits per phase
n_b	number of blades
N_c	number of turns per coil
N_{ph}	number of turns in series per phase
n_s	number of coils in series per phase
Nu	Nusselt number
P	power (W)
p	pressure (Pa), number of poles
P_{cu}	copper losses (W)

P_{dev}	developed power (W)
P_e	eddy current losses (W)
P_f	power factor
P_{in}	input shaft power (W)
P_{out}	output power (W)
P_r	Prandtl number
$\wp$	wetted perimeter (m)
$\dot{Q}$	heat transfer rate into a system (W)
Q	volumetric flow rate (m^3/s)
q	number of slots per pole per phase
R	thermal resistance (K/W)
R or r	radius (m)
R_a	Rayleigh number
R_e	Reynolds number, per phase eddy loss resistance (Ω)
r_i	inner radius of the rotor disc (m)
r_o	outer radius of the rotor disc (m)
R_{ph}	per phase stator resistance (Ω)
$[S]$	assembled global stiffness matrix
s	axial clearance between rotor and stator (m)
T	temperature (°C or K), torque (Nm)
t	thickness (m)
t_{cu}	thickness of the stator (m)
U	internal energy (J/kg)
u_1, u_2	inlet, outlet tangential velocity (m/s)
v_1, v_2	inlet, outlet absolute velocity (m/s)
V_d, V_q	steady-state values of $d-$ and $q-$axis stator voltage components (V)
V_m, V_y, V_{cu}	volume of magnet, rotor yoke and copper, respectively (m^3)
V_s	space phasor of stator voltage (V$\angle$rad.)
$\dot{W}$	rate of doing work (W)
w_1, w_2	inlet, outlet radial velocity (m/s)
W_m, W_y, W_{cu}	weight of magnet, rotor yoke and copper, respectively (kg)
z	number of turns per coil

Greek symbols

α	power factor angle, slot pitch angle
ρ	density (kg/m^3)
ρ_t	resistivity of copper at temperature t (Ωm)
β	coefficient of thermal expansion (K^{-1})

ϵ	emissivity
σ	Stefan-Boltzmann constant ($W/m^2\ K^4$)
ω	angular speed (rad/s)
μ	dynamic viscosity (kg/m s), magnetic permeability (H/m)
τ	angular ratio of PM to channel
τ_p	pole pitch (m)
ϕ_p	flux per pole (Wb)
ν	kinematic viscosity (m^2/s)
λ_T	turbulent parameter
λ_{abc}	instantaneous values of total flux linkages of phases a, b and c (Wb)
λ_{abc1}	instantaneous values of fundamental flux linkages of phases a, b and c (Wb)
λ_{abc3}	instantaneous values of total 3^{rd} harmonic linkages of phases a, b and c (Wb)
λ_m	flux linkage generated by permanent magnets (Wb)
λ_r	space phasor of total stator flux linkages (Wb/*angle*rad.)
λ_d, λ_q	$d-$ and $q-$axis fundamental stator flux linkage components (Wb
γ	equivalent sand grain roughness (m)
Δ	finite difference
η	machine efficiency
θ_{ip}	inter-pole angle (rad.)
θ_m	pole arc angle (rad.)
θ_p	pole pitch angle (rad.)

Subscripts

a	surrounding air
ag	air-gap
amb	ambient
c, *conv*	convection
cs	control surface
cu	copper
cv	control volume
cond or *d*	conduction
dev	developed
e	environment, exit
edy	eddy current
f	friction
h	hydraulic
l	leakage

i	in, inlet
l	energy losses
m	magnet
mo	moment
out	output
p	periphery
r	radiation, rotor
rms	root mean square value
T	turbulent
t	total
wf	windage and friction

Abbreviations

AFM	Axial field machine
AFPM	Axial field permanent magnet
AGE	Air-gap element
CAGE	Cartesian air-gap element
CFD	Computational fluid dynamics
EMF	Electromotive force
FDM	Finite difference method
FE	Finite element
FEM	Finite element method
GA	Genetic algorithm
MMF	Magnetomotive force
PBIL	Population based incremental learning
PM	Permanent magnet
RFM	Radial field machine
RFPM	Radial field permanent magnet
THD	Total harmonic distortion

Overscores

$\bar{}$	average, mean
$\dot{}$	per unit time

Chapter 1

Introduction

1.1 Historical background

The history of electrical machines reveals that the earliest machines were axial field machines (AFMs) though conventional radial field machines (RFMs) became immediately dominant ever since their invention in the early 1830s.

The first primitive working prototype of AFMs ever recorded was Faraday's disc (1821). However, shortly after Davenport (1837) claimed the first patent for a RFM, it has been widely accepted as the mainstream configuration for electrical machines [10, 27]. The reasons for shelving the AFM were multi-fold and may be summarised as follows [21, 49, 61, 63, 100]:

- strong magnetic attraction force between rotor and stator,
- construction difficulties such as cutting slots in laminated cores (slotted version),
- high manufacturing costs involved in fabricating the laminated stator cores.

Although the first PM excitation system was applied to electrical machines as early as the 1830s, the poor quality of hard magnetic materials soon discouraged their use. The invention of Alnico (1932) and especially the rear-earth Neodymium-Iron-Boron (NdFeB) material (1983) have made a *comeback* of the PM excitation system possible.

It is generally believed that the availability of high field PM materials (especially *rare earth* PMs) is the main driving force for exploitation of novel machine topologies and has thus revived AFMs. A fair amount of research work on axial field PM machines has been carried out in both academic institutes and industrial sectors [11, 24, 44]. With a view of achieving performance specifications beyond those of the conventional motor, a new range of AFMs has been evolving.

The market price of rare-earth PMs has been following a stable descending curve in the last decade. A recent small-scaled market survey by the author showed that the *NdFeB PMs* could be purchased in China for less than *US$ 20* per kilogram (2000). With the availability of more and more affordable PM materials, it can be expected that AFMs will play a more important role in the 21^{st} century.

1.2 Axial field machines versus radial field machines

In pace with the application of new materials, innovation in manufacturing technology and the improvements in cooling techniques, further reduction in the weight per unit output of the electrical machine has been made possible. There is an inherent limit to this reduction for machines designed with conventional radial field configurations because of [9, 27, 44, 63, 73]:

- the bottle-neck feature for the flux path at the root of the rotor tooth (see Fig. 1.1(a)),
- cooling problems as a result of the relatively small air-gap volume, and
- much of the rotor core around the shaft is hardly utilised as a magnetic circuit.

These limitations are inherently bound with radial field structures and cannot be removed easily unless a new topology is adopted. The AFM, recognised as having a higher power to weight ratio than that of the RFM, is an attractive alternative to its radial field counterpart [8, 27, 44, 63].

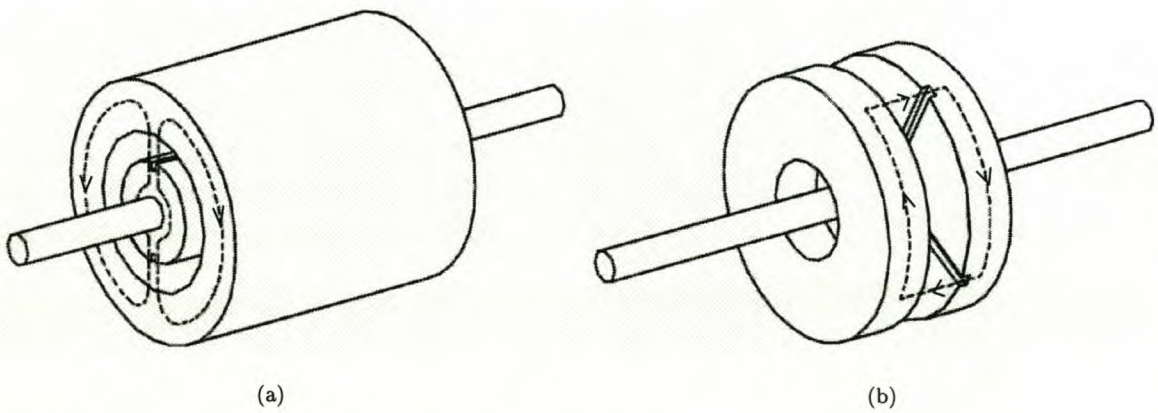

(a) (b)

Figure 1.1: Typical machine structures of (a) radial field machine (RFM) (b) axial field machine (AFM).

Moreover, since the inner core diameter of AFMs is usually much greater than the shaft diameter (see Fig. 1.1(b)), better ventilation and cooling can be expected. In general, the special

properties of AFMs, which are considered advantageous over RFMs in certain applications, can be summarised as follows:

- AFMs have a planar and somewhat adjustable air-gap,
- AFMs usually have a larger diameter to length ratio,
- accessibility of the pole faces facilitates the installing and testing of the machine,
- capability of being designed to possess a higher power to weight ratio with substantial saving in core material,
- the topology of the magnetic circuit of the AFM can be readily varied so that diverse types of AFM may be designed,
- the larger the outer core diameter, the higher the number of poles that can be accommodated, making the AFM a suitable choice for high frequency or low speed operations.

Consequently, axial-field type machines are particularly suitable for certain special-purpose applications where their properties offer distinct advantages over their conventional radial-field counterparts. Some published work dealt with quantitative investigations of RFM and AFM configurations in terms of sizing and power density equations [3, 27, 56, 112]. The comparison between a conventional radial field PM machine and a number of axial field PM machines of different configurations is given in [92], which shows that the AFM has a smaller volume and less active mass for a given power rating than the RFM.

1.3 Classification of PM axial field machines

In principle each type of RFM should have its corresponding AFM version. Generally axial field permanent magnet (AFPM) machines are classified into:

- d.c. commutator machines,
- d.c. brushless machines,
- a.c. synchronous machines.

Similar to its radial field counterpart, the AFPM d.c. commutator machine uses PMs to replace the electromagnetic excitation system. It is still a versatile and economical choice for certain industrial applications such as fans, blowers, power tools, domestic appliances, etc. Practically, brushless d.c. and a.c. synchronous machines have almost the same structure, though their theory and operation principles are quite different. The main difference is in the shape of the operation current waveform. Precisely they are defined as follows [44, 50, 70]:

- The brushless d.c. machine generates a trapezoidal back-EMF waveform and is operated with a rectangular line current waveform (also called a *square-wave* machine)
- The a.c. synchronous machine generates a sinusoidal back-EMF waveform and is operated with sinewave currents (also called a *sinewave* machine)

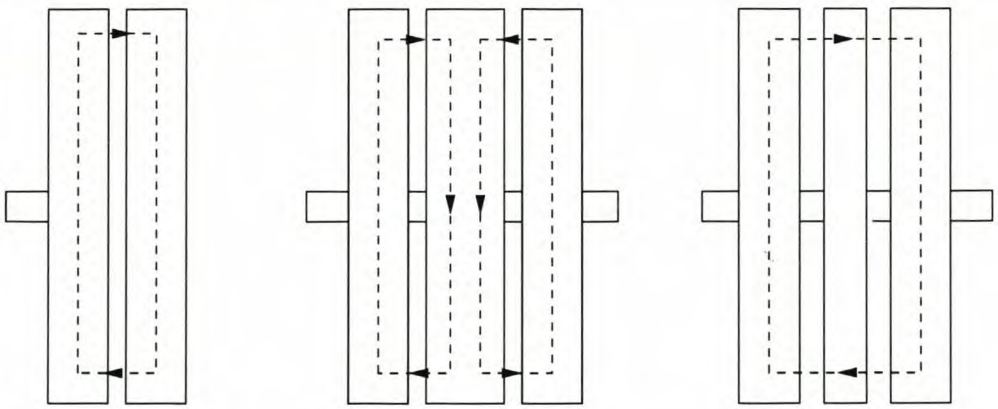

Figure 1.2: Typical topologies of AFMs: (a) single-sided AFM, (b) double-sided AFM, centre element with yoke, and (c) double-sided AFM with a yokeless or coreless stator.

From a construction point of view, AFPM machines can be designed as single-sided or double-sided motors, with or without armature slots, with armature core or coreless, with internal or external PM rotors, with surface mounted or interior PMs and with a single stage or multi-stage. In the case of double-sided configurations (also known as *sandwiched* structures), either the internal stator or internal rotor arrangement can be adopted. The first choice has the advantage of using fewer PMs at the expense of poor winding utilisation while the second one is considered as a particularly advantageous machine structure [12]. The typical topologies of AFMs are illustrated in Fig. 1.2 where the arrows indicate the flux directions.

Slotless armature winding (also called *airgap winding*) arrangements were used with the earliest machines. Chalmers et al compared the slotless armature winding with conventional slotted winding in [24], which details its advantages (e.g. improvement of cogging torque, flux ripple, acoustic noise, saturation, rotor losses, etc.) and disadvantages (e.g. lower winding inductances, higher eddy current losses).

Depending on the application and operating environment, slotless stators may have armature cores or be completely ironless. Ironless configurations eliminate any iron from the armature, thus making the associated eddy current and hysteresis core losses insignificant. It is interesting that slotless AFPM machines are often classified according to their winding arrangements

and coil shapes, namely, *toroidal*, *trapezoidal* and *rhomboidal* forms [12, 24, 37].

A typical example of a toroidal stator PM slotless AFM is the *'TORUS'* developed at the *University of Manchester Institute of Science and Technology* [94, 95]. An AFPM machine with a disc shaped ironless armature was introduced by Campbell (1972) in [7, 8]. This novel design was to a great extent due to the pioneer electric vehicle projects. Researchers at the *University of Rome, La Sapienza* showed more interest in AFPM machines with water cooled ironless stators using rhomboidal shape coils [12, 14, 16, 18]. An air-cooled AFPM machine with an ironless stator was built at the *University of Stellenbosch, South Africa* in 1996, which has proved to be well suitable for high speed applications [64].

1.4 Sizing of axial field machines

It is not an easy task to compare different type of electrical machines. One traditional method is to use the $D_g^2 l_e$ sizing equation, which compares the machines' power on the basis of machine airgap volume. With the evolution of new machine topologies such as AFMs, quantitative studies of the power potential of vastly different machine structures are clearly needed.

The existing traditional sizing equations were primarily for RFMs characterised by *one stator and one rotor* configuration. AFMs, however, often comprise multiple stators/rotors, which implies multiple airgaps. A comparison of the power between AFM and RFM structures was made in [63] by considering the product of total magnetic and electrical loading in each machine. However, the comparison was neither complete nor systematic. Zhang et al [112] compared surface mounted radial field permanent magnet (RFPM) machines with several slotted AFPM machines by using the traditional sizing equation. However, the inconsistent definition of machine volume between RFPM machines and AFPM machines may raise the question of this comparison's fairness.

With a view of eliminating the deficiencies of traditional sizing equations, Huang et al developed the general purpose sizing and power density equations in 1996 [55], in which power density was compared on the basis of total machine volume instead of airgap volume. Special factors were introduced to account for the effects of non-sinusoidal current and back-EMF waveforms. A detailed approach of applying the general purpose sizing equations to AFPM machines was also presented in [56], in which the dual sizing equation for AFPM machines was given as:

$$P_{out} = \frac{1}{1+K_\phi} \cdot \frac{m}{m_1} \cdot \frac{\pi}{2} \cdot K_e \cdot K_i \cdot k_p \cdot K_l \cdot \eta \cdot B_g \cdot A \cdot \frac{f}{p} \cdot (1-K_r^2) \cdot \frac{1+K_r}{2} \cdot D_o^2 \cdot L_{es} \quad (1.1)$$

The overall power density of the AFPM machine is expressed as [56]

$$\xi = \frac{P_{out}}{\frac{\pi}{4} \cdot D_t^2 \cdot L_{es}} \tag{1.2}$$

where D_o is the outer diameter of the armature yoke, D_t is the total outer diameter of the practical machine, and $K_r = D_i/D_o$ is the machine inner/outer diameter ratio.

Both toroidal and double-stator AFPM machines were compared with the conventional induction machine and showed to have higher power densities. The developed sizing equations offer an easy and systematic tool for evaluating capabilities of different machine topologies, despite the fact that their compatibility and fairness still need to be investigated. It has been found that the outer diameter of the stator, D_o, is the most important dimension of AFPM machines and since $D_o \propto \sqrt[3]{P_{out}}$, the outer diameter increases rather slowly with the increase of output power [44]. Therefore, theoretically AFPM machines are preferred for medium to large power applications [44, 56].

1.5 Applications of AFPM machines

The advent of new high-field permanent magnet materials has opened great opportunities for novel topologies of electrical machines with advantageous features such as high efficiency and high power to mass ratio. The disc-type configuration, with axially-directed magnetic field crossing the airgap, has remarkably short axial length and is well suited for operation either as generator or motor. The potential and/or implemented applications are described in the following sections.

Power generator application

The generator application of AFPM machines was always limited to lower power range due to construction and heat dissipation problems. Benefiting from the rapid advances in the fields of material science and industrial technologies, there were attempts to design disc type permanent magnet generators with much higher power ratings [14, 71, 100].

- In view of their disc-shaped profile, AFPM machines are particularly suitable for the development of compact integrated generation systems, which can be used as
  - micro-generating units in remote areas
  - auxiliary power units for military applications [24]
  - aerospace generators for unmanned aircraft and spacecraft [3]
  - integrated flywheel energy storage units (also known as *electromechanical batteries*) for rural area power supply

- With the capability of directly coupling with a wind/hydro turbine and therefore the elimination of a gearbox, the AFPM machine is an attractive solution for
  - wind power generators [24, 75, 93] and
  - small hydro and tidal generators

Electric vehicle and marine propulsion drives

Due to its compactness, high power density and good efficiency, the AFPM machine is an attractive candidate for direct motor-in-wheel drives for electric vehicles [7]. Intensive research has been undertaken by researchers worldwide [12, 16, 86, 66, 105], which has resulted in some viable designs, e.g.

- electric wheelchair drive with *air-cored* stator [11]
- electric scooter drive with *TORUS* configuration [12]
- multi-stage water-cooled electric vehicle (EV) drive with *ironless* stator [16]
- single-stage EV wheel motor drive with *internal* rotor and *interior* PMs [86]
- in-wheel solar-powered vehicle drives (with an efficiency up to 98%) [66, 82]

The use of AFPM machines for EV drives is still facing issues related to costs, cooling means, PM temperature tolerance and optimised control. With an increased number of poles, AFPM machines are suitable for high torque and low speed operation, which makes them a good choice for direct driving of ship propellers [20].

Industrial drives

The printed circuit motor, making use of an ironless disc-rotor, has a low inertial and linear response for control applications. It has been the most widely used AFM in industry for decades [27, 35]. Nowadays, applications of AFPM machines in industrial drives such as fans [47], pumps [13], robots [61, 62] and automation processes is increasing.

Portable consumer products and domestic appliances

Brushless d.c. AFPM machines have been widely used in portable consumer products (e.g. camcorders, headphone stereos, compact disc players, [98] etc.) and domestic appliances such as ceiling fans, food processors, hand-held machine tools, etc. The list of applications in this area is still growing.

1.6 Literature review

The majority of the research work that has been devoted to the AFPM machines was concerned with design criteria, construction techniques and performance analysis. Some earlier published work outlined the difference between AFMs and RFMs and contributed to the general theory of the AFM [8, 9, 36, 37], which formed a useful basis for further research. With the advent of new high field PMs and the advances in power electronics technology, many novel machine topologies have appeared since the last decade [12, 14, 16, 18, 66, 82, 85, 87, 111]. Among these novel designs the configuration consisting of two outer rotor discs (with surface-mounted PMs) and one internal toroidally-wound slotless stator has been studied extensively [12, 15, 17, 19, 57, 94, 95].

1.6.1 Theory of the AFM

AFMs differ substantially from conventional RFMs in machine structure and the direction of flux in the airgap. For AFMs, the torque is produced over a continuum of radii, not just at a single radius as in cylindrical machines. Without any specific theory derived for this type of machine, the earlier design and construction of AFMs in industry was mainly based on the theory and experience of conventional RFMs.

Campbell [8] derived important theoretical principles of the AFM in 1974. Although the derivation was based on an ironless d.c. commutator AFPM machine, the results can be applied generally to all AFMs. The difference in the analysis of RFMs and AFMs was studied and stressed. The important design parameters such as *pole-arc to pole-pitch* ratio K_p and stator *inner to outer radii* ratio K_r were established resulting in some key design criteria. Amongst others, the optimum K_r for achieving maximum output armature power has been frequently applied to AFPM machines design ever since.

Theoretically, Campbell's contribution to the AFMs is significant. However, the inseparability of magnetic flux density from radial dimension discouraged further exploration of this theory. Therefore, it has to be assumed that such a dependence should be removed otherwise a specific magnetic loading independent of machine dimensions may never be defined [8]. Once this assumption is made, the inherent difference between RFMs and AFMs becomes indistinct. Quite often the existing conventional machine theory could be applied to AFPM machines without much modification.

1.6.2 Aspects of magnetic design

Magnet placement

For AFPM machines with slotted core stator, the mounting of PMs could be accomplished by three means, i.e. inset [113], surface-mounted [111], or interior types [86, 87, 113]. Amongst others, AFPM machines with surface-mounted PMs usually possess a relatively large airgap, low q-axis reactance, and near unity saliency ratio, which made them not ideally suitable for synchronous operation. However, the magnetic non-saliency nature of the rotor disc partly removes the source of additional cogging torque. Besides, the physically salient PM poles operate naturally as a fan so that improved ventilation can be achieved. From a construction point of view, surface-mounting of PMs is easy to realise. Thus, it is the most popular choice.

Most of the coreless AFPM machines developed so far have surface-mounted PM poles since with the large airgap winding, the benefits introduced by flux concentration are reduced or even cancelled. Although the surface-mounted design will further increase the reluctance of the magnetic circuit, since the recoil permeability of the PM is close to that of air, the use of high-field PMs could maintain a reasonable level of flux density in the airgap. Besides, the surface-mounted design allows larger stator current before the PM is irreversibly demagnetised and effects of armature reaction could in addition be eliminated. In general, surface mounting of PMs has been considered as undesirable, but necessary [57].

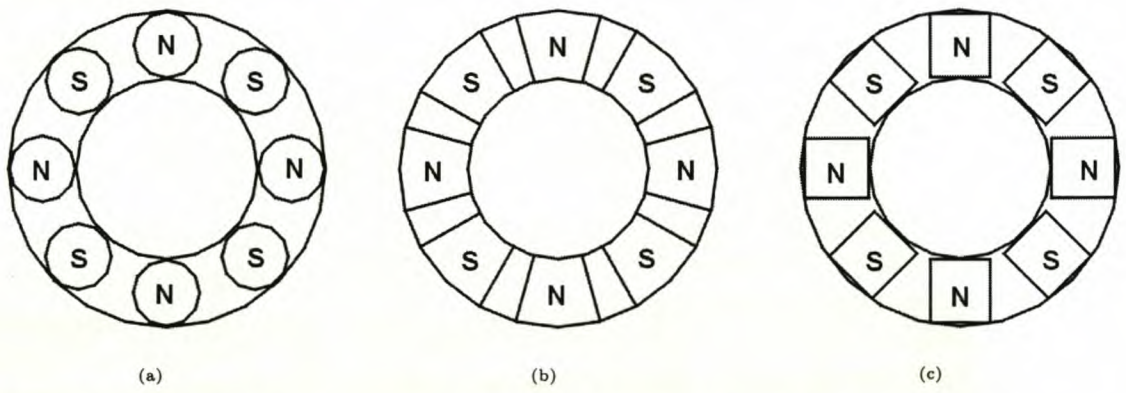

Figure 1.3: Different PM poles used in AFPM machines: (a) circular PM poles, (b) annular sector PM poles and (c) rectangular PM poles.

Pole shape

At an early stage, circular PM poles (Fig. 1.3a) were commonly used in AFPM machines, e.g. the printed circuit motor. In 1975, Campbell compared the circular shape and annular sector shape (Fig. 1.3b) PM poles for AFPM machines and found that the latter could produce much

greater useful flux per pole [9]. To date the annular sector shape has been a popular profile for the surface-mounted PM poles of AFPM machines. In electromagnetic interaction, if the magnet side edges sweep the stator conductors in a relative motion all along their height, a more rectangular waveform of flux distribution is realised, which is desirable for brushless d.c. design.

On the other hand, nowadays, the most common shapes for industrial PMs production are the parallelepiped and cylinder shapes [21], though many special shapes of PM can be manufactured without great technique difficulties. Cutting magnets into desired shapes would inevitably lead to a loss of material. In order to save PM material and therefore to reduce the total cost of the machine, standard PM pieces with rectangular cross-section (Fig. 1.3c) have been proposed [94]. This option sounds quite reasonable for designing sinusoidal AFPM machines, since the overlapping between PM and conductors takes place gradually resulting in a more sinusoidal shape of induced EMF waveform [60]. To further improve the airgap flux profile of the sinusoidal machine, surface-mounted PMs with pole shoes may be considered. This might result in a more sinusoidal flux distribution in the airgap and improve the machine's saliency, but their practicality is a subject for future investigation.

Halbach versus conventional array

It was found that the maximum airgap flux density per unit rotor mass can be achieved with a solid PM rotor (*without back iron*) in an arrangement often called a *Halbach* assembly. Optimisation predicted that a design with a Halbach PM arrangement would have approximately 20% less leakage loss than an equivalent conventional arrangement of the same total mass, with the magnets on the back iron [66].

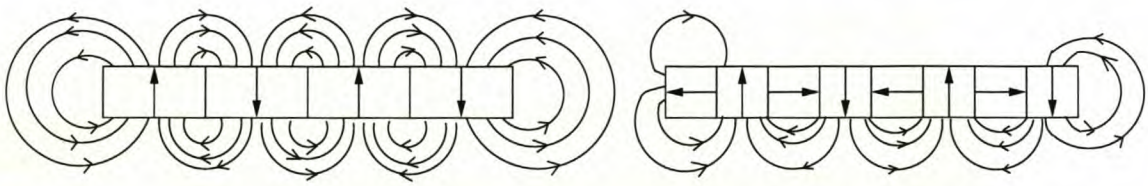

(a) (b)

Figure 1.4: Illustration of flux distribution of (a) a conventional magnet array and (b) a simplified Halbach magnet array.

The ideal Halbach magnet arrangement is the one whose magnetisation direction rotates continuously in a sinusoidal fashion, which is very difficult to realise in reality. Discrete sets of magnets are often used to approximate the ideal array. Since a set of magnets with different

magnetisation direction are needed for each pole, the Halbach magnet array is a more expensive choice when compared with the conventional magnet array. To further simplify the fabrication it is useful to consider a Halbach array consisting of only radial and azimuthal magnetisations [66, 77]. The flux distribution of a conventional magnet array and a simplified Halbach magnet array is illustrated in Fig. 1.4.

Comparative studies of torque production of Halbach and conventional surface-mounted PM synchronous motors was presented in [77]. It has been concluded that the Halbach array always produces higher torque than the conventional array for the same volume of the PMs when no magnetic back iron is present. However, with magnetic back iron the conventional array, with optimised pole-arc to pole-pitch ratio, produces higher torque than the Halbach array up to a certain thickness of the magnets. Above this thickness, the Halbach array again produces a higher torque.

K_r and K_p

In the designing of AFPM machines, the most important design parameters which could greatly affect the machine's performance are the inner to outer radius ratio K_r and the pole-arc to pole-pitch ratio K_p. Almost all the published work relating to the design and performance calculation of AFPM machines is concerned with optimal determination of these parameters [8, 17, 19, 27, 56, 57, 63].

Campbell [8] was probably the first one to identify the importance of K_r. He proved that for AFPM machines, the maximum armature power would be achieved if $K_r = \sqrt{3}$. The subsequent research by other scholars [17, 60] showed that the torque or maximum torque per loading could be realised if the same condition is met. In practical machine design, it should be noted [17, 27, 56, 60] that reducing the optimal value of K_r to a single numeric value is inappropriate since, in fact, it depends on machine topology, frequency, material, and electrical and magnetic loading. However, for a specific machine topology, K_r remains in a relatively narrow band.

Attempts to relate other desired design objectives to K_r were also reported. As an example, Leung et al [63] looked at the optimum K_r for obtaining the maximum power to inertia ratio. In [17], the authors investigated the difference in selecting K_r for realising maximum output torque and maximum torque/weight in the design of the AFPM machine. It was found that with a high number of poles, the maximum efficiency corresponds to a K_r-value which is close to the one which maximises the torque/weight. However, with a low number of poles, the efficiency versus K_r exhibits a flat trend, so that almost the same machine efficiency could be achieved from values of K_r which maximise either the torque or the torque/weight.

The PM pole-arc to pole-pitch ratio K_p is also crucial to a good and cost effective design. This parameter is of great importance since it determines the cost of the PMs and thus the machine. It was found that increasing the width of the PM will increase the flux linkage and leakage as well. Decreasing its width will reduce flux linkage greatly but the reduction of leakage will not be proportional [19]. The 3-D FEM optimisation results showed that K_p should be between 0.75 to 0.85 ($> 2/3$) for brushless d.c. AFPM machine [47] while for sinusoidal AFPM machine, K_p is generally kept as $2/3$ [60].

1.6.3 Aspects of electrical design

Winding utilisation

Unlike RFMs, AFMs may have two working surfaces. The combinations of two rotors with one stator or one rotor with two stators are available. With two stators, less than one half of the copper produces torque, and the majority of the copper produces only heat, which is undesirable. Conversely, with two rotors, as much as three quarters of the winding can be used to produce torque for a toroidally-wound stator, compared with one third to one half for a conventional winding placed in slots [57]. A trapezoidal winding also has a high winding usage though its end-winding may be somewhat longer than that of a toroidally wound winding.

Coil profiles

A trapezoidal shape coil (Fig. 1.5(a)) allows the maximum coil flux linkage, as each coil side embraces the entire pole area. But trapezoidal coils have end-windings of significant length if compared with the length of the active side conductors. Therefore their use leads to a low value of torque being produced per unit of I^2R losses, which is generally undesirable for most machine applications, unless a high number of poles are used resulting in shorter end windings. The toroidally wound coil (Fig. 1.5(b)) has been widely used for the slotless AFPM machine with an iron core.

Much higher values of torque per unit I^2R losses can be achieved by means of winding coils of rhomboidal shape (Fig. 1.5(c)). The length of the end-winding is greatly reduced due to the inclined arrangement of the coil's active sides. In an AFPM machine with a rhomboidal-coil ironless stator winding, the EMF is nearly sinusoidal, whereas iron-cored AFPM machines tend to produce a trapezoidal EMF. The sinusoidal waveform is the result of using short-pitch distributed coils as in a conventional three-phase a.c. winding. Using rhomboidal-shaped coils may further suppress harmonics in the same way as skewed or herringbone coils [16].

In comparison with conventional AFPM machines, the reduced value of the torque constant of AFPM machines with rhomboidal coils is not a significant drawback, as the great reduction

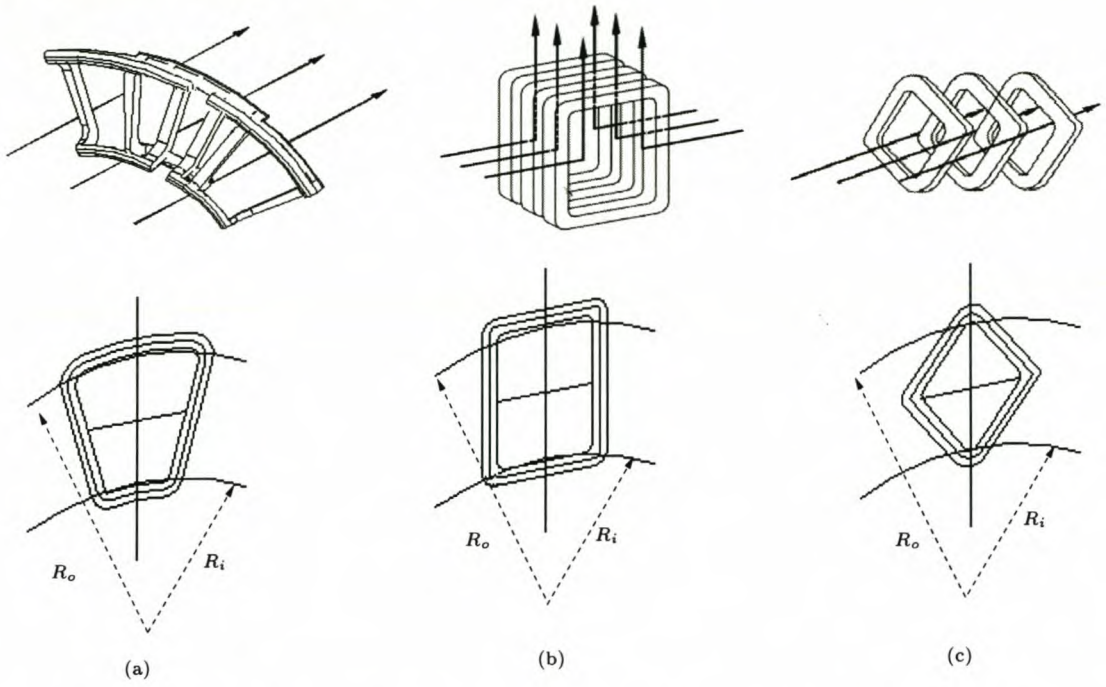

Figure 1.5: Different coil profiles: (a) trapezoidal shape coil, (b) toroidally wound coil and (c) rhomboidal shape coil.

of the I^2R loss together with the possibility of water cooling of the winding [16] allows electric loadings that can be as much as twice those allowed in an iron-cored AFPM machine. However, if water-cooling is not convenient or not necessary, the trapezoidal shape coil is still the desired solution.

Winding thickness

Ofori-Tenkorang et al [77] studied a conventional PM synchronous machine with a slotless armature winding and found that an optimum axial thickness of the armature winding to produce maximum torque per unit copper loss exists. This optimum thickness of copper, in general, decreases with the number of pole pairs mainly because the magnetic field decays faster within the airgap for a high number of pole pairs. Although this conclusion was drawn based on the analysis of a conventional PM synchronous machine, it also makes sense for AFPM machines.

Takano et al [98] presented a new method for estimating the optimum ratio of PM thickness to armature winding thickness for the brushless d.c. AFPM machine. It was concluded that, for the minimum copper loss, the optimum ratio of the PM to winding thickness is 2 : 1 with the axial length and starting torque of the brushless d.c. AFPM machine fixed [98].

Eddy current

In AFPM machines, the winding is located in the main field which is at right angles to its axis. Relative motion of the PMs to the winding causes the field through each conductor to vary periodically and therefore induces eddy currents in the conductor. The loss due to the eddy currents in the conductors depends on both the geometry of the wire cross section and the waveform of the flux density variation. Two typical cases were studied by Carter [23]. As a result the eddy current losses in conductors having rectangular and round cross-sections in an alternating transverse magnetic field are given as follows:

- For a rectangular conductor of cross-section area $S = w \times t$, resistivity ρ and length l, placed in an alternating magnetic field of peak flux density value B_{pk}, frequency $\omega = 2\pi f$ and perpendicular direction to the w side, the losses are:

$$P_e = \frac{1}{24} \cdot \frac{S \cdot w^2 \cdot B_{pk}^2 \cdot \omega^2 \cdot l}{\rho} \tag{1.3}$$

- For a round conductor of cross-section area $S = \pi \cdot r^2$, resistivity ρ, and length l, placed in a pulsating magnetic field of peak flux density B_{pk} and frequency ω the losses are [66, 23]:

$$P_e = \frac{1}{32} \cdot \frac{S \cdot (2r)^2 \cdot B_{pk}^2 \cdot \omega^2 \cdot l}{\rho} \tag{1.4}$$

It can be seen that w in Eqn (1.3) is the breadth of the conductor measured in a direction at right angles to the flux; in Eqn (1.4), this dimension is $2r$. If $w = 2r$ and both conductors have the same cross-section area, the difference in eddy current losses between rectangular and round conductors can be appreciated by their multiplying factors, i.e. $1/24$ for rectangular conductors and $1/32$ for round conductors, respectively.

It is evident that round wires are less prone to eddy currents, but they have a worse filling factor than rectangular conductors. It should be noted that the above analysis (equations 1.4 and 1.5) was based on the following assumptions [23, 66]:

- The flux varies sinusoidally,
- The flux density is the same wherever involved in the derivation,
- The effect of the induced eddy currents, in modifying the distribution of the magnetic flux, is insignificant and therefore may be neglected.

In practical AFPM machines, however, the high order harmonic components in the air-gap flux waveform are often quite significant. Furthermore, in a machine with an ironless winding

arrangement, the alternating tangential field component gives rise to the total eddy current loss in the winding. Taking into account all these aspects, evaluating eddy current loss by using the above equations alone may yield underestimated results. For solving this problem, Caricchi et al [14] proposed that the loss found from the equation may be compensated by multiplying with an empirical factor obtained from an FEM study of the distribution of flux density in the airgap.

1.6.4 Aspects of mechanical design

Cooling design considerations

Very little has been published concerning the cooling design of the AFPM machines [95, 101, 39] in the literature. As the air flow rate plays an important role in the thermal analysis of an air-cooled AFPM machine, a coupled thermofluid model is necessary.

Spooner et al [95] presented a simple lumped-parameter thermal resistance model. An empirical formula for the pressure-flow characteristic of the centrifugal fan was directly employed in the flow rate estimation of the AFPM machines. It is, however, not clear how the flow rate calculation fits in the thermal model and how the convection heat transfer coefficients were obtained. Besides, representing the fan effects of an AFPM machine by directly using centrifugal fan theory may be subject to significant error. It is therefore necessary to develop a reliable method that is applicable to a large number of AFPM machines by combining both the thermal and the fluid flow analysis.

1.6.5 Review of modelling techniques

The modelling of AFPM machines can be done by using either classical analytical approaches or numerical methods. Based on existing conventional machine theory, analytical approaches are capable of quickly predicting machine performance with acceptable accuracy. However, their consistency and reliability in analysing machines with different topologies cannot be ensured. Quite often experimental test or numerical method are introduced for verification.

The concept of the electromagnetic interaction between the mutually coupled magnetic field and electric field, remains the basis of any machine regardless of its configuration. The calculation of the field form factor, harmonic content in the output voltage waveform, and leakage flux, as well as the magnetic forces, all depend on a knowledge of the airgap flux distribution. Thus, it is essential to study the airgap flux distribution in AFMs in this thesis.

In the past, field computation was essentially based on closed form analytical solutions [8, 9, 26, 41, 42] or analog representation with many simplifications and idealisation of the geometry, material characteristics, and boundary conditions associated with the particular problem. The

solutions obtained by these methods were generally approximate and required elaborate test calibration on a vast number of prototypes. Using FEM, more accurate calculation of the electromagnetic field can be achieved at the cost of longer computation time, which is not a serious drawback when only two-dimensional analysis is needed.

The classical approach

Classical theory for conventional machines has been well established. Some published work attempted to use an analog approach on the basis of existing machine theory for the analysis of AFPM machines [54, 61, 62]. Klug discussed the relations between power and external radius and gave formula for calculating magnetic flux density, armature reaction and losses in [61]. It has been found from both experimental tests and calculations that for a typical sinewave AFPM machine with a coreless stator, the ratio of inductances of the phase winding is near unity, i.e. $L_d/L_q \approx 1$. Thus, the analysis of this AFPM machine may be done in a similar way as that of the three-phase cylindrical PM machine [54, 62].

Hrabovcova [54] et al compared several methods for the parameter determination of AFPM machines such as equivalent circuit, reluctance network and experimental test methods. By employing the theory of the classical cylindrical rotor machine with some modifications, the equivalent circuit approach was proved effective and simple provided that the temperature dependence of winding could be accurately predicted. Alternatively, the reluctance network approach can be used, which is a more appropriate method in the sense that it is a more accurate representation of the real magnetic circuit. The basic procedure is that the flux paths are divided into flux tubes of which the circuit analogy are reluctance elements. Each reluctance element contains the properties of the flux tube. In general, the reluctance network is an efficient approach with good accuracy, though not as accurate as FEM [83].

In [34], a new analytical solution was described, which gives a straightforward method of calculating the steady-state behaviour of the AFPM machine for 120^o inverter operation on the basis of a general set of state equations. The proposed method is quite complicated from an implementation point of view. The payoff would be less computation time than for FEM since only one iterative process is involved.

Finite element method

The 3-D FEM analysis has been applied to the modelling of an ironless stator AFPM machine in [4]. Both no-load and load operations are modelled and it has been shown that a good accuracy can be expected even when the first order linear FEM solution is applied to the AFPM machine if the magnetic circuit is far from saturated (large airgap). It was also found that armature reaction for an AFPM machine with an ironless stator is generally negligible.

To reduce the huge computation costs involved in the 3-D FE modelling, two-dimensional FE analysis can be performed. This may be carried out by introducing a cylindrical cutting plane at the mean radius of the magnets [42, 44]. This axial section is unfolded into a two dimensional surface on which the FE analysis can be done by assuming that [66]:

- There is no radial variation of magnetic field in the winding, i.e. no end effects. (3-D analysis shows that the active flux density drops towards the radial ends of the active portion of the machine, but the end winding would link additional end flux)
- There is no axial variation of the magnetic field. (3-D analysis indicates a 10% increase in flux density from the centre to a winding edge due to leakage flux)

Since the above 2-D analysis ($\theta - z$ plane) can not take into account the end effects and radial flux variation, the introduction of another cutting plane along the symmetry plane of a magnet was proposed, on which 2-D FEM analysis can be performed [21]. The $r - z$ plane analysis reflects partly the radial flux behavior and can be used to a certain extent for compensating for the $\theta - z$ plane results. In this way the advantages of FEM analysis that would be lost as a result of simplifying 3-D with 2-D modeling can be partly recovered. The inseparability of $B(r, \theta, z)$ with r [8], which posed as an obstacle for 2-D FEM analysis could be tackled by using the multi-slice modelling scheme as described in Chapter 4.

1.6.6 Optimisation

There is some published work on the design optimisation of AFPM machines. The majority of the literature aimed at maximising or minimising one objective function (e.g. *torque, efficiency, specific torque,* etc.) with respect to a single variable (e.g. *pole-arc to pole-pitch ratio* or *inner to outer radius ratio*), while the other variables are kept constant [8, 19, 26, 47, 63].

A multi-objective design optimisation procedure for AFPM machines by using Quasi-Newton Quadratic extrapolation method is proposed in [105]. However, the approach presented is not convincing and lacks experimental verification and comparison with other optimisation algorithms.

Cvetkovski et al applied the Genetic Algorithms (GAs) to the optimal design of an AFPM synchronous machine in [30], in which the efficiency of the machine was taken as the objective function and all the quantities necessary for the optimal design are made to be dependent on the five optimisation variables, namely, inner radius, outer radius, PM arc angle, PM thickness and airgap length. The necessary inputs are voltage, speed, torque, current density, remanent flux density of the PM, number of poles, number of stator slots and material properties. Again the results obtained were not validated by either tests or numerical calculations.

1.7 Problem statement

The focus of this thesis is on the design and analysis of the AFPM machine with an ironless stator. To make the most of the existing research results and to identify the directions for this research, it is important to synthesize previous research work from literature. Despite extensive research that has been devoted to AFPM machines, the following aspects pertaining to the design and analysis of the AFPM machine have not received adequate consideration:

(i) **Time-stepped FE model**: In the design optimisation of AFPM machines, it has become increasingly important not only to predict their steady-state behaviour but also to determine their transient performance. The time variation of quantities becomes important as do certain parameters that change as a function of the rotor position. This invariably leads to the use of FE time-stepped solutions, which requires the incorporation of the rotor mesh movement with respect to the stator mesh.

To achieve this, several methods have been proposed as described in [99, 89]. As the typical AFPM machine has a large air-gap length, the techniques requiring the discretisation of the air-gap using triangle elements are generally undesirable because: (a) they cannot accommodate free movement and (b) are subject to discretisation errors.

The other category of methods such as the *air-gap element* [1] and *boundary element* [89] techniques are well recognised for their superior accuracy and free movement, though their resulting stiffness matrices have a large profile. Since a generic rotating machine has an annular air-gap, these methods were derived under a polar coordinate system. Note that the AFPM machine possesses a planar and somewhat flat air-gap. The 2-D FEM modelling is normally done by introducing a radial cutting plane, which is unfolded into a flat model. The modelling of the AFPM machine or linear machine requires a basic reformulation of the methods. Since this is associated with the Cartesian coordinate system it is necessary to derive the methods for Cartesian problems.

(ii) **Direct FE optimisation**: The majority of the published work regarding the design optimisation of the AFPM machines is limited to maximising (minimising) an objective function with respect to a single variable. Although the multi-objective design optimisation using the Gradient method or Stochastic method was attempted, these design analyses of the AFPM machines were done by means of the lumped circuit method.

The FEM is, in many instances, used merely to investigate certain design aspects. Note that the models which were developed without the use of numerical field solutions give a good insight into the operation of a machine, but may not be accurate enough for detailed design optimisation. Finite element models, on the other hand, can give an excellent representation of the magnetic field inside the machine, enabling nonlinearity to be accounted for with great accuracy.

Although it has been mentioned in the literature [21, 22, 66] that 2-D FEM has been or should be incorporated into design optimisation of AFPM machines, there are no published works describing the implementation of this approach in any detail.

(iii) **Thermofluid analysis**: Whereas extensive research has been devoted to thermal studies of conventional electrical machines, AFPM machines have received very little attention [95, 101]. Due to the fact that AFPM machines possess relatively large air-gap volume and quite often have multi-gaps, the general perception is that AFPM machines have better ventilation capacity than their radial field counterparts [26, 44].

However, like conventional machines, AFPM machines are also subject to the cooling problem. This can be explained by considering the relationship between the machine's output power and its external diameter [44], i.e. $D_o \propto \sqrt[3]{P_{out}}$. Since the external diameter increases rather slowly with the increase of output power, the existing heat dissipation capacity may be insufficient to cope with excessive heat at certain power ratings, so that more effective means of cooling have to be enforced.

Thus, quantitative studies of the heat dissipation potential for AFPM machines with vastly different topologies are clearly needed. From a design point of view, there is a need to develop an efficient method that is reliable and applicable to a wide range of AFPM machines.

(iv) **Eddy current loss calculation**: The closed-form analytical formula derived in [23, 97] (Eqn. 1.4) has been often used in the AFPM machine design [66, 14, 95], which is basically a one-dimensional approach.

In practical AFPM machines, however, the flux density distribution in the air-gap is much closer to a trapezoidal waveform with significant third and fifth harmonic components. Furthermore, in a machine with an ironless winding arrangement, the field through each conductor has a tangential component of flux density, which can cause serious additional eddy current losses. Taking into account all these features, evaluating eddy current power loss by using only the analytical formula underestimates the results. It is thus necessary to combine FE field modelling with the analytical method for better accuracy.

Besides, as far as the author is aware, the air-cooled AFPM machines with an ironless stator developed to date have been limited to a relatively low power range (below 150 kW). There is a need to investigate the performance capability of this type of AFPM machine in the upper medium power level (e.g. sub-500 kW).

1.8 Approach to problem

As a first step in this thesis the design optimisation of the AFPM machine focuses on the steady-state performance. To address the problems put forward in section 1.7, the design approach that directly incorporates the finite element modelling in a multi-dimensional optimisation procedure is developed and applied to the design optimisation of a 300 kW (at unity power factor) AFPM generator. In order to do an overall optimum design, different design aspects such as cooling analysis, mechanical strength analysis and eddy current loss calculation are also investigated in this study.

To enable the free movement of the rotor mesh with respect to the stator mesh, the Air-Gap Element (AGE) originally proposed by Razek et al [2] is derived for the Cartesian coordinate system. For minimising the large computation overhead associated with CAGE, a time-saving scheme proposed in [40] has been utilised to optimise the derived Cartesian Air-Gap Element (CAGE). The developed finite element time-step model is applied to calculating the steady-state performance of the AFPM machine.

Since the magnetic field distribution in an AFPM machine exhibits a three-dimensional feature, it is generally not accurate to calculate the eddy current loss merely by using a simple one-dimensional analytical method. To overcome this problem the 2-D FE field modelling is introduced to perform accurate field analysis. To exploit the full advantages of the 2-D FE modelling, a multi-layer approach is proposed, which takes into account the variation of the air-gap flux density in the conductors with regard to their air-gap positions. To account for the 3-D effects of the field, i.e. the radial variation of the field, a multi-slice FE modelling scheme is devised.

Thermal analysis is an important aspect for the design optimisation of AFPM machine. From a design point of view, it is preferable to have a simple and efficient method for cooling analysis and design which can be utilised for generic AFPM machines. In this thesis, a thermofluid model of the AFPM machine is developed. The fluid flow model is needed for calculating the air flow rate, which is then used to find the convective heat transfer coefficients. These are important parameters in the subsequent thermal calculation.

Experimental investigations are carried out to determine the accuracy and validity of each of the afore-mentioned models/methods. By implementing these models into a multi-dimensional optimisation procedure, a coherent design optimisation algorithm is formed. An air-cooled 300 kW (at unity power factor) AFPM generator is then designed by using this approach. The performance measurements done on the fabricated prototype are compared with predicted results.

1.9 Thesis layout

The layout of this thesis is briefly described as follows:

Chapter 1: The historic background and literature review on the AFPM machines is summarised and discussed in detail, based on which the research scope of this work is identified.

Chapter 2: In this chapter the methods for calculating the performance characteristics of the AFPM machine are introduced. Both the finite element method and a simple analytical method are described in detail.

Chapter 3: In this Chapter an FE time-step model of an AFPM machine is developed. The theory of a new macro-element is presented, and its implementation within a time-stepped FE code is described. Combined with the circuital equations, the proposed model is capable of simulating the steady-state performance of the AFPM machine for both balanced and rectifier load.

Chapter 4: This chapter presents an efficient method that combines 2-D finite element field solutions and the closed-form formula for calculating eddy current loss in the stator winding of the AFPM machines. To account for 3-D effects of the magnetic field, a multi-slice and a multi-layer scheme are devised.

Chapter 5: This chapter describes the development of a thermofluid model of AFPM machines, which is incorporated into the optimisation process (Chapter 6) for the cooling design.

Chapter 6: Two different multidimensional optimisation algorithms are described and used to optimise the design of the AFPM machine in this chapter. The results of two optimisation case studies are given and discussed.

Chapter 7: In this chapter a brief description of the experimental machines is given. The finite element mechanical strength analysis of the designed AFPM machine is carried out and results are discussed. The construction techniques involved in the construction of the ironless stator AFPM machine are described.

Chapter 8: In this chapter various performance tests of the experimental machine are performed and analysed. The aim of this chapter is to evaluate the performance capability of the air-cooled AFPM machine in the sub 500 kW power level.

Chapter 9: In this chapter the original work performed in this project is summarised and relevant conclusions are drawn. Recommendations pertaining to future research are also made.

Chapter 2

Performance Calculation of the AFPM Machine

This chapter describes the performance calculation of the AFPM machine by applying the finite element method and classical machine theory. The equivalent circuits of the AFPM machine are first established and the FEM is employed for the calculation of the equivalent circuit parameters. The calculations are carried out for the steady-state, and only the fundamental values of voltage, current and flux linkage are considered. The reason for the latter is that the design optimisation of the AFPM machine is done on the basis of fundamental values only.

2.1 Equivalent circuits

To calculate the performance of the AFPM machine it is essential to consider the equivalent circuits of the machine. The fundamental per phase equivalent circuit of the AFPM machine

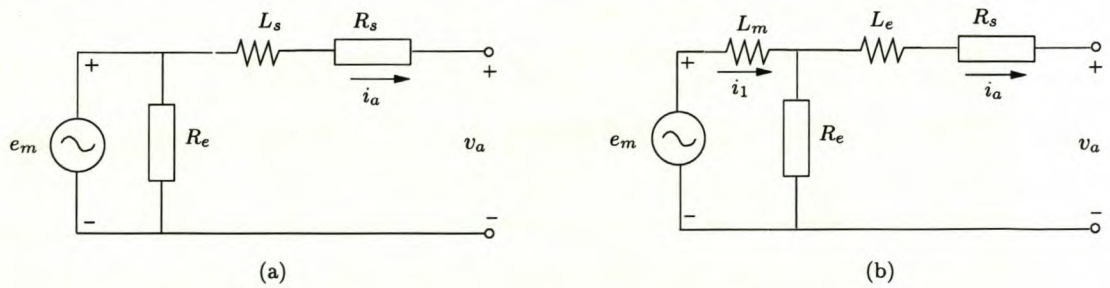

Figure 2.1: Per phase equivalent circuit of the AFPM machine.

may be represented by the circuit shown in Fig. 2.1(a), where R_s is the stator resistance, L_s is the stator inductance, e_m is the induced EMF due to the fundamental air-gap flux linkage λ_m, and v_a and i_a are the fundamental instantaneous phase voltage and current, respectively.

The shunt resistance R_e is the stator eddy current loss resistance, which is defined in the same way as that of the core loss resistance described in [109, 54, 59].

With the 2-D finite element method the total stator flux linkage excluding the endwinding flux linkage can readily be calculated in the analysis [58]. Thus, the stator inductance L_s is split into two terms, i.e. the endwinding leakage inductance L_e and the main inductance L_m. As an approximation, the eddy current loss resistance is shifted as shown in Fig. 2.1(b).

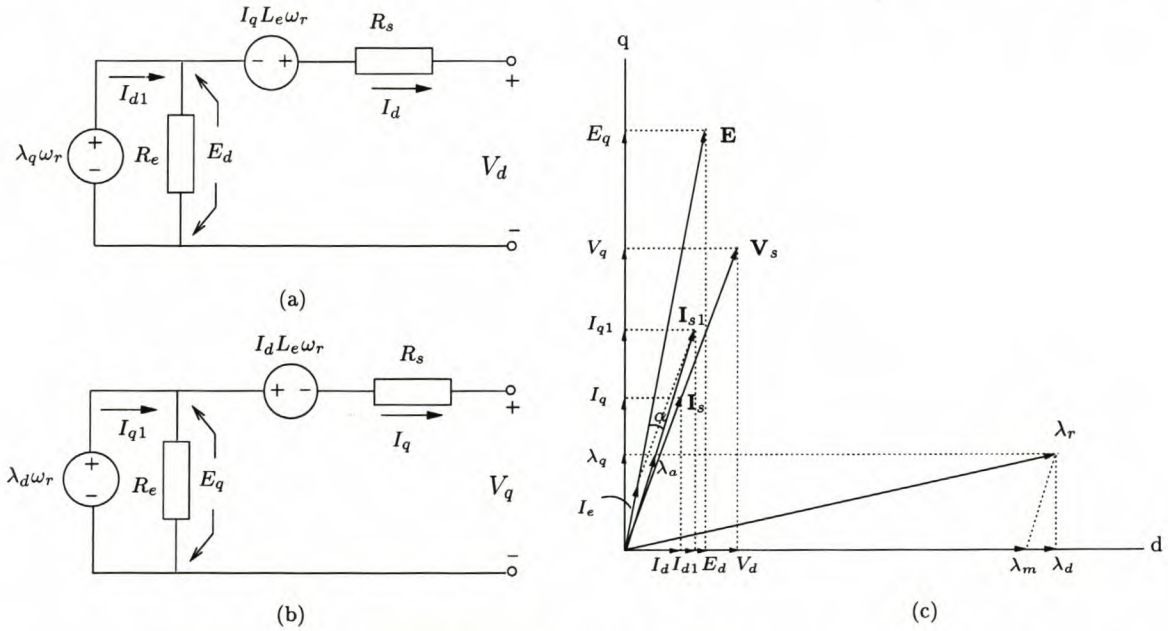

Figure 2.2: Steady-state dq equivalent circuit and phasor diagram of the AFPM machine.

The equivalent circuit of Fig. 2.1(b) in the abc reference frame can be transformed to equivalent circuits in the dq reference frame by using Park's transformation. The resultant dq equivalent circuits are given in Fig. 2.2. The flux linkages λ_d and λ_q are the $d-$ and $q-$ axis stator flux linkage components, which include the total stator flux linkage excluding the end-winding flux linkage. λ_m is the flux linkage produced by the permanent magnets. The parameter ω_r is the electrical speed of the rotor reference frame. In the phasor diagram (unity power factor was assumed) the space phasors $\mathbf{V}_s$ and $\mathbf{I}_s$ represent the stator terminal voltage and current respectively. Note that $\mathbf{I}_{s1}$ includes the equivalent eddy loss current component $\mathbf{I}_e$. It has also been assumed that the eddy losses in PMs and rotor discs are negligible.

2.2 Representation of permanent magnets

The BH demagnetisation characteristics of hard ferromagnetic material can be modelled using the equation of a hyperbola [43] as follows:

$$B = \frac{B_r(H_c - H)}{H_c - aH} \tag{2.1}$$

where a is given by

$$a = \frac{1}{n}\sum_{i=1}^{n}[\frac{H_c}{H_i} + \frac{B_r}{B_i} - \frac{H_c}{H_i} \cdot \frac{B_r}{B_i}] \tag{2.2}$$

where (B_i, H_i) are coordinates of points on the demagnetisation curve. For rare-earth PMs, due to their practically linear demagnetisation curve, the above equation is simplified as:

$$B = B_r - \frac{B_r}{H_c} \cdot H \tag{2.3}$$

There are two models which are commonly used to represent PMs in the finite element modelling of electrical machines, i.e. the *magnetisation vector* model and the *equivalent current sheet* model. Although these two models have different starting points, they result in the same set of equations [89].

In this thesis, the magnets are incorporated into the FE program by adding a meshed thin current layer along the sides of the PMs. For rectangular PMs with the magnetisation direction perpendicular to the surface of the magnet, which is the case for the AFPM machine, the 2-D FE modelling is quite straightforward, i.e.

- Define PMs as a material of permeability $\mu_m = \frac{B_r}{H_c}$;
- Add a meshed thin current sheet along each side of the PM to produce a field in the direction of magnetisation. The linear current density (Amperes/meter) should be equal to the coercive force H_c

2.3 Calculation of equivalent circuit parameters

This section describes how the *dq* equivalent circuit parameters of Fig. 2.2 are determined by using both the FEM and the classical analytical method.

2.3.1 Stator winding resistance

At a certain operating temperature t, the stator winding resistance per phase R_s is calculated according to the following formula (without taking into account skin effect) [59]:

$$R_s = \frac{2\ n_t\ \rho_t(l + l_e)}{k_f n_a A_{cu}/z} \quad \text{where} \quad \rho_t = \rho_{20}\ (1 + 0.0039\ (t_c - 20)) \tag{2.4}$$

and the variables are defined as follows:

n_t	number of turns in series per phase
l	active length of a coil
l_e	endwinding length of a coil
z	number of turns per coil
n_a	number of parallel circuits
A_{cu}	copper area of one side of a coil
k_f	stator winding filling factor
ρ_t	resistivity of copper at temperature t
ρ_{20}	resistivity of copper at 20^oC

The available copper area of the AFPM machine mainly depends on the machine's inner diameter with due allowance for the endwinding arrangement as illustrated in Fig. 2.3.

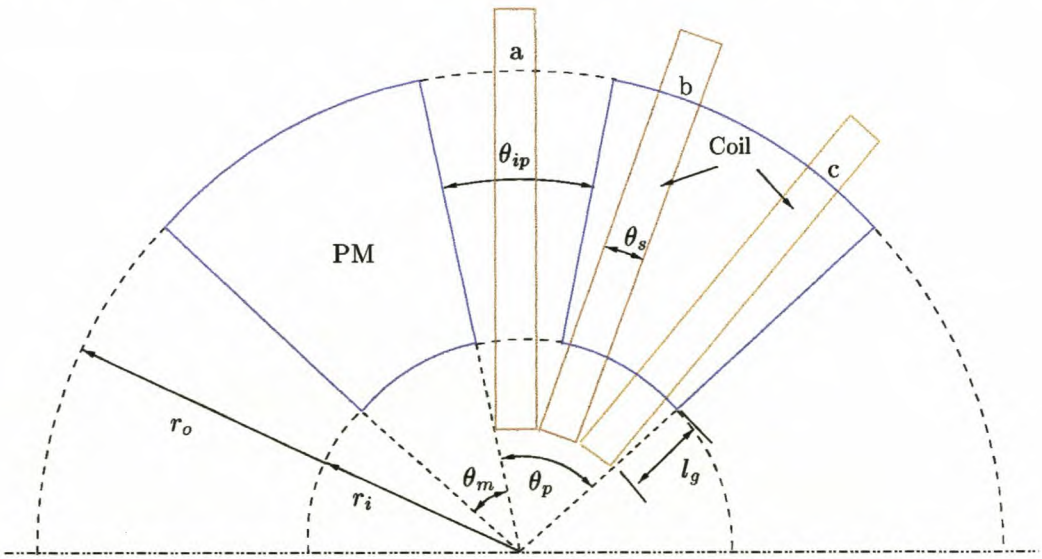

Figure 2.3: Layout and dimensions of AFPM machine showing winding arrangement.

The active copper area is calculated by multiplying the available copper area with a filling factor k_f. To minimise copper loss in the stator winding, thin conductors are used so that the skin effect may be safely ignored in the calculation of the winding resistance.

2.3.2 End-winding leakage inductance

The method of calculating the end-winding leakage inductance L_e of an ironless stator AFPM machine is not readily available in literature. In this section, a simplified analytical approach based on a Brooks coil model [46] is introduced. In the analysis the following assumptions have been made:

(a) the mutual flux linkage between the endwinding phase groups is negligible so that the per phase end-winding inductance may be determined from a single coil model,

(b) for a single-layer winding arrangement, $\tau_c = 4\ a$ where τ_c is the coil pitch length and a is the coil conductor width as shown Fig. 2.4,

(c) the coil is of a square cross-section, i.e. $a = b$.

Fig. 2.4(a) shows a typical coil of the AFPM machine. Imagine that one can take away the middle part (marked by dotted line in Fig. 2.4(b)), then the remaining two end parts are the end-winding under consideration. As an approximation, one may join these two parts together to form a round coil as shown in Fig. 2.4(c).

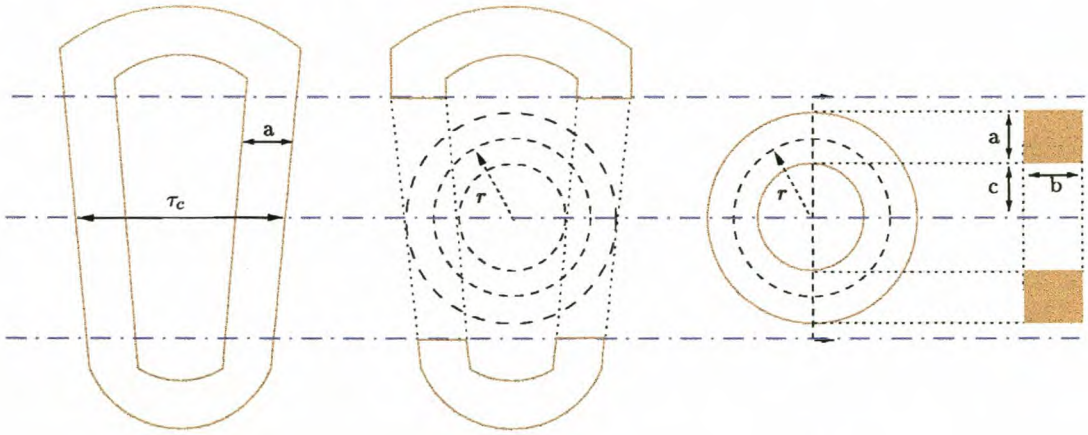

Figure 2.4: The simplified end-winding model of the AFPM machine, where (a) is a typical coil in the AFPM machine, (b) is the end parts of the coil, and (c) is the equivalent Brooks coil representing the endwinding.

It is now possible to calculate the endwinding inductance by directly using the formula given in [46]. Expressed in terms of the AFPM machine's dimensions, the end-winding inductance per phase L_e is

$$L_e = \frac{1.699\ n_s \pi (r_o - r_i + l_g) N_c^2}{2\ p\ n_a} \quad [\mu H] \tag{2.5}$$

where n_s is the number of coils in series per phase, n_a is the number of parallel circuits per phase, N_c is the number of turns per coil, p is the number of poles, l_g is the airgap length, and r_o and r_i are outer and inner radii of the AFPM machine, respectively.

2.3.3 Flux linkage and inductances

To calculate the flux linkage using FEM, it is necessary to specify the phase current $I = \hat{I}\angle\phi$ of the AFPM machine. The amplitude of the current space phasor $\hat{I}$ may be determined from a given rms current density J according to the formula

$$\hat{I} = \sqrt{2} J A_{cu} n_a / z \tag{2.6}$$

Alternatively, it can be calculated from a given copper loss P_{cu} by using

$$\hat{I} = \sqrt{\frac{2P_{cu}}{3R_s}} = I_q \; ; \quad (I_d = 0) \tag{2.7}$$

in which a current angle of 90^0 has been assumed. With the dq current components I_{dq} amplitude known, the instantaneous three phase currents i_{abc} which need to be put in the FE program according to the rotor position can be calculated using the inverse Park transformation as follows:

$$[i_{abc}] = [K_p^{-1}][I_{dq0}] \tag{2.8}$$

where

$$K_p = \frac{2}{3}\begin{bmatrix} cos\theta & cos(\theta - \frac{2\pi}{3}) & cos(\theta + \frac{2\pi}{3}) \\ sin\theta & sin(\theta - \frac{2\pi}{3}) & sin(\theta + \frac{2\pi}{3}) \\ \frac{1}{2} & \frac{1}{2} & \frac{1}{2} \end{bmatrix} \tag{2.9}$$

With a 2-D FE solution the magnetic vector potential A has only a z component, i.e. $A = A(x,y)\cdot\hat{a}_z$ where $\hat{a}_z$ is the unit vector in z direction. The total stator flux linkages of a phase winding λ_{abc} that exclude the end-winding flux linkage can be readily calculated by using:

$$\lambda_{abc} = \int_s B \cdot dS = \int_s \nabla \times A \cdot dS = \oint_c A \cdot dl \tag{2.10}$$

Hence, for finite elements using a first-order triangular mesh, the flux linkage of a coil with z turns, coil area S and length l is given by [99]

$$\lambda = z \sum_{j=1}^{n} \frac{\Delta_j}{S} \left[\frac{\zeta}{3} \sum_{i=1}^{3} A_{ij} \right] l \tag{2.11}$$

where A_{ij} is the nodal value of the magnetic vector potential of the triangular element j, $\zeta = +1$ or $\zeta = -1$ indicates the direction of integration either into the plane or out of the plane, Δ_j is the area of the triangular element j, and n is the total number of elements of the in-going and out-going areas of the coil. It follows that for an AFPM machine with only one pole modelled, the total flux linkage of a phase winding is

$$\lambda_{abc} = \frac{2\,p\,z\,l}{n_a S} \sum_{j=1}^{u} \left[\frac{\Delta_j \zeta}{3} \sum_{i=1}^{3} A_{ij} \right] \tag{2.12}$$

where u is the total number of elements of the meshed coil areas of the phase in the pole region and n_a is the number of parallel circuits of the stator winding.

The 3-D effects of the magnetic field in an AFPM machine are accounted for in the 2-D finite element analysis by using a set of sub-models (slices) of which each n^{th} successive slice is indexed to reflect the variation in the field distribution at different radii r_n. The technique will be discussed in more detail in Chapter 4. With k sub-models the phase flux linkages are calculated according to

$$\lambda'_{abc} = \frac{1}{k} \left[\sum_{n=1}^{k} \lambda_{abc}(n) \right] \tag{2.13}$$

where $\lambda_{abc}(n)$ denotes the total phase flux linkage of the n^{th} sub-model and is obtained by using Eqn. (2.12).

From a machine design perspective, it is of main interest to find the fundamental component of the total flux linkages. The harmonic contents in the calculated flux linkages may be classified into four categories, i.e.

(i) harmonic flux linkages caused by the slotted stator iron-core,

(ii) harmonic flux linkages due to the magnetic saturation of the stator iron-core,

(iii) harmonic flux linkages generated by the stator winding MMF space harmonics,

(iv) harmonic flux linkages due to flat-shaped permanent magnets.

For an AFPM machine with an ironless stator, the harmonics due to (i) and (ii) are absent. In view of the large airgap in an ironless stator AFPM machine, the harmonics caused by (iii) are very small and can be ignored. Thus, the only harmonics needed to account for are those of (iv). These are synchronous harmonic flux linkages which stand still with respect to the fundamental rotating flux wave.

Given these considerations, the flux linkage wave of an AFPM machine is nearly sinusoidal though, for a non-distributed winding, an appreciable 3^{rd} and less significant 5^{th} and 7^{th} harmonics are still present in the total flux linkage waveform [14]. If the 5^{th}, 7^{th} and higher harmonics are ignored, the total flux linkage can be written in terms of a fundamental and a 3^{rd} harmonic, i.e.

$$[\lambda_{abc}] \approx [\lambda_{abc1}] + [\lambda_{abc3}] \tag{2.14}$$

The co-phasal 3^{rd} harmonic flux linkage, including the higher order triple harmonics, can be obtained from the actual three-phase flux linkage as [58]:

$$\lambda_{a3} = \lambda_{b3} = \lambda_{c3} \approx \frac{1}{3}(\lambda_a + \lambda_b + \lambda_c) \tag{2.15}$$

Thus, with the actual total phase flux linkages and the 3^{rd} harmonic flux linkages known from the finite element analysis, the fundamental total phase flux linkages can be calculated by using

$$[\lambda_{abc1}] \approx [\lambda_{abc}] - [\lambda_{abc3}] \tag{2.16}$$

Another way to determine the fundamental total phase flux linkage is to perform a Fourier expansion of the total flux linkage wave. This requires that the rotor and the current space phasor be stepped through an angle of $\pi/2$ electrical radians. This approach, however, will discourage the idea of using the FEM directly in the optimisation process due to the massive increase of computation time.

The use of Eqn. (2.16) is thus of great importance in the whole optimisation process as it enables the fundamental total phase flux linkages of the AFPM machine to be determined by using just one set of field solutions. The fundamental flux linkages are the basis of subsequent performance calculation of the machine such as the terminal voltage and power factor.

With the fundamental total phase flux linkages and rotor position known, the dq flux linkages are calculated using Park's transformation as follows:

$$[\lambda_{dqo}] = [K_p]\,[\lambda_{abc1}] \tag{2.17}$$

From this the speed voltages $E_d = -\lambda_q \omega_r$ and $E_q = \lambda_d \omega_r$ of the equivalent circuits are determined. The $d-$ and $q-$axis inductances L_d and L_q are determined from the following equations:

$$L_d = \lambda_{sd}/I_d \quad \text{and} \quad L_q = \lambda_{sq}/I_q \tag{2.18}$$

where λ_{sd} and λ_{sq} are given by:

$$\lambda_{sd} = \lambda_d - \lambda_m \quad \text{and} \quad \lambda_{sq} = \lambda_q \tag{2.19}$$

where λ_m is the flux linkage produced by the permanent magnets. Note that the endwinding flux linkages are not included in the calculation. As the permeability of the rare-earth PM

materials is very close to that of air, the ratio of the $d-$ and $q-$ inductances is close to unity. The AFPM machine is actually a constant airgap machine.

2.3.4 Eddy current resistance

For an AFPM machine with an ironless stator, associated iron losses are absent. The rotor discs rotate at the same speed as the main magnetic field, thus the core losses in the rotor discs are also negligible. However, the eddy current losses in the stator winding are significant due to the fact that the machine is designed to operate at relatively high frequencies.

A detailed treatment of the calculation of eddy current losses will be given in Chapter 4. As an approximation, one may consider only the eddy losses due to the main flux and fundamental operating frequency of the machine. The eddy current losses (for round conductor) are calculated from [23]

$$P_e = \frac{\pi\ l\ d^4\omega^2}{32\ \rho}(B_x^2 + B_y^2)\ n_c \tag{2.20}$$

where l is the conductor length, ω is the fundamental operation frequency, d is the diameter of the conductor, n_c is the number of conductors, and B_x and B_y are the x- and y-axis components (peak values) of the fundamental flux density wave, respectively. The eddy current loss resistance may be defined as

$$R_e = \frac{3E_a^2}{P_e} \tag{2.21}$$

where E_a is the rms value of the phase EMF and is given by

$$E_a = \sqrt{\frac{E_d^2 + E_q^2}{2}} \tag{2.22}$$

2.4 Performance calculation

From the known dq current components, I_d and I_q, the calculated dq speed voltages, E_d and E_q (section 2.3.3), and the defined eddy loss resistance (section 2.3.4), the $dq1$ current components, I_{d1} and I_{q1} and the current amplitude I_{s1} can be calculated as:

$$\begin{cases} I_{d1} = I_d + E_d/R_e \\ I_{q1} = I_q + E_q/R_e \\ I_{s1} = \sqrt{I_{d1}^2 + I_{q1}^2} \end{cases} \tag{2.23}$$

From the dq current components and from the calculated endwinding leakage inductance L_e, the endwinding leakage flux linkage speed voltages $L_e I_q \omega_r$ and $L_e I_d \omega_r$ are determined. The dq terminal voltage components, V_d and V_q, and the voltage amplitude V_s are calculated from

$$\begin{cases} V_d = E_d + L_e I_q \omega_r - I_d R_s \\ V_q = E_q - L_e I_d \omega_r - I_q R_s \\ V_s = \sqrt{V_d^2 + V_q^2} \end{cases} \tag{2.24}$$

where R_s is the stator winding resistance according to Eqn. (2.4). The power factor is easily calculated from the dq voltage components V_d and V_q and the dq current components I_d and I_q as follows:

$$P_f = cos\ [tan^{-1}(\frac{V_d}{V_q}) \pm tan^{-1}(\frac{I_d}{I_q})] \tag{2.25}$$

The generated kVA and the copper losses of the machine are respectively calculated as

$$S = \frac{3}{2}\ V_s I_s \quad \text{and} \quad P_{cu} = \frac{3}{2}\ I_s^2 R_s \tag{2.26}$$

The steady-state torque of the AFPM machine can be calculated by using the following relation

$$T_e = \frac{3}{2}\ p\ (\lambda_d \cdot I_q - \lambda_q \cdot I_d) = \frac{3}{2}\ p\ \lambda_m I_q \tag{2.27}$$

or more accurately from the vector potential nodal values $[A]_e$ in the air-gap element as described in [1]. For a Cartesian air-gap element (refer to Appendix A for details), the derived formulation takes the form of:

$$T_e = -\frac{p\ (r_o + r_i)}{2\ y_0\ \mu_0} [A]_e^T [T] [A]_e \tag{2.28}$$

where r_o and r_i are the rotor disc outer and inner radius, respectively, y_0 is an arbitrary value in the range of $a \leq y_0 \leq b$ (a and b are y co-ordinates of the low and the upper boundaries of the air-gap element, respectively) and $[T]$ is the matrix defined by:

$$t_{ij} = x_0 \cdot \sum_{n=1}^{\infty} \lambda_n^2 \cdot \frac{e^{\lambda_n(y_0-c)} + e^{\lambda_n(c-y_0)}}{e^{\lambda_n(c'-c)} - e^{\lambda_n(c-c')}} \cdot \frac{e^{\lambda_n(y_0-f)} - e^{\lambda_n(f-y_0)}}{e^{\lambda_n(f'-f)} - e^{\lambda_n(f-f')}} \cdot (a_{ni} b_{nj} - b_{ni} a_{nj}) \tag{2.29}$$

where x_0 is the period for one pole pitch, $\lambda_n = 2\pi n / x_0$ and

$$c \text{ or } f = \begin{cases} b \quad \text{and} \quad c' \text{ or } f' = a \quad \text{if} \quad i \in \{1, 2, \ldots, s\} \\ a \quad \text{and} \quad c' \text{ or } f' = b \quad \text{if} \quad i \in \{s+1, \ldots, t\} \end{cases} \tag{2.30}$$

The total input shaft power can then be calculated by

$$P_{in} = \omega_r \cdot T_e + P_e + P_{wf} \tag{2.31}$$

where ω_r is the angular speed of the machine, and P_{wf} are the wind and friction losses, which are estimated from a prototype machine and kept constant in the optimisation process. The overall torque value is then given as:

$$T_{in} = T_e + \frac{P_{wf} + P_e}{\omega_r} \tag{2.32}$$

The output power is calculated by

$$P_{out} = S \cdot P_f \tag{2.33}$$

The efficiency is given by

$$\eta = \frac{P_{out}}{P_{in}} \tag{2.34}$$

This concludes the calculation of the performance parameters of the AFPM machine by directly coupling the FEM solutions with the classical machine theory, which is then evaluated by the optimisation algorithm as described in Chapter 6.

2.5 Analytical approach

An analytical approximation or lumped parameter circuit approach is often used in the performance calculation of the AFPM machine as a result of its being easy to use and its fast solution time[54, 61, 62]. These analytical methods are very useful tools for the preliminary optimum design of electrical machines and for investigating the tendencies of the optimum dimensions of the machine [30]. However, for a more precise optimisation, numerical methods such FEM or FDM are often used for the sake of better accuracy [59].

The aim of this section is to propose a simple analytical method that can be used to find a set of sub-optimum values as starting points for a more precise optimisation, and to use the method to explain the optimum design of the machine.

2.5.1 Induced Emf

In an AFPM machine a magnetic flux distribution close to a pure sine-wave in the airgap is desired in order to generate a sinusoidal EMF waveform. In the machine design, the fundamental component of the flux distribution is of main interest for investigation. For a sinusoidal distribution of the airgap magnetic flux density the fundamental excitation flux per pole can be found as

$$\phi_p = \int_{-\frac{\pi}{p}}^{\frac{\pi}{p}} \int_{r_i}^{r_o} B_{m1} \cos\frac{p}{2}\theta \; r dr d\theta = \frac{2}{p} B_{m1}(r_o^2 - r_i^2) \tag{2.35}$$

where p is the number of poles, B_{m1} is the amplitude of the fundamental magnetic flux density, and r_o and r_i are the rotor disc outer and inner radii, respectively. The excitation flux per pole calculated in terms of the average airgap magnetic flux density B_g is then [67]

$$\phi_p = \frac{2.22 \; B_g(r_o^2 - r_i^2)}{p} \tag{2.36}$$

where B_g is obtained using the magnetic circuit of the machine and the operating point on the demagnetisation curve of the PMs [60, 67]. For an AFPM machine with N_{ph} turns in series per phase, the r.m.s. value of the fundamental EMF can be readily found as

$$E_{ph} = \sqrt{2}\pi f N_{ph} \phi_p k_{w1} \quad \text{and} \quad k_{w1} = \frac{\sin\frac{q\alpha}{2}}{q \sin\frac{\alpha}{2}} \tag{2.37}$$

where k_{w1} is the winding distribution factor, q is the number of slots per pole per phase, and α is the slot pitch angle.

2.5.2 Current equation

One major disadvantage of the axial field topology is that it is impossible to fill all the volume at radii greater than r_i with torque-producing conductors. In practical AFPM machines, the complete filling of the available area at the inner radius is also impossible due to the existence of the end-windings.

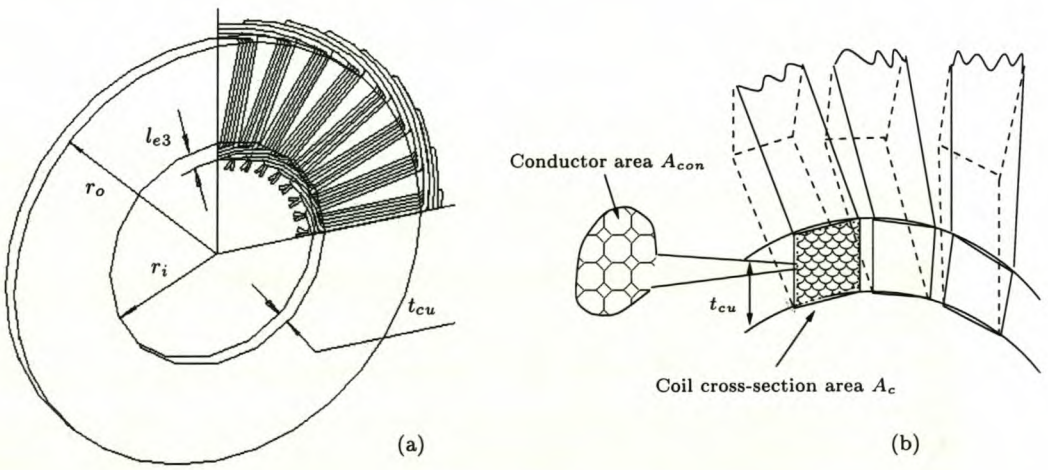

Figure 2.5: Winding layout of an AFPM machine: (a) closely nested coils, and (b) a portion of stator bore filled with conductor.

As shown in Fig. 2.5(a), it may be assumed that the area A_{cu} at a radius of $r_i - l_{e3}$ is completely filled with conductors, in which l_{e3} is close to the air-gap length l_g, i.e. $l_{e3} \approx l_g$. Thus, the corresponding available area A_{cu} for placing the conductors is given by

$$A_{cu} = 2\pi(r_i - l_{e3})\ t_{cu} \approx 2\pi(r_i - l_g)\ t_{cu} \tag{2.38}$$

where t_{cu} is the axial thickness of the stator. As illustrated in Fig. 2.5(b), the relation between a single conductor cross-section area A_{con} and the coil cross-section area A_c is

$$A_{con} = \frac{A_c k_f}{N_c} \tag{2.39}$$

where N_c is the number of turns per coil, k_f is the filling factor, and A_c can be expressed as

$$A_c = \frac{A_{cu}}{m\ p\ q} = \frac{2\pi\ (r_i - l_g)\ t_{cu}}{m\ p\ q} \tag{2.40}$$

where p is the number of poles, m is the number of phases and q is the number of coils per pole per phase. The r.m.s. current in a single conductor I_s can be given as

$$I_s = J_{rms} A_{con} = \frac{I_{ph}}{n_a} \tag{2.41}$$

where J_{rms} is the r.m.s. current density, I_{ph} is the r.m.s. phase current and n_a is the number of parallel circuits per phase. Thus, the phase current is

$$I_{ph} = J_{rms} A_{con} n_a = J_{rms}\ (\frac{A_c k_f}{N_c}) n_a \tag{2.42}$$

The number of turns in series per phase N_{ph} may be given by

$$N_{ph} = \frac{N_c\ p\ q}{2n_a} \tag{2.43}$$

This equation can be re-arranged as follows

$$N_c = \frac{2n_a N_{ph}}{p\ q} \tag{2.44}$$

On substitution of Eqns (2.40) and (2.44) to (2.42), the phase current is thus

$$I_{ph} = \frac{J_{rms} k_f t_{cu} \pi (r_i - l_g)}{m\ N_{ph}} \tag{2.45}$$

2.5.3 Power equation

For an m-phase sinewave AFPM machine the developed power P_{dev} with a power factor angle α (see Fig. 2.2c) is given by

$$P_{dev} = m\ E_{ph}\ I_{ph}\ cos\alpha \tag{2.46}$$

On substitution of Eqn. (2.36), (2.37) and (2.45), it becomes

$$P_{dev} = \frac{4\sqrt{6}}{p} \pi f k_{w1} k_f J_{rms} B_g t_{cu} (k_r - g)(1 - k_r^2) r_o^3 cos\alpha \tag{2.47}$$

where $k_r = r_i/r_o$ and $g = l_g/r_o$. It can clearly be seen that the developed power of an AFPM machine is proportional to r_o^3. A small increase in the machine diameter will increase the machine's rating significantly. By differentiating P_{dev} with respect to k_r, it is found that for a given J_{rms} and r_o the maximum developed power is obtained when

$$k_r = \frac{r_i}{r_o} = \frac{1}{3}(g + \sqrt{g^2 + 3}) \tag{2.48}$$

For a large AFPM machine $g \to 0$, thus $k_r \approx 0.577$. It can be readily seen that the radius ratio k_r is one of the key design parameters for the AFPM machine.

2.5.4 Torque equation

The developed torque T_{dev} at a unity power factor may be determined by

$$T_{dev} = \frac{m\ E_{ph}\ I_{ph}}{\omega_m} \tag{2.49}$$

where $\omega_m = 4\pi f/p$ is the mechanical angular speed. By replacing E_{ph} and I_{ph} with Eqn. (2.37) and (2.45), it becomes

$$T_{dev} = \sqrt{6}\ \pi k_{w1} k_f J_{rms} B_g t_{cu} (k_r - g)(1 - k_r^2) r_o^3 \tag{2.50}$$

2.5.5 Loss calculation

As for conventional machines, the losses in an AFPM machine with an ironless stator comprise of mechanical losses (windage and bearing losses) and electrical losses (copper losses and eddy current losses). The latter are dealt with in this section.

Copper losses

The copper losses P_{cu} of an m-phase sinewave AFPM machine can be calculated by

$$P_{cu} = m\ I_{ph}^2\ R_{ph} \tag{2.51}$$

where R_{ph} is the phase resistance and will be derived in the following text.

As depicted in Fig. 2.6, for a single-turn coil that is axis-symmetric along the vertical axis, the resistance of half a coil can be written as

$$R_{c1} = \rho_{cu} \frac{r_o - r_i + l_e}{A_{con}} \tag{2.52}$$

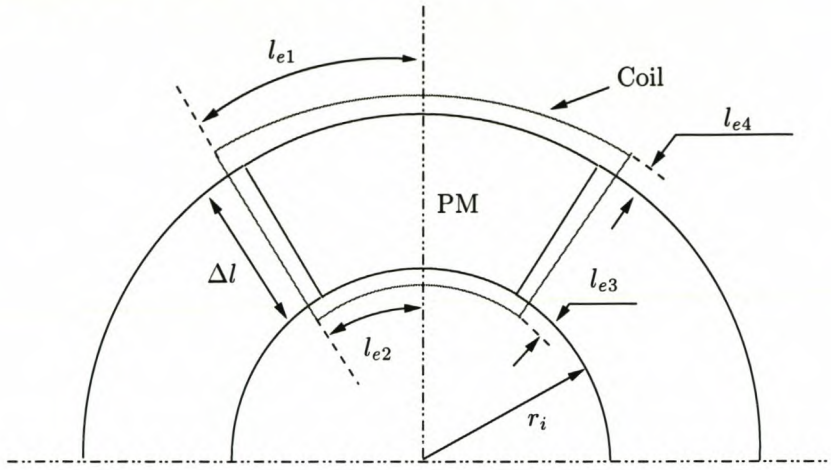

Figure 2.6: Dimensions of a simplified stator coil.

where l_e is the overall length of endwinding and is defined as

$$l_e = \sum_{i=1}^{4} l_{ei} \tag{2.53}$$

As an approximation l_{e1} and l_{e2} may be estimated as follows

$$l_{e1} = \frac{\pi(r_o + l_{e4})}{p} \quad \text{and} \quad l_{e2} = \frac{\pi(r_i - l_{e3})}{p} \tag{2.54}$$

where l_{e3} and l_{e4} may be taken as equal to l_g. Thus l_e becomes

$$l_e = \frac{\pi(r_o + r_i)}{p} + 2l_g \tag{2.55}$$

It can be seen from the above equation that for an AFPM machine with a large number of poles, its endwinding becomes short. On substitution of Eqn. (2.55) to (2.52), the phase resistance is given as

$$R_{ph} = \frac{2R_{c1}N_{ph}}{n_a} = \frac{2\rho_{cu}(r_o - r_i + l_e)N_{ph}}{n_a A_{con}} \tag{2.56}$$

According to Eqn. (2.39), (2.40) and (2.44), A_{con} can be written as

$$A_{con} = \frac{\pi(r_i - l_g)k_f t_{cu}}{m\ n_a\ N_{ph}} \tag{2.57}$$

Substituting Eqn. (2.57) into Eqn. (2.56), we have

$$R_{ph} = \frac{2mN_{ph}^2\rho_{cu}(r_o - r_i + l_e)}{\pi k_f t_{cu}(r_i - l_g)} \tag{2.58}$$

Thus the copper losses can be expressed as

$$P_{cu} = 2\pi J_{rms}^2 \; k_f \; t_{cu} \; \rho_{cu}(r_i - l_g)(r_o - r_i + l_e) \tag{2.59}$$

Replacing l_e with Eqn. (2.55), the above equation can be written in the form of

$$P_{cu} = \frac{2\pi}{p} J_{rms}^2 \; k_f \; t_{cu} \; \rho_{cu} \; [(\pi - p)k_r + p + 2gp + \pi](k_r - g)r_o^2 \tag{2.60}$$

It can be observed that the copper losses are proportional to r_o^2 in an AFPM machine. When Eqn. (2.47) and (2.60) are compared, it is clear that the larger AFPM machines are intrinsically more efficient as the developed power increases faster than the power losses.

Eddy current losses

The eddy current losses in a round conductor of radius R, resistivity ρ and length l placed in a transverse alternating field of peak flux density B_k and frequency f are given by [23]

$$P_e = \frac{\pi^3 B_k^2 f^2 R^4 \; l}{2\rho} \tag{2.61}$$

Since the above equation assumes a pure sinewave magnetic field, the fundamental component of the axial flux density B_{m1} is used for the eddy current loss calculation. The equivalent overall conductor length of an m-phase p-pole AFPM machine may be given by $l = 2 \; m \; n_a \; N_{ph} \; N_{cp} \; (r_o - r_i)$ where N_{cp} is the number of conductors in parallel per turn. The total eddy current losses are then

$$P_e = \frac{m \; \pi^3 B_{m1}^2 f^2 R_{con}^4 n_a N_{ph} N_{cp}(r_o - r_i)}{\rho_{cu}} \tag{2.62}$$

where R_{con} is the radius of the conductor, which is obviously the most influential factor in limiting eddy current losses.

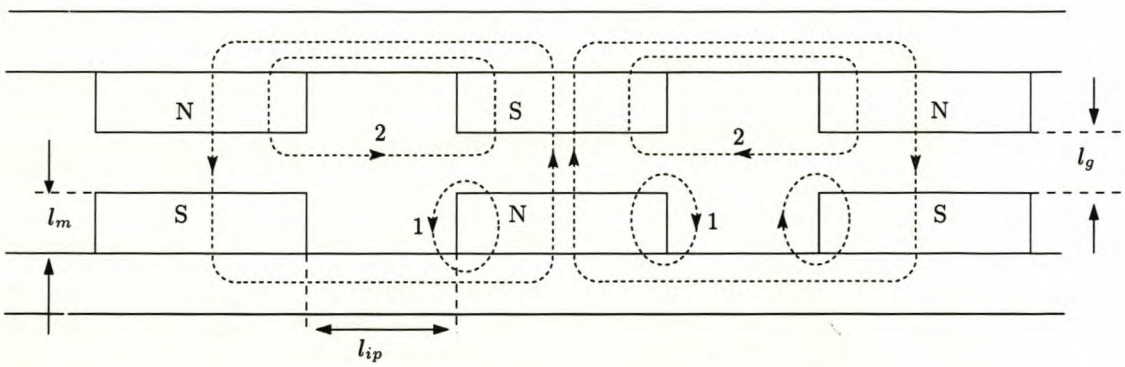

Figure 2.7: Flat model showing the dimensions of the AFPM machine.

2.5.6 Number of poles

The number of poles p in an ac AFPM machine, for a given speed n, is related to the designed operating frequency f according to $p = 120f/n$. As will be shown in this section, the selection of the number of poles for an AFPM machine also depends on other design parameters such as the pole-arc to pole-pitch ratio k and the rotor disc's inner to outer radius ratio k_r.

Fig. 2.7 shows a flat model of an AFPM machine, in which the desired flux path is indicated in solid lines while the leakage flux paths such as patterns *1* and *2* are drawn in dotted lines. Based on a simple airgap permeance model, the following criteria are essential to limit leakage flux and thus maintain maximum possible useful flux [60, 67]:

(i) $l_g < 2\ l_m$, where l_m is the PM height (*polarization direction*) and l_g is the airgap length,

(ii) $l_{ip} > l_g$, where l_{ip} stands for the inter-pole gap length.

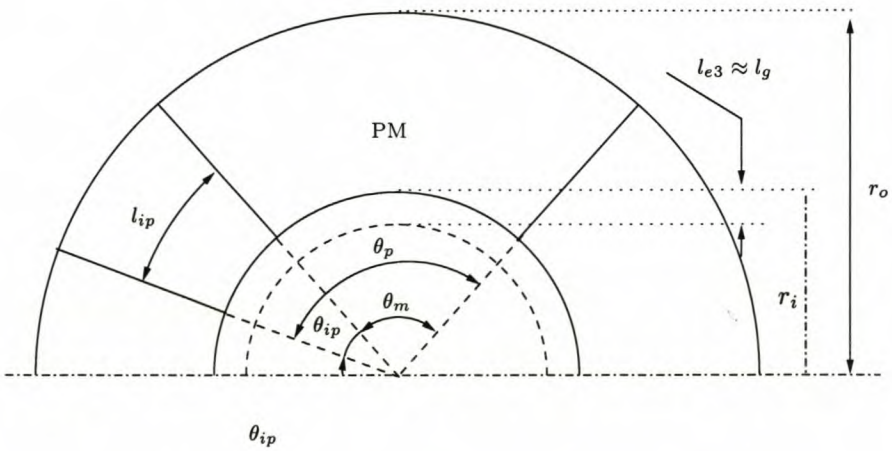

Figure 2.8: Dimensional parameters within a pole pitch.

As shown in Fig. 2.8, the pole-pitch angle θ_p of an AFPM machine is equal to the sum of the magnet pole-arc angle θ_m and the inter-pole angle θ_{ip}, i.e. $\theta_p = \theta_m + \theta_{ip}$. Defining the pole arc to pole pitch ratio $k = \frac{\theta_m}{\theta_p}$, we have

$$\theta_{ip} = \theta_p(1-k) = \frac{2\pi(1-k)}{p} \tag{2.63}$$

The inter-pole length l_{ip} is defined as a linearised distance between two PMs at the average radius and is given by

$$l_{ip} = \frac{\pi(r_o + r_i)(1-k)}{p} \tag{2.64}$$

Thus the number of poles is

$$p = \frac{\pi(r_o + r_i)(1-k)}{l_{ip}} \tag{2.65}$$

To satisfy the second criterion, we have

$$p = \frac{\pi(r_o + r_i)(1-k)}{l_{ip}} < \frac{\pi(r_o + r_i)\ (1-k)}{l_g} \tag{2.66}$$

Based on Eqn. (2.66), the maximum number of poles for a given structure may be defined as

$$p_{max} = \frac{\pi(1+k_r)(1-k)}{g} \tag{2.67}$$

2.5.7 Material consumption

One of the important objectives for the optimisation of PM electrical machines is to minimise the cost of the active material, while ensuring a desired power rating and good efficiency [44]. In the following analysis, the formulae for evaluating the volume and weight of the PM material, the iron yoke and the copper are described.

Permanent magnets

For a p-pole AFPM machine, the overall volume of the magnets V_m is calculated as

$$V_m = 2\pi r_o^2(1-k_r^2)kl_m \tag{2.68}$$

The corresponding weight W_m is then

$$W_m = \rho_m V_m = 2\pi\rho_m r_o^2(1-k_r^2)kl_m \tag{2.69}$$

where ρ_m is the density of the PM material.

Rotor yoke

Similarly, the volume of rotor yoke V_y is

$$V_y = 2\pi(r_o^2 - r_i^2)l_y = 2\pi r_o^2(1-k_r^2)l_y \tag{2.70}$$

where l_y is the thickness of yoke. Hence, the weight of the rotor yoke W_y is given by

$$W_y = \rho_y V_y = 2\pi\rho_y r_o^2(1-k_r^2)l_y \tag{2.71}$$

where ρ_y is the mass density of the yoke.

Copper

Since the end-winding length per turn can be readily calculated by using Eqn. (2.55), the conductor length l_s in a single-turn coil is

$$l_s = 2r_o(1 - k_r + \frac{\pi(1+k_r)}{p} + 2g) \tag{2.72}$$

The total conductor volume of an m-phase AFPM machine V_{cu} may be represented by

$$V_{cu} = mn_a N_{ph} A_{con} l_s = 2n_a m N_{ph} A_{con}(1 - k_r + \frac{\pi(1+k_r)}{p} + 2g)r_o \tag{2.73}$$

On substitution of Eqn. (2.57) into (2.73), it gives

$$V_{cu} = 2\pi k_f t_{cu}(k_r - g)(1 - k_r + \frac{\pi(1+k_r)}{p} + 2g)r_o^2 \tag{2.74}$$

The total weight of the copper is then

$$W_{cu} = 2\pi\rho_{cu} k_f t_{cu}(k_r - g)(1 - k_r + \frac{\pi(1+k_r)}{p} + 2g)\ r_o^2 \tag{2.75}$$

It can be observed from Eqn. (2.69), (2.71) and (2.75) that the weight of all active materials in an AFPM machine are proportional to r_o^2. This suggests that large AFPM machines have higher power to weight ratios.

Based on the above-described analytical method, a simple design program was developed. Although this method is far from precise when compared with the FEM, it is still an efficient and useful tool for the preliminary design and the interpretation of the final optimisation results of the AFPM machine.

Chapter 3

Time-Step Finite Element Model

In this Chapter an FE time-step model of an AFPM machine is developed. A macro-element originally proposed by Abdel-Razek et al. for modelling annular air-gaps in electrical machines is extended to enable the modelling of linear air-gaps. The theory of the new macro-element is presented, and its implementation within a time-stepped FE code is explained. Combined with the circuital equations, the proposed model is capable of simulating the steady-state performance of the AFPM machine for both balanced and rectifier load.

3.1 Circuit equations

As the AFPM machine being investigated operates at a high frequency, the intended generator application is to use it together with a diode bridge rectifier and then invert power back to 3-phase a.c. power. Considering the low winding inductance associated with this machine topology, it is necessary to study the behaviour of the machine with a rectifier loading.

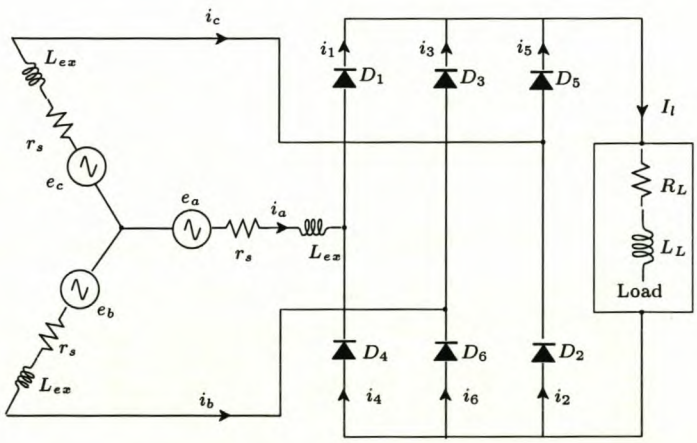

Figure 3.1: An AFPM generator feeding rectifier load.

Figure 3.1 represents an AFPM generator feeding a rectifier load, in which r_s is the per phase stator winding resistance, L_{ex} is the external inductance (e.g. cable inductance), and e_a, e_b and e_c are the three phase EMFs calculated by using total flux linkages that includes armature (stator) flux. The load has resistance R_L and inductance L_L. The diodes $D_1 \rightarrow D_6$ are represented by adjustable resistors that change the magnitudes of these resistances from zero to a large value and vice versa depending on the operating conditions.

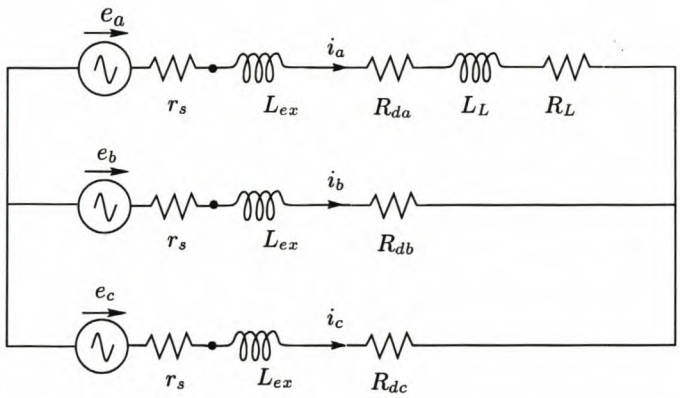

Figure 3.2: A conduction sequence.

For a conduction sequence depicted in Fig. 3.2, the voltage balance equations governing the circuital behaviour in an AFPM machine feeding a rectifier load may be expressed as follows:

$$\begin{cases} e_a - e_b = R_a i_a + L_a \frac{d}{dt} i_a - R_b i_b - L_b \frac{d}{dt} i_b \\ e_b - e_c = R_b i_b + L_b \frac{d}{dt} i_b - R_c i_c - L_c \frac{d}{dt} i_c \\ e_c - e_a = R_c i_c + L_c \frac{d}{dt} i_c - R_a i_a - L_a \frac{d}{dt} i_a \end{cases} \tag{3.1}$$

where i_{abc} are the three phase currents, R_{abc} are instantaneous three phase resistances given as

$$\begin{cases} R_a = r_s + R_{da} + R_L \\ R_b = r_s + R_{db} \\ R_c = r_s + R_{dc} \end{cases} \tag{3.2}$$

in which R_{da}, R_{db} and R_{dc} are the resistance values of the diodes. The instantaneous three phase inductances L_{abc} are given by

$$\begin{cases} L_a = L_{ex} + L_L \\ L_b = L_{ex} \\ L_c = L_{ex} \end{cases} \tag{3.3}$$

Using flux linkages λ_{abc}, Eqn. (3.1) may be written in the form

$$\begin{cases} \dot{\lambda}_a - \dot{\lambda}_b = R_a i_a + L_a \frac{d}{dt} i_a - R_b i_b - L_b \frac{d}{dt} i_b \\ \dot{\lambda}_b - \dot{\lambda}_c = R_b i_b + L_b \frac{d}{dt} i_b - R_c i_c - L_c \frac{d}{dt} i_c \\ \dot{\lambda}_c - \dot{\lambda}_a = R_c i_c + L_c \frac{d}{dt} i_c - R_a i_a - L_a \frac{d}{dt} i_a \end{cases} \tag{3.4}$$

or alternatively expressed as a matrix equation as

$$\begin{bmatrix} \dot{\lambda}_a - \dot{\lambda}_b \\ \dot{\lambda}_b - \dot{\lambda}_c \\ \dot{\lambda}_c - \dot{\lambda}_a \end{bmatrix} = \begin{bmatrix} R_a & -R_b & 0 \\ 0 & R_b & -R_c \\ -R_a & 0 & R_c \end{bmatrix} \begin{bmatrix} i_a \\ i_b \\ i_c \end{bmatrix} + \begin{bmatrix} L_a & -L_b & 0 \\ 0 & L_b & -L_c \\ -L_a & 0 & L_c \end{bmatrix} \frac{d}{dt} \begin{bmatrix} i_a \\ i_b \\ i_c \end{bmatrix} \tag{3.4a}$$

in which flux linkages λ_a, λ_b and λ_c are calculated by using FE analysis (see section 3.2). Eqn. (3.4) is now ready for time-step modelling of the AFPM machine, for as long as i_a is conducting in a positive direction. The subsequent time-stepping requires that both resistance and inductance matrices are redefined according to the new operating mode of the rectifier. Note that the eddy current loss is not taken into account in the above analysis. As described in Chapter 2, a shunt eddy loss resistance may be included in the circuit.

3.2 Finite Element Program

In a time-stepping analysis, FE field solutions are repeatedly used for determining and updating circuit parameters. The model proposed in this thesis makes use of a 2-D FE formulation, and the relevant formulation for the calculation of flux linkages and inductances has been given in Chapter 2.

A non-commercial FE program was acquired for this study. With the source code of the FE solver available, it is possible to invoke an FE field solution and extract useful information at any time during a simulation, which offers great flexibility for directly coupling FEM with the circuital equations in a fully automated time-step simulation.

Besides, the air-gap region of the FE model is represented by a macro element, which is based on an analytical solution and will be described in greater length in the next section.

3.3 The Cartesian Air-Gap Element

The air-gap element (AGE) is a macro-element originally proposed by Abdel-Razek et al [1, 2]. It replaces the finite elements, which would normally be used to discretise the air-gap, with a single macro element. This macro-element is based on the analytical solution of the air-gap field.

The main advantages of the AGE are: (i) the ease with which relative motion between rotor and stator is treated (no need for re-meshing the air-gap), (ii) greater accuracy, since the air-gap field is related to its analytical solution, and (iii) the avoidance of finite-elements with poor aspect ratios, or alternatively the use of a high peripheral density of nodes. The main disadvantage is that the resulting stiffness matrix has a large profile, especially if the number of nodes on the AGE boundary is large. This can lead to large CPU times, although a method for alleviating this problem is proposed in [40].

3.3.1 Theory of the Cartesian Air-Gap Element

Since a typical rotating machine has an annular air-gap, the AGE was initially derived for the polar coordinate system. The modelling of some special electrical machines such as the linear machine or the disc-type rotating machine requires a basic reformulation of the AGE, in order to deal with the rectangular shape of the air-gap. Since this is associated with the Cartesian coordinate system it is necessary to derive the AGE for Cartesian problems. This section presents the development of a Cartesian Air-Gap Element (CAGE). The new CAGE is validated by comparison with results obtained using the standard FE method, in which the air-gap is discretised. A detailed derivation is given in Appendix A.

Consider a generic linear machine, for which the air-gap is as shown in Fig. 3.3. Clearly, in the air-gap region there is no current, and the reluctivity is that of free space, ν_o. In Cartesian coordinates the field in the air-gap region is therefore governed by:

$$\frac{\partial^2 A(x,y)}{\partial x^2} + \frac{\partial^2 A(x,y)}{\partial y^2} = 0 \tag{3.5}$$

in which $A(x,y)$ denotes the z-directed component of the magnetic vector potential. Like conventional electrical machines, special electrical machines such as the axial field and the linear machine also exhibit structural periodicity which in turn leads to periodicity in the magnetic field distribution. In this paper the periodicity is taken to be of the form:

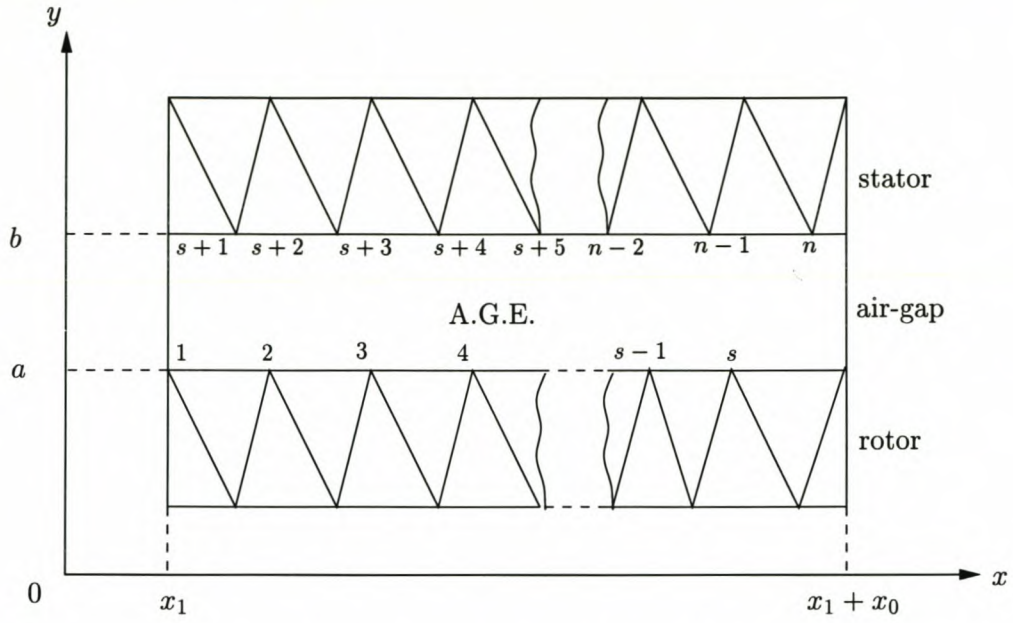

Figure 3.3: Solution domain of the CAGE.

$$A(x,y) = A(x + x_o, y) \tag{3.6}$$

where x_o is the period of the function $A(x,y)$. Applying the technique of separation of variables and applying the boundary condition of Eqn. (3.6), the solution to Eqn. (3.5) is

$$\begin{aligned} A(x,y) =& F_o \cdot y + G_o + \sum_{n=1}^{\infty} (F_n \cdot e^{\lambda_n y} + G_n \cdot e^{-\lambda_n y}) \\ & \cdot (H_n \cos \lambda_n x + K_n \sin \lambda_n x). \end{aligned} \tag{3.7}$$

where $\lambda_n = \pm 2n\pi/x_o$ and F_o, G_o, F_n, G_n, H_n, K_n are constants which are to be determined.

In order to maintain the continuity of A(x,y) at the transition between classical finite-elements and the CAGE (i.e. the lines $y = a$ and $y = b$), the following boundary condition must be satisfied:

$$A(x,c) = \sum_{i=k}^{l} \alpha_i(x,c) \cdot A_i^b \tag{3.8}$$

where A_i^b is the nodal value of the magnetic vector potential at node i on the CAGE boundary, $\alpha_i(x,c)$ is the Lagrange polynomial defined from the shape functions of the adjacent classical elements, and

$$k = \begin{cases} 1 & \text{and } l = s \text{ if } c = a, \\ s+1 & \text{and } l = t \text{ if } c = b. \end{cases}$$

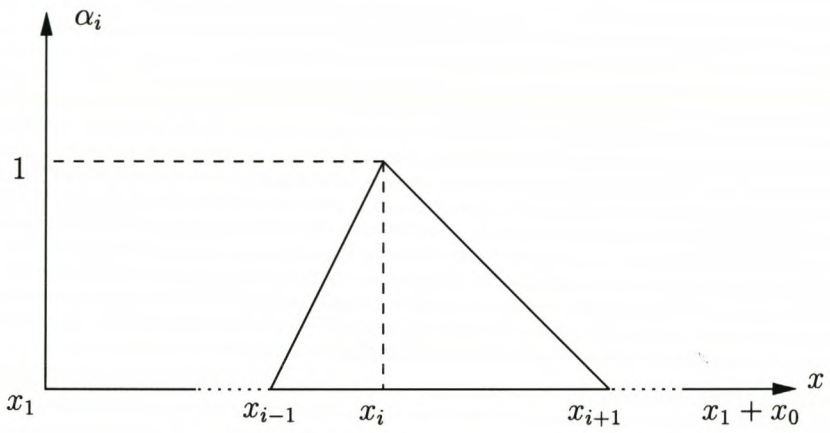

Figure 3.4: Definition of function $\alpha_i(x, c)$.

The nodal shape function $\alpha_i(x, c)$ for the first order triangular element is illustrated in Fig. 3.4. This may be represented as:

$$\alpha_i(x,c) = \begin{cases} \frac{x-x_{i-1}}{x_i-x_{i-1}} & \text{if } x_{i-1} \le x \le x_i \\ \frac{x-x_{i+1}}{x_i-x_{i+1}} & \text{if } x_i \le x \le x_{i+1} \\ 0 & \text{if } x_1 \le x \le x_{i-1} \\ 0 & \text{if } x_{i+1} \le x \le x_1 + x_o \end{cases} \tag{3.9}$$

To facilitate further mathematical manipulation, Eqn. (3.9) is expanded into a Fourier series:

$$\alpha_i(x,c) = a_{0i} + \sum_{n=1}^{\infty} [a_{ni} \cos \lambda_n x + b_{ni} \sin \lambda_n x] \tag{3.10}$$

where a_{0i}, a_{ni} and b_{ni} may be found as:

$$\begin{cases} a_{0i} = \frac{x_{i+1}-x_{i-1}}{x_o} \\ a_{ni} = -\frac{4}{x_o} \cdot \frac{1}{\lambda_n^2} \left[\frac{1}{x_i-x_{i-1}} \sin \frac{\lambda_n(x_i+x_{i-1})}{2} \sin \frac{\lambda_n(x_i-x_{i-1})}{2} \right. \\ \qquad \left. + \frac{1}{x_i-x_{i+1}} \sin \frac{\lambda_n(x_{i+1}+x_i)}{2} \sin \frac{\lambda_n(x_{i+1}-x_i)}{2} \right] \\ b_{ni} = \frac{4}{x_o} \cdot \frac{1}{\lambda_n^2} \left[\frac{1}{x_i-x_{i-1}} \sin \frac{\lambda_n(x_i-x_{i-1})}{2} \cos \frac{\lambda_n(x_i+x_{i-1})}{2} \right. \\ \qquad \left. + \frac{1}{x_i-x_{i+1}} \sin \frac{\lambda_n(x_{i+1}-x_i)}{2} \cos \frac{\lambda_n(x_{i+1}+x_i)}{2} \right] \end{cases} \tag{3.11}$$

The constants in Eqn. (3.7) may now be found by equating $A(x,a)$ and $A(x,b)$ obtained from Eqn. (3.7) with the respective terms obtained by substituting Eqn. (3.10) into Eqn. (3.8). The final result is:

$$A(x,y) = \sum_{i=1}^{t} \alpha_i^{\varepsilon}(x,y) \cdot A_i^b \tag{3.12}$$

where $\alpha_i^{\varepsilon}(x,c)$ is given by:

$$\begin{aligned}\alpha_i^{\varepsilon}(x,c) =& \frac{y-c}{c'-c} \cdot \frac{a_{oi}}{2} + \sum_{n=1}^{\infty} \frac{e^{\lambda_n(y-c)} - e^{\lambda_n(c-y)}}{e^{\lambda_n(c'-c)} - e^{\lambda_n(c-c')}} \\ & \cdot (a_{ni}\cos\lambda_n x + b_{ni}\sin\lambda_n x).\end{aligned} \tag{3.13}$$

The energy functional for the air-gap, $[S]^{\varepsilon}$, is:

$$F_{\varepsilon} = \frac{1}{\mu_o}\int\int_{S_{\varepsilon}} \frac{B^2}{2} dS_{\varepsilon} \tag{3.14}$$

By substituting for B in Eqn. (3.14) using $B = \nabla \times A$, where $A(x,y)$ is given by Eqns (3.12) and (3.13), and then differentiating with respect to A_i for $i = 1 \ldots t$ gives:

$$\frac{\partial F^{\varepsilon}}{\partial [A]^{\varepsilon}} = \frac{1}{\mu_o}[S]^{\varepsilon}[A]^{\varepsilon} \tag{3.15}$$

where the general term of the matrix $[S]^{\varepsilon}$ is:

$$\begin{aligned}S_{ij}^{\varepsilon} =& \frac{x_o}{4}\frac{b-a}{(c'-c)(f'-f)} a_{oi}a_{oj} + \frac{x_o}{2}\sum_{n=1}^{\infty} \frac{\lambda_n}{[e^{\lambda_n(c'-c)} - e^{\lambda_n(c-c')}]} \\ & \cdot \frac{1}{[e^{\lambda_n(f'-f)} - e^{\lambda_n(f-f')}]}[(e^{\lambda_n(b-c)} - e^{\lambda_n(c-b)}) \cdot (e^{\lambda_n(b-f)} + e^{\lambda_n(f-b)}) \\ & -(e^{\lambda_n(a-c)} - e^{\lambda_n(c-a)}) \cdot (e^{\lambda_n(a-f)} + e^{\lambda_n(f-a)})](a_{ni}a_{nj} + b_{ni}b_{nj}).\end{aligned} \tag{3.16}$$

where

$$f = \begin{cases} b \text{ and } f' = a \text{ if } i \in \{1,2,\ldots,s\} \\ a \text{ and } f' = b \text{ if } i \in \{s+1,\ldots,t\} \end{cases}$$

3.3.2 Coupling scheme

The implementation of the CAGE into the standard finite element program is carried out in the same way as for the AGE for annular air-gaps. The energy-related functional is broken down into F^e and F^{ε} and is then minimised with respect to A:

$$\frac{\partial F}{\partial [A]} = \sum_{e=1}^{P} \frac{\partial F^e}{\partial [A]^e} + \frac{\partial F^{\varepsilon}}{\partial [A]^{\varepsilon}} \tag{3.17}$$

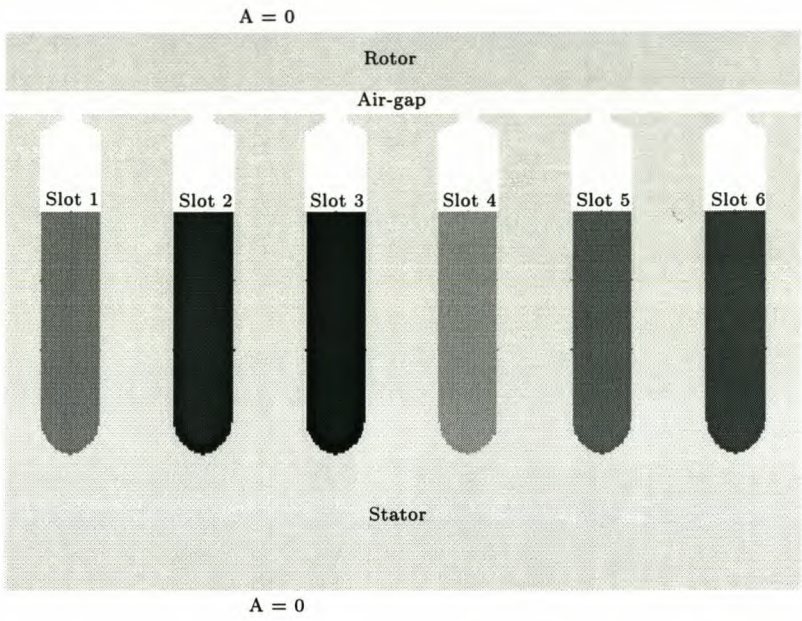

Figure 3.5: Simple linear electrical machine model.

3.3.3 Validation by comparison

In order to validate the CAGE, the simplified linear problem shown in Fig. 3.5 was modelled. Firstly the air-gap was discretised using two layers (120 nodes per layer) of classical first-order triangular elements, and the resulting FE model solved. Then, the CAGE was substituted in place of the discretised air-gap, leaving the rest of the FE mesh unchanged, and solved. Homogeneous Dirichlet conditions were assigned to the top and bottom boundaries, whilst positive periodicity conditions were assigned to the left and right boundaries.

Slots 1 - 6 were excited with balanced three-phase currents at an instant in time, and the air-gap flux density distribution obtained by both methods is plotted in Fig. 3.6. It is evident that the result obtained using the CAGE agrees very well with that obtained using a discretised air-gap. Further examination and verification has also been performed by comparing the respective magnetic stored energies in various parts of the model obtained from both methods, as shown in Table 3.1. It is evident that the results are in very good agreement. The worst discrepancy is about 0.5%.

3.3.4 Minimising the re-calculation time

In order to reduce the time taken to compute the CAGE terms at different rotor positions, the scheme proposed in [99] may be implemented. Close inspection of Eqn. (3.16) and its counterpart for the annular AGE [1] reveals that this scheme can be directly applied to the CAGE without much modification. In this section, the implementation of the time-saving

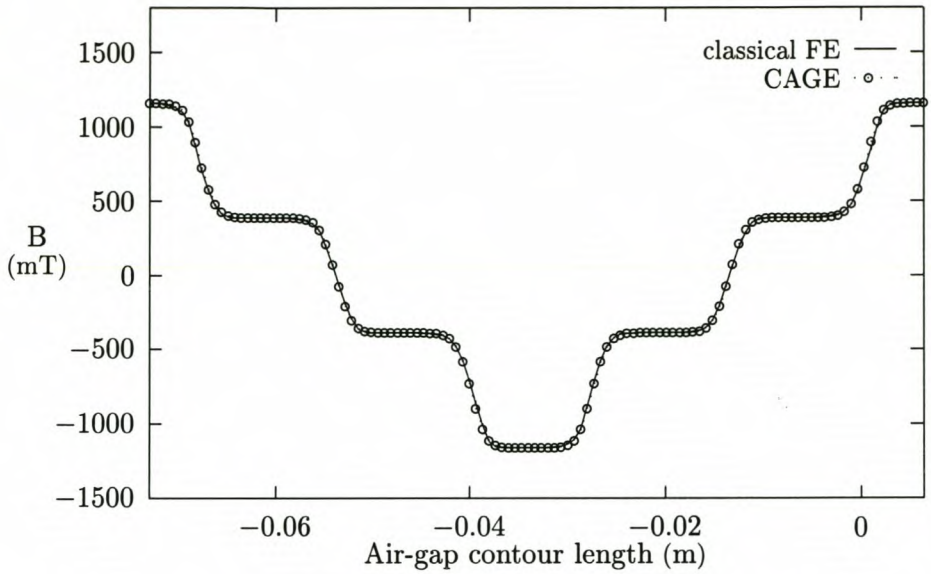

Figure 3.6: Comparison of calculated air-gap flux density by using classical FE and C.A.G.E.

scheme in the CAGE formulation is described briefly. Firstly, the expression for S_{ij} is defined as two parts:

$$S_{ij} = S_1 + S_2 \tag{3.18}$$

where

$$S_1 = \frac{x_o}{4}\frac{b-a}{(c'-c)(f'-f)}a_{oi}a_{oj} \qquad \text{and} \tag{3.19}$$

$$S_2 = \frac{x_o}{2}\sum_{n=1}^{\infty} f(\lambda_n)(a_{ni}a_{nj} + b_{ni}b_{nj}) \qquad \text{where} \tag{3.20}$$

$$\begin{aligned} f(\lambda_n) = & \frac{\lambda_n}{[e^{\lambda_n(c'-c)} - e^{\lambda_n(c-c')}]\cdot[e^{\lambda_n(f'-f)} - e^{\lambda_n(f-f')}]}\cdot \\ & [(e^{\lambda_n(b-c)} - e^{\lambda_n(c-b)})\cdot(e^{\lambda_n(b-f)} + e^{\lambda_n(f-b)}) \\ & -(e^{\lambda_n(a-c)} - e^{\lambda_n(c-a)})\cdot(e^{\lambda_n(a-f)} + e^{\lambda_n(f-a)})] \end{aligned} \tag{3.21}$$

Clearly, S_1 is independent of rotor movement, and needs to be calculated once only. In the second part S_2, $f(\lambda_n)$ is also not affected by the change in rotor position. Therefore, the only terms that are associated with the rotor displacement are a_{ni} and b_{ni}.

Table 3.1: Comparison of the calculated magnetic stored energy in different sub-regions.

Regions	C.A.G.E. (μJ)	Classical FE (μJ)	Discrepancy
Slot1 (Cu)	0.519085776	0.519129716	0.01%
(air)	0.692833408	0.695610829	0.40%
Slot2 (Cu)	2.07633383	2.07650904	0.01%
(air)	2.69936816	2.69670033	0.09%
Slot3 (Cu)	0.519085782	0.519129719	0.01%
(air)	0.692830925	0.699608371	0.09%
Slot4 (Cu)	0.519085777	0.519129716	0.01%
(air)	0.692833425	0.699610829	0.09%
Slot5 (Cu)	2.07633377	2.07650904	0.01%
(air)	2.69936826	2.69670033	0.09%
Slot6 (Cu)	0.519085774	0.519129719	0.01%
(air)	0.692830919	0.695608317	0.40%
Stator iron	0.242891804	0.242665537	0.14%
Rotor iron	0.025792278	0.0254261082	0.14%
Air-gap	35.8157674	35.9925716	0.49%

By defining:

$$\begin{cases} \mathcal{X}_1 = x_i - x_{i-1} \\ \mathcal{X}_2 = x_i + x_{i-1} \\ \mathcal{X}_3 = x_i - x_{i+1} \\ \mathcal{X}_4 = x_i + x_{i+1} \end{cases} \tag{3.22}$$

and $K_n = \frac{4}{\lambda^2 x_0}$, a_{ni} can be expressed as:

$$a_{ni} = -K_n[\frac{1}{\mathcal{X}_1}\sin\frac{\lambda_n(\mathcal{X}_2)}{2}\sin\frac{\lambda_n(\mathcal{X}_1)}{2} + \frac{1}{\mathcal{X}_3}\sin\frac{\lambda_n(\mathcal{X}_4)}{2}\sin\frac{\lambda_n(-\mathcal{X}_3)}{2}] \tag{3.23}$$

When the rotor is moved through a displacement Δx, $\mathcal{X}_1$ and $\mathcal{X}_3$ are not changed. However, $\mathcal{X}_2$ and $\mathcal{X}_4$ become $\mathcal{X}_2 \rightarrow \mathcal{X}_2 + 2\Delta x$ and $\mathcal{X}_4 \rightarrow \mathcal{X}_4 + 2\Delta x$ respectively. The a_{ni} is then written as:

$$a_{ni|+\Delta x} = C_{ni} sin\frac{\lambda_n}{2}(\mathcal{X}_2 + 2\Delta x) + D_{ni} sin\frac{\lambda_n}{2}(\mathcal{X}_4 + 2\Delta x) \tag{3.24}$$

where C_{ni} and D_{ni} are also independent of the rotor position.

They are given by

$$\begin{cases} C_{ni} = \frac{K_n}{\mathcal{X}_1} sin(\frac{-\lambda_n}{2}\mathcal{X}_1) \\ \\ D_{ni} = \frac{K_n}{\mathcal{X}_3} sin(\frac{-\lambda_n}{2}\mathcal{X}_3) \end{cases} \tag{3.25}$$

Expanding Eqn. (3.24) into constant terms and terms containing Δx:

$$a_{ni|+\Delta x} = F_{ni} sin\lambda_n \Delta x + G_{ni} cos\lambda_n \Delta x \tag{3.26}$$

where F_{ni} and G_{ni} are not affected by the rotor movement. They are defined as

$$\begin{cases} F_{ni} = C_{ni} cos\frac{\lambda_n}{2}\mathcal{X}_2 + D_{ni} cos\frac{\lambda_n}{2}\mathcal{X}_4 \\ \\ G_{ni} = C_{ni} sin\frac{\lambda_n}{2}\mathcal{X}_2 + D_{ni} sin\frac{\lambda_n}{2}\mathcal{X}_4 \end{cases} \tag{3.27}$$

Finally, Eqn. (3.26) may be simplified further as follows:

$$a_{ni|+\Delta x} = H_{ni} cos(\lambda_n \Delta x - P_{ni}) \tag{3.28}$$

where H_{ni} and P_{ni} are given by:

$$\begin{cases} H_{ni} = (F_{ni}^2 + G_{ni}^2)^{1/2} \\ \\ P_{ni} = tan^{-1}(F_{ni}/G_{ni}) \end{cases} \tag{3.29}$$

It can be seen that the evaluation of a_{ni} is now reduced to the calculation of a cosine term, which means a significant saving of the computation efforts. Likewise, the re-calculation of b_{ni} can be treated in the same way as shown below:

$$b_{ni|+\Delta x} = H_{ni} sin(\lambda_n \Delta x - P_{ni}) \tag{3.30}$$

3.3.5 Minimising the modelled region

Further minimisation of the computation time may be achieved by exploiting the symmetry and the periodic feature of the geometry and the field distribution of an FE model.

Taking into account symmetry

A typical AFPM machine usually has two running clearances. The means that the modelling of rotor movement may involve two CAGEs, which is certainly undesirable from a computational cost point of view. However, due to the symmetry of an AFPM machine, each half of

the machine from the centre plane of the stator, mirrors the other half.

Furthermore, for an AFPM machine with an ironless stator, there is no tangential field component on the centre plane of the stator so that the Neumann boundary condition can be imposed. For an AFPM machine with an iron-core stator, there is no flux line crossing the centre plane implying a Dirichlet boundary condition. In both cases, it is possible to model only one half of the machine comprising of the rotor disc, the air-gap clearance and a half of the stator.

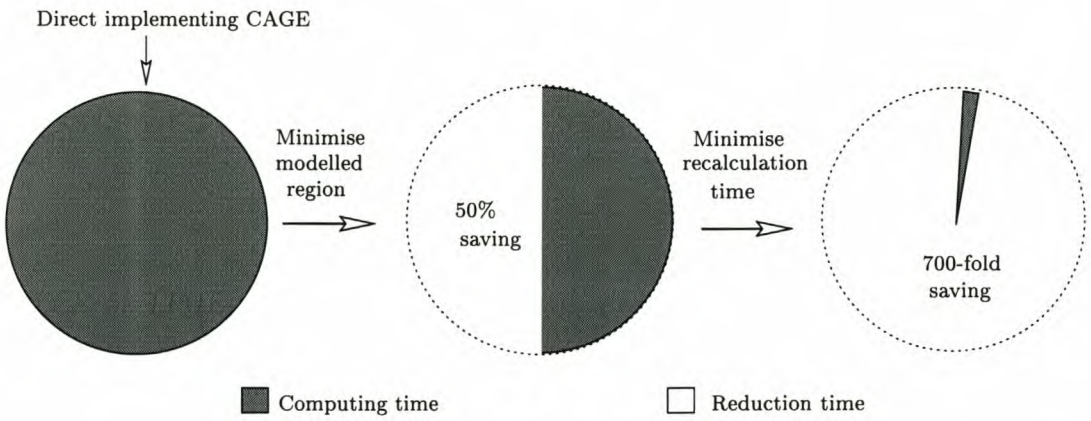

Figure 3.7: Improved calculation speed of the CAGE by using existing time-saving schemes.

Negative periodicity formulation

In the previous sections, the CAGE was derived for the positive periodic boundary conditions. In order to further reduce the CPU time taken, it would be useful to extend the CAGE formulation so that the use of the negative periodic boundary conditions may be accommodated. The immediate advantage of utilising a negative periodic model is that it virtually reduces the number of unknowns to be solved for by a factor of approximately two.

The modification to the CAGE for negative periodic boundary conditions is done in the same manner as that proposed in [40], which proves that the first term S_1 in Eqn. (3.18) disappears, and the second term S_2 is doubled. The general stiffness term for the negative periodicity CAGE is given by:

$$S_{ij} = x_0 \sum_{n=1}^{\infty} f(\lambda_n)(a_{ni}a_{nj} + b_{ni}b_{nj}), \quad \text{where } n = 2m-1,\ m = 1,2,3,\ldots\infty \tag{3.31}$$

Unlike the positive periodicity CAGE, the summation in the above equation is carried out over odd harmonics only, thus implying a further decrease of computation time. As illustrated

in Fig. 3.7, the calculation speed of the CAGE may be significantly improved by using the above-mentioned time-saving methods.

3.3.6 Performance of the FE time-step model: a case study

The merits of the new macro-element and the effectiveness of these time-saving methods are shown in a simple case study, in which the new macro element is coupled with finite elements. The aim is to simulate the induced EMF waveform of a 10 kW ironless stator AFPM machine [60] (also illustrated in Chapter 7) by using finite element time-stepping modelling. Fig. 3.8(a) shows an FE mesh coupled with a CAGE, which spans one pole of the AFPM machine.

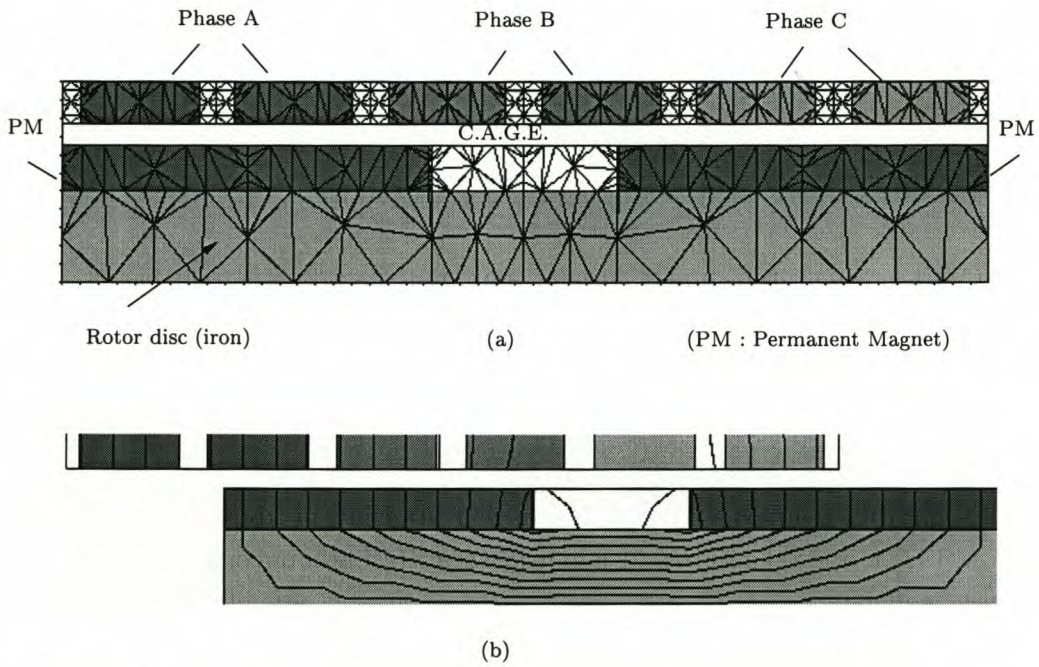

Figure 3.8: Time-step FE model of an ironless stator AFPM machine.

The mesh consists of 622 elements and 447 nodes, of which 138 nodes lie on the boundaries of the CAGE. The air-gap region was modelled using the CAGE. The model was time-stepped over a time interval of 16 ms which corresponds to the rotor moving by one pole-pair, using a time-step of 0.2 ms. This required 80 FE solutions. Fig. 3.8(b) shows the flux plot of the AFPM machine at a certain position. At every rotor position, the total phase flux linkages were determined from the FE field solution, from which the phase EMF $e(t)$ of Eqns (3.1) and (3.4) may be found as:

$$e(t) = \frac{d\lambda}{dt} = \frac{\lambda(\theta_2) - \lambda(\theta_1)}{t_2 - t_1} \tag{3.32}$$

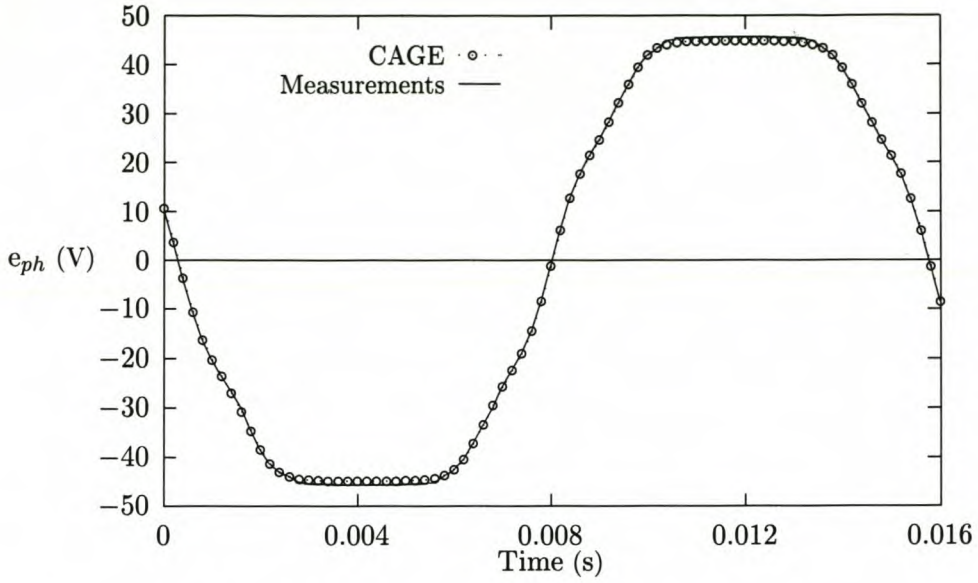

Figure 3.9: Phase EMF as a function of time at 970 rpm.

The total CPU time for this simulation was 107 seconds on a 333 MHz PC (Intel Celeron CPU) running the Redhat Linux operating system. Despite that the modelled region is of a rather simple structure. It is evident that the computational limitations associated with the air-gap element have been greatly alleviated. The calculated EMF induced in the stator phase winding at a shaft speed of 970 rpm is compared with measurement in Fig. 3.9. It is seen that the correlation between calculated and measured EMF is very good.

3.4 Procedure for FE time-stepping

The time-stepping scheme described in this thesis is that the FE field solution is invoked for each time step. Relative to the classical approaches, FEM is computationally expensive whatever the state of the art in computing power [99]. It is not the intention of this thesis to re-evaluate different time-stepping approaches. Due to the relatively simple structure of an AFPM machine from an FE modelling perspective, fast field calculations are expected as shown in section 3.3.

3.4.1 Time-stepping simulation

The time-stepping simulation was performed on the assumption that the rotor speed is constant and the armature reaction is negligible. The solution to the derivative in Eqn. (3.4) is found using a linear approximation for a small time step Δt. Eqn. (3.4) is thus solved as:

$$[\mathrm{i}]_{n+1} - [\mathrm{i}]_n = [\mathrm{L}]^{-1}(\ [\lambda_{abc} - \lambda_{bca}]_{n+1} - [\lambda_{abc} - \lambda_{bca}]_n - [\mathrm{R}] \ [\mathrm{i}]_n \ \Delta t \ ) \qquad (3.33)$$

where [i], [L] and [R] represent phase current, inductance and resistance matrices, respectively. Starting at time ($t = 0$), with initial conditions specified (zero current), the basic procedure is summarised as follows:

1. Invoke an FE field solution to calculate and pre-store a set of flux linkages.
2. Re-position the rotor (from knowledge of its previous position and the rotation speed) and perform a field solution to determine a new set of flux linkages.
3. Calculate the initial EMFs using two sets of flux linkages (Eqn. 3.32) and determine the operating mode of the rectifier (Fig. 3.10) as described in section 3.4.2.
4. Update the resistance and the inductance matrices and calculate the present currents using the above equation and flux linkages.
5. Step the above equation forward in time, return to step 2 and repeat until steady state conditions are reached.
6. Start steady-state simulation and obtain voltages and currents from field solutions and circuit equations.

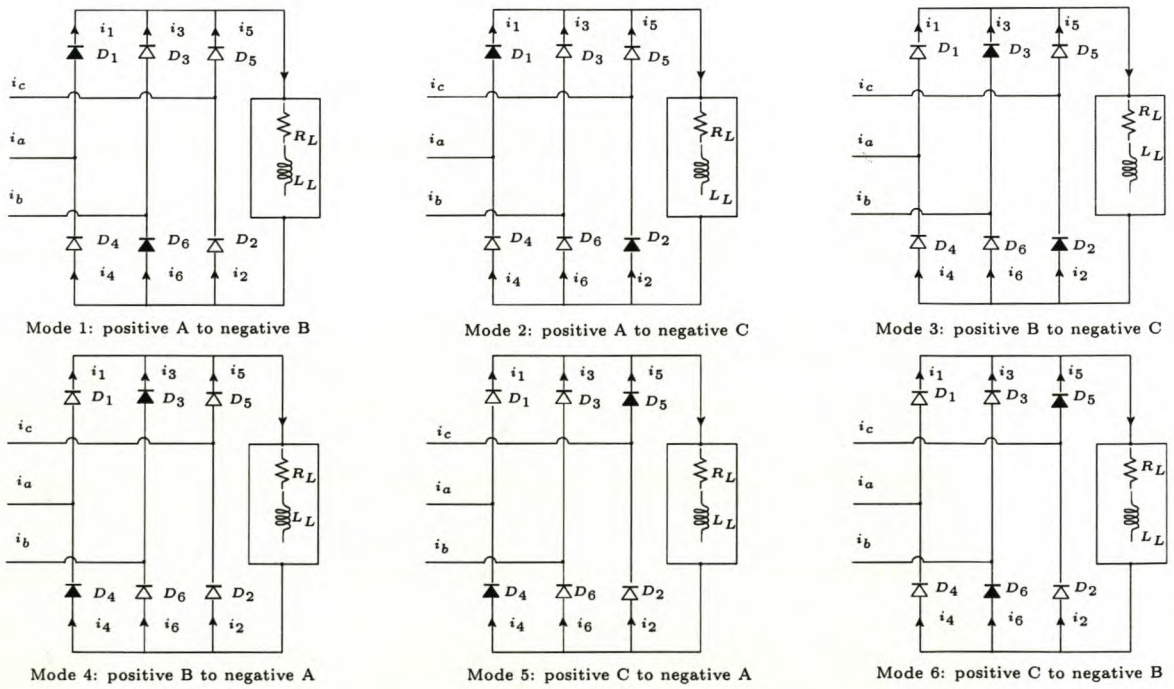

Figure 3.10: The six modes of rectifier operation.

3.4.2 Rectifier operation

In order to attach the correct values to the resistances and inductances, it is crucial to monitor the operating condition of the rectifier in the simulation accurately. The three-phase rectifier operates in cycles of six modes that are dictated by the maximum line voltage at a given instant in time as shown in Fig. 3.10. The diodes in conduction are represented by solid black symbols.

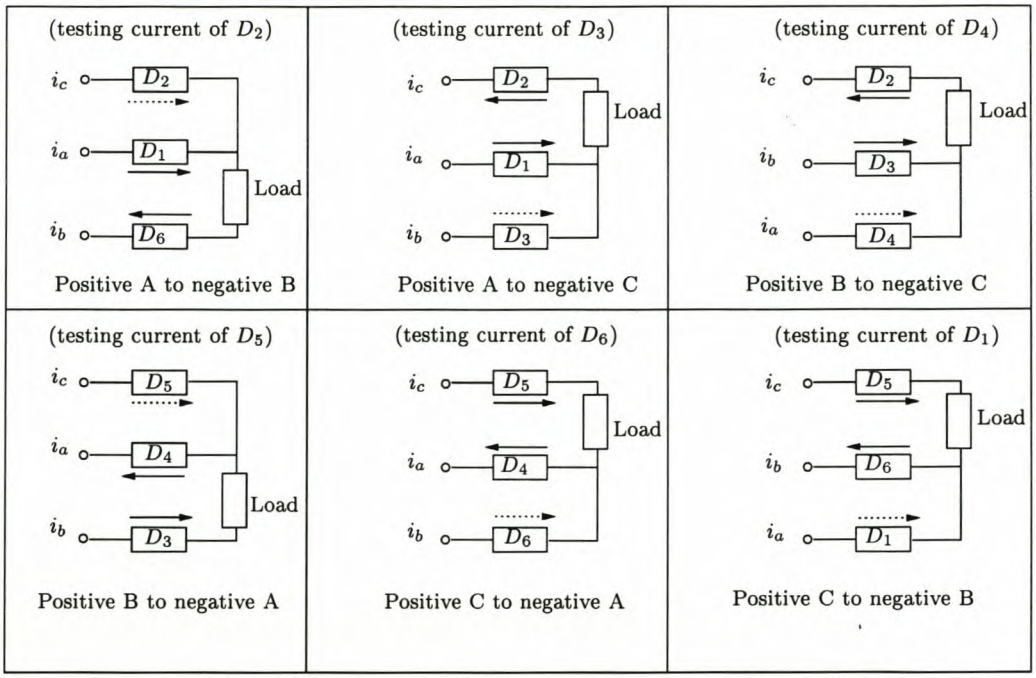

Figure 3.11: State-monitoring of the three-phase diode bridge rectifier.

A diode state-monitoring algorithm given in [99] was used in the simulation. The switching action takes place whenever the testing of the sign of a diode's current picks up a change as shown in Fig. 3.11. The overlap period, i.e. when all three phases conduct, is accounted for by assuming that the resistance of a diode changes linearly with time over a switching period.

By grouping the above-described models/sub-procedures together, a coherent algorithm is formed. The simulation is then carried out and results are compared with measurements in Chapter 8.

Chapter 4

Calculation of Eddy Current Loss

This chapter presents a hybrid method (termed *finite element (FE) aided analytical method*) that combines the 2-D FE field solution and the closed-form formula for eddy current loss calculation. The computational limitations of using 2-D FE modelling are discussed and then a multi-slice FE model is developed to account for 3-D effects. Relevant tests at high frequencies are carried out to validate the method. Other practical aspects affecting the eddy current losses in the designing and constructing of an ironless stator AFPM machine have also been investigated.

4.1 Eddy Losses in an AFPM machine with an ironless stator

In AFPM machines the winding is located in the middle of the air-gap magnetic field (see Fig. 4.1(a)). Motion of the permanent magnets over the winding produces an alternating field through each conductor inducing eddy currents.

The loss due to eddy currents in the conductors depends on both the geometry of the wire cross section and the amplitude and waveform of the flux density. In order to minimise the eddy current loss in the conductors, either Litz wires or thin copper strip conductors can be used in the stator of the AFPM machine as described in [66, 14].

For an AFPM machine with an ironless winding arrangement (as shown in Fig. 4.1(a)), apart from its normal component, the field through each conductor has a tangential component, which can lead to serious additional eddy current loss (see Fig. 4.1(b)). The existence of a tangential field component in the air-gap discourages the use of copper strip conductors as a low cost arrangement. Litz wires allow significant reduction of eddy current loss, but they are more expensive and have fairly poor filling factors.

As a cost effective solution, one may use thin wires for the stator coils. Quite often the coils are made of several parallel wires to distribute the current. However, this may create a new

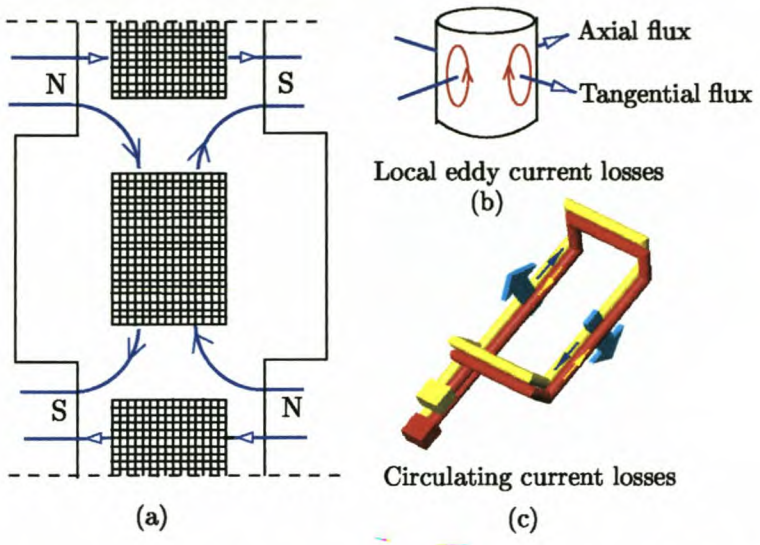

Figure 4.1: Eddy current losses in the ironless stator winding of an AFPM machine.

problem, i.e. unless a complete balance of induced EMF among the individual conducting paths is achieved, a circulating current between any of these parallel paths [90, 102] may occur as shown in Fig. 4.1(c) causing circulating eddy current losses.

When operating at relatively high frequency magnetic fields, these eddy current effects may cause a significant increase of winding losses, which are intensified if there are circulating currents among the parallel circuits. These losses will deteriorate the performance of the AFPM machine. Predicting the winding eddy losses with good accuracy is therefore very important in the design of such machines. In the following sections, these aspects will be dealt with in more detail.

4.1.1 Limiting circulating current losses

To minimise the circulating current in a coil of parallel connections, the normal practice is to twist or transpose the wires in such a fashion that each parallel path occupies all possible layer positions for the same length of the coil. The effect is to equalize the induced EMFs in all parallel paths, and to allow them to be paralleled at the ends without producing eddy circulating currents between the parallel paths.

Figure 4.2 illustrates the effectiveness of suppressing circulating eddy current by wire twisting. Four coils were made with the only difference that the four parallel wires of each coil are: (a) non-twisted, (b) slightly twisted (10 to 15 turns per meter), (c) moderately twisted (25 to 30 turns per meter), and (d) heavily twisted (45 to 50 turns per meter), respectively. All the coils were used to form a portion of an experimental stator, which was placed in the middle

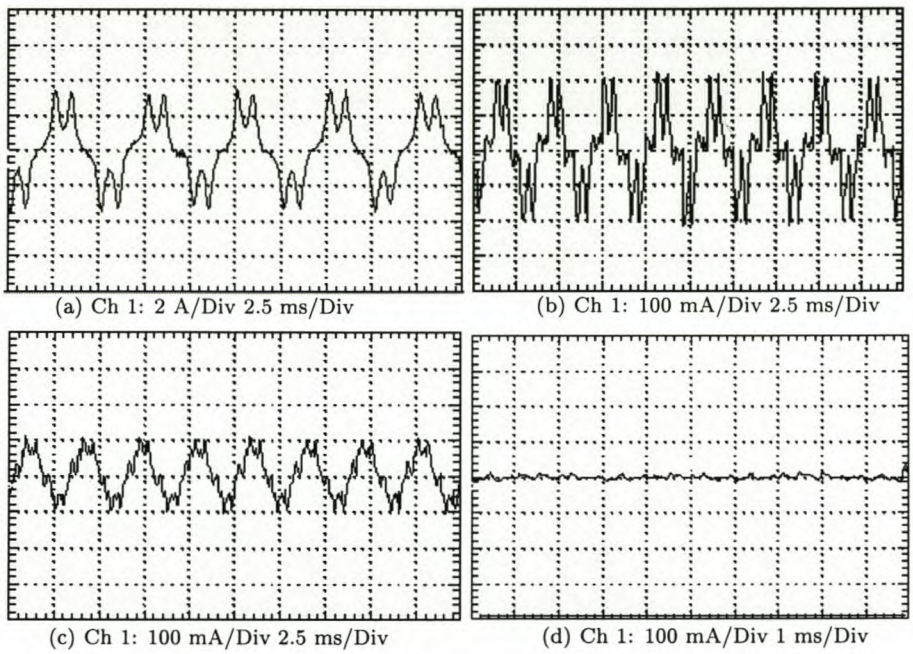

Figure 4.2: Measured circulating current of (a) non-twisted coil, (b) slightly twisted coil, (c) moderately twisted coil, (d) heavily twisted coil.

of two parallel PM rotor discs. The machine was then operating at a fixed speed (400 rpm in this case). The circulating eddy current between two parallel paths was measured and logged on a storage oscilloscope. It can be seen that the circulating eddy current is greatly reduced even with a slightly twisted coil and can generally be ignored in a heavily twisted coil. These twisted wires can easily be manufactured.

The filling factors for the non-twisted and the heavily twisted coils are estimated as 0.545 and 0.5 respectively, which is slightly less than that of the Litz wires (typically from 0.55 to 0.6). However, this is not a big disadvantage if one takes into account the saving in costs. It is thus a viable and cost effective solution for the ironless stator AFPM machines.

It should be noted that due to the low impedance of an ironless stator winding, circulating current could also exist among distributed parallel phase coils if a perfect symmetry of coils cannot be guaranteed. This chapter does not go further into the calculation of circulating current eddy losses in parallel wires. Note that the purpose of using parallel wires instead of a solid conductor is to limit the so-called resistance limited eddy losses as described in the next section.

4.1.2 Resistance limited eddy loss

Eddy current losses may be *resistance limited* when the flux produced by the eddy currents has a negligible influence on the total field [89]. In this case the wire dimensions are small when compared to the skin depth δ. The resistance limited losses may be found by an FE magneto-static solution or the closed-form analytical method. If the machine frequency is high enough so that the current density becomes non-uniform over the turn, the resistance limited approach is no longer valid and one has to use a magneto-dynamic eddy current analysis [89] or a magneto-static solution with Bessel function analysis [97]. In the subsequent analysis, it has been assumed that the eddy current losses are resistance limited, which is usually the case for a normal AFPM machine. The following analysis is based on round conductors. Rectangular or other shape conductors may be analysed in a similar way except that the field orientation should be taken into account [97].

4.2 Analytical method

From a machine design perspective, it is desirable to use a simple analytical method that can easily be included in the design optimisation program for the eddy current loss calculation. The standard analytical formula for resistance limited eddy loss derived in [23] is often used in the AFPM machine design [66, 14, 93, 95]. This method is based on the analytical solution of the eddy loss in a single conductor lying in a transverse alternating field. For a round conductor of diameter d, the eddy current loss P_e is given by:

$$P_e = \frac{\pi l d^4 B_{pk}^2 \omega^2}{32\rho} \tag{4.1}$$

where B_{pk} is the peak flux density, l is the conductor length, ρ is the resistivity and ω is the electrical angular speed. Apparently, this is inherently a 1-D analytical method that assumes a sinusoidal field. As will be shown in the following sections, in an ironless stator AFPM machine, the flux density waveform in the air-gap is often close to a trapezoidal waveform with appreciable 3^{rd} and 5^{th} harmonic contents [14] and the air-gap magnetic field geometry exhibits a 3-D nature. Hence, as pointed out by Sullivan [97], a significant error might be made in the calculation of the eddy current loss in the stator winding by merely using the above 1-D analytical method.

4.3 Finite element aided analytical method

To take into account the 3-D eddy current effects by using an 1-D analytical method, accurate field calculation is essential. After considering the large computing efforts needed in the 3-D FE analysis and its limitations from an implementation point of view, 2-D FE magneto-static

field analysis is performed. The eddy current region in the winding is modelled as a non-conducting area (sometimes called a *fine wire* region) [89]. To include the eddy losses due to the high order harmonic components in the air-gap flux waveform, the calculated flux density distribution is Fourier analysed to determine the amplitude of each flux density harmonic content. The latter is then used to compute the eddy current loss in each conductor using Eqn. (4.1).

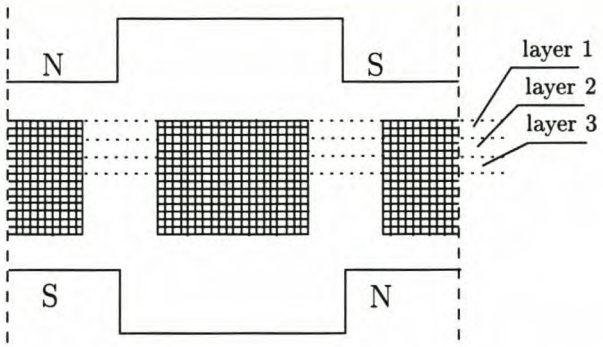

Figure 4.3: The 2-D multi-layer FE model of an AFPM machine.

4.3.1 Multi-layer finite element model

Figure 4.3 shows the developed 2-D FE model of a 40-pole 300 kW ironless stator AFPM machine. Due to the rotary symmetry, only one pole-pitch is necessary to model the entire machine. Let us assume that one can divide the eddy current area of the air-gap winding into a number of thin layers. Then the calculated axial and tangential flux densities at the different conductor layers across the air-gap (at the same radius) can be displayed as in Figs 4.4 and 4.5. It can be observed that the flux density waveform for an ironless stator AFPM machine, varies significantly with air-gap position.

Eddy current loss in the individual conductors depends, therefore, upon the position of the layer in the air-gap. The conductor layer nearer the face of the magnet has the greater flux density values and therefore greater eddy current loss as the eddy current loss P_e is proportional to the 2^{nd} power of the flux density. Thus, accurate prediction of eddy current loss requires the knowledge of field values on each conductor layer, which can then be Fourier analysed and used to compute the eddy current loss in each layer.

As an approximation, one may consider that the flux densities over a conductor cross-section are of the same value. The eddy loss of each conductor layer may be calculated by adding the eddy losses in each conductor. If there are l conductor layers in the eddy current region, the overall eddy loss P_{le} of all conductors is given by:

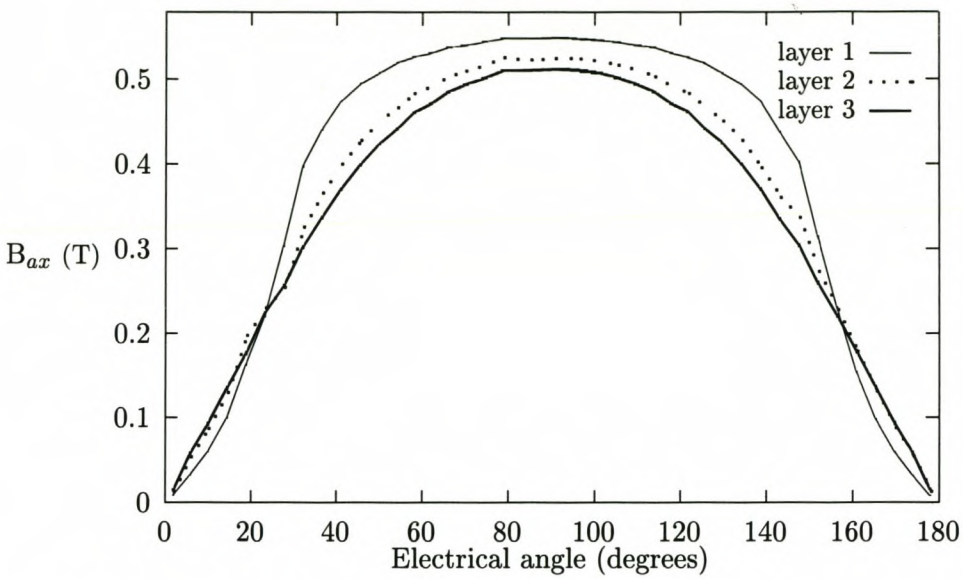

Figure 4.4: Comparison of air-gap axial flux density distribution at different conductor layers across the air-gap.

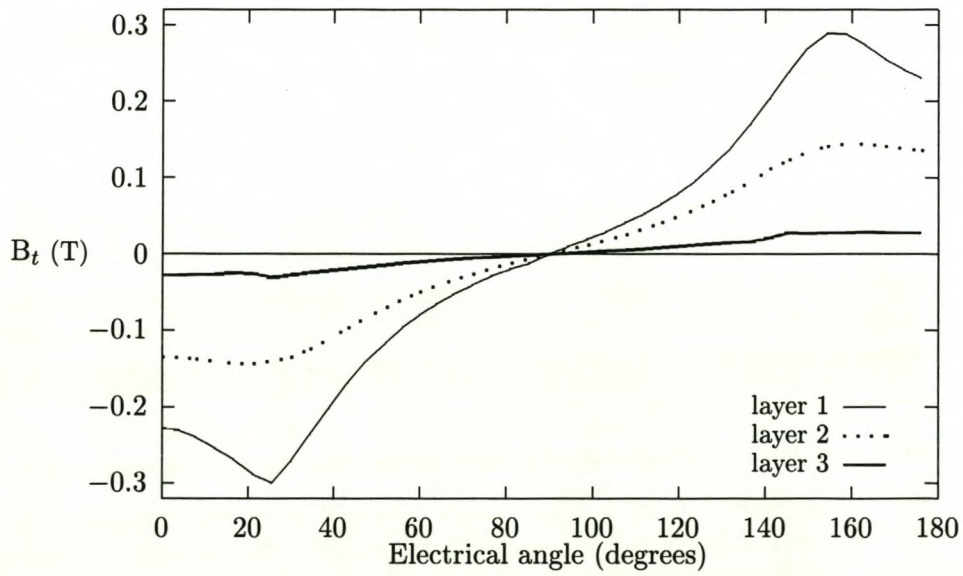

Figure 4.5: Comparison of air-gap tangential flux density distribution at different conductor layers across the air-gap.

$$P_{le} = \frac{\pi l_r d^4 \omega^2}{32\rho} \sum_{i=1}^{n} i^2 \sum_{j=1}^{l} (\dot{B}_{ij}^2 + \ddot{B}_{ij}^2) n_j \tag{4.2}$$

where n_j is the number of conductors in the j^{th} layer, l_r is the radial length of the conductor, ω is the electrical angular speed, and $\dot{B}_{ij}$ and $\ddot{B}_{ij}$ are the tangential and axial peak flux density of i^{th} order of the harmonic in the j^{th} layer respectively. It can be seen that with the 2-D field modelling incorporated, the 1-D analytical method (Eqn. 4.1) has been extended to account for the eddy current loss due to the 2-D field effects.

4.3.2 Computational limitations of 2-D FE modelling

The 2-D FE modelling of an AFPM machine is usually carried out by introducing a radial cutting plane at the average radius, which is then developed into a 2-D flat model. Unlike conventional electrical machines, the flux distribution in an AFPM machine does not present any uniform features in both radial and axial directions.

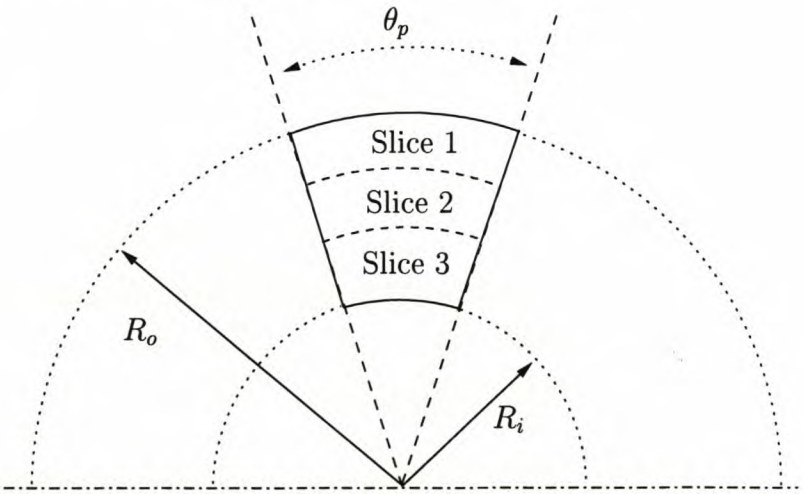

Figure 4.6: Schematic drawing of an AFPM machine showing the slice concept.

Imagine that one can cut a section (equivalent to one pole-pitch of the machine) out of an AFPM machine as shown in Fig. 4.6, which is further divided into several sectors. Each sector may then be unfolded and represented by a 2-D flat FE model (hereafter referred to as *slices*). On solving these 2-D FE models, the air-gap flux distribution of each slice is obtained and plotted on the same coordinate system as shown in Figs. 4.7 and 4.8. Despite the fact that the variation of flux density waveform of each slice is not as great as that of each layer, it is clear that field modelling of an ironless stator AFPM machine is inherently a 3-D problem and a simple 2-D FE model may not be an adequate representation of the problem. This is particularly important when it comes to the eddy current loss calculation as $P_e \propto B^2$ and a

small variation in the flux density may lead to a significant error.

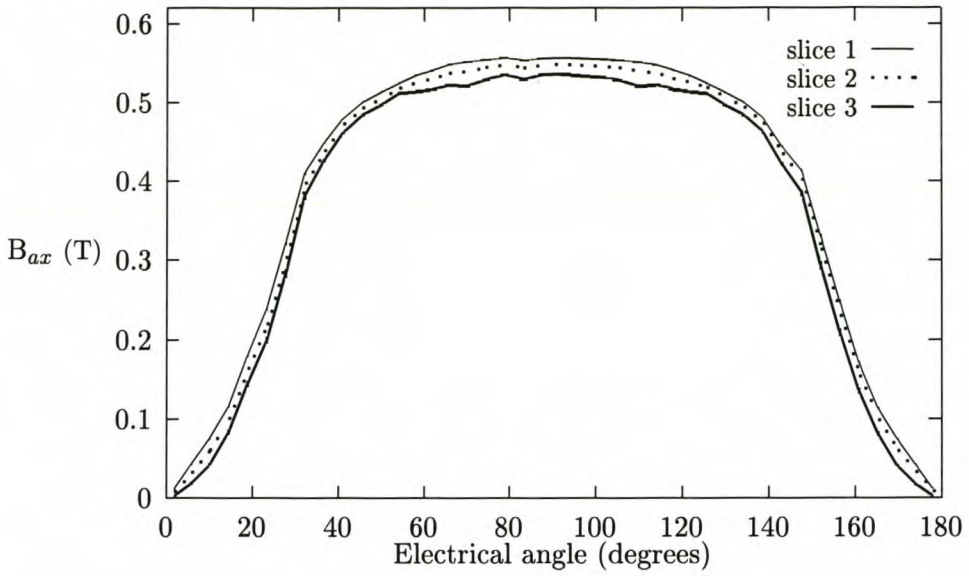

Figure 4.7: Comparison of air-gap axial flux density distribution of different slices.

4.3.3 Including 3-D effects in 2-D FE analysis

This section describes the multi-slice 2-D FE model and its implementation to account for 3-D effects of the magnetic field in the AFPM machine. The use of a 2-D FE model means that the 3-D features of the field distribution can only be represented in an approximate manner.

Multi-slice FE model

The approach that has been developed involves modelling 3-D field distribution of an ironless stator AFPM machine using a sequence of 2-D FE sub-models (slices) as shown in Fig. 4.9. The alignments of the rotors and stators of each successive slice are indexed to reflect the variation in the field distribution at different radii. If there are s such slices, and all are assumed to have the same radial length, then the overall eddy loss in the stator, P_{se} is given by:

$$P_{se} = \frac{1}{s}\sum_{k=1}^{s} P_{(le)k} = \frac{\pi l_r d^4 \omega^2}{32\rho s}\sum_{k=1}^{s}\sum_{i=1}^{n} i^2 \sum_{j=1}^{l}(\dot{B}_{ijk}^2 + \ddot{B}_{ijk}^2)n_j \tag{4.3}$$

where $P_{(le)k}$ is the eddy current loss of the k^{th} slice calculated by Eqn. (4.2), and $\dot{B}_{ijk}$ and $\ddot{B}_{ijk}$ are the tangential and axial peak flux density of the i^{th} harmonic field on the j^{th} conductor layer of the k^{th} slice respectively.

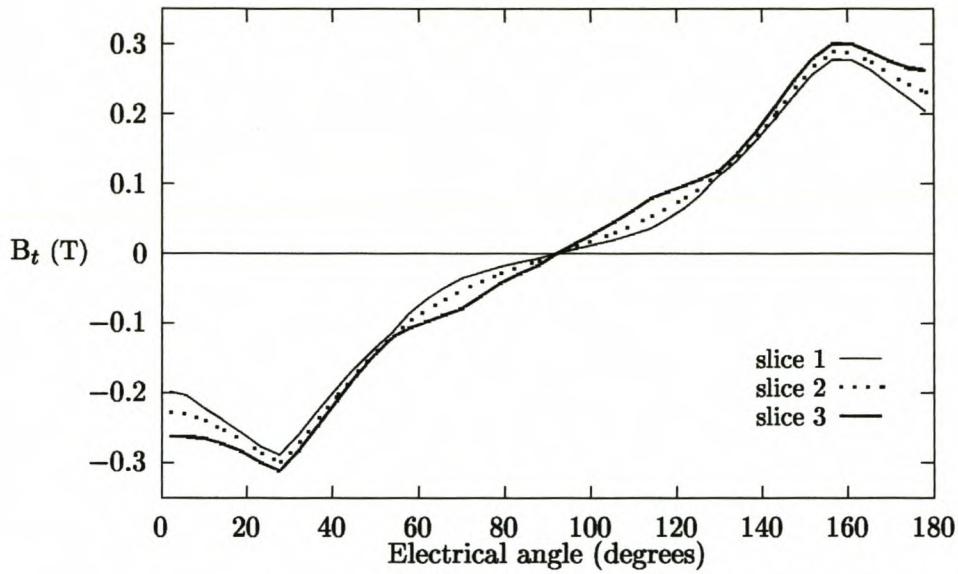

Figure 4.8: Comparison of air-gap tangential flux density distribution of different slices.

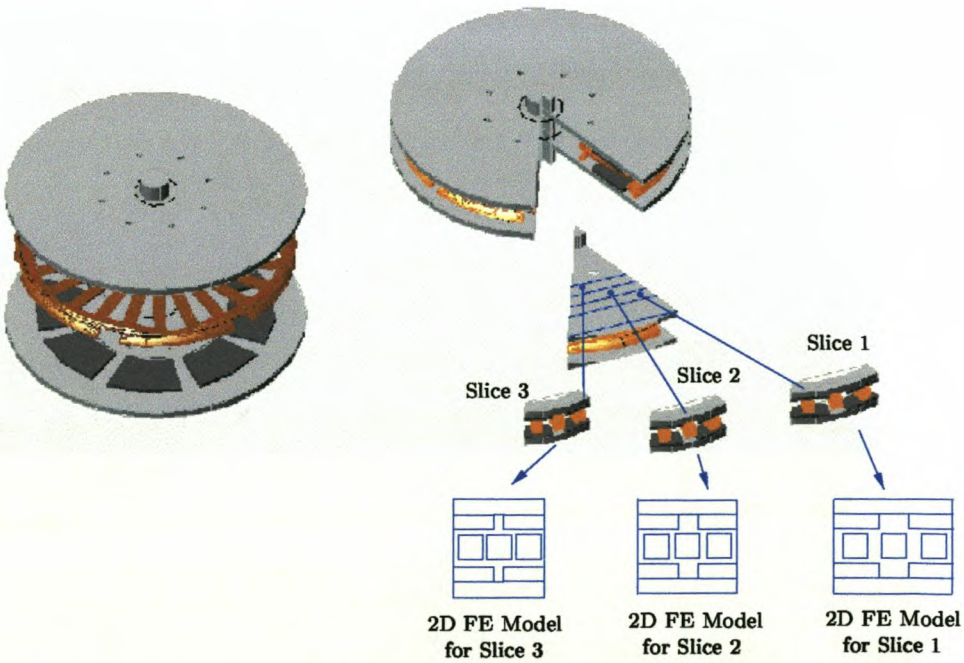

Figure 4.9: The 2-D multi-slice FE model of an AFPM machine.

Obviously, using the method presented here will require several field solutions to be performed at the same rotor position (e.g. a 3-slice model needs three 2-D solutions), which is computationally expensive if a complicated FE model has to be solved. However, considering the relatively simple geometry and large air-gap of ironless stator AFPM machines, the computation efforts involved in solving such a 2-D FE model are usually modest, even more so when a judicious selection of the boundary conditions and the modelled area are possible. Close inspection of the spatial field distribution reveals periodic and symmetrical features, which suggests that one needs to analyse only one or two poles. Since the tangential components of the field on the middle-plane are invariably zero, the Neumann boundary condition applies. This can further reduce the modelled region by half.

Implementation of models

Combining the 2-D multi-layer FE model with the multi-slice FE model, the 3-D effects of the eddy loss modelling in an AFPM machine may be represented in a 2-D fashion. Figure 4.10 shows the procedures for the implementation of the proposed models. To obtain a good representation of the field on each conductor layer, which is crucial to the field harmonic analysis and therefore eddy loss calculation, the conductor region has been modelled with uniformly distributed dense triangles. This could cause difficulties in air-gap region discretisation. The use of a Cartesian Air-Gap Element (CAGE) helps in solving this problem with improved accuracy as discussed in [103].

Application scope and limitations

A combined model utilising an analytical method and a 2-D FE solution has now been fully developed. The proposed method allows calculation of eddy losses in generic AFPM machine winding with 2-D and 3-D effects and non-sinusoidal field distributions.

One limitation of this method is that the eddy current losses in the winding overhangs are not included. For the 2-D FE modelling, the estimation of the eddy losses in the end-winding is very difficult as the leakage field is not readily determined either in magnitude or direction. For winding arrangements with short overhangs, it is possible to ignore the end winding eddy losses in the overall eddy loss calculation without materially compromising the accuracy. However, for the winding arrangements with long end windings, one has to take into account the end winding eddy loss by using empirical formulae or preferably using 3-D FE analysis.

To verify the validity of this method, the experimental investigation described in the next section was also performed.

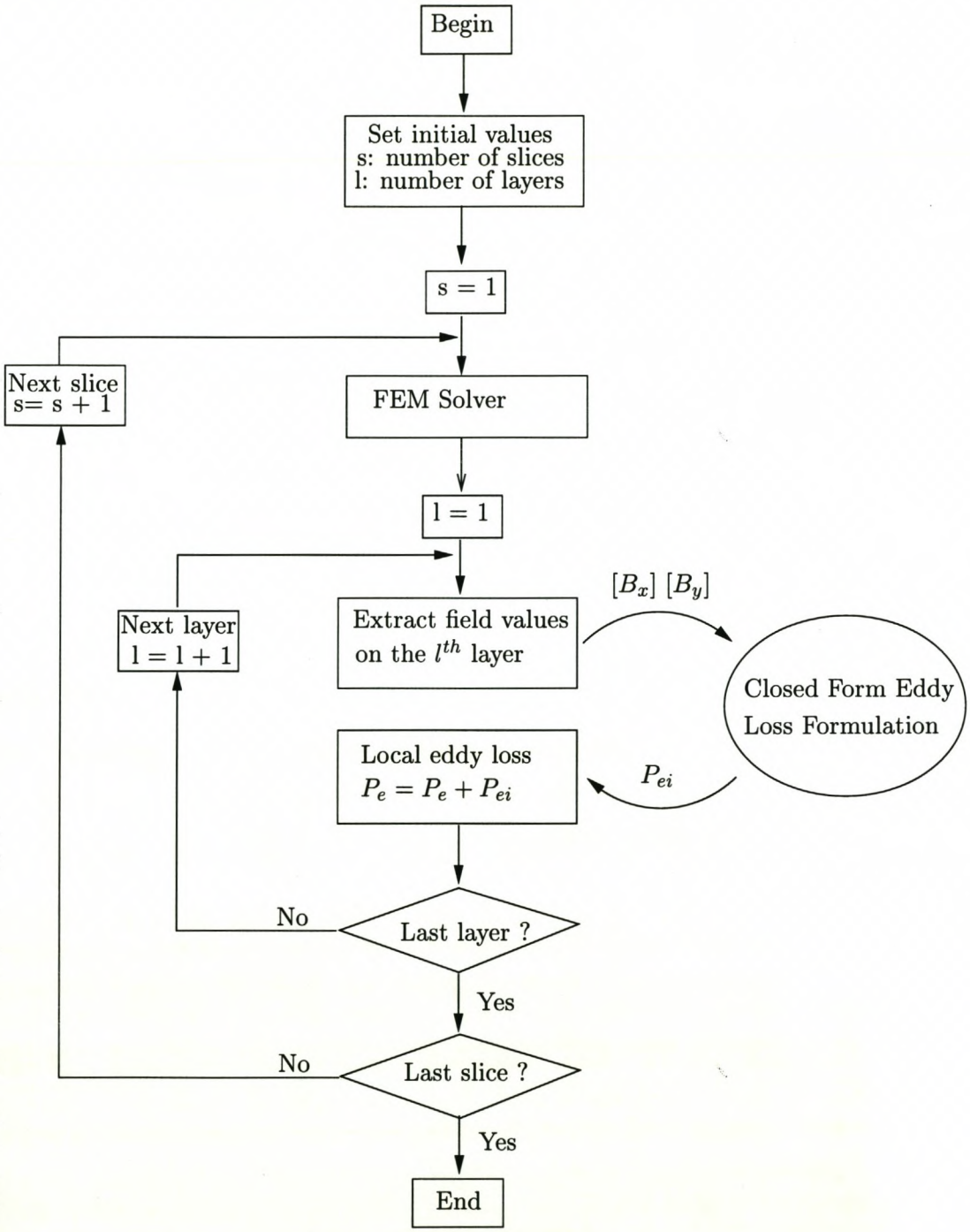

Figure 4.10: Finite element calculation of eddy loss taking into account 3-D effects.

4.4 Experimental method and results

The resistance limited eddy loss in the stator of an AFPM machine may be experimentally determined by measuring the difference in input shaft powers of the AFPM machine at the same speed, first with the stator in, and then by replacing it with the dummy stator (no conductors). The dummy stator has the same dimensions and surface finish as the first stator and is meant to keep the windage losses the same.

4.4.1 Prototype fabrication

A schematic of the experimental test setup for measuring eddy losses is shown in Fig. 4.11. The experimental prototype and driving machine are connected at the shaft via a torque sensor.

To eliminate the effects of possible eddy-circulating current in the windings and eddy current loss in the end-windings caused by end-winding flux linkages, the coils are replaced by bunches of conductors, which are of equivalent length to the permanent magnet. All the conductor groups are then epoxy enforced to form an ironless stator. The finished stator is positioned in the middle of the two rotor discs with the outer end ring (see Fig. 4.11c) mounted outside the supporting frame. A few temperature sensors are also attached to the conductors in order to measure the conductor temperature to be used in the theoretical calculation.

4.4.2 Comparison of results

Fig. 4.12 shows the measured and calculated resistance limited eddy losses of the prototype machine. It is seen that the calculated eddy losses obtained by using the standard analytical formula (Eqn. 4.1) alone yield underestimated values (43% less). The discrepancy between the measured and calculated results becomes large at high speeds. Better accuracy may be achieved using the developed technique. In the simulation, each 2-D FE model uses 5 layers to account for 2-D field effects. Note that the improvement of accuracy from a 3-slice (3 FE solutions) to a 5-slice (5 FE solutions) model is not as significant as that from a 1-slice to a 3-slice model. It may be a good tradeoff between accuracy and CPU time to use a 3-slice FE model.

4.5 Other eddy loss related aspects

4.5.1 Armature reaction effects

Using a 40-pole 766 Hz ironless stator AFPM machine as an example, the simulated effects of armature reaction to the air-gap flux distribution has been demonstrated in Figs 4.13 and 4.14. It is seen that the plateau of the axial field plot is somewhat tilted due to the interaction

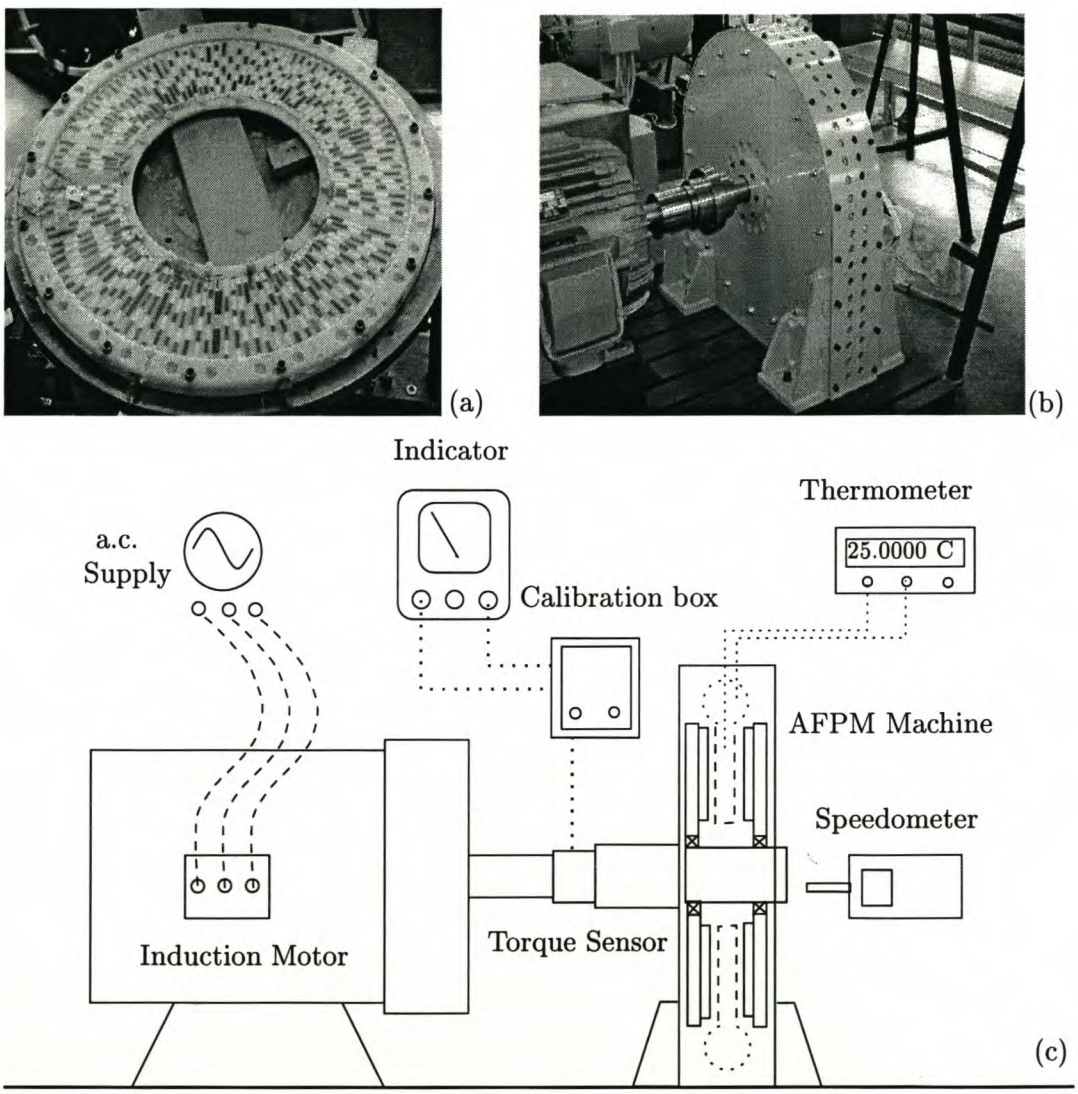

Figure 4.11: Laboratory set for measuring the eddy current loss, where (a) is a specially designed stator, (b) are the experimental machines, and (c) is a schematic of the experimental set-up.

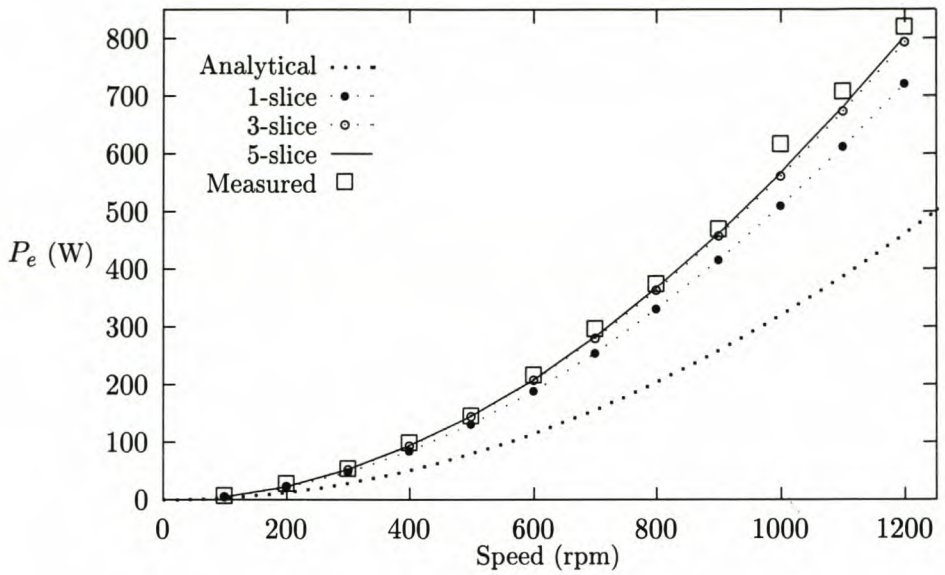

Figure 4.12: Comparison of calculated eddy loss with measurements.

between the flux of the PMs and armature flux generated by the rated current (Fig. 4.13). Similarly, the modified tangential field plot is compared with the original one in Fig. 4.14.

For an ironless stator AFPM machine, the air-gap length is large. As there are few demagnetising components of the armature reaction flux, the air-gap magnetic flux density maintains its maximum value. The influence of the armature reaction on the eddy current losses is usually insignificant though it can be easily accounted for when FE modelling is utilised. The harmonic contents obtained of the air-gap flux density with and without armature reaction are compared in Table 4.1. It is evident that, in this case, the change of the field harmonic composition due to the armature reaction is negligible.

4.5.2 Reducing harmonic-induced eddy losses

Due to the fact that the eddy current loss in the conductors of the AFPM machine stator is proportional to the 2^{nd} power of the field frequency, the high order harmonic components of the air-gap field waveform induce an appreciable amount of eddy losses. To suppress the harmonic contents and therefore their associated eddy losses, a number of techniques, as discussed in Chapter 3, may be adopted. Amongst others, pole shaping is a very effective method and has been shown to work well [26] in correcting the EMF waveform.

To have a better idea of what one may achieve to suppress harmonic induced eddy losses by using pole-shoes, let us consider a very simple case, i.e. designing a flat iron pole-shoe on top of a PM. Assuming that the thickness of the iron piece and the PM are 1mm and 10 mm

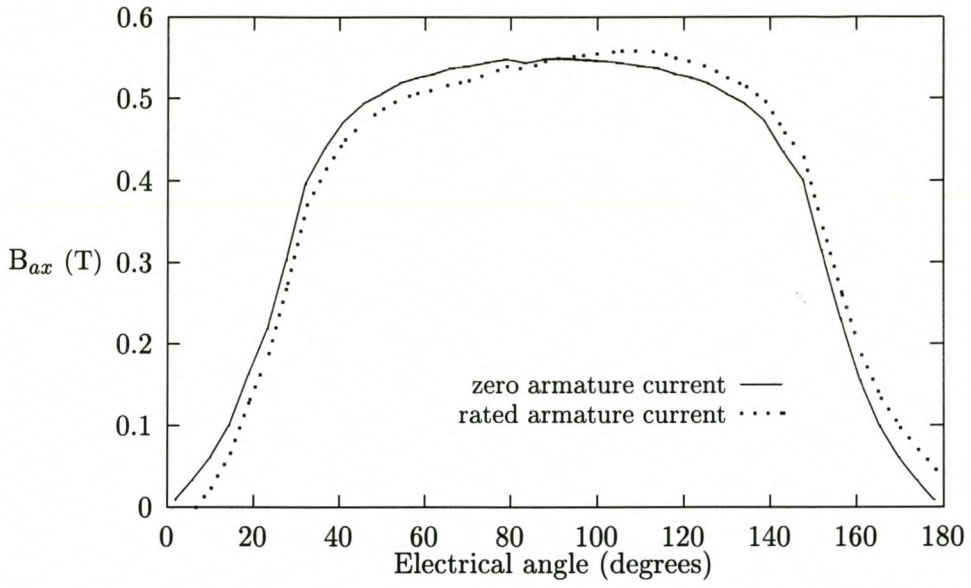

Figure 4.13: Airgap axial field component at no-load and full load conditions.

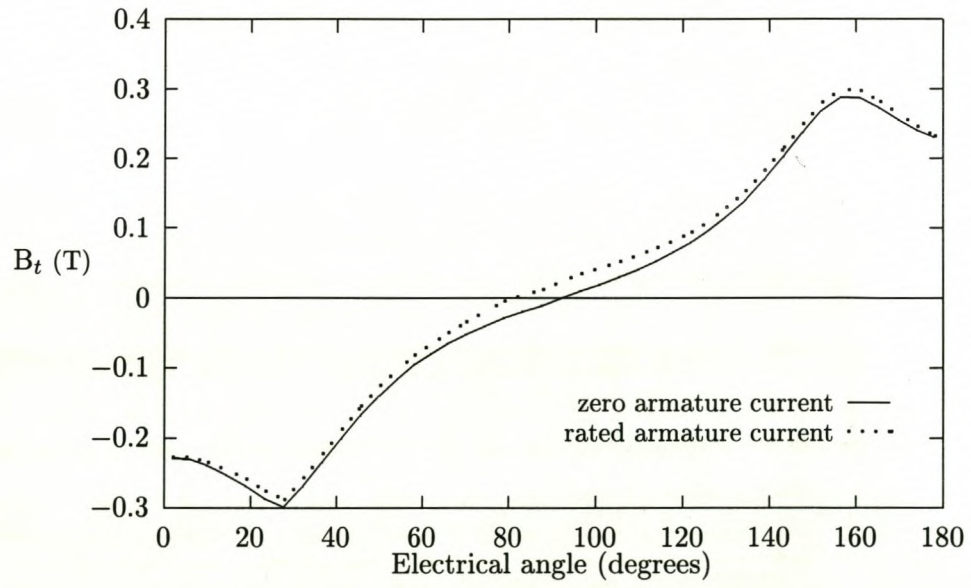

Figure 4.14: Airgap tangential field component at no-load and full load conditions.

Table 4.1: Harmonics content of the axial air-gap flux density with and without armature reaction.

Harmonics	zero armature current	rated armature current
1^{st}	.60246033	.60346784
3^{nd}	.03745759	.03745651
5^{rd}	.04070525	.04099061
7^{th}	.03514609	.03502689
9^{th}	.01230032	.01231397
11^{th}	.00262309	.00304573
13^{th}	.00579739	.00559543
15^{th}	.00312179	.00314908
17^{th}	.00086812	.00083159
19^{th}	.00272939	.00307828

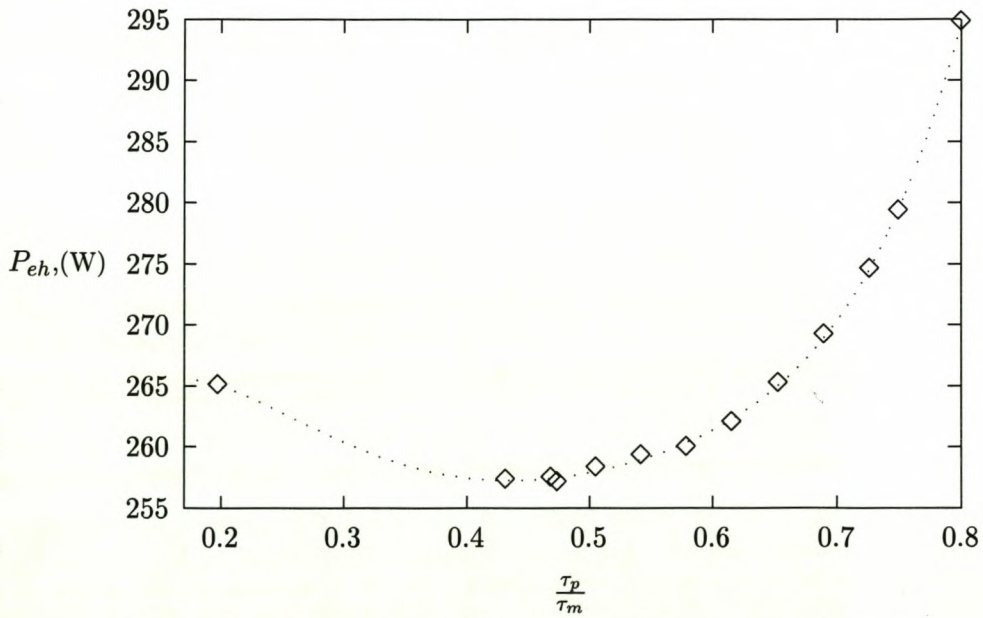

Figure 4.15: Total harmonic eddy loss versus pole-shoe width.

respectively, the only variable is the ratio of the pole-shoe width τ_p to the PM width τ_m. The objective is to minimise the harmonic induced eddy losses while keeping the fundamental field component as intact as possible.

Fig. 4.15 depicts the relationship between the width of the pole-shoe and the eddy loss due to the harmonic contents P_{eh}. The optimum $\frac{\tau_p}{\tau_m}$ is shown at around 0.45. It is seen that harmonic contents may be reduced by using a pole-shoe even of such a simple profile. At this point, one may ask what about the eddy current losses induced in the iron pole shoes. Certainly, the induced eddy losses in the pole shoes may be just as great as or even greater than the amount of the eddy losses being removed. One possible solution is to use composite materials that are less prone to eddy current losses. Note that the example given here is not intended for quantitative use. The full exploitation of the topic demands further studies and is beyond the scope of this research project.

Chapter 5

Thermofluid Analysis of AFPM Machine

This Chapter deals with the thermofluid analysis of AFPM machines. Firstly the fluid flow model of a prototype AFPM machine is developed, where the relationships between flow rate and rotating speed are obtained. With this information available, a lumped-parameter heat transfer model of the AFPM generator is derived and used to estimate the operating temperatures in various parts of the machine for different power generating conditions. Experimental tests are also done on the prototype machine and results are compared with the calculated ones. Based on the above analysis, a relevant insight into the thermal design of the AFPM machine is discussed and recommendations are also made.

5.1 Heat transfer in AFPM machines

During the operation of an electrical machine, energy is lost due to electrical (*hysteresis, eddy current and resistance*) losses and mechanical (*friction and windage*) losses. To ensure a long operational life for the machine, these losses must be eliminated as far as possible from the machine so that the temperature limitations established for the machine materials, such as insulating materials, lubricants and permanent magnets are complied with. In addition to the considerations of the machine operational life, lower operating temperature reduces extra copper losses introduced by the temperature coefficient of the winding resistance.

In this chapter a simple hybrid approach combining the lumped-parameter heat transfer model and air flow model of a typical AFPM machine is developed. The accuracy and consistency of the derived model are assessed by comparing the calculated flow rate and temperature values of a prototype machine with the measured ones. The advantages and disadvantages of the approach are then outlined and conclusions are drawn.

5.1.1 Machine topology

Among a variety of different topologies of AFPM machines, the configuration of one stator and two rotors with surface mounted PMs has been used most widely [12, 20, 24, 25, 57, 65, 66, 95]. The radial channels in the disc rotors have a fan effect so that the air cooling of the stator winding can be improved. Fig. 5.1 shows the layout and active components of an AFPM machine of this topology, which will be used as a typical example for thermofluid analysis in this chapter. The principles covered in this text can be applied in general to AFPM machines.

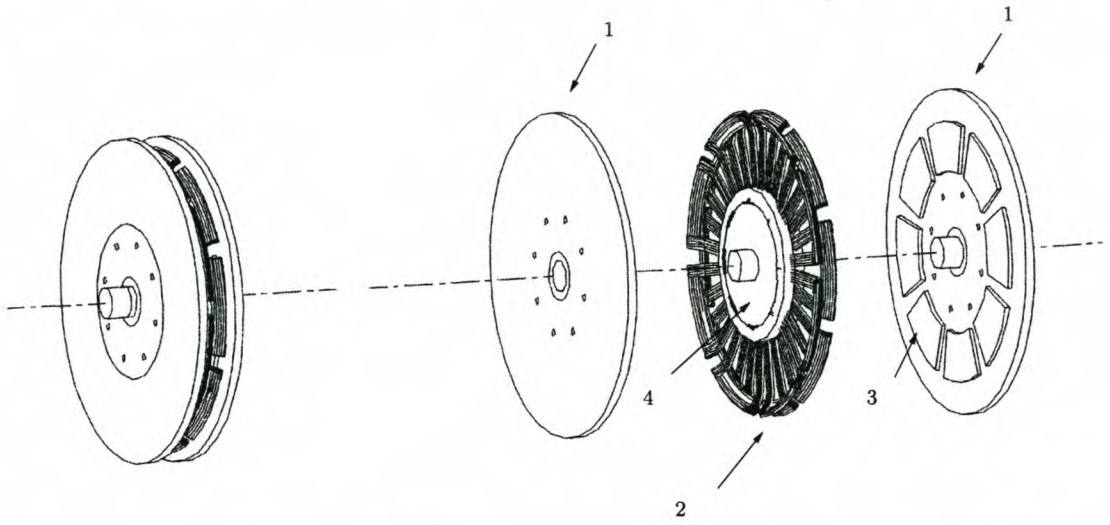

Figure 5.1: Exploded view of an AFPM machine: 1 – rotor disc, 2 – stator winding, 3 – permanent magnet, and 4 – epoxy core.

5.1.2 Heat transfer modes

Heat transfer is a complex phenomenon presenting formidable analytical difficulties. Heat is removed from an electrical machine by a combination of *conduction*, *radiation* and *convection* processes to the ambient air and surroundings.

Conduction

When a temperature gradient exists in a solid body, such as in the copper, steel, PMs or the insulation of an electrical machine, heat is transferred from the high-temperature region to the low-temperature region according to *Fourier's law*, which is given as:

$$\dot{Q} = -kA\frac{\partial T}{\partial x} = \frac{kA}{l}(T_{hot} - T_{cold}) \tag{5.1}$$

where A is the area of the flow path, l is the length of the flow path and k is the thermal conductivity of the material. The latter is experimentally determined and is relatively insen-

sitive to temperature changes. Values of typical materials used for AFPM machines are given in Appendix D.

Radiation

The net radiant energy interchange between two surfaces with a temperature difference is a function of the absolute temperature, the emissivity and the geometry of each surface. If heat is transferred by radiation between two gray surfaces of finite size, A_1 and A_2, the rate of heat transfer may be written as

$$\dot{Q} = \frac{\sigma(T_1^4 - T_2^4)}{\frac{1-\varepsilon_1}{\varepsilon_1 A_1} + \frac{1}{A_1 F_{12}} + \frac{1-\varepsilon_2}{\varepsilon_2 A_2}} \tag{5.2}$$

where σ is the *Stefan-Boltzmann* constant, F_{12} is the shape factor which takes into account the relative orientation of the two surfaces and ε_1, ε_2 are their respective emissivities which depend on the surfaces and their treatment. Some selected emissivities related to AFPM machines are given in Appendix D.

Convection

Convection is the term describing heat transfer from a surface to a moving fluid. The rate of convective heat transfer is given according to *Newton's law of cooling* as:

$$\dot{Q} = hA(T_{hot} - T_{cold}) \tag{5.3}$$

where h is the convection heat transfer coefficient, which is a rather complex function of the surface finish and orientation, fluid properties, velocity and temperature, and is usually experimentally determined. Some important formulae for evaluating convective heat transfer coefficients of AFPM machines are summarised in Appendix D.

5.1.3 Analytical method

For an air-cooled AFPM machine, the air flow is of paramount importance to the cooling of the machine. Let us consider a simple thermal model of the AFPM machine. It comprises of only four control volumes representing the stator, the airgap, the permanent magnets and the rotor disc respectively. According to the conservation of energy, the determination of the air temperature in the air-gap is only possible if the mass flow rate through the air-gap can be somehow predicted, hence the necessity of a reasonable fluid-flow model.

5.2 Fluid flow model

A close examination of the machine structure shown in Fig. 5.1 reveals that an air stream will be drawn through the air inlet holes into the machine and then forced outwards into the

radial channel as the rotor discs rotate. The PMs in fact act as impeller blades. The fluid behaviour of the AFPM machine is much like that of a centrifugal fan.

5.2.1 The ideal radial channel

According to the theory of an ideal impeller, a number of assumptions have to be made to establish the one-dimensional model of the ideal radial channel [32, 91]:

(1) There are no tangential components in the flow through the channel.
(2) The velocity variation across the width or depth of the channel is zero.
(3) The inlet flow is radial, which means that air enters the impeller without pre-whirl.
(4) The pressure across the blades can be replaced by tangential forces acting on the fluid.
(5) The flow is treated as incompressible and frictionless.

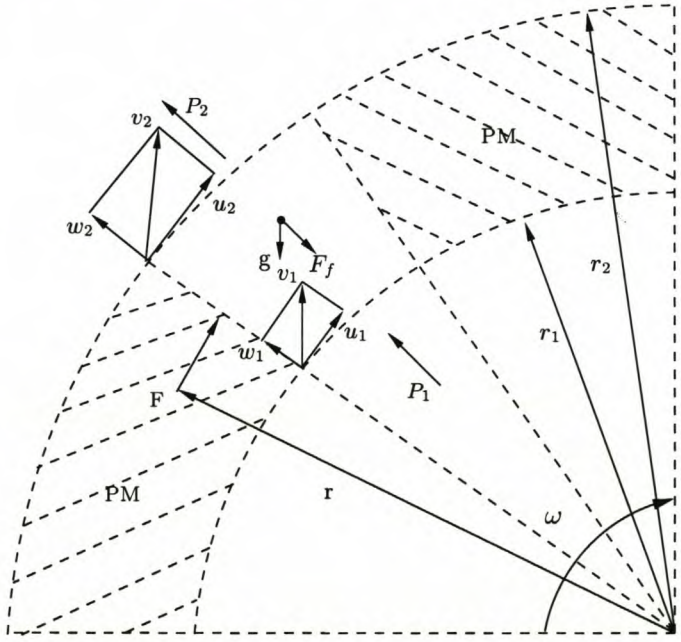

Figure 5.2: Velocity triangles for a PM channel.

Figure 5.2 shows a radial channel with the velocity triangles drawn at the inlet and the outlet. It can be observed that the pressures at the inlet p_1 and the outlet p_2, and friction F_f make no contribution to the sum of the momentum, $\sum M_0$. If gravity is ignored, the general representation of conservation of momentum takes the form [104]:

$$\sum M_0 = \frac{\partial}{\partial t}[\int_{cv} (\vec{r} \times \vec{u})\rho dV] + \int_{cs} (\vec{r} \times \vec{u})\rho(\vec{w} \cdot \vec{n})dA \tag{5.4}$$

For steady-state one-dimensional air flowing between the entrance and exit of the channel, Eqn. (5.4) may be simplified as:

$$\sum M_0 = T_0 = (\vec{r_2} \times \vec{u_2})\dot{m}_2 - (\vec{r_1} \times \vec{u_1})\dot{m}_1 \tag{5.5}$$

where $\dot{m}_2 = \dot{m}_1 = \rho Q$, and $u = \omega r$. The input shaft power $\dot{W}_i$ is then given by:

$$\dot{W}_i = T_0 \cdot \omega = \rho Q \omega^2 (r_2^2 - r_1^2) \tag{5.6}$$

Re-arranging the above equation gives:

$$\frac{\dot{W}_i}{Q} = \rho \omega^2 (r_2^2 - r_1^2) \tag{5.7}$$

Based on the principle of conservation of energy, the input shaft power may be given as:

$$\dot{W}_i = \dot{m}(\frac{p_2 - p_1}{\rho} + \frac{w_2^2 - w_1^2}{2} + z_2 - z_1 + U_2 - U_1) \tag{5.8}$$

If potential $(z_2 - z_1)$ and the internal energy $(U_2 - U_1)$ (friction) are ignored, Eqn. (5.8) may be written in the same units as Eqn. (5.7) as:

$$\frac{\dot{W}_i}{Q} = (p_2 - p_1) + \rho \frac{w_2^2 - w_1^2}{2} \tag{5.9}$$

If Eqns (5.7) and (5.9) are equated and noting that $w_1 = Q/A_1$ and $w_2 = Q/A_2$ (A_1 and A_2 are the cross-section areas of the inlet and outlet of the channel, respectively), the pressure difference Δp between the entrance and exit of the radial channel (shown in Fig. 5.2) may be expressed as:

$$\Delta p = p_2 - p_1 = \rho \omega^2 (r_2^2 - r_1^2) - \frac{\rho}{2}(\frac{1}{A_2^2} - \frac{1}{A_1^2})Q^2 \tag{5.10}$$

Eqn. (5.10) may be termed the *ideal* equation describing the air flow through the radial channel.

5.2.2 The actual radial channel

The actual characteristics of a hydraulic machine differ from the ideal case due to two reasons: (i) the uneven spatial distribution of velocities in the blade passages, and (ii) the leakage and recirculation of flow and hydraulic losses such as friction and shock losses. These are completely different issues [32] and shall be dealt with separately in the following two sections as *slip* and *shock, leakage and friction.*

Slip factor

As a result of the unbalanced velocity distribution of the leading and trailing edges of a PM channel and the rotation effects [91], there exists, according to Stodola [91, 76], a *relative eddy* within the blade passage shown in Fig. 5.3. This results in the reduction of the tangential

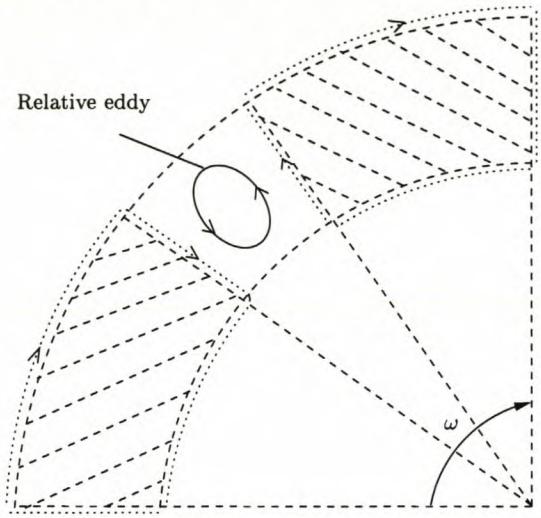

Figure 5.3: The relative eddy in the PM channel.

velocity components and is called *slip*, which is usually accounted for using a *slip factor*. For purely radial blades, the *Stanitz* slip factor k_s ($80^\circ < \beta_2 < 90^\circ$) is

$$k_s = 1 - 0.63\pi/n_b \tag{5.11}$$

where n_b is the number of the blades. When applying a slip factor, the pressure relations (Eqn. 5.10) becomes

$$\Delta p = \rho\omega^2(k_s r_2^2 - r_1^2) + \frac{\rho}{2}(\frac{1}{A_1^2} - \frac{1}{A_2^2}) \cdot Q^2 \tag{5.12}$$

Shock, leakage and friction

Energy losses due to friction, separation of the boundary layer (shock loss) and leakage should also be considered in the flow analysis. As illustrated in Fig. 5.4, if the total volumetric flow rate through the PM channel is Q_t, the pressure difference between the PM exit and the entrance will cause a *leakage* or recirculation of a volume of fluid Q_l, thus reducing the flow rate at outlet to $Q = Q_t - Q_l$. The Q_l is a function of mass flow rate and discharge and leakage path resistances. The leakage flow reaches its maximum when the main outlet flow is shut.

These losses can be accounted for by introducing a pressure loss term Δp_l in Eqn. (5.12) as follows [91]

$$\Delta p = \rho\omega^2(k_s r_2^2 - r_1^2) + \frac{\rho}{2}(\frac{1}{A_1^2} - \frac{1}{A_2^2}) \cdot Q^2 - \Delta p_l \tag{5.13}$$

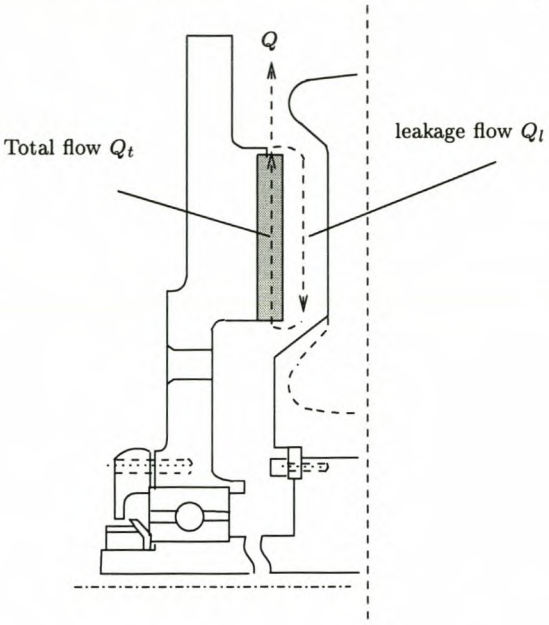

Figure 5.4: Leakage flow in an AFPM machine (not to scale).

System losses

As the air passes through the AFPM machine, the system pressure loss due to friction must be taken into account. The sum of these losses is given by:

$$\Delta p_f = \frac{\rho Q^2}{2} \sum_{i=1}^{n} \frac{k_i}{A_i^2} \tag{5.14}$$

where k_i and A_i are the loss coefficient and the cross section area of the flow path i, respectively.

There are a number of sections through which the air flows in the AFPM machine (see Fig. 5.5). They are:

(1) Entry into the rotor air inlet holes
(2) Passage through rotation short tube
(3) Bending of air from pipe to annulus (90°)
(4) Round bend air passage (90°)
(5) Contraction of air in the tapering passage
(6) Bending of air through the 90° elbow
(7) Entry to the permanent magnet channels
(8) Expansion of air through the tapering enlargement
(9) Abrupt expansion of the air on the exit of the channel
(10) Expansion as the air leaves the opening of the parallel rotor discs

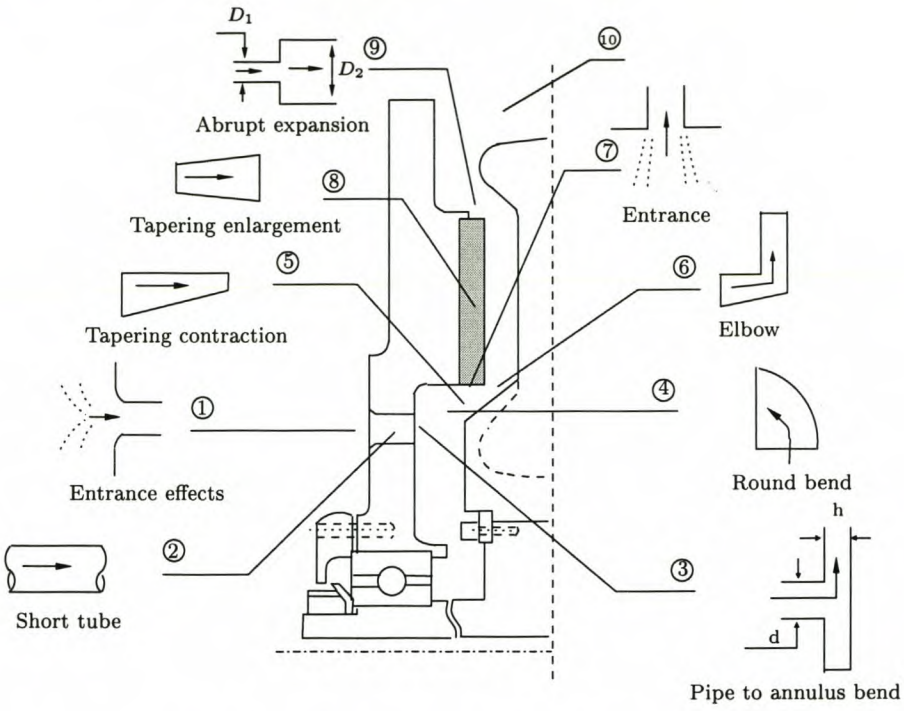

Figure 5.5: System losses of AFPM machine.

The loss coefficients associated with each section in Eqn. (5.14) are readily available in the literature [76, 29, 69]. Where the section is not circular, use has been made of the hydraulic diameter to characterize the cross section. The hydraulic diameter is defined as $D_h = 4A/\wp$ where A is the cross-sectional area of the flow path and $\wp$ is the wetted perimeter.

The loss coefficient for a pipe is given by $\lambda L/d$ where λ is a friction factor obtained as a function of Reynolds number Re and surface roughness from a *Moody diagram* [72]. To facilitate numeric calculations, the Moody diagram may be represented by [29]:

$$\begin{cases} \lambda = 8[(\frac{8}{Re})^{12} + \frac{1}{(A+B)^{3/2}}]^{1/12} \\ A = [2.457 \cdot ln\{\frac{1}{(7/Re)^{0.9} + 0.27\gamma/D}\}]^{16} \\ B = [\frac{37530}{Re}]^{16} \end{cases} \tag{5.15}$$

where $Re = \frac{\rho D_h Q}{\mu A}$ and where γ is the equivalent sand grain roughness.

5.2.3 Characteristics

It is now possible to relate the theoretical prediction obtained from the ideal flow model to the actual characteristic by accounting for the various losses discussed above.

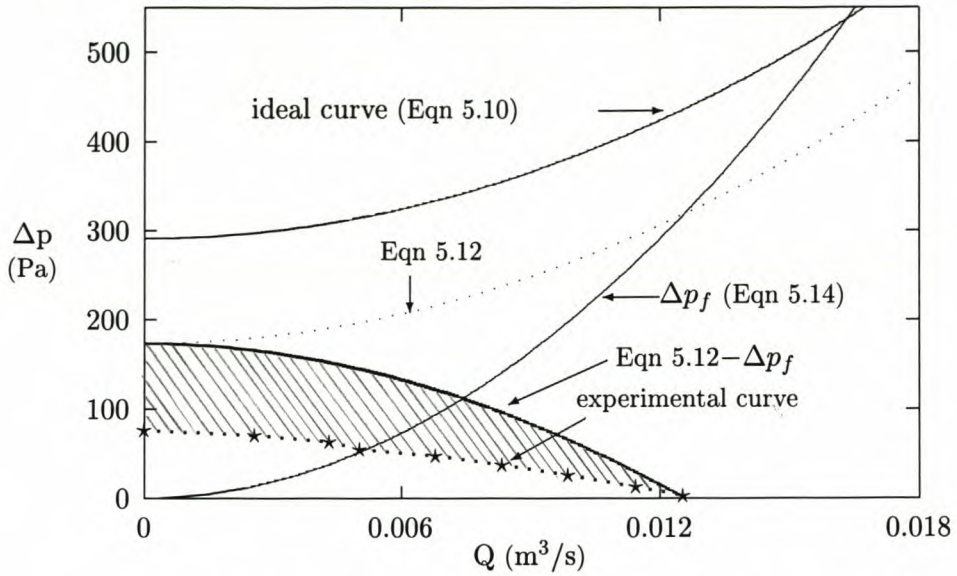

Figure 5.6: Losses and characteristic curves at 1200 r.p.m.

Assuming that the AFPM machine (shown in Fig. 5.1) operates at a constant speed of 1200 r.p.m., the ideal developed pressure characteristic for a radial channel is a function described by Eqn. (5.10) as shown in Fig. 5.6. After introducing the slip factor, the resultant curve is shown as a dotted line as Eqn. (5.12). It was not possible to obtain a suitable correlation in the literature [96] for the pressure loss due to shock and leakage as was the case for the slip.

The calculated characteristic curve without considering shock and leakage losses (Eqn. (5.12) - Δp_f) shown in Fig. 5.6 is significantly higher than the experimental one. The shaded area in Fig. 5.6 represents the shock and leakage losses. It can be seen that at low flow rates the shock and leakage losses are greater but tend to zero at the maximum flow rate. The calculated maximum flow rate point corresponds with the experimental curve. Although it could be a coincidence, it may be assumed at this stage that the influence of shock and leakage losses at the maximum flow rate is insignificant.

Since the AFPM machine (Fig. 5.1) has two identical co-axial rotating discs operating on the same stator, it may be treated as two identical fans in parallel. The characteristic curve presented in Fig. 5.6 represents only half of the AFPM machine. The characteristic curve of the whole machine may be obtained by adding flow rate at the same pressure.

5.2.4 Experimental investigation

Due to the nature and complexity of thermofluid analysis, the form of the system characteristics curve can at best be established by test. In order to check the validity of the above-described fluid flow model, the following experiments were performed.

Flow and pressure measurements

The AFPM machine of Fig. 5.1 at no load was driven by a d.c. motor and allowed to operate as a conventional fan as shown in Fig. 5.7. The machine was set up with a discharge duct to provide good conditions for observing the flow. Along one side of the duct, several tapping points were made for measuring the static pressure with a Manometer. Near the outlet of the duct, provision was made whereby the velocity could be measured using a hot-wire anemometer probe.

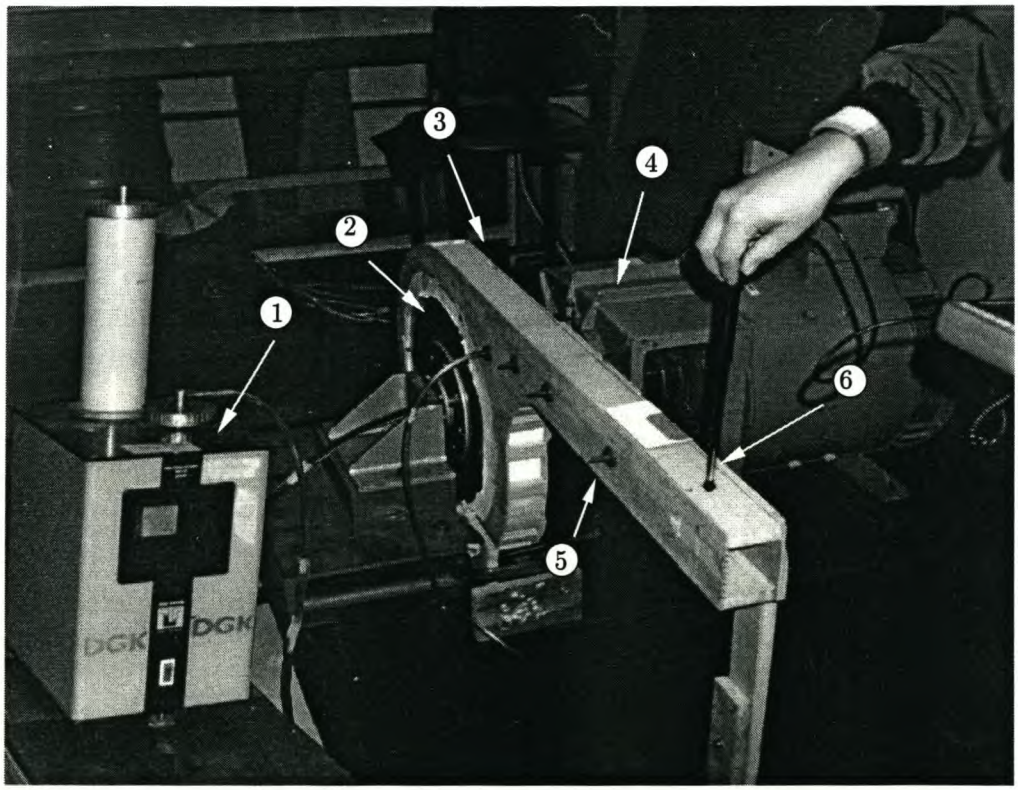

Figure 5.7: The experimental set-up, where 1 – manometer, 2 – AFPM machine, 3 – discharge duct, 4 – drive machine, 5 – pressure tapping point, 6 – wind speed probe.

To vary the flow rate, the test duct was fitted at its outer end with an obstruction. The test was started with no obstruction at the end of the discharge duct. The only resistance was then the duct friction, which was small and could be readily computed out of results. As the

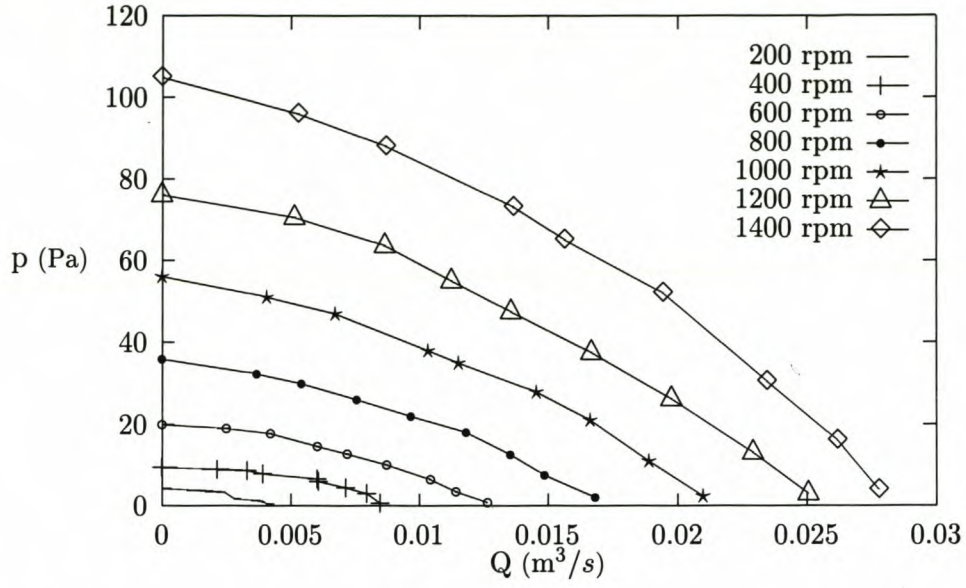

Figure 5.8: Measured characteristic curves of the AFPM machine ($\rho = 1.177\ kg/m^3$).

end of the duct was obstructed progressively, the flow was reduced and the static pressure increased to a maximum at zero volumetric flow rate.

The static pressure difference Δp was measured as a function of volumetric flow rate $\dot{Q} = A \cdot v$ for different motor speeds varying from 200 to 1400 rpm. The results are plotted in Fig. 5.8. Note that the pressure losses occuring in the discharge duct have been subtracted from the measured values.

Volumetric flow rate

Figure 5.9 shows both the computed and measured volumetric flow rate of the AFPM machine of Fig. 5.1 at different operating speeds. It can be seen that the correlation between the computed and measured results is good. This confirms that shock and leakage losses, as previously assumed, become less significant as the operating point is approached.

Now, the fluid flow model of the AFPM machine has been established and shown to behave well. Using this flow model, the mass flow rate of an AFPM machine can be readily predicted, which is indispensable for the thermal calculation of the AFPM machine described in the following sections.

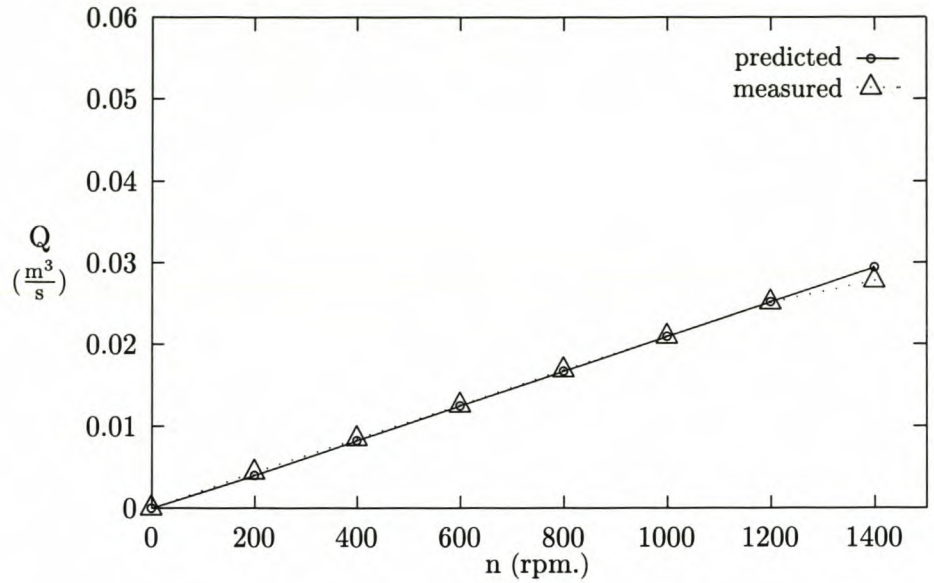

Figure 5.9: Calculated and measured volumetric flow rate at different speeds.

5.3 Lumped parameter thermal model

Lumped-parameter circuits, consisting of a network of thermal resistances, nodal temperatures and heat sources, have been used extensively to represent the complex distributed thermal parameters of electrical machines [95, 33].

5.3.1 Thermal resistance circuit

Fig. 5.10a shows a sectional view of an AFPM machine. It can be observed that the AFPM stator is symmetrical from a heat transfer perspective and each half of the machine from the centre line mirrors the other half. It is therefore reasonable to model only half of the machine as shown in Fig. 5.10b.

The heat source terms $\dot{Q}_{cu}$, $\dot{Q}_{edy}$ and $\dot{Q}_{wf}$ stand for copper losses and eddy current losses in one half of the stator winding and windage frictional losses in one rotor disc, respectively. The heat flowing through each path of the thermal resistance circuit is given by a temperature difference divided by a thermal resistance (see Table 5.1). For conduction the thermal resistance depends on the thermal conductivity of the material and the length and cross-sectional area of the heat flow path and may be expressed as $R = l/kA$. The thermal resistance for radiation between two surfaces may be given by [31]

$$R_{rad} = \frac{\frac{1-\varepsilon_1}{\varepsilon_1 A_1} + \frac{1}{A_1 F_{12}} + \frac{1-\varepsilon_2}{\varepsilon_2 A_2}}{\sigma[(T_1+273)+(T_2+273)][(T_1+273)^2+(T_2+273)^2]} \tag{5.16}$$

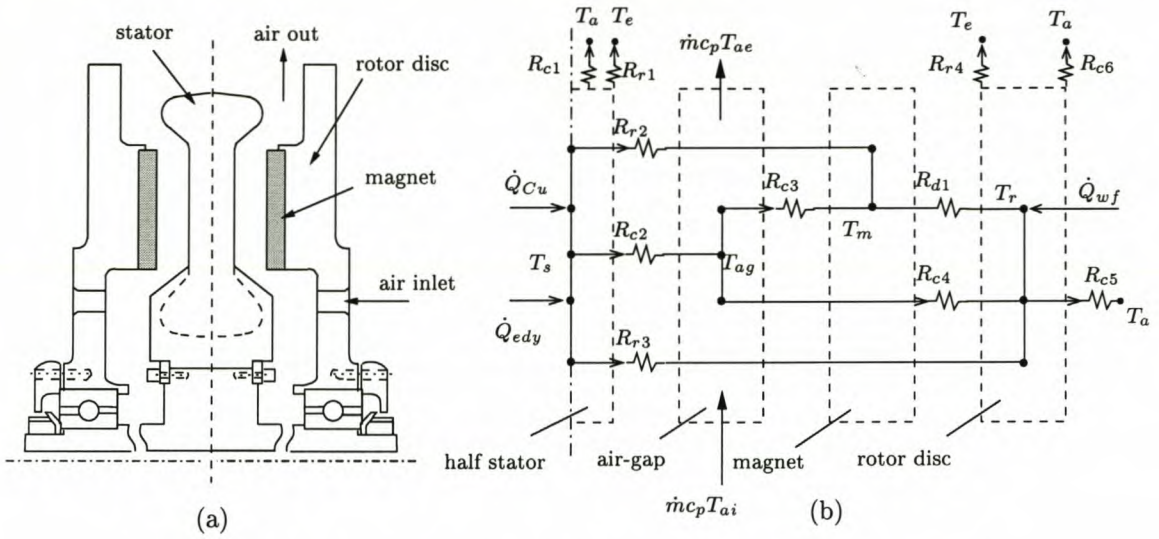

Figure 5.10: The thermal resistance circuit of an AFPM machine.

In this equation it is seen that the radiation thermal resistance depends on the difference of the third power of the absolute temperature, the surface spectral property ε and the surface orientation taken into account by a form factor F. Convective heat transfer from a surface to a moving fluid depends on the heat transfer coefficient, the determination of which is a complex problem, usually necessitating the use of empirically determined correlations. No convection heat transfer correlations relating to the specific topology of AFPM machines are available and for this reason potentially suitable existing correlations are dealt with in the next section.

5.3.2 Convection heat transfer coefficients

The rotating disc system plays a major role in the cooling and ventilation of the AFPM machine. Accurately determining the convection heat transfer coefficients needs thorough theoretical and experimental investigations because of the complexity of flow regimes. In this section the convection heat transfer coefficients in different parts of the AFPM machine are evaluated exploiting a number of existing models.

Free rotating disc

The average heat transfer coefficient at the outside surface of a rotating disc may be evaluated using the formula developed for a free rotating plate [108], i.e.

$$\bar{h} = \frac{k}{R} \cdot \overline{Nu} \tag{5.17}$$

Table 5.1: Definition of thermal resistances.

Symbols	Definition
R_{c1}	Convection resistance from stator end-winding to open air
R_{c2}	Convection resistance from half the stator to air-gap
R_{c3}	Convection resistance from air-gap to permanent magnets
R_{c4}	Convection resistance from air-gap to rotor disc plate
R_{c5}	Convection resistance from rotor disc to open air
R_{c6}	Convection resistance from rotor radial periphery to open air
R_{r1}	Radiation resistance from stator end-winding to environment
R_{r2}	Radiation resistance from half the stator to permanent magnets
R_{r3}	Radiation resistance from half the stator to rotor disc
R_{r4}	Radiation resistance from rotor radial periphery to environment
R_{d1}	Conduction resistance from permanent magnets to rotor disc

where R is the radius of the disc and the average Nusselt number $\overline{Nu}$ is given according to the different flow conditions as follows:

(i) For combined effects of free convection and rotation in laminar flow (Fig. 5.11a) [108]

$$\overline{Nu} = \frac{2}{5} \cdot (Re^2 + Gr)^{\frac{1}{4}} \tag{5.18}$$

where $Re = \frac{\omega R^2}{\nu}$, $Gr = \frac{\beta g R^3 \pi^{\frac{3}{2}} \Delta T}{\nu^2}$ and ΔT is the temperature difference between the disc surface and the surrounding air.

(ii) For a combination of laminar and turbulent flow with the transition at $r_c = (2.5 \times 10^5 \nu/\omega)^{1/2}$ (Fig. 5.11b) [108]

$$\overline{Nu} = 0.015 \cdot Re^{\frac{4}{5}} - 100 \cdot (\frac{r_c}{R})^2 \tag{5.19}$$

It is instructive to compare the heat transfer capabilities between a rotation disc and a stationary disc. Considering the AFPM machine depicted in Fig. 5.1, which has a diameter of 0.4 m and rotates at 1260 rpm., the convection heat transfer coefficient may be calculated as 41 W/m^2 K, which is about ten times that of the same disc at standstill. Alternatively, one can say that the effective heat dissipation area of the same disc can be increased by a factor of 10 when rotating.

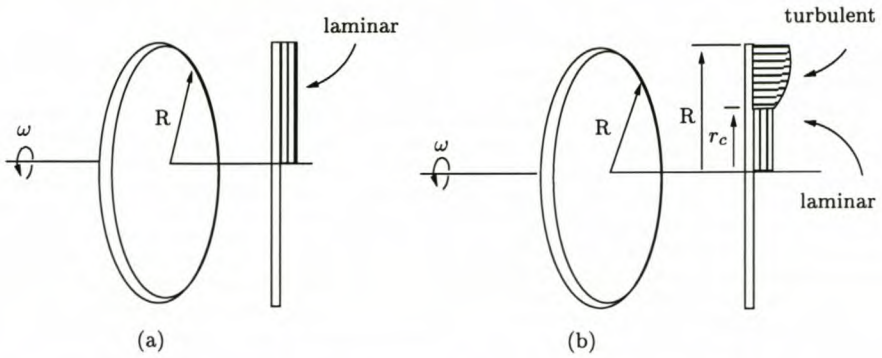

Figure 5.11: Free rotating disc: (a) in laminar flow, (b) transition from laminar to turbulent flow.

Rotor radial peripheral edge

The heat transfer correlations for the radial periphery of the rotor disc are similar to those of a rotating cylinder in air. In this case the average heat transfer coefficient is given as

$$\bar{h}_p = (k/D)\overline{Nu} \tag{5.20}$$

where $\overline{Nu} = 0.133 \cdot Re_D^{2/3} Pr^{1/3}$, D is the diameter of the cylinder and $Re_D = \omega D^2/\nu$. Note that a uniform temperature distribution in the cylinder is normally assumed when Eqn. (5.20) is used. If these equations are applied to the rotor disc, the average heat transfer coefficient around the radial periphery can be computed, which is about 95 W/m^2 K, and therefore justifies its inclusion in the thermal resistance circuit. Since h_p is proportional to the rotational speed ω, it may be concluded that the rotor periphery plays an increasingly important role in the heat dissipation as ω increases.

Rotor-stator system

As seen in Fig. 5.1, the main heat transfer region consists of surface-mounted PMs with radial channels between the PMs. Due to centrifugal effects, there is a forced flow through the PM channels, which increases the local heat transfer rate compared with that of a free disc. The relative increase will depend on the gap ratio, $G = \frac{s}{r_o}$, where s is the clearance between the rotor and the stator, the mass flow rate and the rotational speed of the system having been taken into consideration [78].

Having radial channels and thick impellers, an air-cooled AFPM machine may be regarded as a poorly designed fan from a fluid flow perspective. Its tangential velocity component is much larger than the radial component. Thus, the heat transfer rate near the rotating disc shows more dependence on the rotational Reynolds number, which is defined as [79]

$$Re = \rho\omega^2 r_o/\mu \tag{5.21}$$

where ω is the angular velocity of the rotating disc, and r_o is the radius of the disc.

Owen [81] provided an approximate solution for the flow between a rotating and a stationary disc, which relates the average Nusselt number to the moment coefficient of the stator-side rotor face, C_{mo}, by the following equation.

$$\begin{cases} \overline{Nu} = Re_r C_{mo}/\pi \\ \\ C_{mo} Re_r^{1/5} = 0.333\lambda_T \end{cases} \tag{5.22}$$

where λ_T is a *turbulence parameter* given as a function of volumetric flow rate, Q, as follows

$$\lambda_T = \frac{Q}{\nu r_o} Re_r^{-\frac{4}{5}} \tag{5.23}$$

Applying Owen's approximate solution [81] to the same AFPM machine operating at a speed of 1260 r.p.m. with a measured radial flow of 0.026 m^3/s between rotor and stator, the estimated average heat transfer coefficient from the stator across the air-gap to the rotating disc is 94 W/m^2 K.

As discussed in [79], it has been shown that for a small gap ratio ($G < 0.1$) the flow in the air-gap space between the rotor and stator can be treated as a boundary layer. Whilst it is not absolutely true that the convective heat transfer coefficient from the stator to the air flow is close to that of the air flow to a rotating disc, the same heat transfer coefficient has been assumed in the thermal circuit simulation.

5.3.3 Conservation of energy

If conservation of energy is applied, the rate of internal energy change of a control volume may be written as follows:

$$\frac{\Delta U}{\Delta t} = \dot{Q_{in}} - \dot{Q}_{out} + \dot{m}_{in} i_{in} - \dot{m}_{out} i_{out} \tag{5.24}$$

where $\dot{m}$ is the mass flow rate, i is the *enthalpy* and U is the internal energy.

For steady-state conditions, $\frac{\Delta U}{\Delta t} = 0$ and therefore,

$$0 = \dot{Q_{in}} - \dot{Q}_{out} + \dot{m}_{in} i_{in} - \dot{m}_{out} i_{out} \tag{5.25}$$

Equation (5.25) is applied to each part (the half-stator, air-gap, magnet and rotor disc) of the AFPM machine shown in Fig. 5.10 to obtain a set of equations with the temperatures of the parts being the only unknowns. The heat flowing in each path is given as a temperature

difference divided by a thermal resistance. The values used for the heat source terms are given in Table 5.2 [65]. This set of equations is rather complex but is readily solved using for example, the *Gauss-Seidel* iteration.

Table 5.2: Heat source terms for the AFPM machine [65].

Description	$\dot{Q}$
Bearing frictional losses	106 W
Stator eddy current losses	23 W
Magnet eddy current losses	3 W
Stator copper losses (rated)	360 W
Stator copper losses (overload)	1440 W

5.3.4 Experimental validation

The AFPM machine was driven by a d.c. motor and operates as a generator feeding a rectifier load. Both rated and overload (double the rated current) operating conditions were monitored.

Temperature measurements

The temperatures of the rotating disc and the peripheral edge of the windings were measured using a digital infrared thermometer. The average winding temperature was measured using an electrical resistance method [33]. The basic procedure is described as follows:

The machine was run for long enough to ensure steady-state conditions. The driving motor was then shut down and when the machine came to a standstill, the electrical resistances of the three phases of the windings were measured as a function of time. A suitable curve was fitted to these resistance measurements and the resistance that the winding would have had when the machine was shut down was determined by extrapolating back in time.

To ensure the validity of the measurements, the first resistance reading should be taken within 30 seconds after switching off the power to the driving motor. The average temperature rise in the stator winding is then obtained by using the following equation:

$$\Delta T = \frac{R_2 - R_1}{R_1}(K + T_1) + T_1 - T_0 \tag{5.26}$$

where K is a constant ($K = 235$ for copper winding, $K = 228$ for aluminum winding), T_0 is the ambient temperature, T_1 is the cold winding temperature, R_1 and R_2 are the measured cold and hot winding resistances.

Comparison of results

Based on the afore-described thermal and fluid models, a combined thermo-fluid model was formed and implemented on computer. Selected calculated results are shown and compared with the measured ones as follows.

Table 5.3: Predicted and measured temperature rises (*rated current*).

Machine parts*	Calculated*, (^oC)	Measured*, (^oC)
Stator winding	27.8	23.3
Rotor disc plate	14.1	11.2
Rare-earth PM	13.7	-
End-winding	-	21.5
Air-gap flow	7.6	-
*Conditions**	$T_{amb} = 23.75\ ^oC$ $I_{ph} = 30\ A$	n = 1,217 r.p.m.

The computed values of temperature rise in various parts of the AFPM machine are compared with relevant measurements in Tables 5.3 and 5.4. The predicted temperature values are invariably higher than the measured ones (10% higher). One possible reason is that the end-winding is partially located above the PM top edge and its heat flow path is not necessarily through the PMs. Including the end-winding losses as internal heat losses may result in slightly over-estimated temperature values in the analysis.

It is justifiable to say that the calculated results agree well with the tested ones considering the fact that the developed thermo-fluid model is basically one-dimensional. The developed thermofluid model is combined with the FE optimisation program described in Chapter 6.

Table 5.4: Predicted and measured temperature rises (*over-load current*).

Machine parts †	Calculated †, (^oC)	Measured †, (^oC)
Stator winding	102.1	95.1
Rotor disc plate	27.3	25.5
Rare-earth PM	27.6	-
End-winding	-	65.4
Air-gap flow	30.1	-
Conditions †	$T_{amb} = 24\ ^oC$ $I_{ph} = 60\ A$	n = 1,263 r.p.m.

5.4 Insights into the cooling design

The main aim of this Chapter was the development and verification of a thermo-fluid model for analysing and predicting the thermal behaviour of AFPM machines. The comparison between the calculated results and the measurements has shown that the developed model can perform the thermal calculations with reasonable accuracy.

The air flow through the AFPM machine is not optimised from a minimum energy loss point of view. This is evident from the tortuous path through which the air flows. By taking into consideration to a greater degree sound fluid mechanics practice, an improved mass flow rate can be achieved with a subsequent reduction in the operating temperature and hence a longer service life.

The entrance effects, bending, tapering, and tee connection, which are normally referred to as 'minor losses' in the conventional large fluid flow system analysis, can no longer be considered as small losses in the flow analysis of the AFPM machine. As an example, the entrance losses of the air flow in the AFPM machine (shown in Fig. 5.1) accounts for approximately 22% of the total system pressure losses of the machine.

The air intakes of AFPM machines are, in many instances, round holes through rotor discs in the vicinity of the machine shaft. The suction holes should be perpendicular to the flat rotor disc so that the entrance loss for the flow from the atmosphere into the hole is reduced. This is equivalent to the *flanged entrance* described in [6]. Usually, fluid stream lines conform nicely to the contour of a well rounded entrance. The precise curvature of the entrance profile is unimportant, but it must be free from irregularities. The length of the cylindrical channel through the rotor disc should be from 1/4 to 1/2 its diameter [6]. Following these guidelines, an optimum air entrance design may be achieved, in which the loss is small.

The outer overhangs of the AFPM machines physically serve as a shroud in the rotor-stator system. They cause extra frictional loss, but they also help prevent recirculation of discharged hot air (also referred to as *ingress* [80]), which is not desirable from a cooling point of view. The ingress can be serious when an AFPM machine is operated at low speed or the physical saliency of the PM rotor disc is removed (e.g inset or buried PM arrangement). For an AFPM machine with surface-mounted PMs running at a reasonable speed, a superimposed radial flow is generated through the radial channels between adjacent PMs on the rotor disc. As the superimposed flow is increased, the pressure drop across the shroud causes the system to be pressurised, and ingress can be prohibited [80].

Chapter 6

Optimisation

This chapter describes the design optimisation of the AFPM machine. The aim of the optimisation procedure is to minimise the weight of PM material used on the rotor discs, while ensuring a rated output power, desired phase voltage and sufficient cooling capacity. The objective function and constraints are directly calculated by using FEM. Two different optimisation algorithms are used for the unconstrained design optimisation of the AFPM machine.

6.1 Mathematic formulation for objective optimisation

Ideally the optimisation of an electrical machine can be formulated as a general constrained optimisation problem with more than one objective (e.g. minimisation of the manufacturing costs and losses, maximisation of the efficiency and output power). Finding the extremum (Extr) of vector-optimisation problems may be defined as:

$$\text{Extr}\ [F(\vec{x})] = \text{Extr}\ [f_1(\vec{x}), f_2(\vec{x}), \ldots, f_k(\vec{x})] \tag{6.1}$$

subject to specified equality and inequality constraints:

$$h_i(\vec{x}) \leq 0 \quad (i = 1, 2, \ldots m) \tag{6.2}$$

$$g_j(\vec{x}) = 0 \quad (j = 1, 2, \ldots p) \tag{6.3}$$

and specified limits for the independent variables:

$$\vec{x}_{min} \leq \vec{x} \leq \vec{x}_{max} \tag{6.4}$$

where $F : \Re^n \rightarrow \Re$ is the vector objective function with the objectives $f_i(\vec{x})$ to be minimised, $h_i, g_j : \Re^n \rightarrow \Re^k$ are the vector-mappings defining equality and inequality constraints respectively, $\vec{x} = \{x_1, x_2, \ldots, x_n\}$ is the vector of design variables for the optimisation, and $\vec{x}_{min}$

and $\vec{x}_{max}$ are vectors of lower and upper bounds for the design variables.

In practical vector optimisation problems there is virtually no solution vector $\vec{x}$ for which each individual objective $f_i(\vec{x})$ gains its minimum. One common practice is to transform vector optimisation problems from multi-objective optimisations into single objective optimisations using the method of objective weighting. Although objective weighting always leads to a non-inferiority feasible solution, the estimation of the weighting factors and the optimisation starting point is a subjective choice, and their influence can rarely be estimated in advance.

Alternatively, optimisation can be carried out to minimise only one objective function while restricting the others with appropriate constraints. Most constraints are upper or lower bound inequality constraints, which means constrained optimisation procedures are required. The optimisation is thus done for a feasible region, in which all the constraints are satisfied for the design variables.

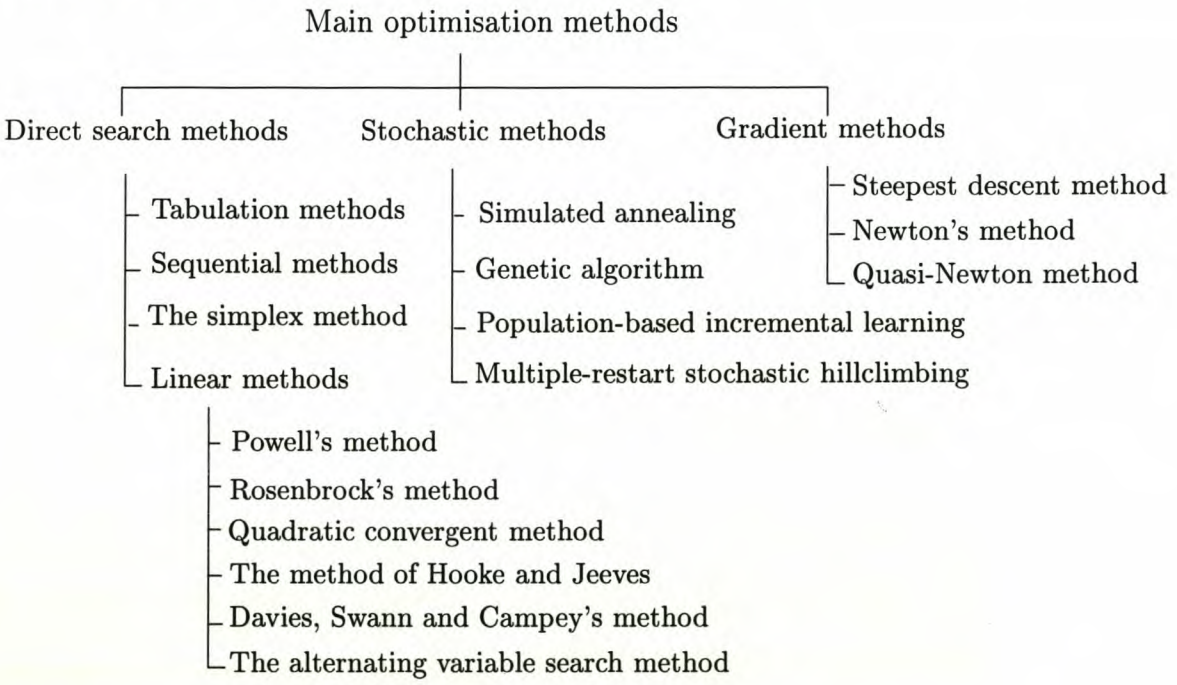

Figure 6.1: Main constrained optimisation techniques.

6.2 Optimisation algorithms

In non-linear optimisation problems both the objective and constraint functions may be non-linear. There is no general agreement as to the best optimisation method or approach. The extremely vast subject of non-linear optimisation techniques can be classified into three categories, i.e. *direct search methods*, *stochastic methods* and *gradient methods*. A brief summary

of the main constrained optimisation techniques is given in Fig. 6.1.

Deterministic optimisation techniques such as the *steepest-descent*, *conjugate gradient*, and *quasi-Newton* methods have been used as standard tools for solving local optimisation problems for decades. These algorithms are usually gradient-based and subject to errors due to discretisation of the objective function and the approximation of the derivative by using difference methods [45, 44, 88]. Other non-gradient methods (e.g. *Powell's method*) evaluate only the objective function without calculating its derivatives, which is an advantage [59, 84]. However, there is a common problem to these optimisation techniques, i.e. the risk of finding a local minimum rather than the absolute minimum [59, 84]. This is the inherent nature of all deterministic methods and is a difficult problem to overcome [45, 48, 84].

During the last decade the stochastic methods have become more popular in the optimisation of electrical machines because they show a high probability of finding a global minimum and are simple to use. Amongst others, the *genetic algorithm* (GA) has been applied for the design optimisation of various electrical machines[30, 51, 44]. A modified version of the GA, *Population-based incremental learning* (PBIL) algorithm, has been successfully used for optimisation of PM universal motors [107]. In general, stochastic methods are not as efficient as most deterministic optimisation algorithms.

In this chapter both Powell's method and the Population-Based Incremental Learning (PBIL) algorithm are described briefly and then used for the design optimisation of the AFPM machine. The reasons for using these methods are:

- to compare the effectiveness of the linear maximisation (minimisation) method (Powell's method) with that of a stochastic method (PBIL) and
- to verify the optimum design results by using two completely different algorithms.

6.2.1 Powell's method

Powell's method [84, 59] is basically an iterative method. Each r^{th} iteration of the procedure maximises (minimises) the objective function along n linearly independent directions, L_1, L_2, ..., L_n. The initial set of n vector directions are the co-ordinate directions. After each iteration a new direction is defined which is used to form the vector directions for the next iteration. After n iterations, a set of n mutually conjugate vector directions are obtained so that the maximum (minimum) of a quadratic function is found. A flow chart of Powell's method is shown in Fig. 6.2.

To ensure a reasonable convergence, specially designed tests have been incorporated into the process. This is because occasionally the procedure tends to select nearly dependent

directions, resulting in possibly premature termination of the process. The test is performed by defining an extra vector point P_e further along the proposed new direction $L_{no} : P_0 \rightarrow P_n$ after each iteration. If the function values of these vector points $f_0 = F(P_0)$, $f_n = F(P_n)$, $f_e = F(P_e)$ satisfy either

$$f_e \leq f_0 \quad \text{and/or}$$
$$(f_0 - 2f_n + f_e)(f_0 - f_n - \Delta f)^2 \leq \frac{1}{2}\Delta f(f_o - f_e)^2. \tag{6.5}$$

where $\Delta f = max_i(f_i - f_{i-1})$ is the greatest increase of the function value along one of the directions of the iteration, then the old directions are kept for the next iteration with the starting vector point moved to P_n. Otherwise, the new direction L_{no} is incorporated for the next iteration and the next starting point is changed to P_e. The other important step is to discard the direction corresponding to the largest increase of Δf, which is essential to avoid linear dependence in the optimisation process.

The optimisation procedure is finished when the following criterion is met

$$|f_n - f_0| \leq \xi \frac{|f_n| + |f_0|}{2} \tag{6.6}$$

where ξ is the fractional tolerance of the function value and f_0 and f_n are the start and final function value of one iteration, respectively.

6.2.2 PBIL algorithm

Genetic algorithms (GAs) are evolutionary search algorithms based on natural selection and genetic recombination, and were first proposed by Holland [51, 30]. GAs encode the solution as a population of binary strings. Each solution is associated with a *fitness* value determined from the objective function.

The fundamental operators used in the search process of GAs are *reproduction*, *crossover* and *mutation*. The reproduction mechanism creates a new generation from the old generation based on the fitness measure of an individual and the average fitness of the population. In the reproduction process, the genetic material (chromosome) goes from the parents into a new gene. This exchange of part of the genetic material among chromosomes is called crossover, which is the main operation in GA. The mutation plays the role of regenerating lost genetic material by causing sporadic and random alteration of the bits of the binary strings. GAs are characterised by their population size, crossover type, crossover rate and elitist selection.

PBIL is an abstraction of the GA that maintains the statistics contained in a GA's population, but leaves out the crossover operation [5, 107]. The algorithm uses a real valued probability

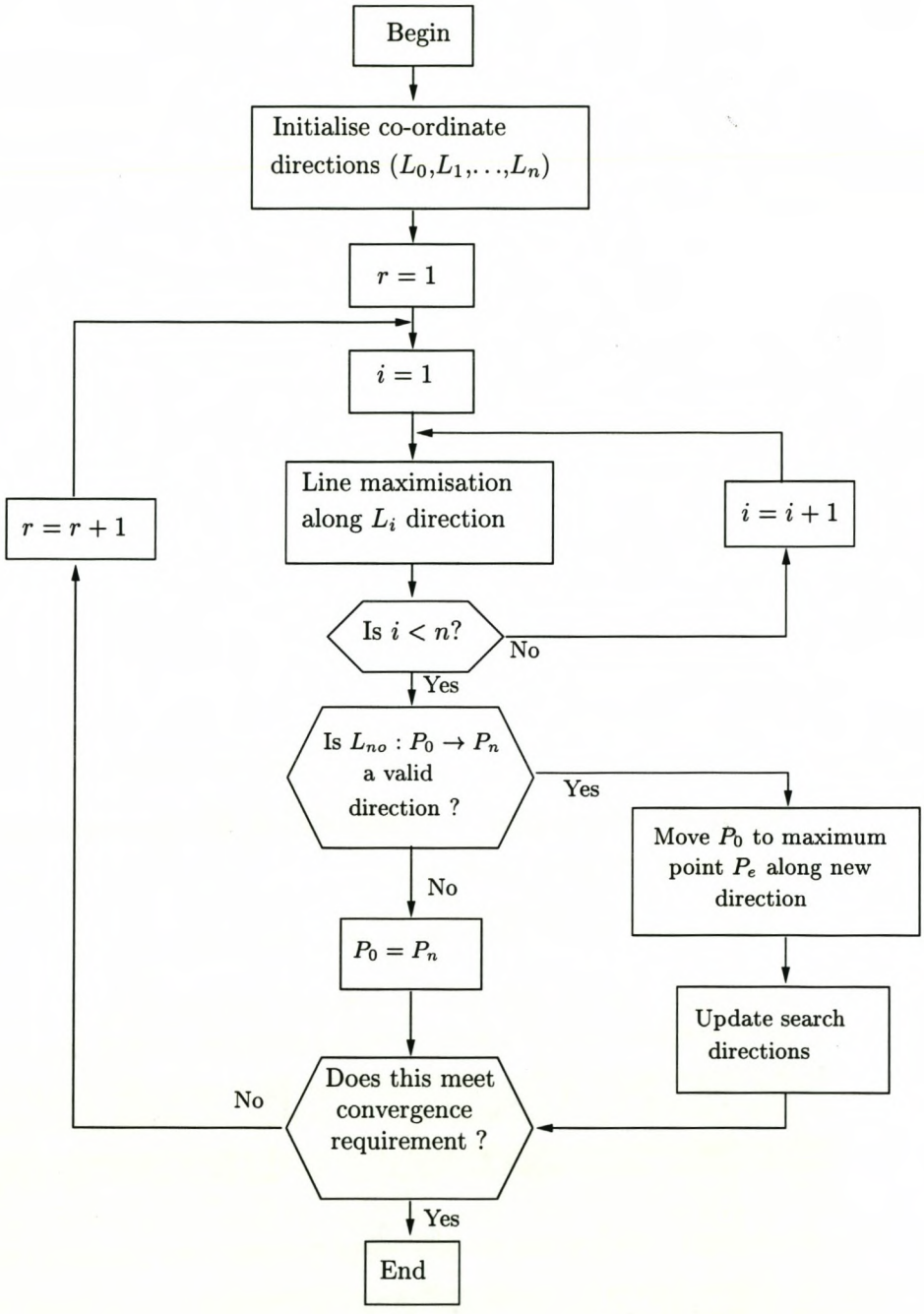

Figure 6.2: Flow chart of Powell's method.

vector which, when sampled, reveals a high evaluation solution vector with high probability. As in the GA, the solution is encoded into a binary vector of fixed length. Initially the values of the probability vector are set to 0.5. A number of solution vectors (as the population in GAs) are generated based on the probabilities of the probability vector. The probability vector moves towards the generated solution vector with the highest evaluation (fitness value). This probability vector can thus be considered a prototype for the high evaluation vectors of the function space being explored. Each bit of the probability vector is updated using:

$$p_i = p_i \cdot (1 - \delta_l) + \delta_l \cdot s_i \tag{6.7}$$

where p_i is the probability of generating a one in the bit position i, s_i is the i^{th} position in the solution vector for which the probability vector is being changed and δ_l is the *learning rate*. The learning rate is the amount the probability vector is changed after each cycle.

A new set of solution vectors is produced after each update of the probability vector. The entries in the probability vector start to drift towards either 0 or 1, as the search progresses, to represent a high evaluation solution vector. The use of mutation in PBIL is for the same reason as in the GA, i.e. to prevent premature convergence. Mutations perturb the probability vector with a small probability in a random direction. The process is carried out in each randomly chosen bit position for each solution using the following equation:

$$\begin{cases} p_i = p_i \cdot (1 - \delta_m) + \Gamma \cdot \delta_m \\ \Gamma = 0 \text{ or } 1. \end{cases} \tag{6.8}$$

where δ_m is the *mutation rate* and Γ is an integer that is randomly assigned 1 or 0. PBILs are generally characterised by their number of samples, learning rate, number of vectors to update from and mutation rate. The flow chart of the PBIL algorithm is shown in Fig. 6.3. PBIL has been shown to work as well, or better, than the GA [107]. The main advantage of the PBIL over the GA is that since the PBIL is characterised by fewer parameters and their values are less problem related, as little problem-specific knowledge as possible is needed.

6.3 Constrained optimisation

Engineering design is inherently a constrained optimisation process. The constraints are usually the required performance indices. Constrained optimisation problems are generally transformed to unconstrained ones, and are then optimised using one of the main optimisation methods described above. Some commonly used techniques are: penalty function, exact penalty function, feasible direction method, augmented Lagrangian function, and sequential unconstrained minimisation [106, 110].

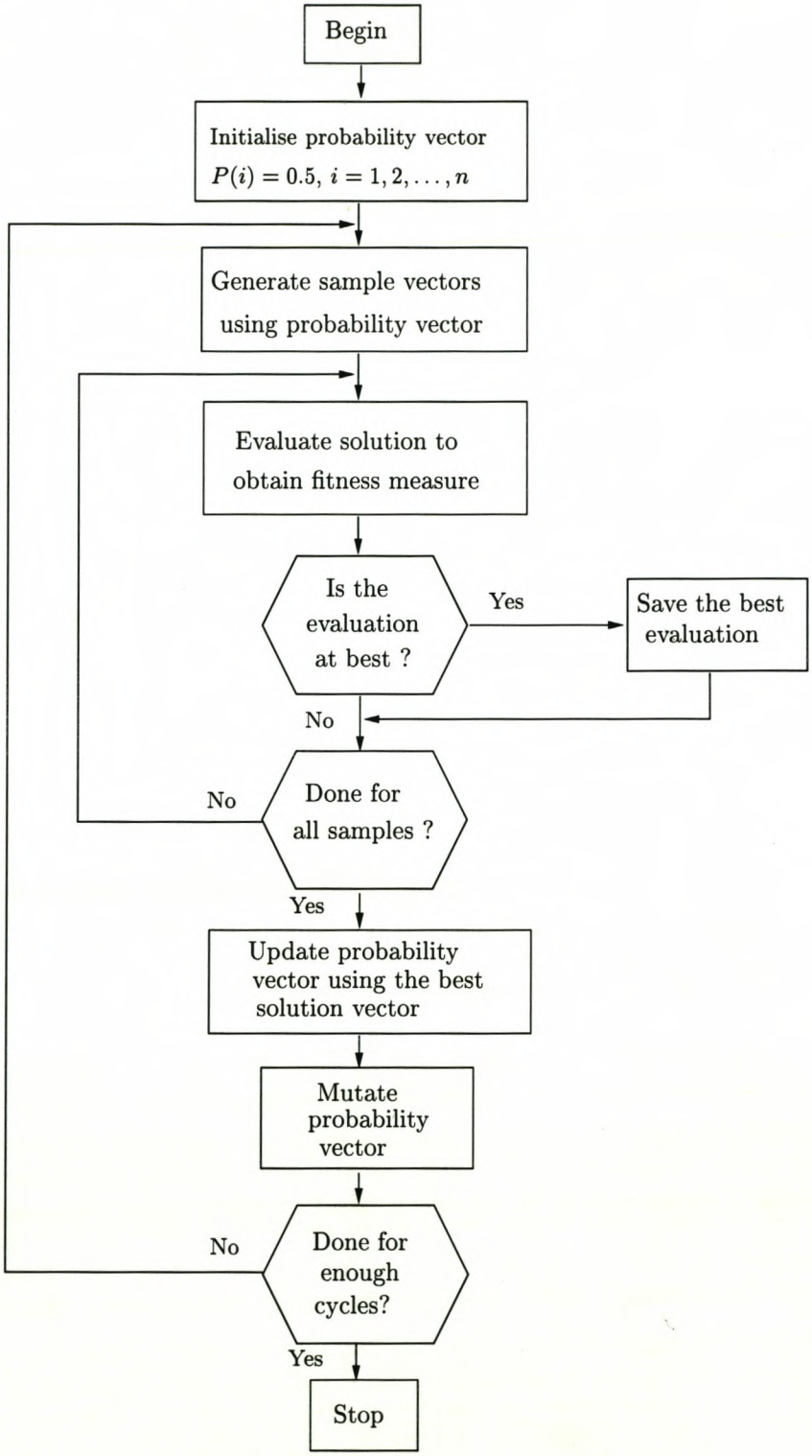

Figure 6.3: Flow chart of PBIL algorithm.

In this thesis the penalty function is used together with Powell's method. The objective function is modified by adding terms or functions that penalise any increased constraint violation. The resultant objective function is then:

$$F(\vec{x}, w) = f(\vec{x}) + \sum_{i=1}^{u} w_i \epsilon_i(\vec{x}) \tag{6.9}$$

where $f(\vec{x})$ is the function to be minimised, w_i are weighting factors and $\epsilon_i(x)$ are functions which penalise infeasibility. The aim of this thesis is to design a 300 kW AFPM generator that uses the minimum volume of PM material, V_m, and delivers a rated power of not less than 300 kW at a specified rated speed. The objective function is then V_m, which is subject to the output power constraint. As an example, the function to be minimised may be defined by:

$$F(\vec{x}, w) = V_m(\vec{x}) + w\epsilon \tag{6.10}$$

where

$$\epsilon = \begin{cases} 0 & : P_o(\vec{x}) \geq 300 \\ (300 - P_o(\vec{x}))^2 & : P_o(\vec{x}) < 300 \end{cases}$$

Thus the constrained optimisation problem can readily be solved by unconstrained optimisation routines although a suitable value of weighting factor w may only be found through a trial-error process. When several weighting factors are necessary, this process can be somewhat complicated. Due to the nature of the stochastic search, PBIL algorithms do not require the use of penalty functions in the objective functions.

6.4 Optimisation procedure and results

The machine characteristics are calculated using finite element analysis and classical machine theory. The finite element program used was originally developed by Cambridge University and revised by the author for modelling of the AFPM machine. The air-gap is represented by a macro element, which has been extended by the author for a rectangular shaped air-gap (Chapter 3), and the rest of the FE model is discretised using first order triangular elements. An optimised profile reduction scheme [40] is incorporated into the program for fast stiffness terms evaluation and therefore less solution time.

The current-sheet approach [89] is used for representing permanent magnets and the Newton-Rhapson algorithm is employed in the non-linear solver. The key variables of the machine geometry are parameterised so that the whole FE analysis can be directly incorporated into the design optimisation process.

6.4.1 Variables to be optimised

The geometric layout of an AFPM machine with an ironless stator is shown in Fig. 6.4. Only five variables of the machine are selected to be optimised. These are the PM thickness, h_m, magnet width to pole pitch ratio $\frac{\tau_m}{\tau_p}$, stator winding thickness, h_s, rotor disc inner diameter, r_i, and the air-gap clearance g. The rotor outer diameter r_o, the rated speed and the number of poles, p, are kept constant in the optimisation. The comparison done in previous studies [68] reveals that the design of an AFPM machine using purely electromagnetic calculations without taking into account mechanical strength requirements may lead to an unrealistically thin rotor disc. This is especially true when designing a high pole number AFPM machine as the flux per pole is inversely proportional to the number of poles. The attraction force between the rotor discs is, however, independent of the number of poles. To rectify this problem, the mechanical strength analysis is therefore of paramount importance in determining the thickness of the rotor disc h_r. The FE analysis of the mechanical strength will be described in Chapter 7.

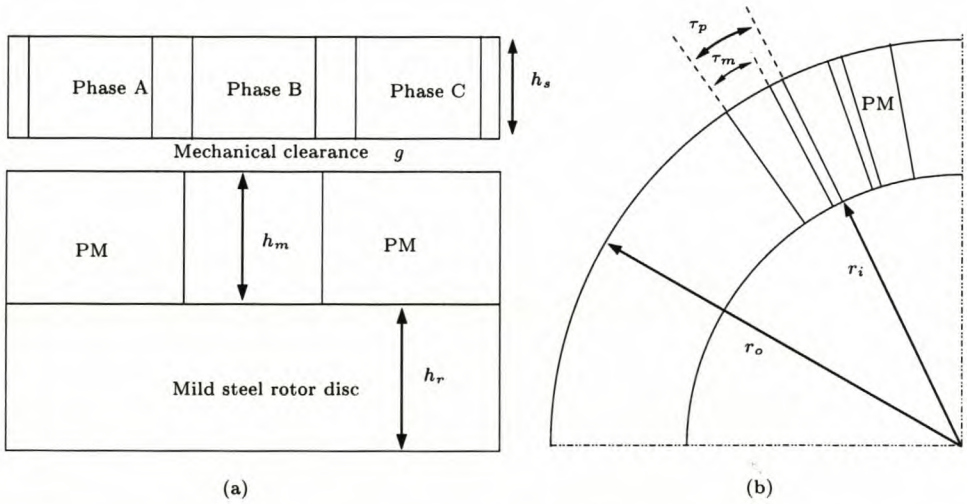

Figure 6.4: Geometric layout of AFPM machine showing design variables: (a) a linearised section of the radial cutting plan, (b) rotor disc with PMs.

To facilitate the construction of the ironless stator, single layer, trapezoidal shape coils are used in the stator. The winding arrangements such as the number of coils per phase per pole, number of parallel circuits per phase, and number of parallel wires per coil have been pre-defined. With the number of poles and rated speed known, the conductor size has been chosen in such a manner that the skin effect is negligible and the induced eddy loss within the conductor is resistance limited as described in Chapter 4.

6.4.2 Performance parameters and constraints

In the design optimisation process, the output characteristics of the AFPM machine are the output power, power factor, efficiency, eddy current loss, current density, phase voltage, phase current, number of turns per coil, the weight of the active materials (PM, iron, copper), power density, torque, attraction force between rotor discs and the thermal behaviour in the different parts of the machine.

The copper losses are kept constant in the design program. An iterative procedure, making use of the thermo-fluid model established in Chapter 5, has been used to evaluate the maximum allowable losses that the machine can handle. The estimated full-load copper loss is about 5 kW [68]. For a medium power rating electrical machine with forced air-cooling over stator winding and F class insulation, the allowable stator winding current density is between 9 – 12 A/mm^2. Hence, the maximum current density is set at 11 A/mm^2 in the design program. The performance parameters to be optimised have been selected as the mass of the PM material and the efficiency.

Optimise for minimal mass of PM material

The optimisation problem for minimising the total mass of the PM material W_m can be expressed as: MIN[W_m] subject to the following constraints:

$$\begin{cases} P_e(\vec{x}) & \geq & P_o \\ J(\vec{x}) & \leq & J_a \\ V_{ph}(\vec{x}) & \leq & V_a \\ T_s(\vec{x}) & < & T_a. \end{cases} \tag{6.11}$$

where W_m is the total mass of the PM material used, P_o is the desired output power, J_a is the maximum current density, V_a is the maximum phase voltage at the rated output power, and T_a is the temperature limit of the stator winding.

Optimise for maximum efficiency

The optimisation problem for maximising the machine efficiency η can be expressed as: MAX[η] subject to the constraints:

$$\begin{cases} P_e(\vec{x}) & \geq & P_o \\ J(\vec{x}) & \leq & J_a \\ V_{ph}(\vec{x}) & \leq & V_a \\ W_m(\vec{x}) & \leq & W_m \\ T_s(\vec{x}) & < & T_a. \end{cases} \tag{6.12}$$

where η is the machine efficiency at rated output power P_o and W_m is the maximum mass of the PM material used at P_o.

6.4.3 Optimisation procedure

In the optimisation process, the FE analysis is done at a fixed rotor position. The mechanical losses were estimated and kept constant in the calculation. Fig. 6.5 illustrates the basic structure of the optimisation program. Powell's method requires an initial value for each of the variables. If it is too far from the real optimum, then the optimisation may end up being trapped in a local optimum in the vicinity of the initial value [106], which will lead to the necessity of testing with different sets of starting values to verify the optimum point. In the present optimisation, a few different sets of starting points were used and the results were found to be sufficiently close to one another.

When the PBIL algorithm is used, it does not really matter what starting values are used. Each design variable $\vec{x}_k$ is assigned to a fixed length, ℓ_k, of a binary sequence, b_k, and the resultant binary vector b is:

$$b = [b_1, b_2, \ldots, b_n]^T \tag{6.13}$$

which represents a randomly generated chromosome (gene) in the discretised design domain. The precision is proportional to the length of the binary chromosome $\ell = \sum \ell_k$. A total of 30 sample bits, 6 bits per independent variable, were used in the present optimisation. The step sizes for the variables are 0.00005 m for the air-gap g, 0.0001 m for the PM height h_m, 0.0001 m for the stator thickness, 0.0005 m for the rotor inner radius r_i, and 0.005 for the PM width to pole pitch ratio. The number of bits and step size per variable were chosen to ensure the largest feasible range. The stopping rule of the PBIL algorithm is that the optimisation cycles have to reach a pre-set number of generations.

During the optimisation process, the mesh of the FE model changes as the optimisation progresses. Occasionally some of the elements may be badly shaped or ill conditioned resulting in poor accuracy or even no solution. It is therefore necessary to check that the model dimensions are reasonable before the FE mesh is constructed.

6.4.4 Results of the optimised AFPM machine

Starting from the same initial design, the optimisation was done using both Powell's method and the PBIL algorithm according to the two different design objectives, i.e. the optimum AFPM machine for maximum efficiency and minimum PM material, respectively. A comparison of the effectiveness between the two methods was also done. Table 6.1 shows that both optimisation algorithms give similar results. The PBIL optimisation results give a slightly

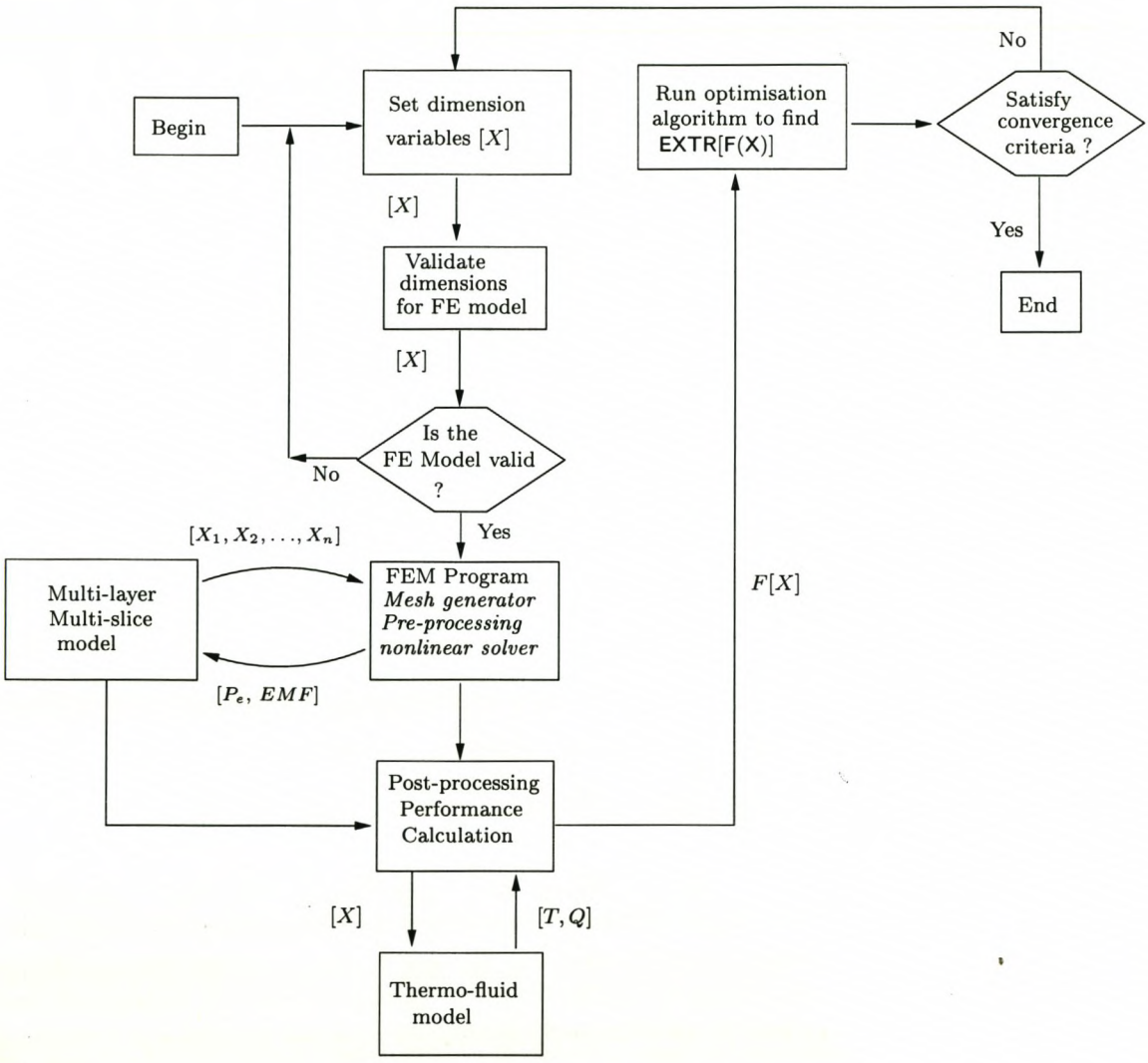

Figure 6.5: Schematic diagram of the optimisation program showing the basic structure.

better solution in these two case studies. However, Powell's method is a lot more efficient than the PBIL algorithm as it used only a fraction of the CPU time that the PBIL required. The output characteristics of each optimised design are summarised in Table 6.2.

Table 6.1: Optimisation results of Powell and PBIL methods.

Objective functions ⇒	MAX[F($\vec{x}$)] ; $F(\vec{x}) = \eta\%$			MIN[F($\vec{x}$)] ; $F(\vec{x}) = W_m$		
Variables [$\vec{x}$] ⇓	Initial values	Powell results	PBIL results	Initial values	Powell results	PBIL results
PM height (mm)	11	11.12	11.1	10	10.7	10.5
PM width/pole pitch	0.76	0.78	0.72	0.66	0.72	0.72
Stator thickness (mm)	17.8	18.5	15.6	12	15.7	16.3
Air-gap clearance (mm)	2	2.5	2.745	2	2.75	2.75
Rotor inner diameter (mm)	490	490.3	495	380	499.6	506
$F(\vec{x})$	96.67%	96.97%	97.2%	28.9 kg	24.2 kg	23.2 kg
CPU time (h) ⇒	-	≈ 1	≈ 13	-	≈ 1	≈ 13

The PBIL optimisation satisfies all the constraints for a maximum efficiency design, whereas Powell's method failed to meet the phase voltage limit with a small violation. Moreover, the optimisation process using Powell's method tends to stop at a local optimum, which is characterised by a low diameter ratio K_r, a large amount of PM material, and a thick stator. This is understandable since the optimisation attempts to achieve a winding design with a greater active length to overhang ratio, and thus a greater output power per unit copper losses. It was found effective to use the PM mass as a constraint in the optimisation with Powell's method. The PBIL optimisation needs no such constraint as it finds the optimum design of efficiency with quite a low PM material consumption.

For the design of minimum PM material, Powell's method produces an optimum design that meets all the limits. Although the PBIL optimisation came up with a design using less PM material, the output power is a bit lower than the required value. The two dimensional geometric layout of a quarter of the rotor disc and a section of the unfolded cutting plane at the rotor average radius, optimised for maximum efficiency, is shown in Fig. 6.6(a), whereas the relevant geometric layout optimised for minimum PM material is given in Fig. 6.6(b). It was found that the diameter ratio K_r is about 0.68 for the maximum efficiency design and around 0.7 for minimum PM consumption design. By minimising the PM material, lower eddy current losses and a lighter machine are also achieved.

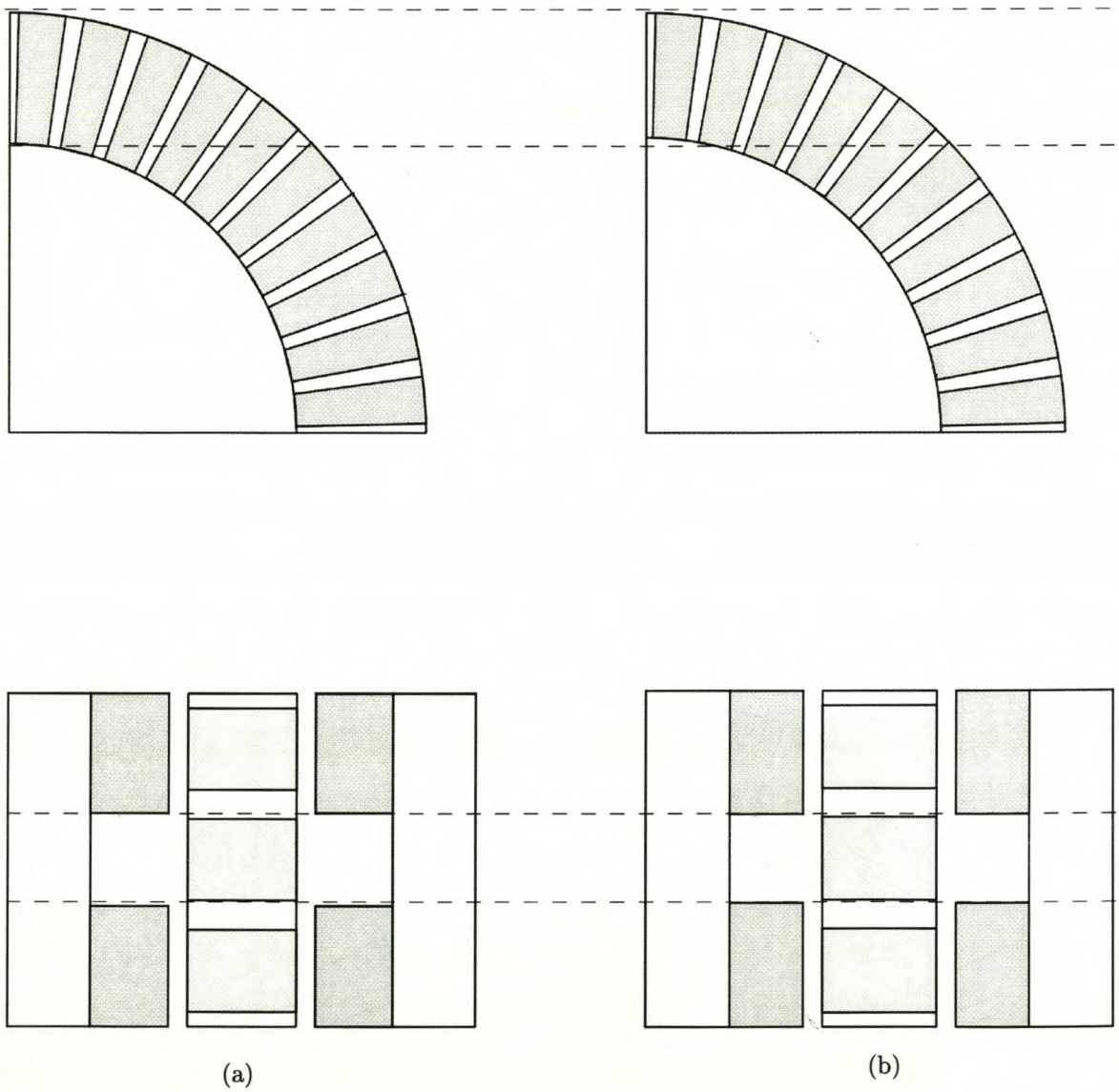

Figure 6.6: Geometric layout of the optimised AFPM machine structures (a) optimised design for maximum efficiency (b) optimised design for minimal PM mass.

Table 6.2: Comparison of performance results of Powell and PBIL methods.

Objective functions ⇒	MAX[F($\vec{x}$)] ; $F(\vec{x}) = \eta\%$			MIN[F($\vec{x}$)] ; $F(\vec{x}) = W_m$		
Performance index	Constraint	Powell	PBIL	Constraint	Powell	PBIL
P_{out} (kW)	≥ 300	308	306.5	≥ 300	300.2	294
J (A/mm^2)	≤ 11	10.19	10.55	≤ 11	10.52	10.31
$K_r = r_i/r_o$	-	0.681	0.688	-	0.694	0.703
V_{ph} (rms) (V)	≤ 330	334.98	316.5	≤ 330	317.5	314.7
I_{ph} (rms) (A)	-	312.64	323.5	-	321	312.3
P_{eddy} (kW)	-	3.17	2.377	-	2.32	2.3
Power factor	-	0.997	0.998	-	0.997	0.997
Efficiency $\eta\%$	-	96.97	97.2	-	97.16	97.11
Mass of PM (kg)	≤ 30	29.84	25.57	-	24.2	23.2
Total active mass (kg)	-	82	80.2	-	78.3	77.1
P_{out}/active mass (kW/kg)	-	3.76	3.82	-	3.83	3.81
Power density (10^6W/m^3)	-	10.85	8.96	-	8.86	8.599

Based on the results investigated above, it can be said that both Powell's method and the PBIL algorithm are suitable tools for the design optimisation of the AFPM machine. Powell's method is an efficient method, though it may occasionally fail to go further than the local optimum. Using the PBIL algorithm implies a high probability in finding the global optimum. The only disadvantage is that it is very time consuming. However, it can be argued that, with the high computing power available, the PBIL algorithms may be a good choice for electrical machine design. The most important properties of PBIL algorithms are summarised as follows:

- they work with a coded string representing the parameters instead of using parameters themselves
- they use the objective function itself and not the derivatives
- they search for the optimum based on the stochastic principle and therefore have a high probability of locating the global optimum.

Chapter 7

Experimental Machines

In this Chapter, the experimental machines that have been studied in this thesis are briefly described. The FE mechanical strength analysis for the final design of a 300 kW AFPM generator is carried out and results are discussed. The production techniques involved in the construction of the ironless stator AFPM machine are described.

7.1 Details of experimental machines

Two ironless stator AFPM machines [64, 67] previously designed and constructed in the electrical machines laboratory of the University of Stellenbosch have been tested to investigate different design aspects of AFPM machines covered in this study. Figures 7.1 and 7.2 are the photographs of the two experimental machines, i.e. the brushless d.c. AFPM generator (AFPM-I) used in the thermofluid analysis (Chapter 5) and the double-stage sinewave AFPM generator (AFPM-II) used in the eddy losses studies (Chapter 4).

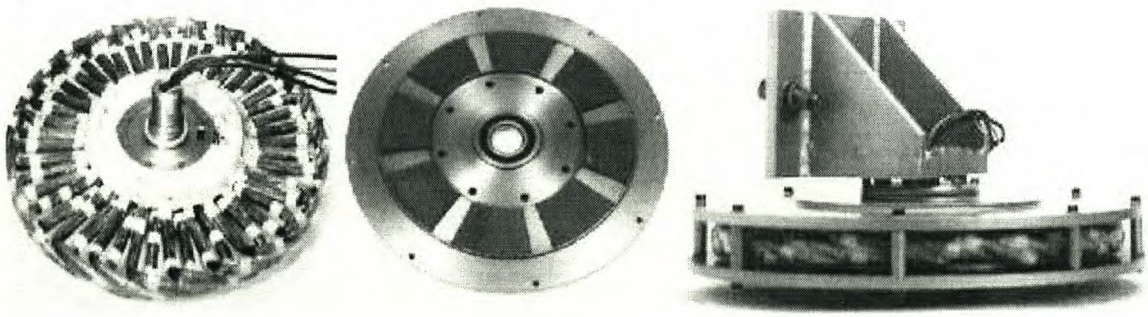

(a) (b) (c)

Figure 7.1: The brushless d.c. AFPM-I machine: (a) stator, (b) rotor disc, and (c) the assembled machine.

In the experimental AFPM-I (Fig. 7.1), the ironless stator is stationary and two end discs are

rotating. The PM segments are surface-amounted on the two rotor discs to provide the axial field. The rotor discs are connected at outer periphery by a number of pillars. The stator is mounted on the stationary hollow shaft, through which the connection of winding terminals to the outside is made.

The experimental AFPM-II (Fig. 7.2) is a double-stage AFPM machine consisting of two ironless stationary stators and three rotating rotor discs. The two stators are mounted on the external frames. They are connected in parallel along the stator's outer periphery to the bus-bars mounted on the one side of the machine casing.

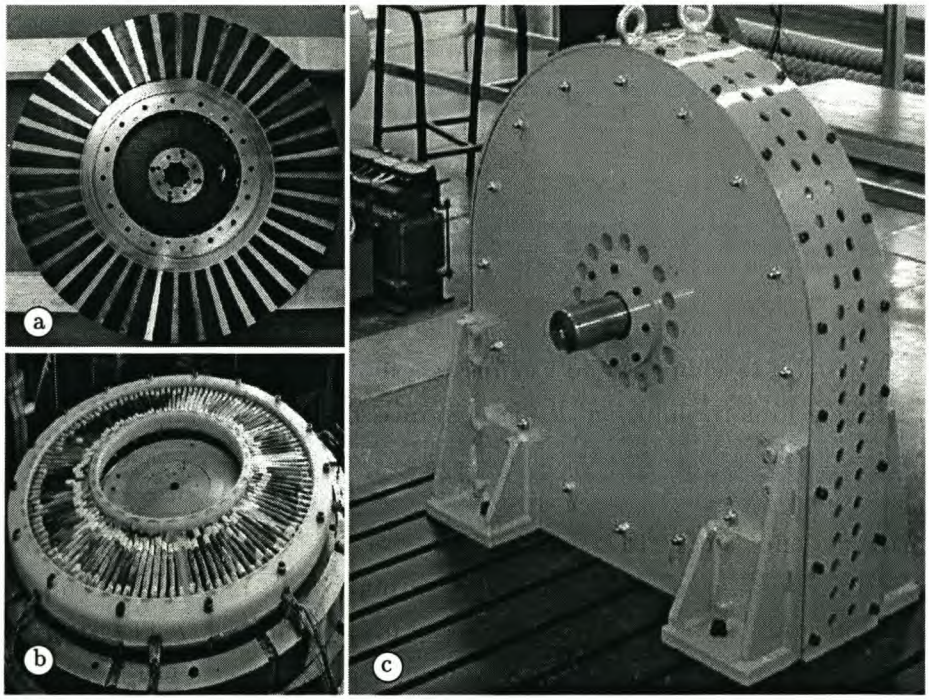

Figure 7.2: The double-stage synchronous AFPM-II machine: (a) rotor disc with surface mounted PM segments, (b) ironless stator, and (c) the assembled machine.

To verify the optimisation design of the AFPM machine, an AFPM machine optimised for minimal PM material (Chapter 6) has been built. Fig. 7.3 shows the constructed 300 kW air-cooled ironless stator AFPM machine (AFPM-III). The single stator is mounted on one side of the external frame. To balance out the strong centrifugal forces exerting on the PMs on the high speed spinning discs, provision has been made on the rotor inner surface to secure each PM in its position.

The stator winding consists of a number of single-layer trapezoidal-shape coils, which have the advantage of being easy to make and have relatively short overhangs. The assembly of

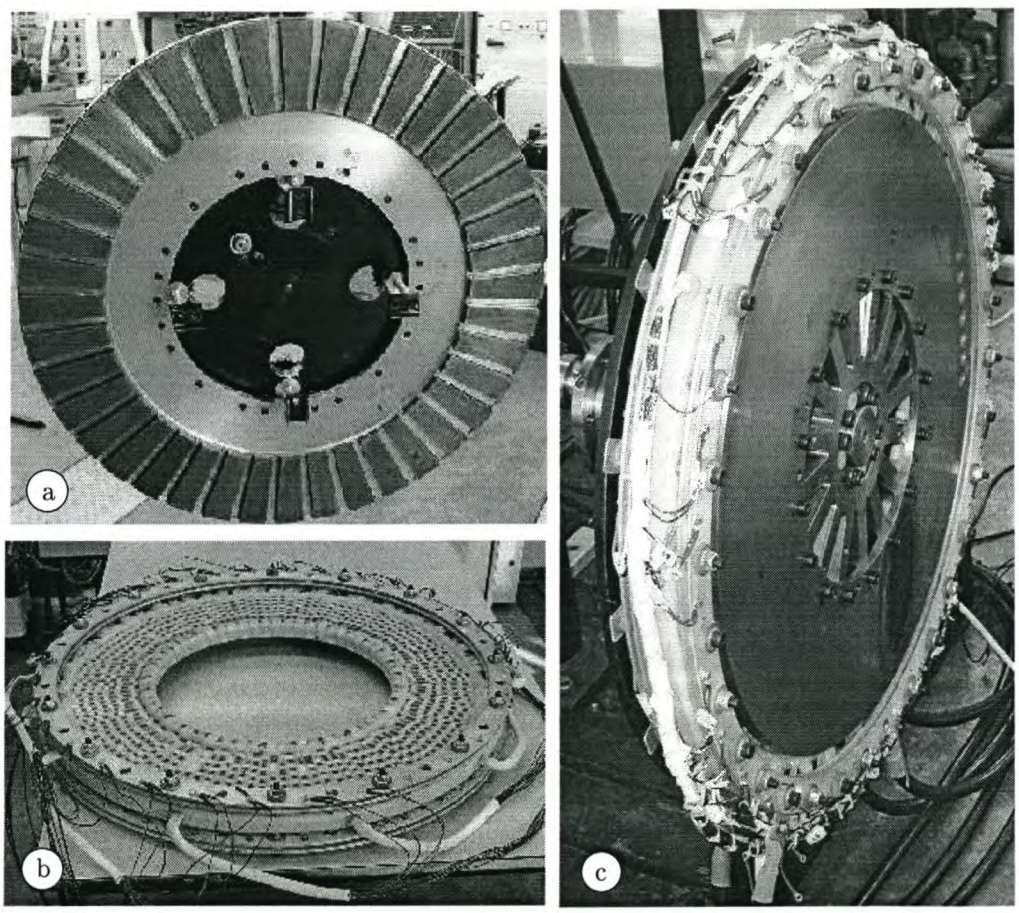

Figure 7.3: The designed single-stage synchronous AFPM-III machine: (a) rotor disc with surface mounted PM segments, (b) ironless stator with busbars, and (c) the assembled machine.

the stator is made possible by bending the ends of the coils by a certain angle so that the active conductors lie evenly in the same plane and the end windings nest closely together. The windings are held together in position by using a composite material of epoxy resin and hardener. The engineering drawing of the AFPM-III machine is shown in Fig. 7.4.

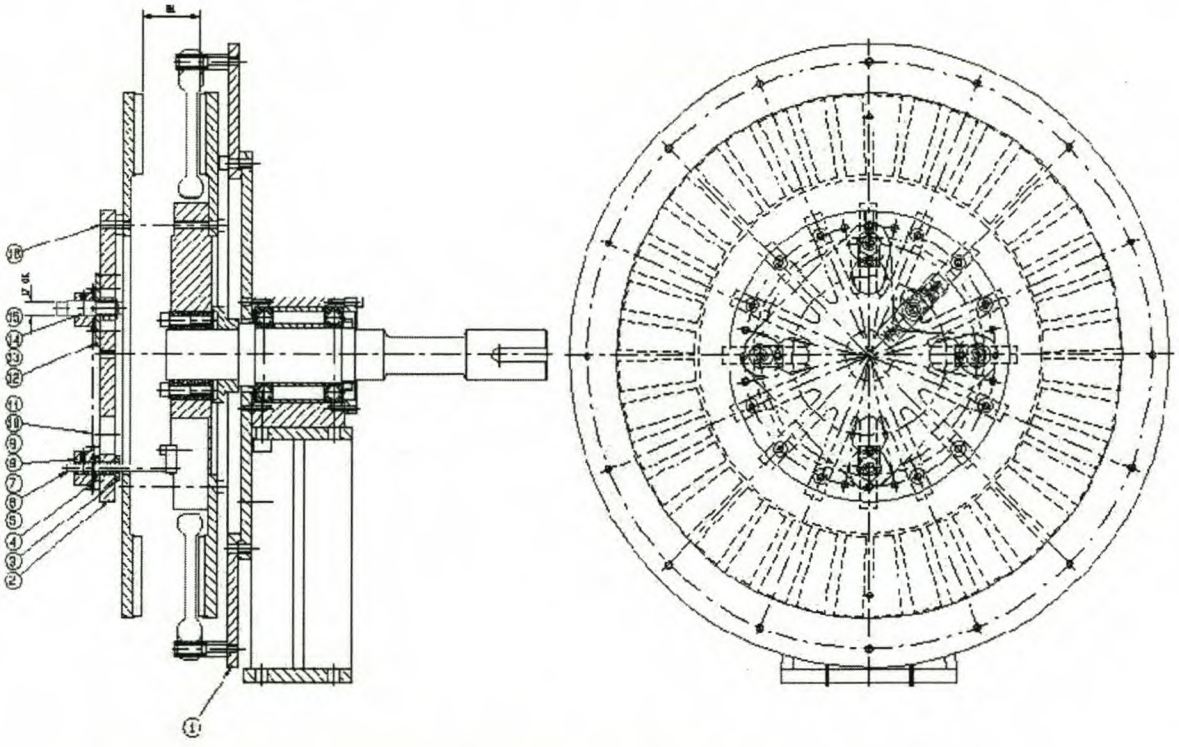

Figure 7.4: Scale drawing of the designed (300kW) AFPM-III machine.

One common feature of the three AFPM machines described here is that they all have ironless stators. The key data of the experimental machines are given in Table 7.1.

7.2 Mechanical design features

In the mechanical design of an AFPM machine, the method of obtaining a uniform airgap between the rotor disc and the stator is an important consideration. Therefore, the methods of fixing the rotor discs onto the shaft and the stator onto the stand (frame) are very important. Improper methods of fixing, or misalignment in the assembling of the stator and the rotor will cause vibration, noise and deteriorate in electrical performance.

With regard to cooling in an air-cooled AFPM machine, the entry losses of the air flow can be quite high if the machine-air-inlet is poorly designed. It is important to reduce these losses without weakening the mechanical structure for better cooling.

Table 7.1: Design data of experimental AFPM machines.

	AFPM-I	AFPM-II	AFPM-III
Power (kW)	11	300	300
Number of poles	8	40	40
Number of stage	1	2	1
Speed (rpm)	1500	2300	2300
Outer diameter (mm)	320	680	720
Diameter ratio	0.6225	0.579	0.6939
PM width/pole pitch	0.8	0.67	0.72
Airgap clearance (mm)	2×2.5	2×1	2×2.75
Total active mass (kg)	21.7	85.4	78.31
Power/active mass (kW/kg)	0.5	3.6	3.83
Efficiency	86.5%	96%	97.16%

To summarise, attention should be paid to the following aspects of mechanical design:

Shaft: The load torque, the critical speed and the vibration should be taken into account in the shaft design.

Rotor: (i) The deflection of the rotor disc due to the strong magnetic attraction force, (ii) the means of mounting and securing the magnets on the rotor discs to counteract the strong centrifugal force due to the high speed rotation, and (iii) the balancing of the rotor discs.

Stator: (i) The strength and rigidity of the resin reinforced stator and frame, and (ii) the positioning and spacing of the coils to ensure perfect symmetry.

Cooling: The air inlet and air flow paths through the machine should be carefully designed in order to ensure a better mass flow rate and therefore better cooling.

Assembly: An effective mechanism to facilitate the assembling and dismantling of the machine for maintenance.

7.3 Mechanical strength analysis

The deflection of the rotor discs due to the strong magnetic pull may have the following undesirable effects on an AFPM machine:

- closing the running clearance between the rotor disc and the stator.

- loosing or breaking permanent magnets.
- reducing air-flow discharging area thus deteriorating the cooling capacity.
- non-uniform airgap causing a drift in electrical performance from the optimum.

The rotor discs account for roughly 50% of the total active mass of an AFPM machine. Hence, the optimal design of the rotor discs is of great importance to realise a design of high power/mass ratio. All these aspects make the mechanical stress analysis of the rotor disc a necessity.

7.3.1 Attraction force between rotor discs

The attraction force between two parallel rotor discs can be calculated by using the *virtual work* method, i.e.

$$F = -\frac{\Delta W}{\Delta x} = -\frac{W_2 - W_1}{x_2 - x_1} \tag{7.1}$$

where W is the total magnetic stored energy in the machine and Δx is the small variation of the airgap length. The accurate prediction of the attraction force is a prerequisite for the mechanical stress analysis in the following section.

7.3.2 Mechanical stress analysis of rotor disc

The structure of the rotor discs of the designed 300 kW AFPM machine was modelled with the aid of an FEM program. The aim was to find a suitable thickness of the rotor disc, which satisfies the critical strength requirements of the rotor disc with a low iron content. The two opposing rotor discs are kept apart by a hub-like structure, which was designed to improve the air flow and reduce the total mass. In the FE simulations, it was assumed that the forces/moments on the hub structure were balanced out resulting in negligible deflection thereof. The maximum tolerable deflection of the rotor disc was set to be 0.3 mm so that the PMs would not suffer any excessive forces that have the potential to break the magnets or peel them off from the steel disc.

As the magnetic attraction force exert on each outer disc structure is the same, it was sufficient to model only one disc. Due to the cyclical symmetry of the disc structure, only one sixteenth of the rotor disc was analysed using 4-node shell-elements, with symmetrical boundary conditions applied (Fig. 7.5). The axial magnetic attraction force was calculated as 14.7 kN and applied in the form of a constant 69.8 kPa pressure load over the total area that the PMs occupy. The stiffness provided by the magnets was not included to keep the design on the conservative side. As the rotor discs are mounted on the centre support hub, additional boundary constraints were defined so that there is no axial displacement in the vicinity of the

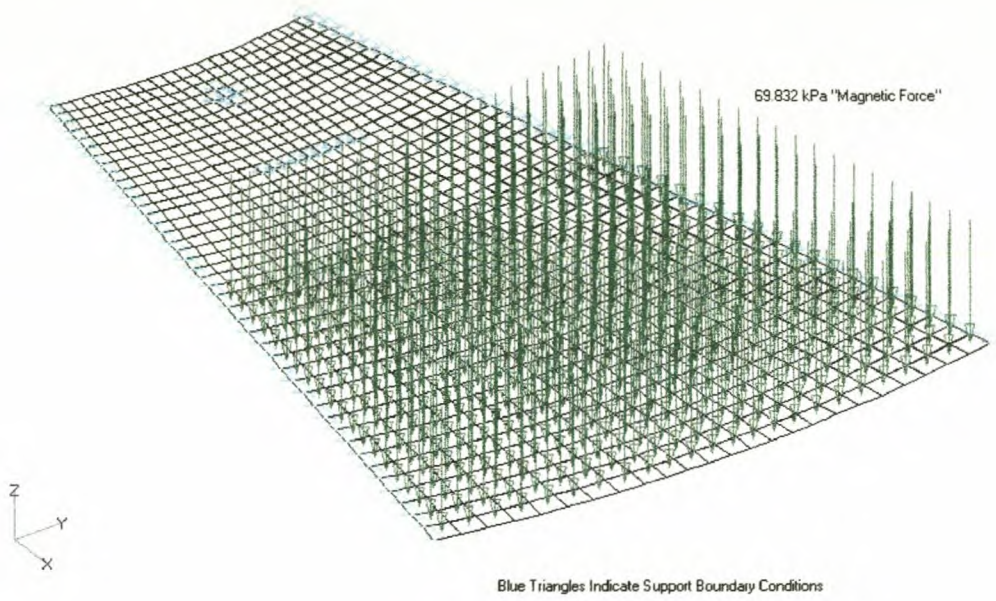

Figure 7.5: Finite Element model for analysing the mechanical stress of a rotor disc.

mounting bolts and contact area.

The linear FE static analysis was performed for a number of options. Based on the analysis the rotor disc thickness was chosen as 17 mm with a maximum deflection of 0.145 mm. Fig. 7.6 shows the deflection (blown-up) and the Von Mises stress distribution of the laboratory prototype 17 mm disc. The maximum stress of 35.6 MPa is much lower than the typical yield strength of mild steel that is in the region of 300 MPa. Previous studies [68] show that the bending of the rotor disc decreases towards its outer periphery. The rotor disc may be machined in such a way that the disc becomes thinner towards the outer periphery. As shown in Table 7.2, the tapered disc uses approximately 10% less iron than the straight disc. The maximum deflection increases by only 0.021 mm with the tapered disc, which is negligible. This can effectively save the active mass of the machine without compromising the mechanical strength.

If manufacturing costs are taken into account for small production volumes, it is better to use a steel disc with uniform thickness. Of course, using a uniform disc means a heavier rotor disc. It can, however, be argued that the extra machining work needed for producing a tapered rotor disc may be more expensive than the material saved. As long as the added mass can

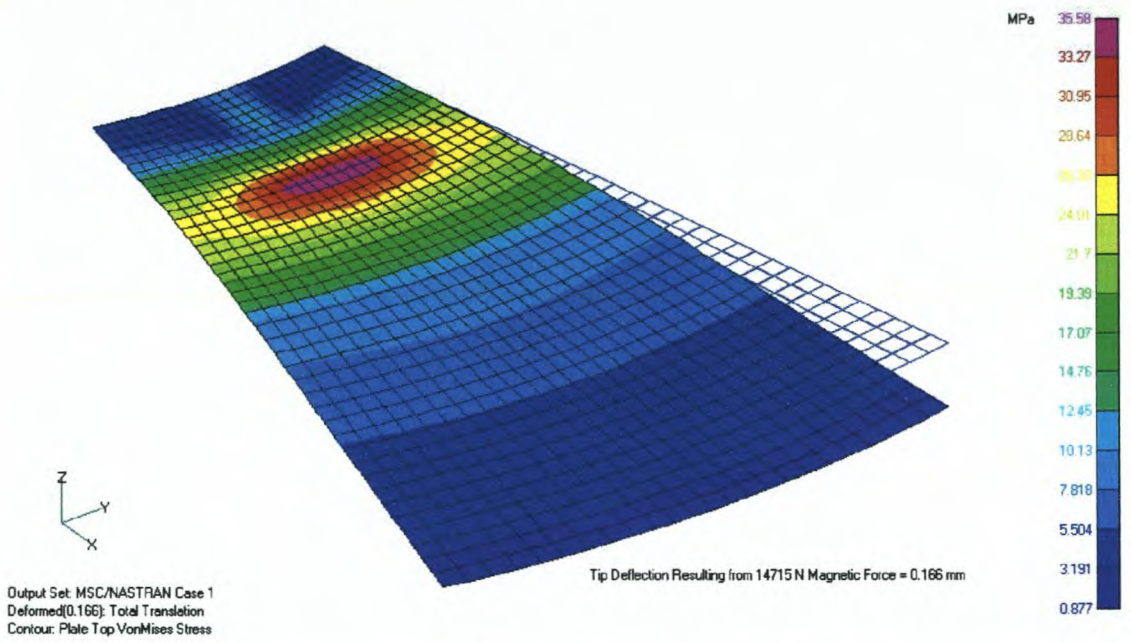

Figure 7.6: Deflection (blown-up) and Von Mises Stress distribution of a rotor disc.

be tolerated, this option is viable for small production volumes and for laboratory prototypes.

From an FE modelling perspective, the shell element is not the best choice for modelling a relatively thick plate. However, it has been shown in previous modelling [68] that FE models using both axial-symmetric-elements and shell-elements give very close results.

Table 7.2: Comparison of different designs of rotor disc.

Parameter	Straight disc	Tapered disc
Weight, kg	39.184	31.296
Max. Deflection, mm	0.145	0.166
Max. Von Mises stress, Mpa	35.6	33.4

7.4 Axial force on the stator

As a result of the interaction of alternating currents flowing in conductors and the tangential component of the magnetic field, there is an axial magnetic force f_y on each half of the coil as shown in Fig. 7.7. When the stator is located in the middle of the airgap, the forces on each side of the stator should cancel each other. The instantaneous axial force on the stator

can be simulated by using the FE time-step model described in Chapter 3.

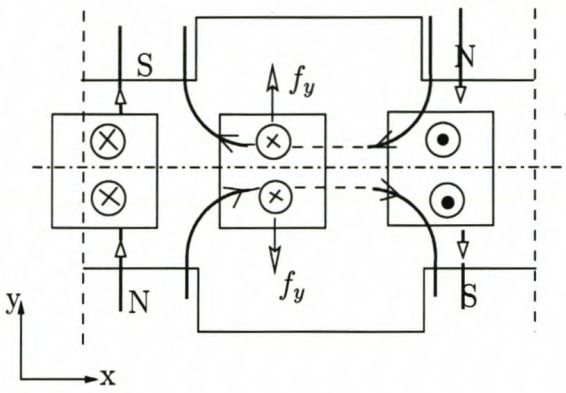

Figure 7.7: Schematic diagram showing the axial force exerted on stator.

Assuming the stator of the AFPM III machine is 1 mm off centre, the simulated axial forces on each side of the stator (f_1 and f_2) as shown in Fig. 7.8 will not be the same, resulting in an unbalanced force on the stator Δ_f. This unbalanced force may cause extra vibration and thus have an adverse effect on the mechanical strength of the epoxy reinforced stator.

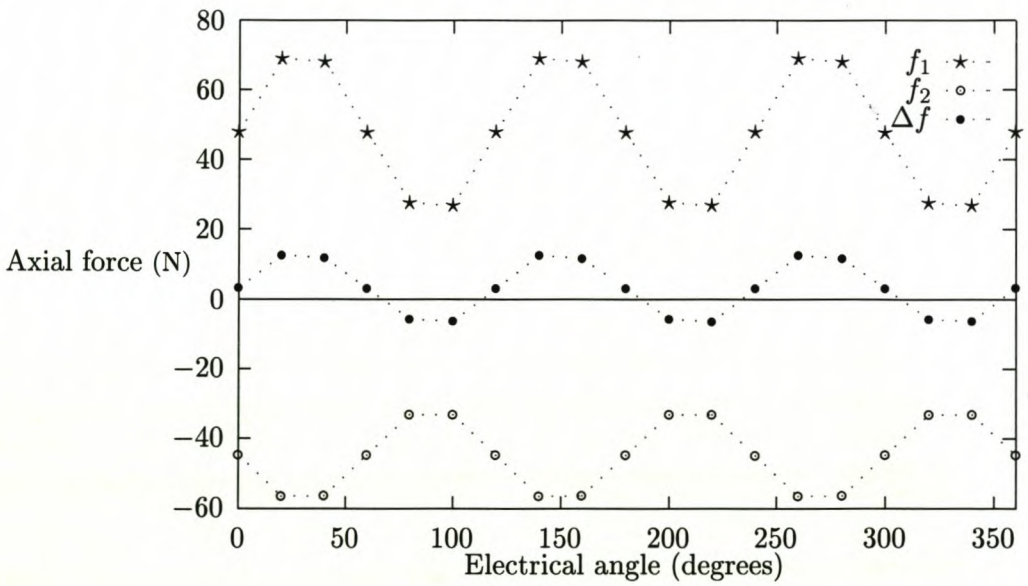

Figure 7.8: Unbalanced axial force exerted on the stator.

7.5 Thermal expansion of the epoxy encapsulated stator

Due to the excessive heat generated in the stator winding and the resultant thermal expansion, an epoxy encapsulated stator is subject to certain deformation. When the deformation is significant, it may cause physical contact between the stator and the magnets resulting in substantial damage to the stator and the magnets.

To access the severity of the thermal expansion of the stator, the following experiment was performed, in which the rated current (16 A) was conducted through a coil in the epoxy encapsulated stator. A thermal coupler and a roundout meter were used to measure the coil temperature and surface deformation respectively. Figure 7.9 shows the thermal expansion of the stator at different temperatures. It was found that the relationship between the stator deformation and its temperature is almost linear. On average the deflection of the stator surface is about 0.0056 mm per degree Celsius resulting in a 0.5 mm deflection at a temperature of 117^oC. This suggests that a large running clearance between the stator and the rotor be recommended.

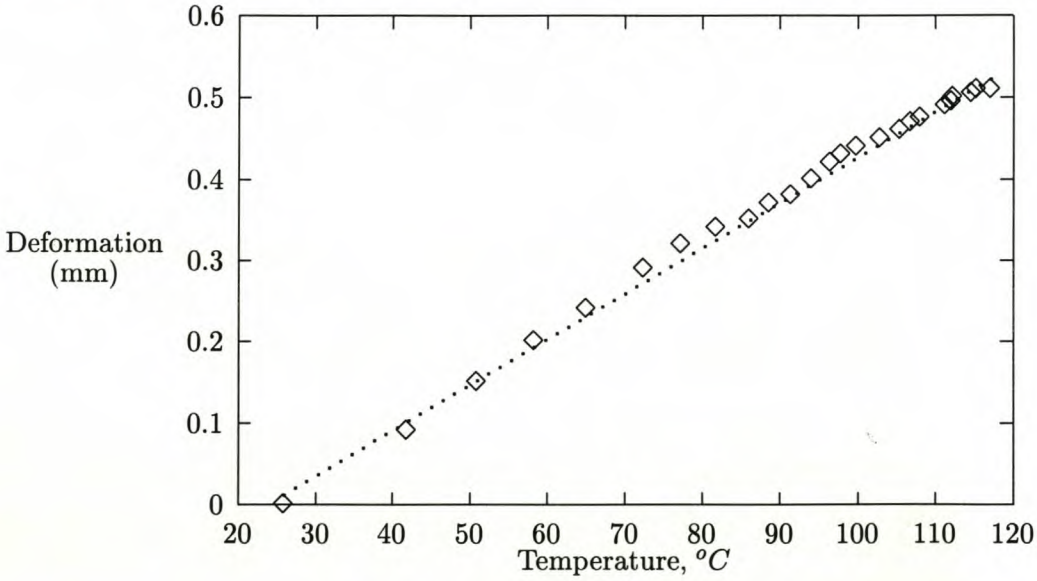

Figure 7.9: Thermal expansion of the stator for different temperatures.

7.6 Production techniques

Resulting from the practical mechanical design issues, summarised in the previous section, the following production techniques have been devised in the manufacturing process of a 300 kW AFPM machine prototype.

The principle of eliminating the eddy circulating currents in a stator coil comprised of parallel wires by means of wire-twisting has been described in Chapter 4. To carry out the twisting of wires and the making of a coil simultaneously, the ideal coil-winding system may be designed in such a way that it employs two d.c. motors, one for twisting and the other for feeding the wires onto the former. The speed of feeding wires is a fraction of that of twisting the wires.

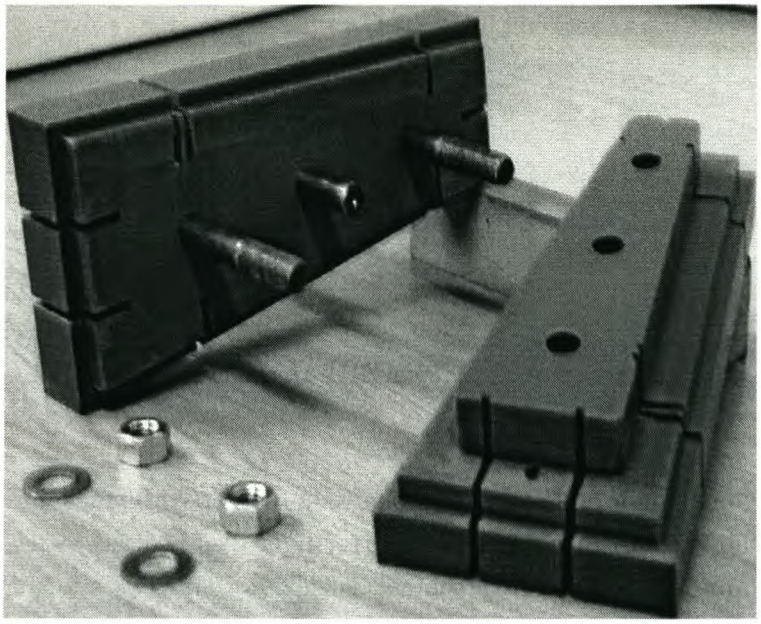

Figure 7.10: The former for winding the coil.

To design such a system requires a vast amount of time and is beyond the scope of this research. Instead, a rather simple system has been designed and used in this process. The wires were first twisted by using a small motor coupled with a counter and then manually wound on a former as shown in Fig. 7.10.

For an ironless stator with parallel coils, the coils should be placed and spaced in a consistent way so as to minimise possible circulating currents among the parallel coils. To realise this, an iron mould with guide slots was initially proposed (see Fig. 7.11).

With all the coils in position, the composite material, a mixture of epoxy and hardener, was then filled into the mould and cured in a heated oven. Because of the difficulty of releasing the cured stator from the slotted structure of the mould, each spacing block that forms a guide slot was replaced by several removable pins of different sizes. This has proved to be a better approach since taking the stator out of the mould is easy after the pins have been removed. Fig. 7.12 shows the mould with the guide pins and all the coils placed in position.

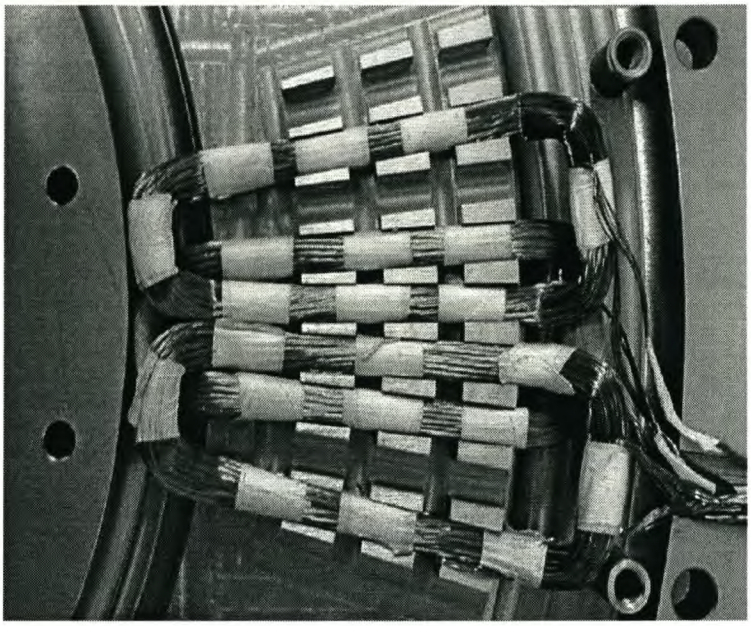

Figure 7.11: The mould with guide slots for positioning the coils.

To handle the strong attraction force between rotor discs and to simplify the assembly and dismantling process of the AFPM machine, an assembly mechanism was designed. It operates in such a way that as the shaft is rotated, the four synchronising gears turn at the same speed shifting the mounting disc up or down depending on the turning direction. When the rotor disc moves in towards the other disc, it provides a type of blocking mechanism to counteract the attraction force. A photograph of the assembly tool is shown in Fig. 7.13.

As described in Chapter 5, the AFPM machines investigated in this thesis operate as centrifugal fans from a fluid mechanics perspective. The air flow is drawn into the machine through the air inlets that are located in the vicinity of the shaft. The thermofluid analysis done on machine AFPM-I reveals that the energy losses of the air flow associated with the air inlets account for nearly 22% of the total air flow losses. It is therefore important to achieve a reasonable air inlet design by taking into account sound fluid mechanics practice. In the new design of the 300 kW AFPM machine (AFPM-III), the hub part serves as both air intake and supporting structure for the rotor discs (see Fig. 7.14). It certainly allows more access to air at the intakes and has a clearly defined flow path. Furthermore, it also acts as a centrifugal fan increasing the pressure gradient through the AFPM machine.

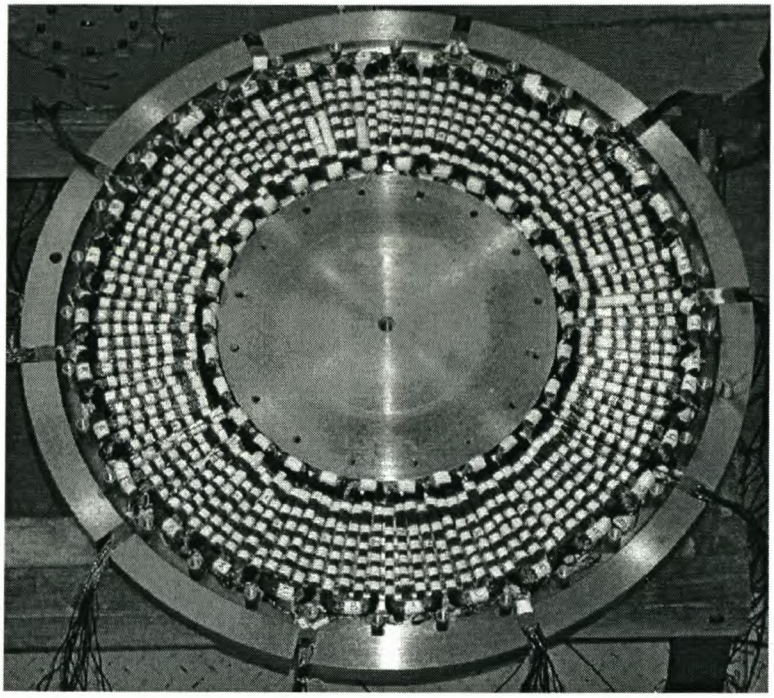

Figure 7.12: The mould with all the coils in position.

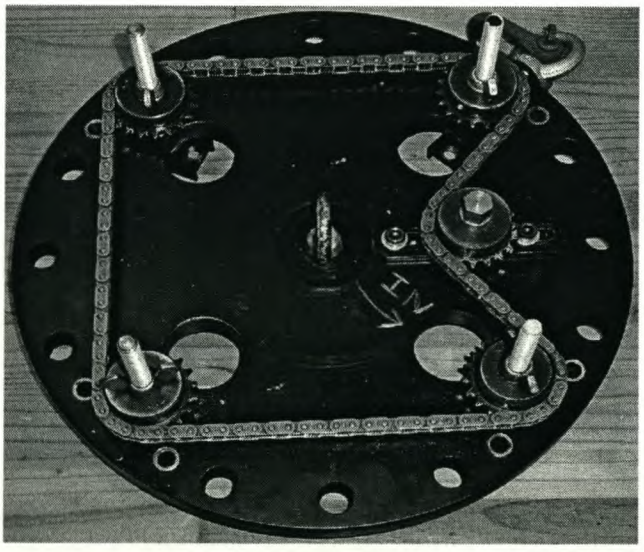

Figure 7.13: The tool for assembling and dismantling of AFPM machine.

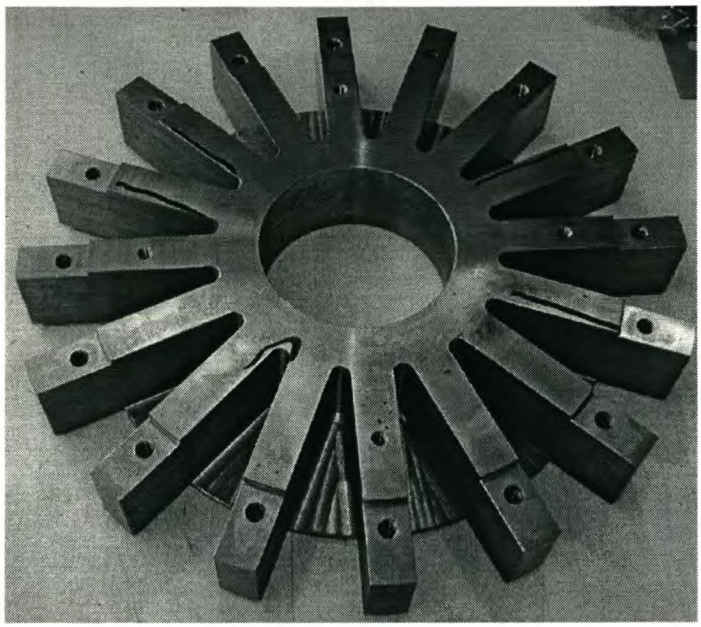

Figure 7.14: The hub-part of the designed (300 kW) AFPM machine.

7.7 Experimental equipment

The experimental equipments used in the experimental investigations are briefly described as follows:

Torque: Torque was measured by a torque sensor mounted between the prime mover and the generator.

Fluid Flow: A specially designed intake tube system and a manometer were used to measure the static air pressure (as shown in Fig. 7.15).

Airgap Field: The airgap flux density distribution was measured by built-in testing coils

Temperature: The winding temperature was measured by thermocouple sensors, while the outer surface temperature was measured by a digital infrared thermometer

Electric Load: A water load system comprised of a water tank, heating elements, water pipes, and a cooling tower was built for the load test of the designed 300 kW AFPM generator (see Appendix E for photographs).

Drive Motors: the prime movers used in the tests were a 10 kW d.c. machine (for eddy current measurement) and a 600 kW induction machine (see Appendix E for photograph) for full power test.

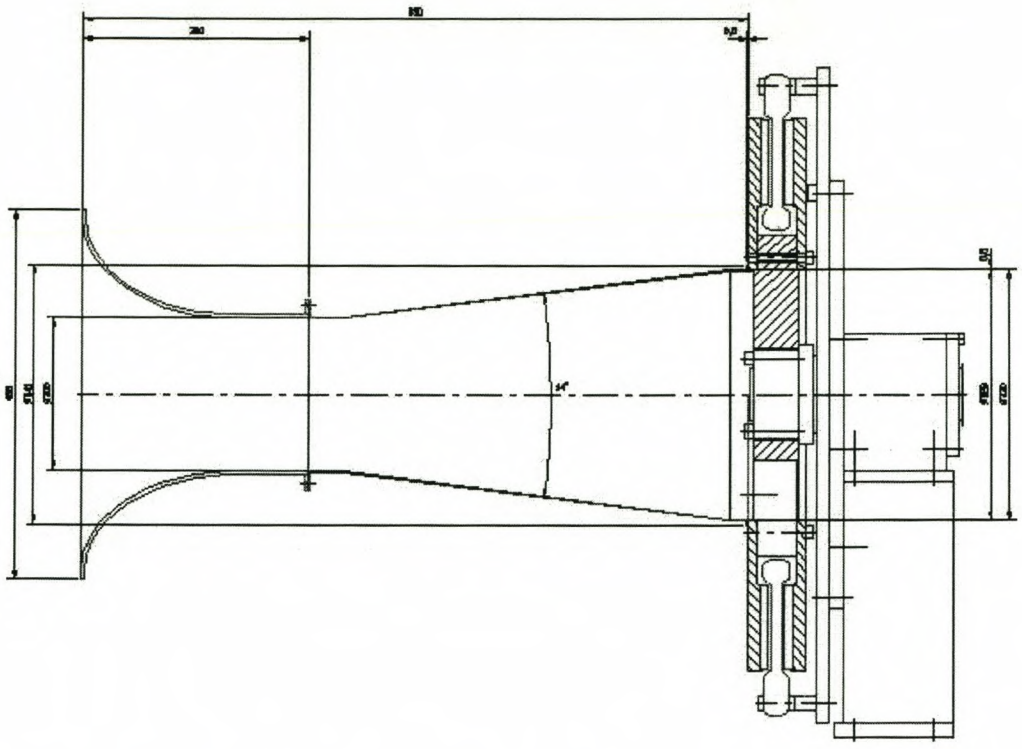

Figure 7.15: The intake tube system used in the flow measurement.

Chapter 8

Performance of the Prototype AFPM Machine

The performance tests on the prototype AFPM machine were carried out in the laboratory and were analysed. The aim of this chapter is to show the practical steady state behaviour of the AFPM machine and to verify the models (*thermofluid*, *multi-slice/multi-layer eddy loss*, *time-stepped models*) described in this thesis. Essentially, the performance of an AFPM machine is similar to that of a conventional machine, however the AFPM machine also has its own special features which will be discussed in the following sections.

8.1 Machine data and test rig

The performance tests of the prototype AFPM machine focused on its generation mode, i.e. the AFPM machine was operated as a generator driven by a variable speed induction machine drive. A re-configurable water-cooled bank of resistors was used as a load. The water cooling system consists of a water tank, pipe system and a cooling tower of 400 kW capacity. The design details for the AFPM machine under test are given in Table 8.1. A schematic diagram of the test rig is shown in Fig. 8.1.

8.2 Mechanical loss measurement

Energy losses found in electrical machines are mainly composed of mechanical and electromagnetic losses. Due to the large attraction force between the rotor and stator of the AFPM machine, bearing loss may contribute significantly to the total mechanical loss within the machine depending on the mechanical design [28]. The specific AFPM machine upon which this study focuses is constructed in such a way that the rotors are directly mounted on the shaft without using bearings. The bearing loss within the machine is thus absent and the mechanical loss of the machine is only due to the windage loss.

In order to facilitate testing of the experimental machine, the AFPM machine was mounted on a stand, in which two bearings were utilised. Since these bearing are not necessarily a part of the experimental machine, it is justifiable to subtract bearing losses from the measured mechanical loss. The test setup for measuring the mechanical losses is depicted in Fig. 8.2, where the experimental AFPM machine is driven by a small d.c. machine. To eliminate any eddy current loss while retaining the same air flow condition, a dummy stator, fabricated by moulding the mixture of epoxy and fabric glass into exactly the same physical dimension as the real stator, is placed in the AFPM machine. The mechanical loss is calculated from speed and torque measurements.

The measured results are shown in Fig. 8.3, in which curves 1 and 2 represent the mechanical losses of the AFPM machine versus the speed with the machine air inlet open and closed respectively. When the machine air inlet is closed, the measured mechanical loss comprises bearing and windage losses. The bearing loss is usually more predominant than the wind friction loss component [28].

Table 8.1: Design data for the AFPM generator.

Rated line voltage	550 V (Star connection)
Rated phase current	320 A
Number of poles	40
Number of stages	1
Rated maximum speed	2300 rpm
Axial length	72 mm
Outer diameter	720 mm
Inner diameter	500 mm
Pole arc/pole pitch	0.72
Air-gap clearance	2.75 mm
Number of coils	60
Type of winding	Single layer trapezoidal
Turns per coil	51
Connection	20 parallel circuits per phase
Conductor	12 parallel conductors per coil (twisted)
Conductor size	0.42 mm
Resistance per phase	0.0133 Ω

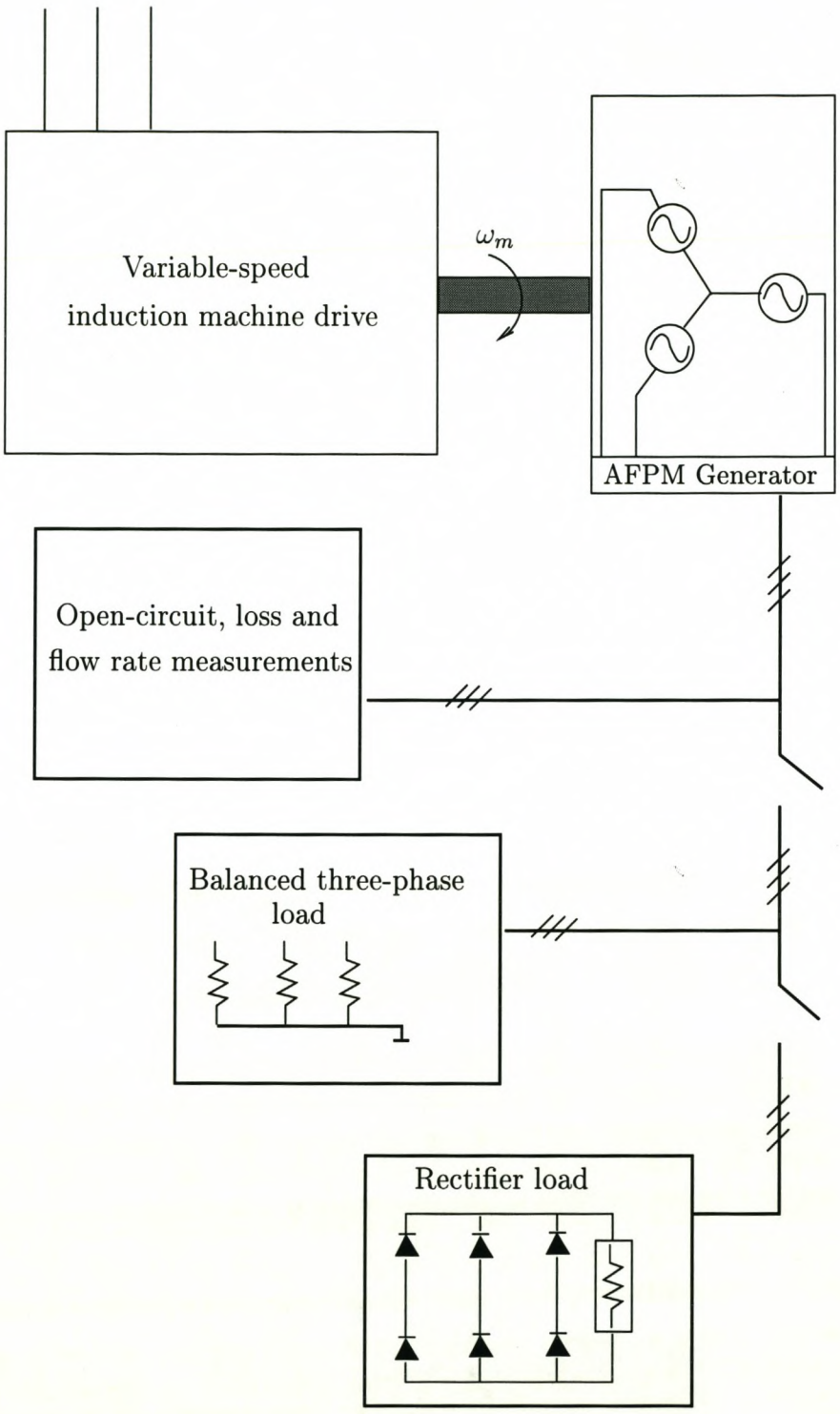

Figure 8.1: A schematic diagram of the re-configurable test-rig.

The difference between these two curves serves as a good indication of the amount of power lost in moving the air through the AFPM machine. As described in Chapter 5, losses occurred at several stages of the air passage. It has been found that the highest energy loss occurred at the machine air intake, which implies that the optimum design of the air intake hub is of great importance to minimise the entry losses without materially compromising air flow rate.

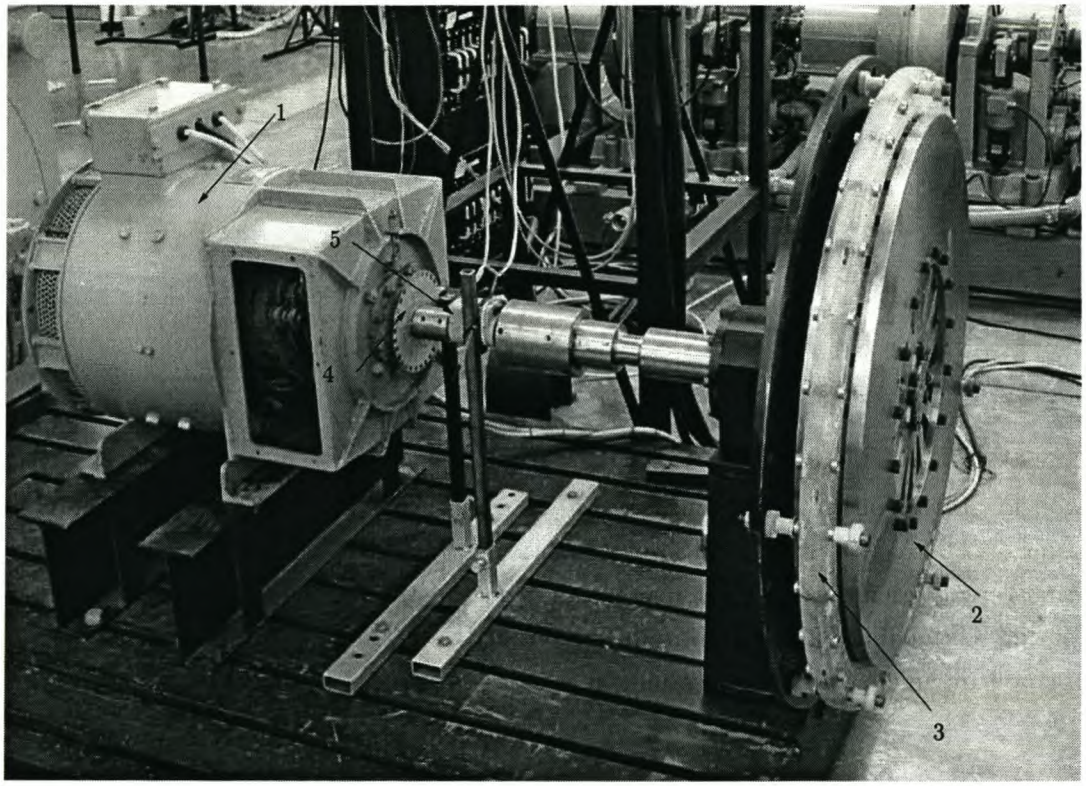

Figure 8.2: The experimental set-up for mechanical loss measurements, where 1 – d.c. machine, 2 – rotor disc of the AFPM machine, 3 – dummy stator, 4 – speed measurement, and 5 – torque sensor.

8.3 Eddy current loss measurement

The eddy current losses in an AFPM machine are in the form of resistance limited eddy loss and eddy circulating current loss as discussed in Chapter 4. The latter also comprises circulating currents between the parallel wires and circulating current between the parallel phase windings. All of these losses are experimentally determined and compared with the calculated results where applicable.

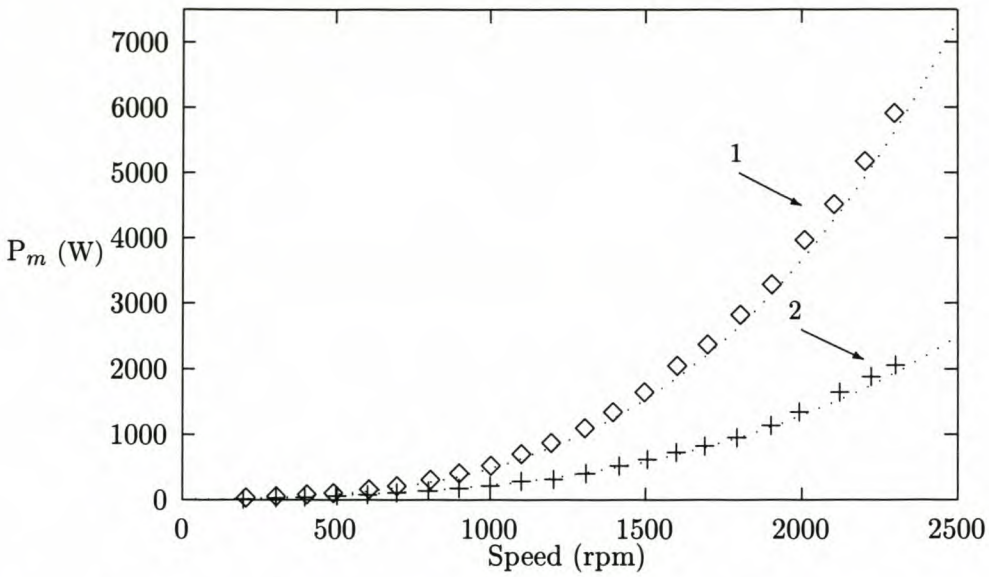

Figure 8.3: Measured mechanical losses versus rotating speeds for different flow conditions: 1 – when air intake is open, 2 – when air intake is closed.

8.3.1 Circulating eddy loss measurement

As shown in Table 8.1, each coil of the AFPM machine consists of 51 turns of twisted parallel conductors. The circulating current between parallel conductors is measured by a current probe through which the data is logged onto a storage oscilloscope. It can be seen in Fig. 8.4 that the circulating current between parallel wires is generally negligible. This confirms that the circulating current between parallel wires can be effectively minimised by simply twisting/transposing the parallel wires.

However, the circulating currents between parallel connected phase coils cannot be easily removed even if great attention is paid to ensure a symmetrical placement of the coils. As shown in Fig. 8.5, the circulating currents between parallel connected phase coils are quite significant even at low speeds.

When the speed rises, the amplitudes of the circulating currents do not change much. This is reasonable since the winding impedance $X_l = 2\pi f L$ increases as the phase voltage increases resulting in a fairly constant current. Assuming that the RMS phase circulating current is about 2 Amperes (12.5% rated current), the additional loss introduced is estimated to be 64 Watts. For the ironless stator AFPM machine with parallel connected phase coils, this problem is almost inherent due to the relatively low phase inductance and may not be easily solved. However, this is not a big disadvantage if one considers the absence of iron loss in an

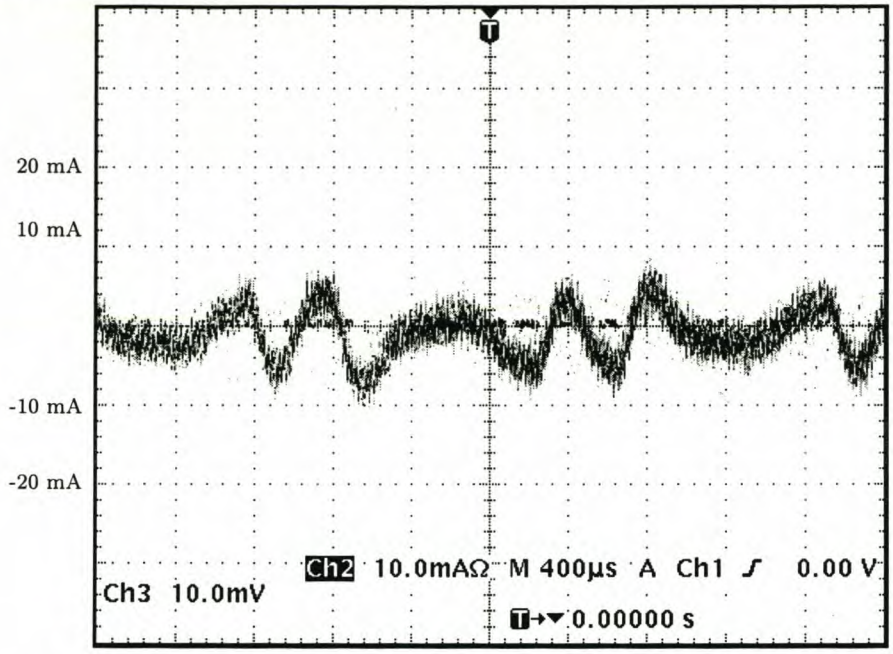

Figure 8.4: Measured circulating currents between conductors of a coil at no-load.

ironless stator. Of interest is that the circulating currents between parallel connected phase coils are significantly reduced as soon as the AFPM machine is connected to the load [67].

8.3.2 Resistance limited eddy loss measurement

The resistance limited eddy loss is measured according to the same procedure as described in Chapter 4. To avoid the eddy circulating current loss in the measurement, the parallel coils of each phase were disconnected. Fig. 8.6 compares the measured and predicted eddy current losses. The calculated eddy loss agrees very well with the measurements. This implies that the standard eddy loss formulation enhanced by the multi-slice and multi-layer FE field model can predict eddy current loss in an AFPM machine accurately. It can also be seen that the eddy current loss accounts for a significant portion of the total no-load loss of the AFPM machine.

8.4 Open circuit airgap flux and phase EMF

The shape of the open-circuit airgap flux density waveform serves as a valuable means to verify that the field models of the AFPM machine proposed in previous Chapters are viable. The airgap flux density (axial component) waveform was measured with a concentrated test coil that was wound using 10 turns of 0.125 mm wire.

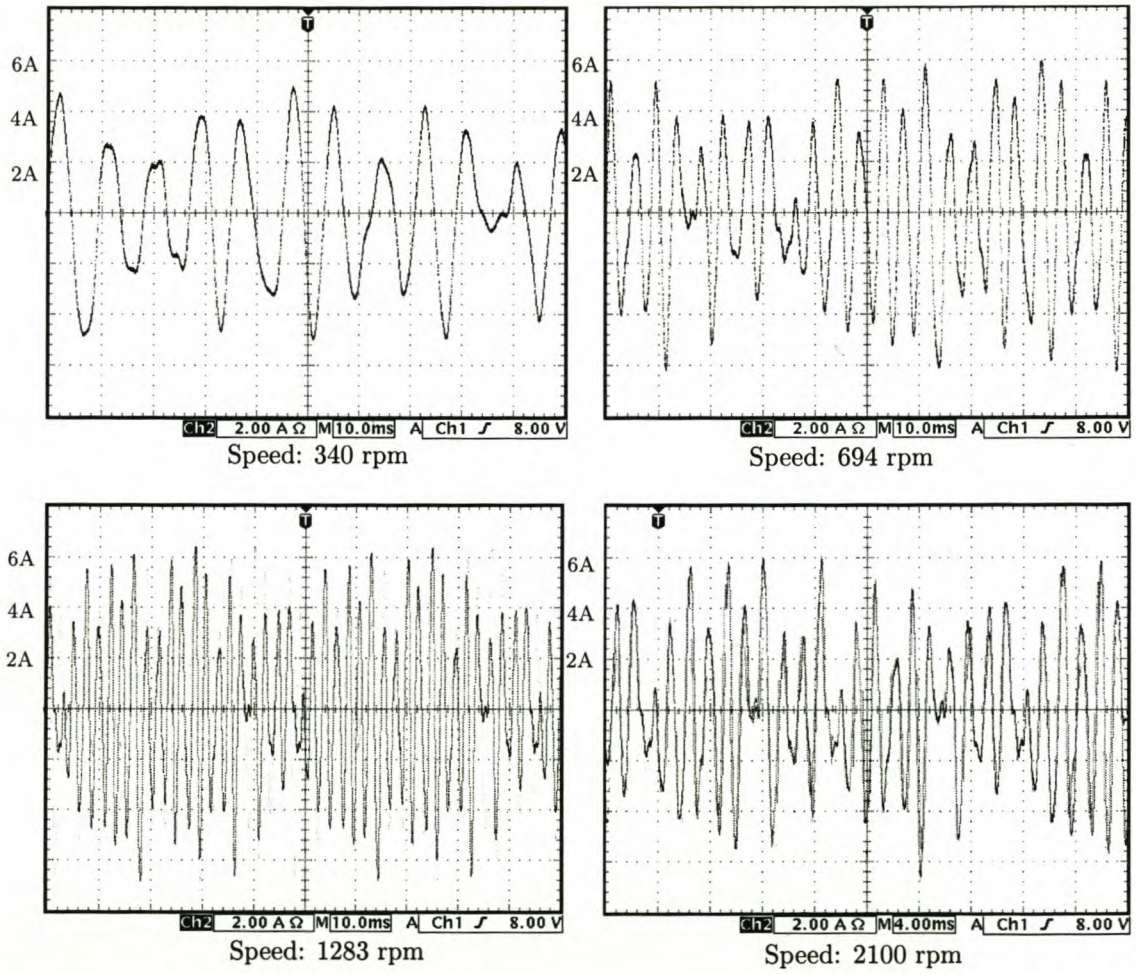

Figure 8.5: Measured circulating currents between parallel connected coils of a phase at no-load.

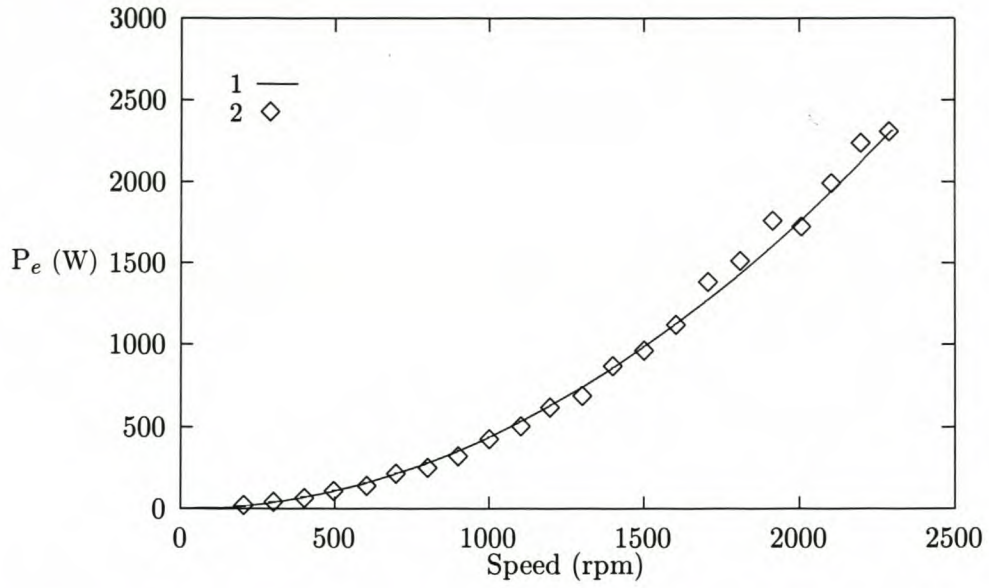

Figure 8.6: Eddy current loss versus rotating speed, where 1 – calculated eddy loss by using the multi-slice and multi-layer FE model, and 2 – measured eddy loss.

The test coil has dimensions corresponding with one pole pitch of the AFPM machine and was fixed on the surface of a stator coil. The induced voltage in the test coil for zero stator current at a specific speed was measured and converted into flux density value according to the relation given in [64]. To ensure an exact comparison the calculated field values were also extracted along a contour on the coil surface. The predicted and measured field density waveforms, shown in Fig. 8.7, are in close agreement. A Fourier transform of both graphs indicates a difference in the 5^{th} order harmonic as shown in Fig. 8.8. This is possibly due to the imperfection in the test coil placement which also manifests itself in the asymmetry of the flux density waveform.

Fig. 8.9 shows both the measured and predicted no-load phase voltage at rated speed. It is clear that excellent agreement is obtained. In the calculation of the no-load phase voltage, the time-stepped FE model described in Chapter 3 was utilised. The agreement proves that the developed FE time-stepped model behaves well.

The constructed AFPM machine uses annular sector magnets and it was found that the computed phase voltages obtained by using the one-slice or the multi-slice FE model appear to be indistinguishable. Therefore, the FE simulation carried out for the AFPM machine was based mainly on the one-slice model. The multi-slice model is activated only when necessary (e.g. for eddy current loss calculation).

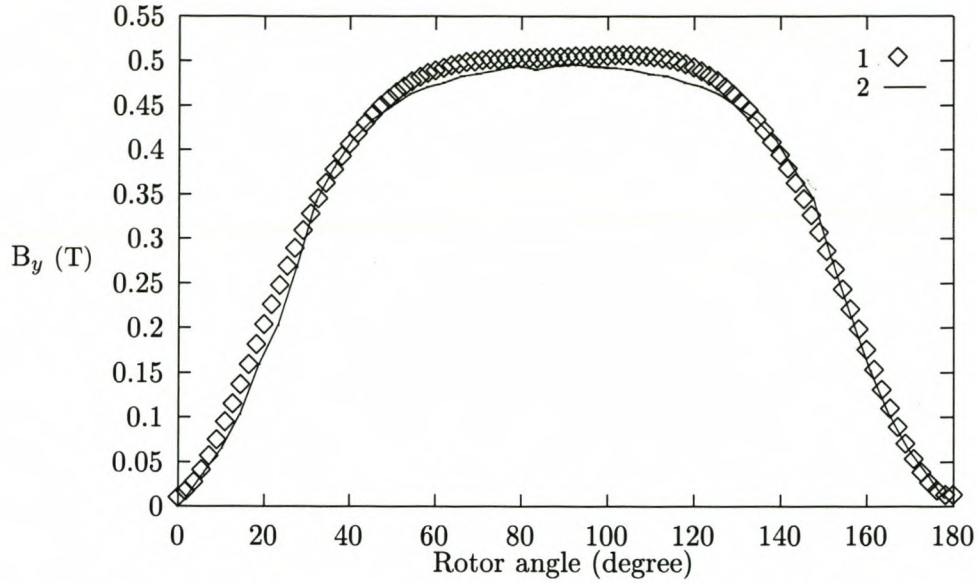

Figure 8.7: Flux density in the airgap, where 1 – measured airgap flux density, and 2 – calculated airgap flux density.

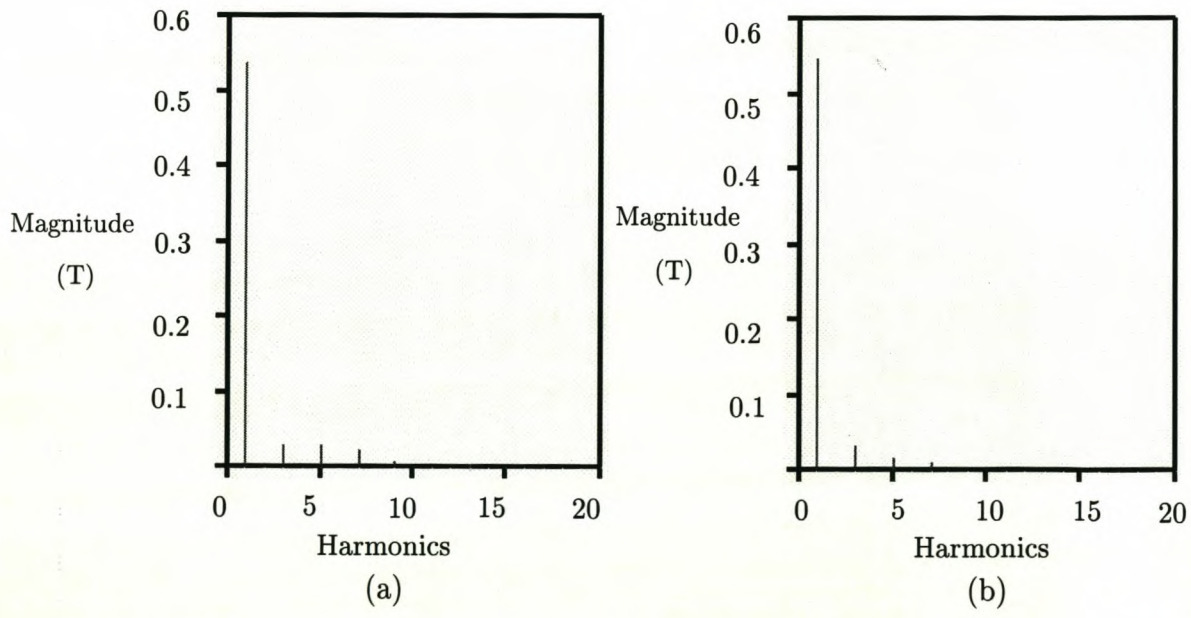

Figure 8.8: Space harmonic distribution of flux density in the airgap: where a – measured airgap flux density, and b – calculated airgap flux density.

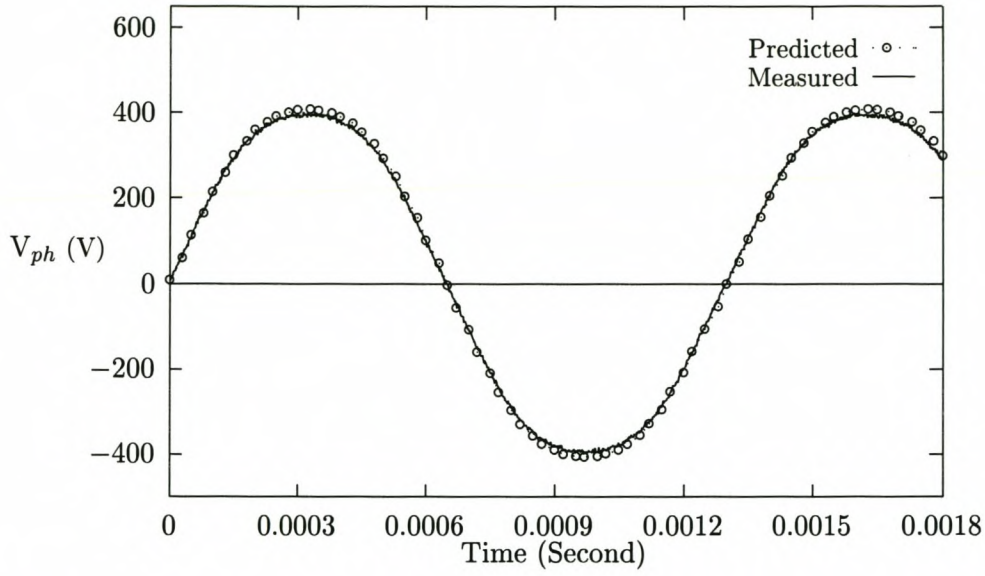

Figure 8.9: Comparison of predicted and measured no-load phase voltages (2300 rpm).

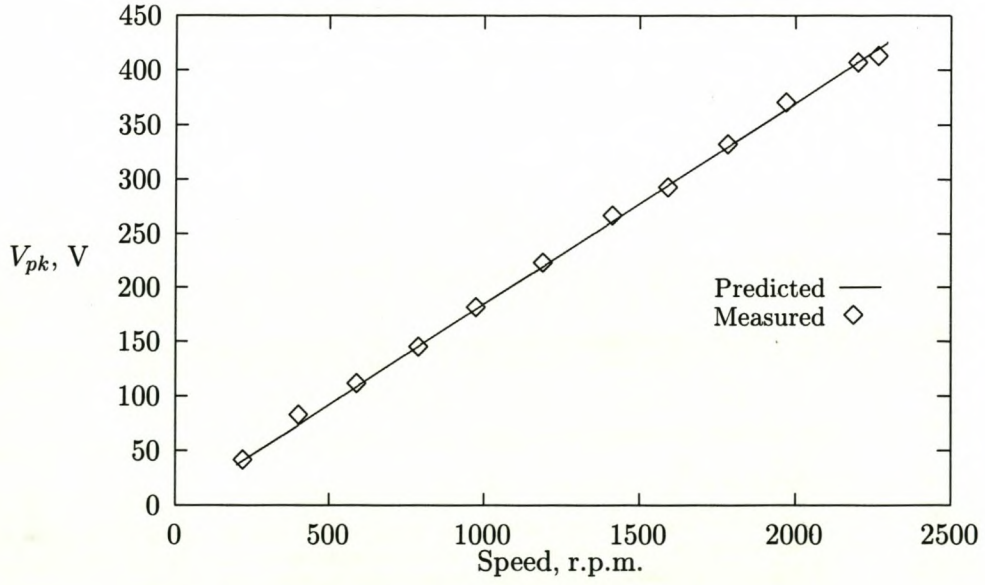

Figure 8.10: Peak phase voltage versus speed at no-load.

However, it should be noted that the multi-slice FE model is necessary to account for the radial irregularity of the magnetic field if certain profiles of PMs such as rectangular [94] or hybrid forms [25] of magnets are used. Further validation is done by comparing the measured and computed phase voltages (peak value) at different rotating speeds. It can be seen in Fig. 8.10 that the results correlate very well.

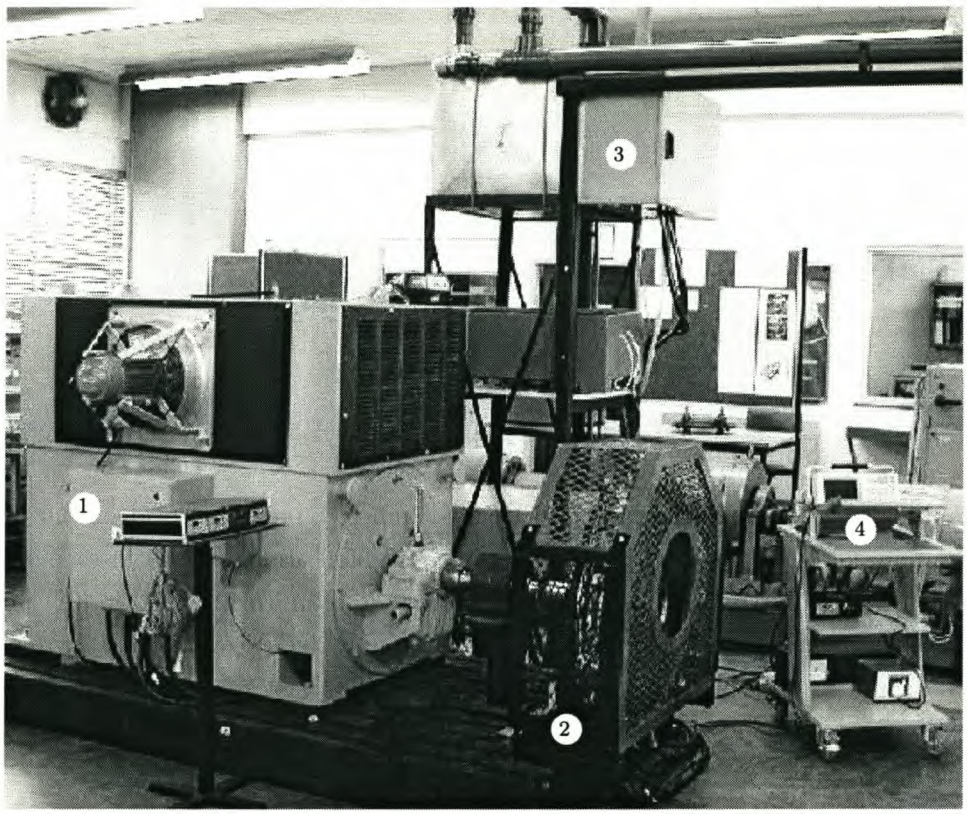

Figure 8.11: Testing setup of the designed (300 kW) AFPM machine under balanced three-phase load: where 1 - 600 kW induction machine, 2 - AFPM generator, 3 - water-cooled resistive load, and 4 - measuring equipment.

8.5 Balanced three-phase operation

For the next tests, the water-cooled bank of resistance was configured into a balanced three-phase load and then connected across the AFPM machine terminals. A 600 kW induction machine was used as prime mover. The testing setup is shown in Fig. 8.11. A series of tests were carried out at different rotating speeds. In consideration of the high spinning speed of the rotor disc and associated large centrifugal force acting on the PMs, the tests were carried out at a reduced speed and full current condition.

Table 8.2: Predicted and measured load current for balanced three-phase operation.

Speed (rpm)	Predicted phase current (A)	Measured phase current (A)	Predicted output power (kW)	Measured output power (kW)
510	56.18	51.74	10.98	10.2
799	88.02	80.23	26.96	24.72
1008	111.05	110.42	42.92	42.3
1204	132.64	131.32	61.22	60.06
1356	149.39	144.20	77.66	74.28
1403	154.57	152.95	83.14	81.48
1608	177.15	173.97	109.21	106.2
1795	197.75	194.02	136.09	132.18
1950	214.83	209.35	160.61	154

The same conditions were simulated using the FE computer program. The load resistance value used in the computation under various load conditions was compensated with an estimated temperature factor. The results are presented and compared in Table 8.2. Agreement between measured and predicted values is shown to be well within the limits of experimental accuracy.

8.6 Rectifier loading

The test with the rectified resistive load requires that the water-cooled resistance bank be rewired The verification of the machine model for operation with the rectifier load is carried out by comparing the measured and predicted steady-state phase current and voltage waveforms under different load conditions, i.e. light-current operation (Fig. 8.12 and 8.13), medium-current operation (Fig. 8.14 and 8.15) and full-current operation (Fig. 8.16 and 8.17). Again for safety reason, all the tests were performed at about 1500 rpm up to full current. In all the cases, the correlation between measured and predicted results is seen to be excellent.

8.6.1 Varying load condition

For the following set of tests, the AFPM machine was run at a constant speed (1400 rpm). A number of load conditions were measured. The relationship between the dc output voltage and the load current is illustrated graphically in Fig. 8.18. It can be seen that the dc voltage was 424 V on no-load and 396 V on rated current regulation. The percentage voltage regulation for this specific AFPM machine is about 6.59%.

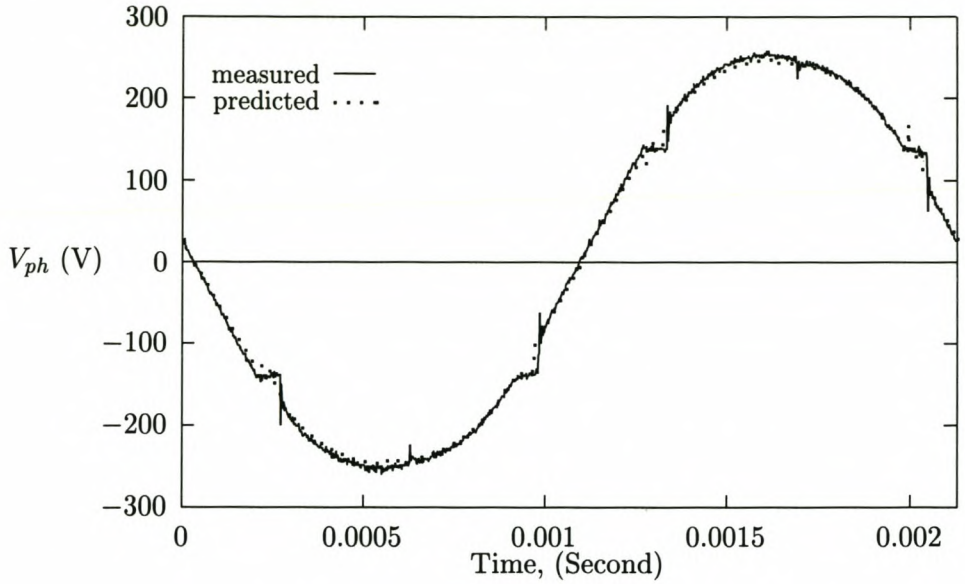

Figure 8.12: Phase voltage under light-current condition.

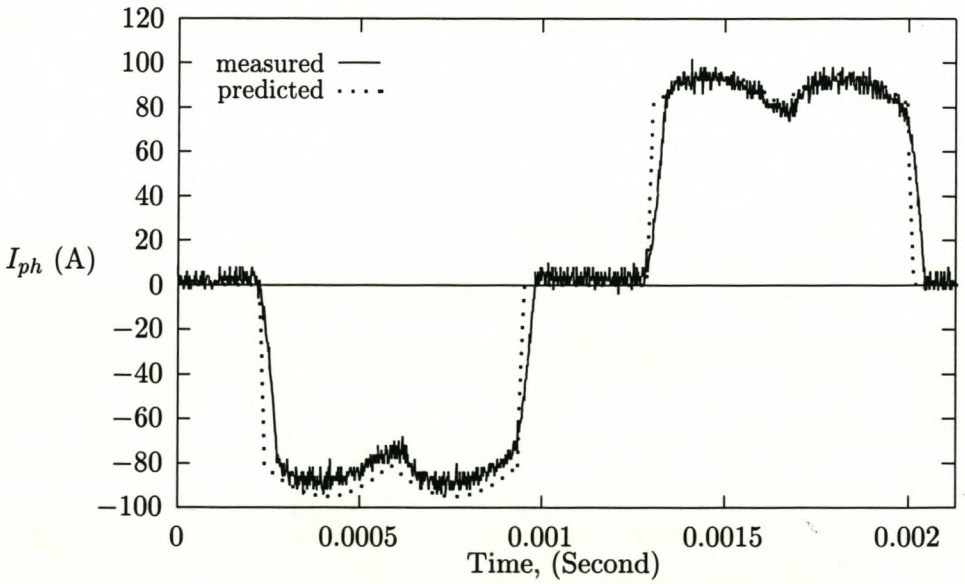

Figure 8.13: Phase current under light-current condition.

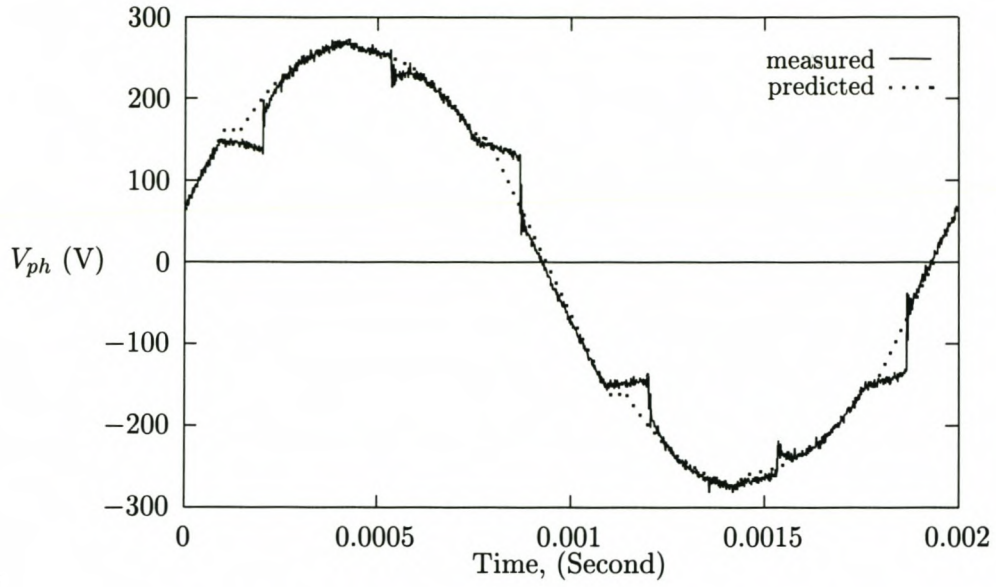

Figure 8.14: Phase voltage under medium-current condition.

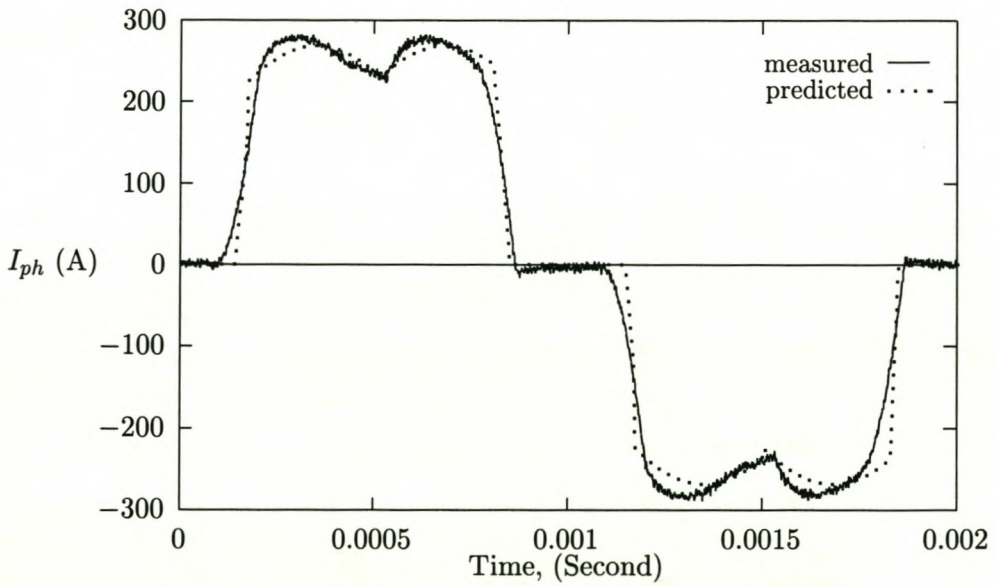

Figure 8.15: Phase current under medium-current condition.

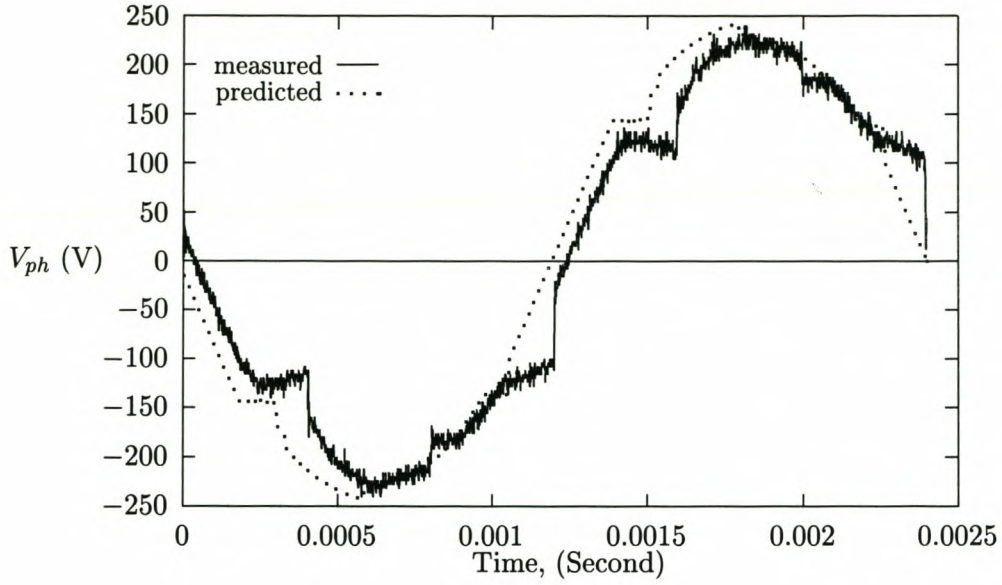

Figure 8.16: Phase voltage under full-current condition.

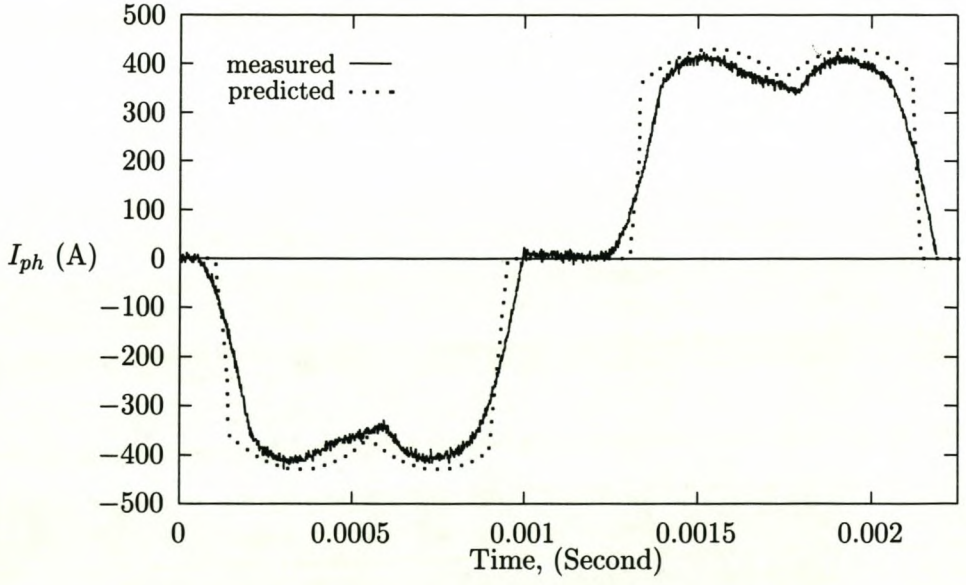

Figure 8.17: Phase current under full-current condition.

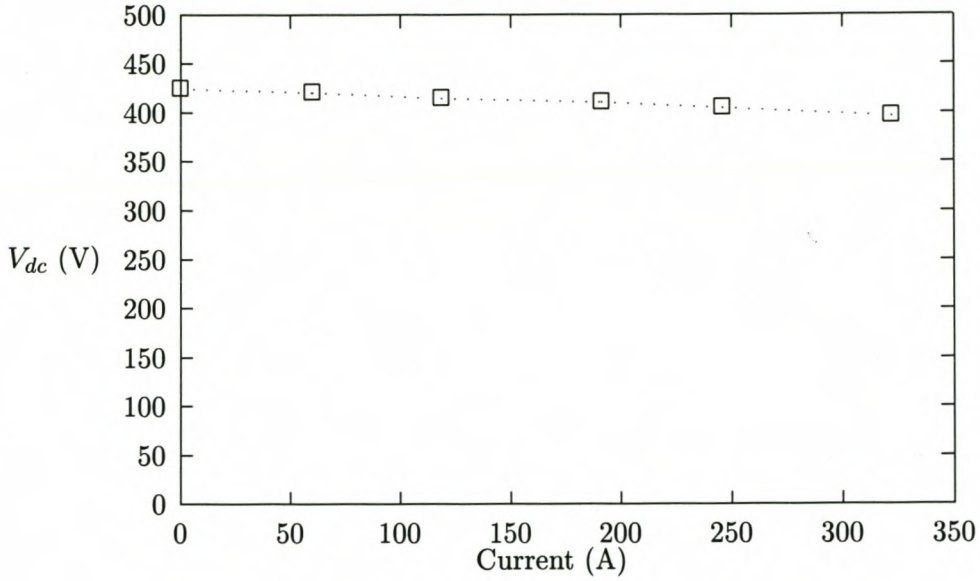

Figure 8.18: Measured dc voltage regulation characteristic with resistive load.

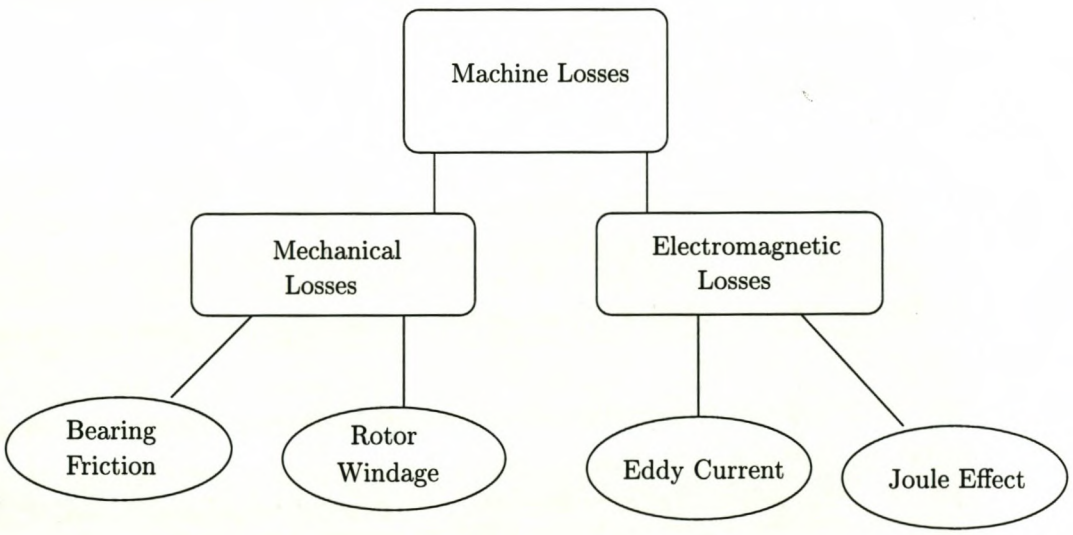

Figure 8.19: Loss mechanisms in an AFPM machine with an ironless stator.

8.7 Losses and efficiency

Energy losses found in an AFPM machine, like in any electrical machine, are primarily composed of mechanical and electromagnetic losses. Fig. 8.19 shows the different mechanisms that cause these losses.

At rated speed (2300 rpm), the rated output power of the AFPM machine at unity power factor is designed to be 300 kW. Taking into account the mechanical loss, eddy current loss and copper loss, the total mechanical input power is then 313.2 kW. This gives a machine efficiency of 95.8% at that speed. The total losses are 13.2 kW, of which 2360 Watts are eddy current losses, 5887 Watts are mechanical losses and 4940 Watts are copper losses. It has been found that in the simulation, except for the mechanical losses that were somewhat underestimated, other losses agreed well with the predicted ones. As mentioned previously, the optimum design of the hub section of the AFPM machine may significantly reduce the associated high windage losses and therefore result in a higher efficiency.

8.8 Flow and thermal behaviour

In this section, both the air flow and thermal behaviour of the constructed AFPM machine have been experimentally evaluated. The predicted and measured air flow rate and temperature distribution are compared to verify the flow and the thermal model described in Chapter 5.

8.8.1 Air flow-rate measurement

The air flow-rate measurement is carried out by measuring inlet air pressure difference Δp, which is then used for calculating mass flow-rate $\dot{m}$ according to the following equation:

$$\dot{m} = \sqrt{2 \cdot \rho \cdot \Delta p} \cdot A_d \tag{8.1}$$

where A_d is the cross section area of the inlet duct. Fig. 8.20 shows the setup of the flow measurement. A specially designed inlet duct with a bell mouth was mounted to the inlet (hub) of the AFPM machine. A few tapping points were made on the inlet duct for pressure measurements. Note that the pressure drop through the bell mouth and inlet duct was assumed to be negligible.

The measured pressure difference versus operating speed is given in Fig. 8.21. It was found that the static pressure difference is proportional to the 2^{nd} power of the rotation speed. This implies that slightly increasing the operating speed of the AFPM machine may improve its cooling significantly. If you combine this with Eqn. (8.1), it is not difficult to see that the relation between volumetric flow-rate and machine speed is linear. Fig. 8.22 shows both

the computed and measured volumetric flow rate of a 300 kW prototype AFPM machine at different operating speeds. It can be seen that the correlation between the computed and measured results is good.

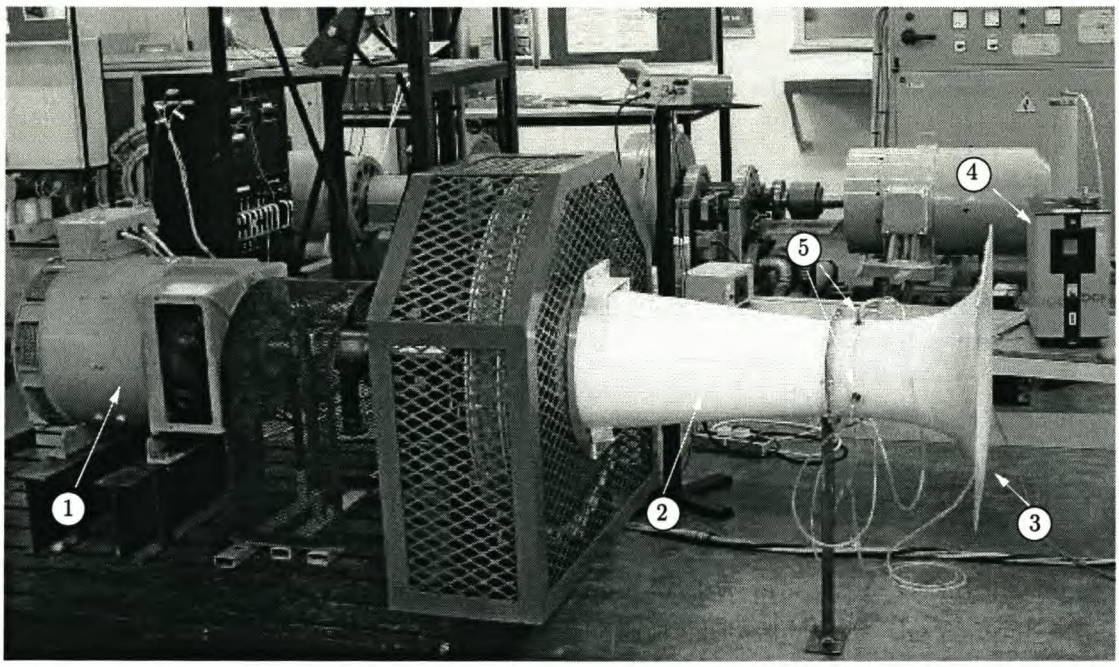

Figure 8.20: Flow measurement of the prototype AFPM machine, where 1 - d.c. machine drive, 2 - inlet duct, 3 - bell mouth, 4 - manometer, and 5 - pressure tapping point.

8.8.2 Machine temperature measurement

Temperature rise of the stator winding is measured by using thermocouple sensors, while the outer surface temperature of the machine is measured by a digital infrared thermometer. Firstly, the AFPM machine was operated at a constant speed of 1400 rpm under no-load conditions where the machine temperature rise is attributed to the eddy current and windage losses only.

Then the AFPM machine was connected up for load tests. Given the nature of the temperature test, the AFPM machine needs to run at a constant high speed for an extended time. For safety reasons, the test was scaled down to a lower speed and reduced power. The machine was running at about 1400 rpm with a r.m.s. phase current of 246 A. The machine temperatures were taken at a time interval of 5 minutes until the temperatures stabilised. Table 8.3 gives both measured and simulated temperature values. It can be seen that for no-load test, close agreement between measured and calculated results is obtained. For the load test,

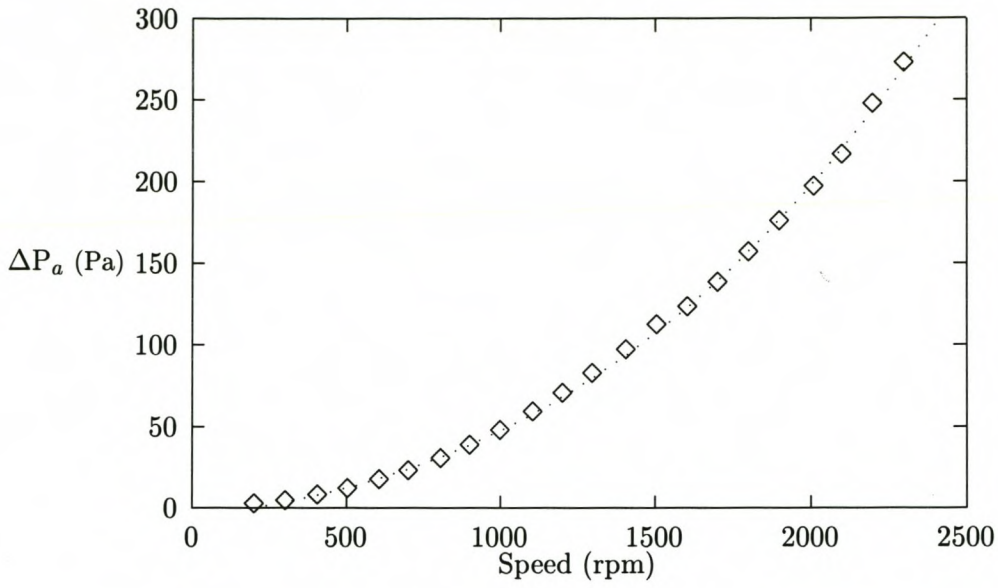

Figure 8.21: Measured static air pressure at different rotating speeds.

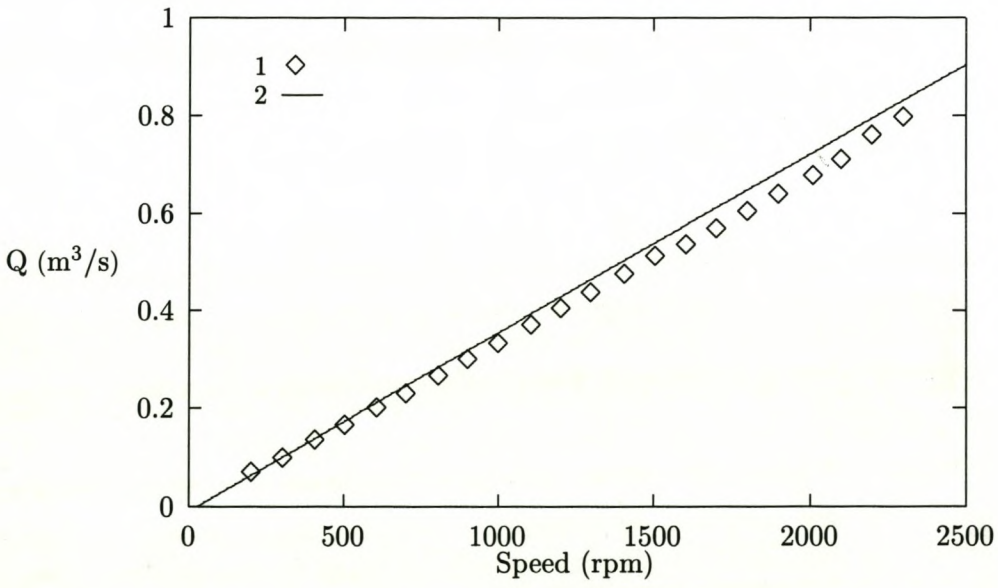

Figure 8.22: Volumetric flow rate versus machine speed, where 1 – measured volumetric flow rate, and 2 – calculated volumetric flow rate.

the measured stator temperature is higher than the predicted one. This may be due to the thermocouples that were all placed in the inner end-winding of the stator winding where the temperature is the highest, whereas the predicted values are the average temperatures of the stator.

Table 8.3: Comparison of measured and predicted machine temperatures.

No-load test $\Rightarrow$ $T_{amb} = 16\ ^oC$ $n = 1414\ r.p.m.$		
Machine part	Predicted temperature rise ^oC	Measured temperature rise ^oC
Stator winding	17.25	17.2
Air-gap	2.4	-
Rotor disk	2.92	2.7
Permanent Magnet	3.03	-
Load test $\Rightarrow$ $T_{amb} = 14.6\ ^oC$ $n = 1402\ r.p.m.$ $I_{ph} = 243\ A$ (rms)		
Machine part	Predicted temperature rise ^oC	Measured temperature rise ^oC
Stator winding	45.72	56.25
Air-gap	4.47	-
Rotor disk	5.46	3.9
Permanent Magnet	5.5	-

Chapter 9

Conclusion and Recommendations

This thesis describes the analysis, design optimisation and construction of an air-cooled 300 kW (at unity power factor) AFPM generator with an ironless stator. Part of the study resulted in solving new problems and, in other instances, the study contributed to improving some commonly used techniques in this field. This Chapter summarises the original work that has been performed and the relevant insights gained through this research. Recommendations for future research work are also proposed.

9.1 Original work

In this thesis the following new work has been presented:

- An air-cooled, 300 kW (at unity power factor), 766 Hz, ironless stator AFPM generator has been designed, fabricated and investigated. The generator has a very good efficiency, compact structure and excellent cooling capacity. It is well suited for power generation applications to be integrated with internal combustion engines (ICE), heat engines and some renewable energy systems such as wind turbines. To the best knowledge of the author, the power rating and the operating frequency (766Hz) of the generator is the highest in the world in its kind.

- The Cartesian Air-Gap Element (CAGE) has been derived and verified. This new macro element has been optimised by using a number of existing time-saving schemes, which make it very attractive in the FE time-stepped modelling of AFPM and/or linear machines. The implementation of the CAGE in the FE time-stepped modelling of an AFPM generator for balanced three phase operation and rectifier loading has been successfully carried out.

- The accuracy in calculating the eddy current loss of an AFPM machine by using an analytical method has been drastically improved. This was accomplished by combining

the 2-D FE field solutions with the closed-form analytical method. A novel multi-layer and multi-slice simulation scheme has also been devised to take into account the 3-D effects of the field distribution. All results have been compared and verified by experimental test results.

- A thermofluid model of an air-cooled AFPM machine has been developed, which consists of a fluid-flow model and a heat transfer model. The fan effects in an air-cooled AFPM machine have been studied by using general fan/pump theory. Given the flow rate obtained by fluid-flow analysis, the key heat transfer coefficients were calculated according to the rotating disc theory. Experimental investigations were conducted to test and verify each developed model.

- Both the Powell method and the PBIL algorithm have been applied to the multi-dimensional design optimisation of an AFPM generator, in which the FE calculation has been directly incorporated for accurately determining the performance indexes of the AFPM machine. No published work that made use of this approach for the design optimisation of the AFPM machine has been found in literature.

9.2 Features of AFPM machines with an ironless stator

AFPM machines offer an alternative to radial field PM machines. The distinct properties such as high power to weight ratio, compact disc-type shape and diverse topologies have made this type of machine an excellent candidate for certain special-purpose applications. Essentially, each type of RFPM machine has its equivalent AFPM version. Amongst others, the AFPM machine with a double-sided configuration and an internal ironless stator, which forms the main theme of this research, has the following special features:

1. With an ironless stator the core losses that normally exist in an electrical machine are eliminated, leading to better efficiency and the opportunity for a high frequency design. In addition, the considerable saving of the core material in the stator reduces the fabrication cost and increases the power to weight ratio of the machine.

2. Due to the large air-gap the armature reaction effect is greatly reduced. In the meantime, a good voltage regulation can be expected as a result of the low impedance of the stator winding. All these aspects make this topology particularly suitable for brushless d.c. and synchronous machines.

3. The topology of double-sided rotor discs with an internal stator has two working surfaces, which means better winding usage. The planar airgaps at both sides of the stator provide a large heat dissipation area. Moreover, the surface-mounted PMs have fan effects, which may substantially improve the cooling capacity of the AFPM machine when operated at high speeds.

4. Because of its disc shape and large diameter to axial length ratio, it is possible to stack more units in the axial direction to increase power output. Furthermore, a modular concept may be adopted in the design and commercial production, which will lead to a high degree of standardisation in both the manufacturing and maintenance and therefore the reduction of overall costs.

5. The main disadvantage of the topology is that, due to the existence of double air-gaps and the ironless air-cored stator, a large magnetising MMF is required. This will inevitably lead to the consumption of a large volume of high-field PM material and to an increase in the costs of the machine.

9.3 Insights into the AFPM machine design

In this section, the relevant insights into the design of AFPM machines gained through this research are summarised.

9.3.1 Calculation of performance parameters

The overall design methodology presented in the thesis was to use a combination of the classical circuit approach and FE field models to minimise computation time in an optimisation process. The developed method has been shown to give excellent results for both balanced three-phase operation as well as rectifier loading. Experimental verification of the developed field models and simulation techniques suggests that the aim of this project has been achieved satisfactorily.

The developed Cartesian Air-Gap Element (CAGE) has been successfully verified and implemented for the time-stepped modelling of the AFPM machine. It has been shown that the high computation overhang normally associated with this element may be substantially reduced by applying a number of time-saving schemes. Given its superior accuracy and free movement, the CAGE is a good solution for the time-stepped modelling of any electrical machine with a flat airgap.

A simple analytical method has been described in Chapter 2. Because it is easy to use and has a fast solution time, this analytical method may be used to obtain a preliminary optimum design or to show the tendencies of the optimum dimensions of the AFPM machine. However, for a more precise optimisation, FE field modelling is necessary in order to obtain more accurate and reliable results. The simple analytical method may be used to find a set of sub-optimum values as starting points for the subsequent FE solution based optimisation. The method can also be used to explain the optimum design of the machine.

9.3.2 Eddy current losses

As a result of the field analysis and experimental investigation described in Chapter 4 and the measured results shown in Chapter 8, it is possible to state that using the standard analytical formula to account for the eddy losses in an ironless stator AFPM machine leads to a significant error (up to 43%), which becomes even worse at high speeds.

Accurate results can be obtained by using the developed hybrid method that combines the two dimensional FE field solution and the standard analytical formula, in which a multi-layer and multi-slice FE modelling technique was devised to account for three dimensional field distribution. Note that using this method will require several FE solutions to be performed at one rotor position. In the simulation a 5-layer and 3-slice FE model was used and the results agree closely with those obtained from measurements.

Based on the experimental tests performed on a specially designed stator and on the final constructed AFPM machine, the following can be concluded.

- The eddy circulating currents between parallel wires can be effectively minimised by using twisted wires. These twisted wires can be easily manufactured and are therefore cost-effective when compared with Litz wires.
- However, the circulating currents between parallel connected phase coils cannot be easily removed even if great care was taken to ensure a symmetrical placement of the coils. These circulating currents are quite significant even at low speeds. When the speed rises, the amplitudes of the circulating currents do not change much. This is reasonable since the winding impedance $X_l = 2\pi f L$ increases with speed as the phase voltage increases, resulting in a fairly constant circulating current.

9.3.3 Optimisation algorithms

Both Powell's method and the PBIL algorithm have been applied to the optimisation of the AFPM machine. Powell's method is more efficient than the PBIL algorithm as it needed only a fraction of the CPU time that the PBIL required. However, the PBIL optimisation found slightly better solutions in all the case studies. The optimisation was carried out according to two different design objectives, i.e. maximum efficiency and minimum PM consumption, respectively.

For the design of the maximum efficiency, the optimisation process using Powell's method was often trapped at a local optimum, which is characterised by a low diameter ratio K_r, large amount of PM material, and a thick stator. It was found effective to modify the objective function by adding a function that assigns a positive penalty for increased PM mass in the

optimisation with Powell's method. The PBIL optimisation needs no such constraint as it finds the optimum design of efficiency with quite a low PM material consumption.

For the design of minimum PM material, both methods produced similar results, though the PBIL optimisation found a design using slightly less PM material. It was found that the diameter ratio $K_r = 0.68$ for the maximum efficiency design and $K_r = 0.7$ for minimum PM consumption design. By minimising the PM material, an overall better design can be obtained with lower eddy current losses, high efficiency and high power to weight ratio.

9.3.4 Thermofluid analysis

The thermofluid model of an AFPM machine has been developed for the first time. Note that the calculation of the air temperature in the air-gap is only possible if the mass flow rate through the air-gap is accurately predicted. Thus, a reasonable fluid-flow model is necessary. These models have been experimentally verified and implemented in the design optimisation program with success.

It has been found that the losses associated with entrance effects, bending, tapering, and tee connection, which are usually regarded as *minor losses* in the conventional large fluid flow system, accounted for a substantial portion of pressure losses in an AFPM machine. Amongst others, the entrance losses of the air flow at the air inlet of an AFPM machine may account for a quarter of the total system pressure losses of the machine.

From the fluid-flow analysis and tests, it was found that the static pressure difference is proportional to the 2^{nd} power of the rotation speed. However, the volumetric flow-rate is directly proportional to the machine speed. The gradient is dependent on the overall system losses through the machine. It is clear that the air flow through the prototype AFPM machine is not optimised from a minimum energy loss point of view. By taking into consideration to a greater degree sound fluid mechanics practice, an improved mass flow rate can be achieved without incurring substantial mechanical losses.

9.3.5 Mechanical strength analysis

Due to the strong magnetic attraction force, the rotor discs are subjected to certain deflection, which may cause serious mechanical and electrical problems. On the other hand, the rotor discs account for roughly 50% of the total active mass of an AFPM machine. Hence, the optimal design of the rotor discs is of great importance to realise a design of high power/mass ratio. All these aspects make the mechanical strength analysis of the rotor disc a necessity.

The maximum tolerable deflection of the rotor disc was set to be 0.3 mm so that the PMs do

not suffer any excessive forces that have the potential to break the magnets or peel them off from the steel disc. It has been shown that the bending of the rotor disc decreases towards its outer periphery. Thus, the rotor yoke may be machined into a tapered disc with roughly 10% saving of iron material. The increase of disc deflection is negligible. This can effectively save the active mass of the AFPM machine without compromising the mechanical strength.

From the thermal expansion test on the epoxy encapsulated stator winding, it was found that the relationship between the stator deformation and its temperature is almost linear. On average the deflection of the stator surface is about 0.0056 mm per degree Celsius resulting in a 0.5 mm deflection at a temperature of 117 ^oC. This may be due to the air contents of the epoxy resin resulting from the process of stator construction. It can be concluded that a relatively large running clearance between the stator and the rotor be recommended.

9.4 Performance of the prototype AFPM machine

The designed 300kW AFPM machine was built and tested. Due to a very low phase inductance in the ironless stator AFPM machine, the output voltage varied almost linearly with the load current. With the output via a diode bridge rectifier to a resistive load, the measured percentage dc voltage regulation of the machine was found to be 6% from no-load to full-load current.

When operated with a balanced three-phase resistive loading the waveform of the stator phase voltage and current were shown to be very close to sinusoidal. Despite the fact that at the nominal speed of 2300 rpm the no-load loss is rather high due to (i) the large eddy current losses associated with the high operating frequency (766 Hz) and (ii) the excessive windage loss at the air inlet hub, the measured performance of the prototype AFPM machine, on the whole, was highly satisfactory.

Although the thermal tests were configured for a reduced current (77% of rated current) at 1400 rpm, it was shown that the cooling capacity of the AFPM machine was excellent. The air flow-rate measurements on the prototype AFPM machine proved that a volumetric flow rate of 0.8 m^3/s can be expected at the rated speed, which is almost twice as much as the air flow at the tested speed. It can be expected that the machine temperatures will be well within limits for the rated operation.

At rated speed (2300 rpm), the rated output power of the AFPM machine was designed to be 300 kW. By taking into account the mechanical loss, eddy current loss and copper loss, the total mechanical input power therefore was 313.2 kW. This gives the machine an efficiency of 95.8% at that speed. The total losses were 13.2 kW, of which 2360 W were eddy current

losses, 5887 W were mechanical losses and 4940 W were copper losses. It was found that in the simulation, except for the mechanical losses that were somewhat underestimated, other losses correlated well with the predicted ones. As mentioned previously, the optimum design of the hub section of the AFPM machine may significantly reduce the associated high windage losses and therefore will result in a higher efficiency.

9.5 Recommendations

This thesis considers the design aspects and optimisation of an AFPM machine with an ironless stator. Some of the directions in which future research into this type of AFPM machine can proceed are described as follows:

- Because of the large diameter to length ratio of the AFPM machine, it is particularly suitable for high pole number and low speed machines such as wind/hydro generators. The air cooling capacity of an AFPM machine is greatly reduced at low speeds, which requires the use of additional cooling techniques such as heat-pipes, an auxiliary cooling fan or water ducts. All these aspects need to be investigated in further research.

- To remove the circulating currents among the parallel connected phase coils, preferably all the phase coils may be connected in series. This will lead to a high voltage machine. However, this will not be difficult in this type of AFPM machine due to the special features of its structure. Compared with conventional high voltage machines, the high voltage AFPM machine may prove to be advantageous from a cost perspective. There is a need to do further research on this topic. The potential application is for HVDC light transmission.

- It has been found that the excessive windage losses at the air inlet hub of the prototype AFPM machine account for a large portion of the total no-load losses. It is necessary to optimise the air inlet hub section to ensure a high flow rate with reduced mechanical losses. This will also help improve the overall efficiency of the machine.

References

[1] A. A. Abdel-Razek, J. L. Coulomb, M. Feliachi, and J. C. Sabonnadiere. The Calculation of electromagnetic torque in saturated electric machines within combined numerical and analytical solutions of the field equations. *IEEE Trans. MAG-17(6):3250–3252*, (1981).

[2] A. A. Abdel-Razek, J. L. Coulomb, M. Feliachi, and J. C. Sabonnadiere. Conception of an air-gap element for the dynamic analysis of the electromagnetic field in electric machines. *IEEE Trans. MAG-18(2):655–659*, (1982).

[3] G. A. J. Amaratunga, P. P. Acarnley, and P. G. McLaren. Optimum magnetic circuit configurations for PM aerospace generators. *IEEE Trans. AES-21(2):230–255*, (1985).

[4] J. D. Angelo, M. V. K. Chari, and P. Campbell. 3-D FE solution for a PM axial field machine. *IEEE Trans. PAS-102(1):83–90*, (1983).

[5] S. Baluja. Population-based incremental learning: A method for integrating genetic search based function optimization and competitive learning. Technical report, Carnegie Mellon University, Pittsburgh, United States, (1994).

[6] C. H. Berry. *Flow and fan - principle of moving air through ducts.* The Industrial Press, New York, (1954).

[7] P. Campbell. A new wheel motor for commuter cars. *Electrical Review, (190), pp.332–333*, (1972).

[8] P. Campbell. Principle of a PM axial field DC machine. *Proceedings of IEE, vol.121, no.1, pp.1489–1494*, (1974).

[9] P. Campbell. The magnetic circuit of an axial flux DC electrical machine. *IEEE Trans. MAG-11(5):1541–1543*, (1975).

[10] P. Campbell. *Permanent magnet materials and their application.* Cambridge University Press, Cambridge, UK, (1994).

[11] P. Campbell, D. J. Rosenberg, and D. P. Stanton. The computer design and optimization of axial field PM motor. *IEEE Trans. PAS-100(4):1490–1497*, (1981).

[12] F. Caricchi, F. Crescimbini, E. Fedeli, and G. Noia. Design and construction of a wheel-directly-coupled axial-flux PM motor prototype for EVs. *IEEE-IAS Annual Meeting, IAS-29, part 1, pp.254–261*, (1994).

[13] F. Caricchi, F. Crescimbini, and O. Honorati. Low-cost compact PM machine for adjustable-speed pump application. *IEEE Trans. IA-34(1):109–116*, (1998).

[14] F. Caricchi, F. Crescimbini, O. Honorati, G. L. Bianco, and E. Santini. Performance of core-less winding axial-flux PM generator with power output at 400Hz - 3000 rev/min. *IEEE Trans. IA-34(6):1263–1269*, (1998).

[15] F. Caricchi, F. Crescimbini, O. Honorati, and E. Santini. Performance evaluation of an axial-flux PM generator. *Proceedings of ICEM'92, Paris, vol.2, pp.761–765*, (1992).

[16] F. Caricchi, F. Crescimbini, F. Mezzetti, and E. Santini. Multistage axial-flux PM machines for wheel-direct-drive. *IEEE Trans. IA-32(4):882–888*, (1996).

[17] F. Caricchi, F. Crescimbini, A. D. Napoli, O. Honorati, T. Lipo, G. Noia, and E. Santini. Development of a IGBT inverter driven axial-flux PM synchronous motor drive. *Proceedings of EPE'91, Firenze, vol.3, pp.482–487*, (1991).

[18] F. Caricchi, F. Crescimbini, A. D. Napoli, and M. Marcheggiani. Prototype of electric-vehicle-drive with twin water-cooled wheel direct-drive motors. *IEEE Annual Power Electronics Specialists Conference (PESC'96), part 2, pp.1926–1932*, (1996).

[19] F. Caricchi, F. Crescimbini, A. D. Napoli, and E. Santini. Optimum CAD-CAE design of axial flux permanent magnets motors. *Proceedings of ICEM'92, Paris, vol.2, pp.637–641*, (1992).

[20] F. Caricchi, F. Crescimbini, and E. Santini. Basic principle and design criteria of axial-flux PM machines having counter-rotating rotors. *IEEE Trans. IA-31(5):1062–1068*, (1995).

[21] F. Caricchi, F. Crescimbini, E. Santini, and C. Santucci. Influence of the radial variation of the magnet pitches in slot-less PM axial flux motors. *IEEE-IAS Annual Meeting vol.1, pp.18–23*, (1997).

[22] F. Caricchi, F. Crescimbini, E. Santini, and C. Santucci. FEM evaluation of performance of axial flux slotted PM machines. *IEEE-IAS Annual Meeting vol.1, pp.12–18*, (1998).

[23] G. W. Carter. *Electromagnetic field in its engineering aspects.* Longmans, (1954).

[24] B. Chalmers, E. Spooner, O. Honorati, F. Crescimbini, and F. Caricchi. Compact permanent magnet machines. *Electric Machines and Power Systems, vol.25, no.6, pp.635–648*, (1997).

[25] B. J. Chalmers, W. Wu, and E. Spooner. An axial-flux permanent-magnet generator for a gearless wind energy system. *IEEE Trans. EC-14(2):251–257*, (1999).

[26] C. C. Chan. *Axial-field electrical machines with yokeless armature core.* PhD thesis, University of Hong Kong, Hong Kong, (1982).

[27] C. C. Chan. Axial-field electrical machines: design and application. *IEEE Trans. EC-2(2):294–300*, (1987).

[28] P. Chandler and D. Patterson. Counting the losses in very high efficiency machine design. *World Renewable Energy Congress, Perth, Australia*, (1999).

[29] D. Chisholm. *Two-phase flow in pipelines and heat exchangers.* George Godwin, New York, (1983).

[30] G. Cvetkovski, L. Petkovska, M. Cundev, and S. Gair. Mathematical model of a PM axial field synchronous motor for a genetic algorithm optimisation. *Proceedings of ICEM'98, Istanbul, vol.2, pp.1172–1177*, (1998).

[31] R. T. Dobson. Lecture notes on heat transfer. Department of Mechanical Engineering, University of Stellenbosch, (2000).

[32] J. F. Douglas, J. M. Gasiorek, and J. A. Swaffield. *Fluid mechanics.* Longman Scientific & Technical, England, 3nd edition, (1995).

[33] R. H. Engelmann and W. H. Middendorf, editors. *Handbook of electric motors.* Marcel Dekker, Inc., New York, (1995).

[34] N. Ertugrul and P. P. Acarnley. Analytical solution of the system equations of the axial field permanent magnet synchronous motor drive. *Proceedings of ICEM'92, vol.2, pp.785–789*, (1992).

[35] P. D. Evans and J. F. Easham. Disc-geometry homopolar synchronous machine. *Proceedings of IEE, vol.127,pt.B, no.6, pp.299–307*, (1980).

[36] P. D. Evans and J. F. Easham. Double-disc alternator with ac-side excitation. *IEE Proceedings B, EPA-130(2), pp.95–102*, (1983).

[37] P. D. Evans and J. F. Easham. Slot-less alternator with ac-side excitation. *Proceedings of IEE, vol.130, no.6, pp.399–406*, (1983).

[38] M. Feliachi. *Contribution au calcul du champ electromagnetique par la methode des elements finis en vue d'une modelisation dynamique de machines electriques.* PhD thesis, Laboratorie de Genie Electrique de Paris, Paris, (1981).

[39] R. Ficheux, F. Caricchi, O. Honorati, and F. Crescimbini. Axial flux permanent magnet motor for direct drive elevator systems without machine room. *IEEE-IAS Annual Meeting, Rome, vol.1, pp.190-197*, (2000).

[40] T. Flack and A. Volschenk. Computational aspects of time-stepping finite element analysis using an air-gap element. *Proceedings of ICEM'94, Paris*, (1994).

[41] E. P. Furlani. A method for predicting the field in axial field motors. *IEEE Trans. MAG-28(5):2061–2065*, (1992).

[42] E. P. Furlani. Computing the field in permanent magnet axial-field motors. *IEEE Trans. MAG-30(5):3660–3663*, (1994).

[43] J. Gieras. Performance calculation for small dc motors with segmental permanent magnets. *Transaction of SA IEE. 82(1):14–21*, (1991).

[44] J. F. Gieras and M. Wing. *Permanent magnet motor technology: design and applications.* Marcel Dekker, Inc., New York, (1997).

[45] A. Gottvald, K. Preis, C. Magele, O. Biro, and A. Savini. Global optimization methods for computational electromagnetics. *IEEE Trans. MAG-28(2), pp.1537–1540*, (1992).

[46] L. Grover. *Inductance calculations - working formulas and tables.* Dover, New York, (1962).

[47] C. Gu, W. Wu, and K. Shao. Magnetic field analysis and optimal design of DC permanent magnet core-less disk machines. *IEEE Trans. MAG-30(5) part 2, pp.3668–3671*, (1994).

[48] S. Hamarat, K. Leblebicioglu, and H. B. Ertan. Comparison of deterministic and non-deterministic optimization algorithms for design optimization of electrical machines. *Proceedings of ICEM'98, vol.3, pp.1477–1482*, (1998).

[49] R. Hanitsch, R. Belmans, and R. Stephan. Small axial-flux motor with permanent magnet excitation and etched air-gap winding. *IEEE Trans. MAG-30(2):592–594*, (1994).

[50] J. R. Hendershot and T. J. E. Miller. *Design of brushless permanent magnet motors.* Magna Physics Publishing & Oxford Science Publications, (1994).

[51] J. H. Holland. *Adaption in nature and artificial systems.* Bradford Books, United States, (1994).

[52] J. P. Holman. *Heat transfer.* McGraw-Hill Inc.,(UK), London, 7th edition, (1992).

[53] S. R. Hoole. *Computer-aided analysis and design of electromagnetic devices.* Elsevier Science Publishing Co., Inc., New York, (1989).

[54] V. Hrabovcova and V. Brslica. Equivalent circuit parameters of disc synchronous motors with PM. *Electrical Drives and Power Electronics Symposium (EDPE'92), Slovakia, pp.348–353*, (1992).

[55] S. Huang, J. Luo, F. Leonardi, and T. A. Lipo. A general approach to sizing and power density equations for comparison of electrical machines. *IEEE-IAS Annual Meeting, San Diego, CA, pp.836–842*, (1996).

[56] S. Huang, J. Luo, F. Leonardi, and T. A. Lipo. A comparison of power density for axial flux machines based on general purpose sizing equations. *IEEE Trans. EC-14(2):185–192*, (1999).

[57] C. C. Jensen, F. Profumo, and T. Lipo. A low loss permanent magnet brushless DC motor utilizing tape wound amorphous iron. *IEEE Trans. IA-28(3):646–651*, (1992).

[58] M. Kamper, F. V. der Merwe, and S. Williamson. Direct finite element design optimisation of cageless reluctance synchronous machine. *IEEE Trans. EC-11(3):547–555*, (1996).

[59] M. J. Kamper. *Design optimisation of cageless flux barrier rotor reluctance synchronous machine.* PhD thesis, University of Stellenbosch, Stellenbosch, (1996).

[60] M. J. Kamper. Notes on axial flux permanent magnet machines. Electrical Machines Group, University of Stellenbosch, (1999).

[61] L. Klug. Axial field ac servomotor. *Electrical Drives and Power Electronics Symposium (EDPE'90), Slovakia, vol.1, pp.154–159*, (1990).

[62] L. Klug and R. Guba. Disc rotor ac servomotor. *Electrical Drives and Power Electronics Symposium (EDPE'92), Slovakia, pp.341–344*, (1992).

[63] W. S. Leung and C. C. Chan. A new design approach for axial-field electrical machine. *IEEE Trans. PAS-99(4):1679–1685*, (1980).

[64] N. Lombard. Design and evaluation of an ironless stator axial flux permanent magnet machine. Master's thesis, University of Stellenbosch, (1997).

[65] N. F. Lombard and M. J. Kamper. Analysis and performance of an ironless stator axial flux PM machine. *IEEE Trans. EC-14(4):1051–1056*, (1999).

[66] H. C. Lovatt, V. S. Ramdenand, and B. C. Mecrow. Design of an in-wheel motor for a solar-powered electric vehicle. *Proceedings of IEE: Electric Power Application, vol.145, no.5, pp.402–408*, (1998).

[67] D. Mbidi. Design and evaluation of a 300 kW double stage axial flux permanent magnet generator. Master's thesis, University of Stellenbosch, (2001).

[68] D. Mbidi, K. vd Westhuizen, R. Wang, M. Kamper, and J. Blom. Mechanical design considerations of double stage axial-flux permanent magnet machine. *IEEE-IAS 35th Annual Meeting, Rome, vol.1, pp.198-201*, (2000).

[69] D. S. Miller. *Internal flow systems.* BHRA (Information Services), The Fluid Engineering Centre, Cranfield, Bedford MK43 0AJ, UK, 2nd edition, (1990).

[70] T. J. E. Miller. *Brushless permanent magnet and reluctance motor drives.* Clarendon Press, Oxford, UK, (1989).

[71] A. R. Millner. Multi-hundred horsepower permanent magnet brushless disk motors. *IEEE Applied Power Electronics Conference and Exposition (APEC'94), pp.351–355*, (1994).

[72] A. F. Mills. *Basic heat and mass transfer.* Richard D. Irwin, Inc., (USA), (1995).

[73] G. K. Miti and A. C. Renfrew. Field weakening performance of the TORUS motor with rectangular current excitation. *Proceedings of ICEM'98, Istanbul, vol.1, pp.630–633*, (1998).

[74] N. Mohan, T. Undeland, and W. Robbins. *Power electronics: converters, applications, and design.* John Wiley & Sons Inc., (1995).

[75] E. Muljadi, C. P. Butterfield, and Y.-H. Wan. Axial flux, modular, permanent magnet generator with a toroidal winding for wind turbine applications. *IEEE Trans. IA-35(4):831–836*, (1999).

[76] B. R. Munson, D. F. Young, and T. H. Okiishi. *Fundamentals of fluid mechanics.* John Wiley & Sons, Inc., New York, 2nd edition, (1994).

[77] J. Ofori-Tenkorang and J. H. Lang. A comparative analysis of torque production in halbach and conventional surface-mounted permanent magnet synchronous motors. *IEEE-IAS Annual Meeting, Orlando, pp.657–663*, (1995).

[78] J. M. Owen. The effect of forced flow on heat transfer from a disc rotating near a stator. *International Journal of Heat and Mass Transfer, vol.14, pp.1135–1147*, (1971).

[79] J. M. Owen. The Reynolds analogy applied to flow between a rotating and a stationary disc. *International Journal of Heat and Mass Transfer, vol.14, pp.451–460*, (1971).

[80] J. M. Owen. Air cooled gas turbine discs: a review of recent research. *International Journal of Heat and Fluid Flow, vol.9, no.4, pp.354-365*, (1988).

[81] J. M. Owen. An approximate solution for the flow between a rotating and a stationary disk. *ASME Journal of Turbomachinery, vol.111, no.4, pp.323-332*, (1989).

[82] D. Patterson and R. Spee. The Design and development of an axial-flux PM brush-less DC motor for wheel drive in a solar powered vehicle. *IEEE Trans. IA-31(5):1054-1061*, (1995).

[83] J. Perho and E. Ritchie. A motor design using reluctance network. *Proceedings of 2nd ISTC-UEES'96, pp.309-314*, (1996).

[84] M. Powell. An efficient method for finding the minimum of a function of several variables without calculating derivatives. *Computer Journal, vol.7, pp.155-162*, (1964).

[85] F. Profumo, A. Tenconi, Z. Zhang, and A. Cavagnino. Design and realization of a novel axial flux interior PM synchronous motor for wheel-motors applications. *Proceedings of ICEM'98, Istanbul, vol.3, pp.1791-1796*, (1998).

[86] F. Profumo, A. Tenconi, Z. Zhang, and A. Cavagnino. Novel axial flux interior PM synchronous motor realized with powdered soft magnetic materials. *IEEE-IAS Annual Meeting vol.1, pp.152-159*, (1998).

[87] F. Profumo, Z. Zhang, and A. Tenconi. Axial flux machines drives: a new viable solution for electric cars. *IEEE Trans. IE-44(1):39-45*, (1997).

[88] S. Ratnajeevan, H. Hoole, and M. Haldar. Optimisation of electromagnetic devices: circuit models, neural networks and gradient methods in concept. *IEEE Trans. MAG-31(3):2016-2019*, (1995).

[89] S. J. Salon. *Finite element analysis of electrical machines.* Kluwer Academic Publishers, Norwell, Massachusetts, (1995).

[90] M. G. Say. *Alternating current machines.* Pitman Publishing Inc., London, (1983).

[91] A. T. Sayers. *Hydraulic and compressible flow turbomachines.* McGraw-Hill Book Company, London, (1990).

[92] K. Sitapati and R. Krishnan. Performance comparisons of radial and axial field permanent magnet brushless machines. *IEEE Trans. IA-37(5):1219-1226*, (2001).

[93] L. Soderlund, A. Koski, H. Vihriala, J.-T. Eriksson, and R. Perala. Design of an axial flux PM wind power generator. *Proceedings of 8th International Conference on Electrical Machine and Drives (ICEMD'97), pp.224-228*, (1997).

[94] E. Spooner and B. J. Chalmers. Toroidally-wound, slotless, axial-flux, PM, brushless-DC motor. *Proceedings of ICEM'88, vol.3, pp.81–86*, (1988).

[95] E. Spooner and B. J. Chalmers. TORUS: a slotless, toroidal-stator, permanent-magnet generator. *Proceedings of IEE, vol.139, part B, pp.497–506*, (1992).

[96] P. Strachan, F. Reynaud, and T. von Backström. The hydrodynamic modeling of torque converters. *SAIMechE. R&D Journal, vol.8, no.1, pp.21 - 29*, (1992).

[97] C. R. Sullivan. Computationally efficient winding loss calculation with multiple windings, arbitrary waveforms, and two-dimensional or Three-Dimensional Field Geometry. *IEEE Trans. PE-16(1):142-150*, (2001).

[98] H. Takano, T. Itoh, K. Mori, A. Sakuta, and T. Hirasa. Optimum values for magnet and armature winding thickness for axial-field PM brushless DC motor. *IEEE Trans. IA-28(2):350–357*, (1992).

[99] A. F. Volschenk. *Finite element analysis of a salient-pole generator feeding a rectifier load.* PhD thesis, University of Cambridge, Peterhouse, (1993).

[100] R. Wallace, T. A. Lipo, L. A. Moran, and J. A. Tapia. Design and construction of a PM axial flux synchronous generator. *Proceedings of International Conference on Electrical Machine and Drives, Milwaukee WI, pp.MA1(4.1–4.3)*, (1997).

[101] R. Wang, R. Dobson, and M. Kamper. Thermofluid analysis of an axial flux permanent magnet (AFPM) generator. *SAIMechE. R&D Journal, vol.17, no.1, pp.18 - 26*, (2001).

[102] R. Wang and M. Kamper. Evaluation of eddy current losses in axial flux permanent magnet (AFPM) machine with an ironless stator. *IEEE-IAS 37th Annual Meeting Record, Pittsburgh*, (2002).

[103] R. Wang, H. Mohellebi, T. Flack, M. Kamper, J. Buys, and M. Feliachi. Two-dimensional Cartesian air-gap element (CAGE) for dynamic finite element modeling of electrical machines with a flat air gap. *IEEE Trans. MAG-38(2):1357–1360*, (2002).

[104] F. M. White. *Fluid mechanics.* McGraw-Hill Book Company, New York, (1994).

[105] A. H. Wijenayake, J. M. Bailey, and P. J. McCleer. Design optimization of an axial gap PM brushless dc motor for electric vehicle applications. *IEEE-IAS Annual Meeting, pp.685–691*, (1995).

[106] S. Williamson and J. Smith. The application of minimisation algorithms in electrical engineering. *Proceedings of IEE, vol.127, part A, no.8, pp.528–530*, (1980).

[107] M. Wing. *Analysis of an energy efficient permanent magnet brushless universal motor.* PhD thesis, University of Cape Town, Cape Town, (1996).

[108] W. Y. Wong. *Heat transfer for engineers.* Longmans, (1977).

[109] L. Xu, X. Xu, T. Lipo, and D. Novotny. Vector control of a synchronous reluctance motor including saturation and iron loss. *IEEE Trans. IA-27(5):977–987*, (1991).

[110] W. Zangwill. Nonlinear programming via penalty functions. *Management Science, vol.13, pp.344–358*, (1967).

[111] Z. Zhang, F. Profumo, and A. Tenconi. Analysis and experimental validation of performance for an axial flux PM brushless DC motor with powder iron metallurgy cores. *IEEE Trans. MAG-33(5):4194–4196*, (1997).

[112] Z. Zhang, F. Profumo, and A. Tonconi. Axial flux versus radial flux permanent magnet motors. *Electromotion, vol.3, pp.134–140*, (1996).

[113] Z. Zhang, F. Profumo, and A. Tonconi. Axial flux wheel machines for electric vehicles. *Electric Machines and Power Systems, vol.24, no.8, pp.883–896*, (1996).

Appendix A

Derivation of Cartesian Air Gap Element (C.A.G.E.)

A.1 Background

One common problem in the FEM modelling of electric machines is that the finite elements in the air-gap region often have poor aspect ratios. To obtain an accurate field solution several layers of elements may be required, This may significantly increase the number of unknowns. Furthermore, if the time stepping scheme is needed, the finite elements in the air-gap may become distorted during the calculation. Re-meshing the air-gap to eliminate the distortion introduces additional complication and inconvenience. To overcome these problems, Razek and Feliachi [1, 2, 38] proposed the Air Gap Element (A.G.E.) concept, which demonstrates superior and consistent accuracy over classical elements. Due to the nature of the A.G.E., all terms can be calculated very accurately, irrespective of the relative position of the rotor to the stator. Therefore A.G.E. is a good option for dynamic field analysis of electrical machines.

With this element, however, the sparsity of the final system matrix is partially lost due to the large bandwidth introduced by the AGE [89]. Considering the fact that rotor movement will necessitate the recalculation of all the stiffness terms associated with the A.G.E., using AGE will be very time consuming indeed. Even more so if one realises that the stiffness terms for A.G.E. are each a summation of n Fourier terms. Closer examination of the composition of the stiffness-terms of the A.G.E. reveals that recalculation of terms can be dramatically speeded up by updating only motion-related components of the stiffness matrix [99].

Since the generic rotating electrical machine has an annular air-gap, the A.G.E. was initially introduced for a polar coordinate system. The axial flux machine, however, possesses a planar and somewhat flat air-gap. The 2-D FEM modelling is normally done by introducing radial cutting planes, which are apparently more closely associated with the Cartesian coordinate

system. Therefore, it is necessary to derive the A.G.E. for the Cartesian problems. In the following sections, the derivation of the Cartesian Air-Gap Element (CAGE) is given in details. The validation of the CAGE and its application are also shown in [103]. The derived formulae should also be applicable to some linear electric machines.

A.2 Finite element concepts

For generic electrical machines, the two dimensional Cartesian representation of a magnetic field can be written using Poisson's equation

$$\frac{\partial}{\partial x}\left(\nu\frac{\partial \vec{A}}{\partial x}\right)+\frac{\partial}{\partial y}\left(\nu\frac{\partial \vec{A}}{\partial y}\right)=-\vec{J} \tag{A.1}$$

where $\vec{A}$ is the magnetic vector potential along the z coordinate, $\vec{J}$ is the current density and ν is the magnetic reluctivity. The boundary conditions associated with Eqn. (A.1) can be classified into three types, i.e.

1. Dirichlet boundary conditions: $\vec{A}=c$, where c is a specified value,
2. Neumann boundary conditions: $\frac{\partial \vec{A}}{\partial n}=0$, which means that flux lines penetrate a Neumann boundary orthogonally,
3. Binary boundary conditions: $\vec{A}_i=m\vec{A}_j+n$, where m and n are factors linking the two nodal values, $\vec{A}_i$ and $\vec{A}_j$.

In general, rotating machines have identical pole pitches. The binary conditions (also called *periodic constraints*) are often used to reduce the computation efforts radically. Axial flux machines and linear machines can also benefit from it to some extent.

By using variational techniques, the partial differential equations of the field problem can be formulated in terms of a variational expression called the *energy functional.* The field solution of Eqn. (A.1) can be obtained by minimising the *energy functional* F

$$F=\int\int_S\left[\int_0^B \vec{H}\cdot d\vec{B}-\vec{J}\cdot\vec{A}\right]dS \tag{A.2}$$

where the first term is the magnetic stored energy, the second is the input energy in the solution domain S, $\vec{B}$ is the magnetic flux density and $\vec{H}$ is the magnetic field intensity.

The finite element analysis method is used with a discretised model of small sub-regions, called elements. The elements are connected at node points and their vertices become the element

boundaries. The unknown field variable over each element is approximated by continuous functions expressed in terms of the nodal values of the field variable. The functions defined over each finite element are termed shape functions. In each element the field variable, magnetic vector potential A, may be approximated as

$$A^e = \sum_{k=1}^{n} \alpha_k^e(x,y) A_k^e \tag{A.3}$$

in which n is the number of nodes in the element, A_k^e is the nodal potential value of the element and $\alpha_k^e(x,y)$ is the shape function.

By discretising the solution domain S into m finite elements, the energy functional F can be expressed in the form of

$$F = \sum_{e=1}^{m} F_e \tag{A.4}$$

where F_e is the energy functional in a particular element, which may be given by

$$F_e = \int\int_{S_e} [\frac{1}{2\mu} |\nabla \times (\sum_{k=1}^{n} \alpha_k^e \vec{A}_k^e)|^2 - J \sum_{k=1}^{n} \alpha_k^e \vec{A}_k^e] dS_e \tag{A.5}$$

The Eqn. (A.2) is minimised when the first derivative of the energy function with respect to every vertex value $\vec{A}_i$ is zero, i.e.

$$\frac{\partial F}{\partial A_i} = \sum_{e=1}^{m} \frac{\partial F_e}{\partial A_i} = 0 \tag{A.6}$$

The solution of the minimisation function when using a Cartesian coordinate system per element is:

$$\frac{\partial F}{\partial A_i} = \int\int_{S_e} \left[\frac{1}{\mu} (\frac{\partial \alpha_i^e}{\partial x} \sum_{k=1}^{n} \frac{\partial \alpha_k^e}{\partial x} A_k + \frac{\partial \alpha_i^e}{\partial y} \sum_{k=1}^{n} \frac{\partial \alpha_k^e}{\partial y}) - J\alpha_i^e \right] dxdy \tag{A.7}$$

The minimisation of Eqn. (A.7) is carried out for all the elements of the field region and can be expressed in matrix form in which the unknown vector potential is determined

$$[S] \cdot [A] = [J] \tag{A.8}$$

where J is the forcing vector and S is the stiffness matrix which is nonlinear, symmetric, sparse and band structured. The equation system (A.8) is solved by applying the Newton-Raphson method

$$A^{k+1} = A^k - [\frac{\partial}{\partial A^k} S^k A^k]^{-1} (S^k A^k - J) \tag{A.9}$$

where A^k and A^{k+1} are vector potential values at two successive iterations.

A.3 Field solution of the Cartesian AGE

A.3.1 Field representation of the CAGE

In air-gap region (Fig. A.1), there is no current presence and ν is a constant value. The Eqn. (A.1) is simplified as

$$\frac{\partial^2 A}{\partial x^2} + \frac{\partial^2 A}{\partial y^2} = 0 \tag{A.10}$$

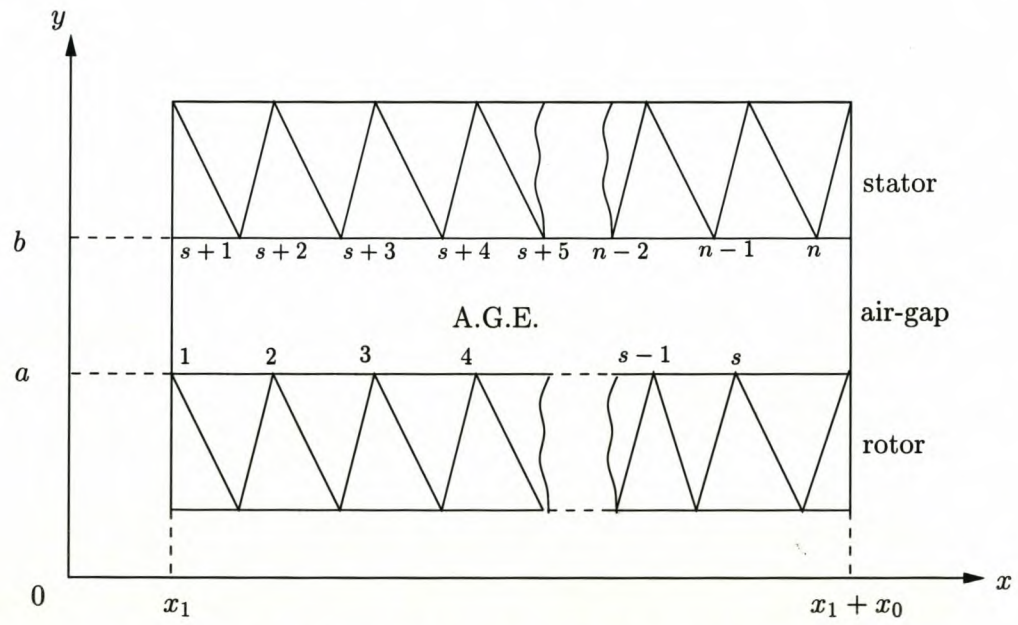

Figure A.1: Definition of Cartesian Air-Gap Element (C.A.G.E.).

Similar to conventional electrical machines, the special machines such as axial field and linear machines also exhibit certain periodic features in structure. In the Cartesian system, if $A(x, y)$ is a periodic function, it may be either of the two cases, i.e.

$$A(x, y) = A(x + x_o, y) \quad \text{or} \quad A(x, y) = A(x, y + y_o) \tag{A.11}$$

where x_o and y_o are periods of function $A(x, y)$ for each case, respectively. The following derivation assumes the first type of periodic condition. The dual case for the second type of

periodic condition can be readily resolved using the same procedures. Applying the variable-separation technique and taking into account the first periodic constraint, the solution of Eqn. (A.10) is given as follows

$$A(x,y) = F_0 \cdot y + G_0 + \sum_{n=1}^{\infty}(F_n \cdot e^{\lambda_n y} + G_n \cdot e^{-\lambda_n y})(H_n \cos \lambda_n x + K_n \sin \lambda_n x) \qquad (A.12)$$

where $\lambda_n = \pm\frac{2\pi n}{x_o}$ and F_0, G_0, F_n, G_n, H_n, K_n are arbitrary constants.

A.3.2 Field superposition

Due to the linearity of the electromagnetic field in the air-gap, the field superposition principle may be used to further simplify field representation. As shown in Fig. A.2, the generic air-gap field A can be treated as the superposition of two independent fields, A_1 and A_2, with partially different constraints.

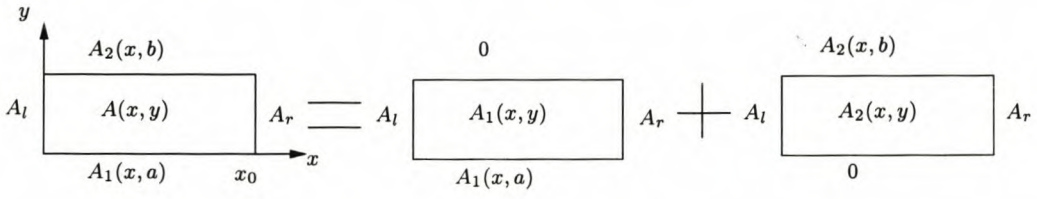

Figure A.2: Principle of air-gap field superposition.

Hence,

$$A(x,y) = A_1(x,y) + A_2(x,y) \qquad (A.13)$$

For the nodes of the CAGE adjoining the stator, $A_1(x,y)|_{y=b} = 0$ while for the nodes connecting the rotor, $A_2(x,y)|_{y=a} = 0$. Thus,

$$A_1(x,b) = F_{10} \cdot b + G_{10} + \sum_{n=1}^{\infty}(F_{1n} \cdot e^{\lambda_n b} + G_{1n} \cdot e^{-\lambda_n b})(H_{1n} \cos \lambda_n x + K_{1n} \sin \lambda_n x) = 0 \quad (A.14)$$

Since the above equation holds for any x in the domain, the conditions stated below must be valid:

$$\frac{G_{10}}{F_{10}} = -b \quad \text{and} \quad \frac{G_{1n}}{F_{1n}} = -e^{2\lambda_n b} \qquad (A.15)$$

Therefore, the $A_1(x,y)$ can be expressed as

$$A_1(x,y) = a_{10}(y-b) + \sum_{n=1}^{\infty} e^{\lambda_n b}[e^{\lambda_n (y-b)} - e^{\lambda_n (b-y)}][a_{1n} \cos \lambda_n x + b_{1n} \sin \lambda_n x] \qquad (A.16)$$

where $a_{10} = F_{10}$, $a_{1n} = F_{1n} \cdot H_{1n}$ and $b_{1n} = F_{1n} \cdot K_{1n}$. Similarly, $A_2(x, y)$ is written as follows

$$A_2(x,y) = a_{20}(y-a) + \sum_{n=1}^{\infty} e^{\lambda_n a}[e^{\lambda_n(y-a)} - e^{\lambda_n(a-y)}][a_{2n}\cos\lambda_n x + b_{2n}\sin\lambda_n x] \tag{A.17}$$

On the substitution of Eqn. (A.16) and (A.17), Eqn. (A.13) becomes

$$\begin{aligned} A(x,y) =& a_{10}(y-b) + \textstyle\sum_{n=1}^{\infty} e^{\lambda_n b}(e^{\lambda_n(y-b)} - e^{\lambda_n(b-y)})(a_{1n}\cos\lambda_n x + b_{1n}\sin\lambda_n x) + \\ & a_{20}(y-a) + \textstyle\sum_{n=1}^{\infty} e^{\lambda_n a}(e^{\lambda_n(y-a)} - e^{\lambda_n(a-y)})(a_{2n}\cos\lambda_n x + b_{2n}\sin\lambda_n x) \end{aligned} \tag{A.18}$$

For each horizontal boundary (Fig. A.1), Eqn. (A.18) is represented by

- on the boundary between CAGE and rotor ($y = a$)

$$A(x,a) = a_{10}(a-b) + \sum_{n=1}^{\infty} e^{\lambda_n b}[e^{\lambda_n(a-b)} - e^{\lambda_n(b-a)}][a_{1n}\cos\lambda_n x + b_{1n}\sin\lambda_n x] \tag{A.19}$$

- on the boundary between CAGE and stator ($y = b$)

$$A(x,b) = a_{20}(b-a) + \sum_{n=1}^{\infty} e^{\lambda_n a}[e^{\lambda_n(b-a)} - e^{\lambda_n(a-b)}][a_{2n}\cos\lambda_n x + b_{2n}\sin\lambda_n x] \tag{A.20}$$

A.4 Shape function

A.4.1 Fourier expansion of A(x,c)

From Eqn. (A.19) and (A.20) it can be readily seen that both equations are of similar format to the Fourier series. To ensure the continuity of $A(x, y)$ on the two horizontal adjoining boundaries, $A(x, c)$ is written as

$$A(x,c) = \sum_{i=k}^{l} \alpha_i(x,c) A_i^b \tag{A.21}$$

where α_i is the Lagrange polynomial defined from the shape functions of the adjacent classical elements, A_i^b is the nodal value on the CAGE boundaries, and

$$k = \begin{cases} 1 & \text{and } l = s \text{ if } c = a, \\ s+1 & \text{and } l = t \text{ if } c = b. \end{cases}$$

To facilitate further mathematical manipulation, Eqn. (A.21) is also developed into a Fourier series.

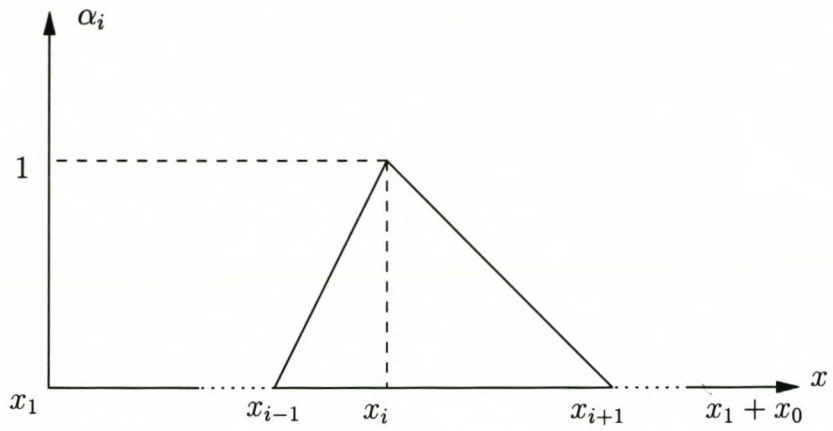

Figure A.3: Definition of function α_i.

- For $y = a$, it is

$$A(x,a) = \sum_{i=1}^{s} A_i \cdot [\frac{1}{2}a_{0i} + \sum_{n=1}^{\infty}(a_{ni}\cos\lambda_n x + b_{ni}\sin\lambda_n x)] \tag{A.22}$$

- For $y = b$, it becomes

$$A(x,b) = \sum_{j=s+1}^{t} A_j \cdot [\frac{1}{2}a_{0j} + \sum_{n=1}^{\infty}(a_{nj}\cos\lambda_n x + b_{nj}\sin\lambda_n x)] \tag{A.23}$$

A.4.2 Definition of $\alpha_i(x,c)$

For the consistency of adjacent edges of the CAGE, the shape functions associated with the classical elements have to be utilised in forming the special CAGE One important feature of the shape functions is that

$$\alpha_i(x_k,c) = \begin{cases} 1 \text{ if } i = k \\ 0 \text{ if } i \neq k \end{cases} \tag{A.24}$$

As shown in Fig. A.3, in the case of first order triangle elements $\alpha_i(x,c)$ can be approximated by the following equation [38]

$$\alpha_i(x,c) = \begin{cases} \frac{x-x_{i-1}}{x_i-x_{i-1}} & \text{if } x_{i-1} \leq x \leq x_i \\ \frac{x-x_{i+1}}{x_i-x_{i+1}} & \text{if } x_i \leq x \leq x_{i+1} \\ 0 & \text{if } x_1 \leq x \leq x_{i-1} \\ 0 & \text{if } x_{i+1} \leq x \leq x_1 + x_o \end{cases} \tag{A.25}$$

The Fourier coefficients a_{0i}, a_{ni} and b_{ni} can be calculated using

$$\begin{cases} a_{0i}=\frac{2}{x_o}\int_{x_1}^{x_1+x_o}\alpha_i(x,c)dx \\ a_{ni}=\frac{2}{x_o}\int_{x_1}^{x_1+x_o}\alpha_i(x,c)\cdot\cos\lambda_n x dx \\ b_{ni}=\frac{2}{x_o}\int_{x_1}^{x_1+x_o}\alpha_i(x,c)\cdot\sin\lambda_n x dx \end{cases} \tag{A.26}$$

From Eqn (A.25) and (A.26), the following are obtained

$$\begin{cases} a_{0i}=\frac{x_{i+1}-x_{i-1}}{x_o} \\ a_{ni}=-\frac{4}{x_o}\cdot\frac{1}{\lambda_n^2}[\frac{1}{x_i-x_{i-1}}\sin(\frac{\lambda_n}{2}(x_i+x_{i-1}))\sin(\frac{\lambda_n}{2}(x_i-x_{i-1})) \\ \quad +\frac{1}{x_i-x_{i+1}}\sin(\frac{\lambda_n}{2}(x_{i+1}+x_i))\sin(\frac{\lambda_n}{2}(x_{i+1}-x_i))] \\ b_{ni}=\frac{4}{x_o}\cdot\frac{1}{\lambda_n^2}[\frac{1}{x_i-x_{i-1}}\sin(\frac{\lambda_n}{2}(x_i-x_{i-1}))\cos(\frac{\lambda_n}{2}(x_i+x_{i-1})) \\ \quad +\frac{1}{x_i-x_{i+1}}\sin(\frac{\lambda_n}{2}(x_{i+1}-x_i))\cos(\frac{\lambda_n}{2}(x_{i+1}+x_i))] \end{cases} \tag{A.27}$$

A.4.3 Coefficients identification

Through comparison of Eqn (A.19), (A.20), (A.22) and (A.23), the relations between the relevant coefficients can be easily established as follows

$$\begin{cases} a_{10}=\frac{1}{2(a-b)}\cdot\sum_{i=1}^{s}a_{0i}\cdot A_i \;\;;\;\; a_{20}=\frac{1}{2(b-a)}\cdot\sum_{j=s+1}^{t}a_{0j}\cdot A_j \\ a_{1n}=\frac{\sum_{i=1}^{s}a_{ni}\cdot A_i}{e^{\lambda_n b}[e^{\lambda_n(a-b)}-e^{\lambda_n(b-a)}]} \;\;;\;\; a_{2n}=\frac{\sum_{j=s+1}^{t}a_{nj}\cdot A_j}{e^{\lambda_n a}[e^{\lambda_n(b-a)}-e^{\lambda_n(a-b)}]} \\ b_{1n}=\frac{\sum_{i=1}^{s}b_{ni}\cdot A_i}{e^{\lambda_n b}[e^{\lambda_n(a-b)}-e^{\lambda_n(b-a)}]} \;\;;\;\; b_{2n}=\frac{\sum_{j=s+1}^{t}b_{nj}\cdot A_j}{e^{\lambda_n a}[e^{\lambda_n(b-a)}-e^{\lambda_n(a-b)}]} \end{cases} \tag{A.28}$$

Substituting Eqn. (A.28) into Eqn. (A.18), the function $A(x,y)$ is given as

$$\begin{aligned} A(x,y)=&\sum_{i=1}^{s}A_i\left\{\frac{y-b}{a-b}\cdot\frac{a_{0i}}{2}+\sum_{n=1}^{\infty}\frac{e^{\lambda_n(y-b)}-e^{\lambda_n(b-y)}}{e^{\lambda_n(a-b)}-e^{\lambda_n(b-a)}}(a_{ni}\cos\lambda_n x+b_{ni}\sin\lambda_n x)\right\}+ \\ &\sum_{j=s+1}^{t}A_j\left\{\frac{y-a}{b-a}\cdot\frac{a_{0j}}{2}+\sum_{n=1}^{\infty}\frac{e^{\lambda_n(y-a)}-e^{\lambda_n(a-y)}}{e^{\lambda_n(b-a)}-e^{\lambda_n(a-b)}}(a_{nj}\cos\lambda_n x+b_{nj}\sin\lambda_n x)\right\} \end{aligned} \tag{A.29}$$

If we put it in a more concise format, Eqn. (A.29) is then

$$A(x,y)=\sum_{i=1}^{t}\alpha_i^{\epsilon}(x,y)\cdot A_i^b \tag{A.30}$$

where $\alpha_i^\epsilon(x,y)$ is

$$\alpha_i^\epsilon(x,y) = \frac{y-c}{c'-c} \cdot \frac{a_{0i}}{2} + \sum_{n=1}^{\infty} \frac{e^{\lambda_n(y-c)} - e^{\lambda_n(c-y)}}{e^{\lambda_n(c'-c)} - e^{\lambda_n(c-c')}} \cdot (a_{ni}\cos\lambda_n x + b_{ni}\sin\lambda_n x) \tag{A.31}$$

and

$$c = \begin{cases} b \text{ and } c' = a \text{ if } i \in \{1,2,\ldots,s\} \\ a \text{ and } c' = b \text{ if } i \in \{s+1,\ldots,t\} \end{cases} \tag{A.32}$$

A.5 Stiffness matrix

A.5.1 Energy functional of the CAGE

Since in the air-gap region $\vec{J} = 0$ and ν is a constant, the energy functional F_ϵ is simply

$$F_\epsilon = \frac{1}{\mu_0} \int\int_{S_\epsilon} \frac{B^2}{2} dS_\epsilon \tag{A.33}$$

The differentiation of Eqn. (A.33) with regard to A_i for each node gives

$$\frac{\partial F_\epsilon}{\partial A_i} = \frac{1}{\mu_0} \int\int_{S_\epsilon} \sum_{j=1}^{t} \nabla\alpha_i^\epsilon \cdot \nabla\alpha_j^\epsilon A_j dS_\epsilon = \frac{1}{\mu_0} \int\int_{S_\epsilon} \nabla\alpha_i^\epsilon \cdot \nabla A^\epsilon dS_\epsilon \tag{A.34}$$

where $A^\epsilon = \sum_{j=1}^{t} \alpha_j^\epsilon A_j$. From vector identity $\nabla \cdot (\phi\vec{A}) = \phi\nabla\cdot\vec{A} + \vec{A}\cdot\nabla\phi$ and the known condition $\Delta A^\epsilon = 0$, the following relations can be obtained

$$\nabla A^\epsilon \cdot \nabla\alpha_i^\epsilon = \nabla \cdot (\alpha_i^\epsilon \nabla A^\epsilon) \tag{A.35}$$

Thus Eqn. (A.34) can be given as

$$\frac{\partial F_\epsilon}{\partial A_i} = \frac{1}{\mu_0} \int\int_{S_\epsilon} \nabla \cdot (\alpha_i^\epsilon \nabla A^\epsilon) dS_\epsilon \tag{A.36}$$

Applying Green's theorem, it can be further simplified as

$$\frac{\partial F_\epsilon}{\partial A_i} = \frac{1}{\mu_0} \int_{C_\epsilon} \alpha_i^\epsilon \nabla A^\epsilon \cdot \vec{n} dC_\epsilon = \frac{1}{\mu_0} \int_{C_\epsilon} \alpha_i^\epsilon \frac{\partial A}{\partial n} dC_\epsilon \tag{A.37}$$

where $\vec{n}$ is a unit vector normal to the contour C_ϵ and pointing outwards, C_ϵ stands for the boundary of the domain S_ϵ. Thereby, the terms of stiffness matrix are defined as follows

$$\frac{\partial F^\epsilon}{\partial A_i} = \frac{1}{\mu_0} \sum_{j=1}^{t} S_{\epsilon ij} A_j \quad \text{where} \quad i = 1,2,\ldots,t \tag{A.38}$$

and

$$S_{\epsilon ij} = \int_{C_\epsilon} \alpha_i^\epsilon \frac{\partial \alpha_j^\epsilon}{\partial n} dC_\epsilon \tag{A.39}$$

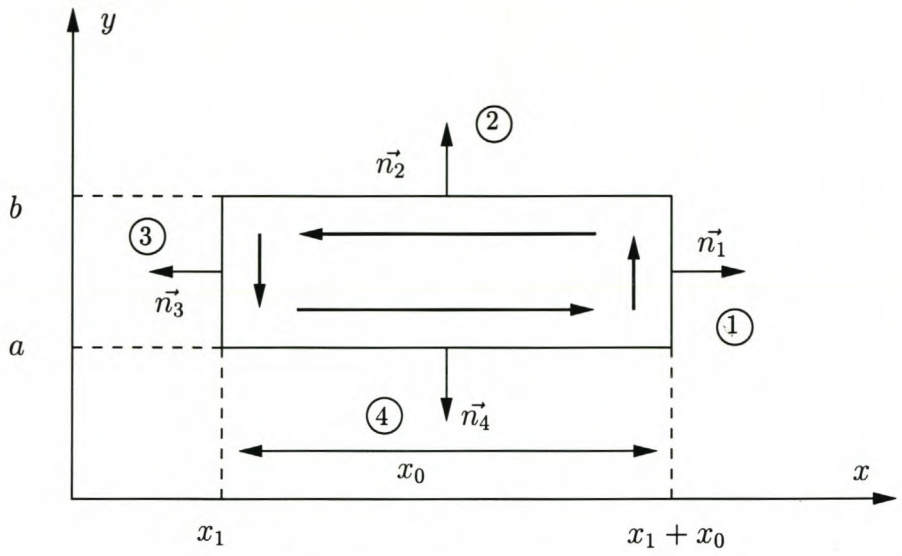

Figure A.4: Integrating path for Cartesian A.G.E. stiffness matrix terms, where $\vec{n_1}$, $\vec{n_2}$, $\vec{n_3}$ and $\vec{n_4}$ are positive directions of $\vec{n}$ on each edge of the C.A.G.E. and x_o is the periodic length of the C.A.G.E.

Written in Matrix format, it becomes

$$\frac{\partial F^{\epsilon}}{\partial [A]^{\epsilon}} = \frac{1}{\mu_0}[S]^{\epsilon}[A]^{\epsilon} \tag{A.40}$$

A.5.2 Expression of stiffness matrix

Under the Cartesian coordinate system, Eqn. (A.39) is decomposed according to the integrating path described in Fig. A.4.

$$\begin{aligned} S_{\epsilon ij} = & \int_a^b \alpha_i^{\epsilon}(x_1 + x_o, y) \frac{\partial \alpha_j^{\epsilon}(x_1+x_o,y)}{\partial x} dy + \int_{x_1+x_o}^{x_1} \alpha_i^{\epsilon}(x, b) \frac{\partial \alpha_j^{\epsilon}(x,b)}{\partial y} d(-x) + \\ & \int_b^a \alpha_i^{\epsilon}(x_1, y) \frac{\partial \alpha_j^{\epsilon}(x_1,y)}{\partial(-x)} (-dy) + \int_{x_1}^{x_1+x_o} \alpha_i^{\epsilon}(x, a) \frac{\partial \alpha_j^{\epsilon}(x,a)}{-\partial y} dx \end{aligned} \tag{A.41}$$

It can be observed that the first and the third terms cancel each other because of the fact that

$$\begin{cases} \alpha_i^{\epsilon}(x_1, y) = \alpha_i^{\epsilon}(x_1 + x_o, y) \\ \frac{\partial \alpha_j^{\epsilon}(x_1,y)}{\partial x} = \frac{\partial \alpha_j^{\epsilon}(x_1+x_o,y)}{\partial x} \end{cases} \tag{A.42}$$

Thus Eqn. (A.41) is reduced to

$$S_{\epsilon ij} = \int_{x_1}^{x_1+x_o} [\alpha_i^\epsilon(x,b)\frac{\partial \alpha_j^\epsilon(x,b)}{\partial y} - \alpha_i^\epsilon(x,a)\frac{\partial \alpha_j^\epsilon(x,a)}{\partial y}]dx \tag{A.43}$$

According to Eqn. (A.31), $\frac{\partial \alpha_i^\epsilon(x,y)}{\partial y}$ is obtained as

$$\frac{\partial \alpha_i^\epsilon(x,y)}{\partial y} = \frac{1}{c'-c}\cdot\frac{a_{0i}}{2} + \sum_{n=1}^{\infty}\frac{\lambda_n[e^{\lambda_n(y-c)}+e^{\lambda_n(c-y)}]}{e^{\lambda_n(c'-c)}-e^{\lambda_n(c-c')}}\cdot(a_{ni}\cos\lambda_n x + b_{ni}\sin\lambda_n x) \tag{A.44}$$

Comparison of Eqn (A.31) and (A.44) shows that both of them are of a similar form. To facilitate further mathematical transformation, these two equations are written as below

$$\alpha_i^\epsilon(x,y) = u_0 + \sum_{n=1}^{\infty} u_n\cdot(a_{ni}\cos\lambda_n x + b_{ni}\sin\lambda_n x) \tag{A.45}$$

$$\frac{\partial \alpha_j^\epsilon(x,y)}{\partial y} = v_0 + \sum_{m=1}^{\infty} v_m\cdot(a_{mj}\cos\lambda_m x + b_{mj}\sin\lambda_m x) \tag{A.46}$$

where u_0, u_n, v_0 and v_m are defined as

$$\begin{cases} u_0 = \frac{y-c}{c'-c}\cdot\frac{a_{0i}}{2} \\ u_n = \frac{e^{\lambda_n(y-c)}-e^{\lambda_n(c-y)}}{e^{\lambda_n(c'-c)}-e^{\lambda_n(c-c')}} \\ v_0 = \frac{1}{f'-f}\cdot\frac{a_{0j}}{2} \\ v_m = \frac{\lambda_m[e^{\lambda_m(y-f)}+e^{\lambda_m(f-y)}]}{e^{\lambda_m(f'-f)}-e^{\lambda_m(f-f')}} \end{cases} \tag{A.47}$$

where $m, n \in \{1, 2, \ldots, \infty\}$ and

$$f = \begin{cases} b \text{ and } f' = a \text{ if } i \in \{1,2,\ldots,s\} \\ a \text{ and } f' = b \text{ if } i \in \{s+1,\ldots,t\} \end{cases} \tag{A.48}$$

Multiplying Eqn. (A.45) by (A.46) gives

$$\begin{aligned} \alpha_i^\epsilon(x,y)\frac{\partial \alpha_j^\epsilon(x,y)}{\partial y} = & u_0\cdot v_0 + u_0\cdot\textstyle\sum_{m=1}^{\infty} v_m\cdot(a_{mj}\cos\lambda_m x + b_{mj}\sin\lambda_m x) + v_0\cdot\sum_{n=1}^{\infty} u_n\cdot \\ & (a_{ni}\cos\lambda_n x + b_{ni}\sin\lambda_n x) + \textstyle\sum_{m=1}^{\infty} v_m\cdot(a_{mj}\cos\lambda_m x + b_{mj}\sin\lambda_m x) \\ & \cdot\textstyle\sum_{n=1}^{\infty} u_n\cdot(a_{ni}\cos\lambda_n x + b_{ni}\sin\lambda_n x) \end{aligned} \tag{A.49}$$

Due to the nature of trigonometric functions, the following relations exist

$$\begin{cases} \int_{x_1}^{x_1+x_o} \sin\lambda_n x dx = \int_{x_1}^{x_1+x_o} \sin\lambda_m x dx = 0 \\ \int_{x_1}^{x_1+x_o} \cos\lambda_n x dx = \int_{x_1}^{x_1+x_o} \cos\lambda_m x dx = 0 \\ \int_{x_1}^{x_1+x_o} \sin\lambda_n x \cdot \cos\lambda_m x dx = 0 \\ \int_{x_1}^{x_1+x_o} \cos\lambda_n x \cdot \sin\lambda_m x dx = 0 \\ \int_{x_1}^{x_1+x_o} \sin\lambda_n x \cdot \sin\lambda_m x dx = \xi \\ \int_{x_1}^{x_1+x_o} \cos\lambda_n x \cdot \cos\lambda_m x dx = \xi \end{cases} \tag{A.50}$$

where $\lambda_n = \frac{2\pi n}{x_o}$, $\lambda_m = \frac{2\pi m}{x_o}$, and

$$\begin{cases} \xi = 0 \quad \text{when } n \neq m \\ \xi = \frac{x_o}{2} \quad \text{when } n = m \end{cases} \tag{A.51}$$

Therefore the integral of Eqn. (A.49) over the range $[x_1, x_1 + x_o]$ is simply

$$\int_{x1}^{x_1+x_o} \alpha_i^\epsilon(x,y) \frac{\partial \alpha_j^\epsilon(x,y)}{\partial y} dx = u_0 \cdot v_0 \cdot x_o + \frac{x_o}{2} \sum_{n=1}^{\infty} u_n \cdot v_n (a_{ni} \cdot a_{nj} + b_{ni} \cdot b_{nj}) \tag{A.52}$$

Combining Eqn (A.43), (A.49) and (A.50), the formula for the stiffness terms is given as

$$\begin{aligned} S_{ij}^\epsilon = & \frac{x_o}{4} \frac{b-a}{(c'-c)(f'-f)} a_{0i} a_{0j} + \frac{x_o}{2} \sum_{n=1}^{\infty} \frac{\lambda_n}{[e^{\lambda_n(c'-c)} - e^{\lambda_n(c-c')}][e^{\lambda_n(f'-f)} - e^{\lambda_n(f-f')}]} \\ & [(e^{\lambda_n(b-c)} - e^{\lambda_n(c-b)})(e^{\lambda_n(b-f)} + e^{\lambda_n(f-b)}) - (e^{\lambda_n(a-c)} - e^{\lambda_n(c-a)}) \\ & (e^{\lambda_n(a-f)} + e^{\lambda_n(f-a)})](a_{ni} a_{nj} + b_{ni} b_{nj}) \end{aligned} \tag{A.53}$$

where c, c', f and f' are given in Eqn (A.32) and (A.48), respectively.

Appendix B

Incorporating CAGE into FE: Program List

B.1 Determining stiffness terms

mkaget ( )	**Make Cartesian Air-Gap Element (CAGE) Terms**
n	n-th Fourier term
lan	Lambda(n)=2.pi.n/thao, where thao=xo
sum	sum of the Fourier terms
a, b	respective y-coordinate of CAGE top/low boundary
ns, nt	respective node number on lower/top CAGE boundary
rthet(i)	contains x-coordinate of the i-th node on a or b
ani, anj	Fourier Coefficients
bni, bnj	Fourier Coefficients
coefa	Fourier Coefficients
aoi,aoj	(theta(i+1)-rthet(i-1))/thao, where
thao	period satisfies periodicity on left/right limits
th1-3	The x1-3 send to coefa and coefb subs
c, ch	a or b depending on i,j
e, eh	a or b depending on i,j
i, j	the indexes of the [ixj] matrix
nfour	number of terms of the Fourier expansion
term1-6	the six terms contained in the Fourier expansion
s(i,j)	terms being calculated for [ixj] matrix
razidex	the index of the razek terms relating to FE node

```
subroutine mkcaget(fname,n_ptch,thao)
parameter (lu = 9)
```

```
      implicit double precision (a-h,o-z)
      double precision a,b,hn,pn
      integer ns,nt,i,j,n
      dimension rthet(481),an(481,481),bn(481,481),razidex(481)
      double precision coefa,coefb,aoi,aoj,thao
      double precision th1,th2,th3,c,ch,e,eh
      double precision fact(481,3),factor
      integer nfour,np,npp,n_ptch,ip
      double precision lan,sum,pi,st1,st2,bh,bp,ap
      double precision term1,term2,term3,term4,term5,term6
      dimension s(481,481),terms(481),sterm1(481,481)
      dimension ah(481,481),ap(481,481),bh(481,481),bp(481,481)
      double precision ani1(481,481),bni1(481,481),la(481)
      character*25 o_file1,i_file,o_file2,fname
      character*1 esc,bot*20
      esc = CHAR(27)
      bot = esc//'[23;01H'//esc//'[2K'//esc//'[23;01H'
      pi=4.0d0*atan(1.0d0)
      i_file= 'temp/cage.age'
      o_file1='temp/cage.res'
      o_file2='temp/cage.rtm'
      open (lu,file=i_file,form='formatted')
      rewind lu
      read (lu,*) a,b
      read (lu,*) ns,nt,nfour,np
      read (lu,*) (rthet(i),i=1,nt)
      read (lu,*) (razidex(i),i=1,nt)
      close (lu,status='keep')
      npp=np/2.0
      if (mod(n_ptch,2).eq.0) then
      print *,' CAGE Periodicity: Positive'
      ip=1
      else if (mod(n_ptch,2).eq.1) then
      print *,' CAGE Periodicity: Negative'
      ip=2
      end if
      thao=dfloat(ip)*thao
c     The factor terms are calculated. There are 4 cases
c     two of which give the same factors:
```

```
c     i)  i.le.ns, j.le.ns
c     ii)  i.gt.ns, j.gt.ns
c     iii) i.le.ns, j.gt.ns
c     iv)  i.gt.ns, j.le.ns
c     iii) and iv) give identical factors thus only the
c          first three cases are evaluated
      c=a
      ch=b
      e=a
      eh=b
      do n=1,nfour,ip
      lan=2.0d0*pi*dble(n)/thao
      la(n)=lan
      term1=lan/((dexp(lan*(c-ch))-dexp(lan*(ch-c)))*
     &   (dexp(lan*(e-eh))-dexp(lan*(eh-e))))
      term2=dexp(lan*(b-ch))-dexp(lan*(ch-b))
      term3=dexp(lan*(b-eh))+dexp(lan*(eh-b))
      term4=dexp(lan*(a-ch))-dexp(lan*(ch-a))
      term5=dexp(lan*(a-eh))+dexp(lan*(eh-a))
      fact(n,1)=term1*(term2*term3-term4*term5)
      end do
      c=b
      ch=a
      e=b
      eh=a
      do n=1,nfour,ip
      lan=2.0d0*pi*dble(n)/thao
      term1=lan/((dexp(lan*(c-ch))-dexp(lan*(ch-c)))*
     &  (dexp(lan*(e-eh))-dexp(lan*(eh-e))))
      term2=dexp(lan*(b-ch))-dexp(lan*(ch-b))
      term3=dexp(lan*(b-eh))+dexp(lan*(eh-b))
      term4=dexp(lan*(a-ch))-dexp(lan*(ch-a))
      term5=dexp(lan*(a-eh))+dexp(lan*(eh-a))
      fact(n,2)=term1*(term2*term3-term4*term5)
      end do
      c=b
      ch=a
      e=a
      eh=b
```

```
      do n=1,nfour,ip
      lan=2.0d0*pi*dble(n)/thao
      term1=lan/((dexp(lan*(c-ch))-dexp(lan*(ch-c)))*
     &  (dexp(lan*(e-eh))-dexp(lan*(eh-e))))
      term2=dexp(lan*(b-ch))-dexp(lan*(ch-b))
      term3=dexp(lan*(b-eh))+dexp(lan*(eh-b))
      term4=dexp(lan*(a-ch))-dexp(lan*(ch-a))
      term5=dexp(lan*(a-eh))+dexp(lan*(eh-a))
      fact(n,3)=term1*(term2*term3-term4*term5)
      end do
      do n=1,nfour,ip
      do i=1,nt
      lan =2.0d0*pi*dble(n)/thao
c     To calculate an(i), bn(i) all the expressions for the delta
c     angles are needed: tha1-5, and thb1-5.  Once again KEEPING
c     PERIODICITY in mind: Subroutines fourcoefa and fourcoefb
c     calculate the coefficients ani, anj, bni, bnj, etc. It uses
c     lan,thetas(i-1,i,i+1)
      if (i.eq.1) then
      th1=rthet(ns)-thao/dble(ip)
      else
      th1=rthet(i-1)
      end if
      if (i.eq.(ns+1)) th1=rthet(nt)-thao/dble(ip)
      th2=rthet(i)
      if (i.eq.nt) then
      th3=rthet(ns+1)+thao/dble(ip)
      else
      th3=rthet(i+1)
      end if
      if (i.eq.ns) th3=rthet(1)+thao/dble(ip)
      call fourcoefa(ip,thao,lan,th1,th2,th3,coefa)
      ani=coefa
      ani1(n,i)=ani
      call fourcoefb(ip,thao,lan,th1,th2,th3,coefb)
      bni=coefb
      bni1(n,i)=bni
      call setupa(thao,lan,th1,th2,th3,hn,pn)
      ah(n,i)=hn
```

```
ap(n,i)=pn
call setupb(thao,lan,th1,th2,th3,hn,pn)
bh(n,i)=hn
bp(n,i)=pn
end do
end do
do i=1,nt
do j=i,nt
if (ip.eq.1) then
if (i.ne.1) aoi=(rthet(i+1)−rthet(i−1))/thao
if (j.ne.1) aoj=(rthet(j+1)−rthet(j−1))/thao
if (i.eq.1)  aoi=(rthet(2)−(rthet(ns)−thao))/thao
if (i.eq.ns) aoi=((rthet(1)+thao)−rthet(ns−1))/thao
if (j.eq.1)  aoj=(rthet(2)−(rthet(ns)−thao))/thao
if (j.eq.ns) aoj=((rthet(1)+thao)−rthet(ns−1))/thao
if (i.eq.(ns+1))aoi=(rthet(ns+2)−(rthet(nt)−thao))/thao
if (i.eq.nt) aoi=((rthet(ns+1)+thao)−rthet(nt−1))/thao
if (j.eq.(ns+1))aoj=(rthet(ns+2)−(rthet(nt)−thao))/thao
if (j.eq.nt) aoj=((rthet(ns+1)+thao)−rthet(nt−1))/thao
if (i.lt.(ns+1)) then
c=a
ch=b
end if
if (i.gt.ns) then
c=b
ch=a
end if
if (j.lt.(ns+1)) then
e=a
eh=b
end if
if (j.gt.ns) then
e=b
eh=a
end if
st1=thao/4.0d0∗(b−a)
st1=st1/((c−ch)∗(e−eh))
st1=st1∗aoi∗aoj
sterm1(i,j)=st1
```

```
end if
sum=0.0d0
do n=1,nfour,ip
lan=2.0d0*pi*dble(n)/thao
if (i.le.ns.and.j.le.ns) then
factor=fact(n,1)
else if (i.gt.ns.and.j.gt.ns) then
factor=fact(n,2)
else if(i.gt.ns.and.j.le.ns.or.i.le.ns.and.j.gt.ns)then
factor=fact(n,3)
end if
term6=ani1(n,i)*ani1(n,j)+bni1(n,i)*bni1(n,j)
st2=factor*term6
if ((i.eq.1).and.(j.eq.(ns+1))) then
terms(n)=fact(n,3)
end if
sum=sum+st2
end do
st2=sum*thao/2.0d0/dble(ip)
if (ip.eq.1) s(i,j)=st2+st1
if (ip.eq.2) s(i,j)=st2
s(j,i)=s(i,j)
end do
end do
open (lu,file=o_file1,form='formatted')
rewind lu
do i= 1,nt
do j= i,nt
write (lu,*) s(i,j)
end do
end do
close (lu,status='keep')
do i=1,ns
do n=1,nFour
an(n,i)=ah(n,i)*dcos(ap(n,i))
bn(n,i)=bh(n,i)*dcos(bp(n,i))
end do
end do
open (lu,file=o_file2,form='formatted')
```

```
      rewind lu
      write (lu,*) nfour,nt,thao,ip
      if (ip.eq.1) then
      write (lu,*) ((sterm1(i,j),j=1,nt),i=1,nt)
      end if
      write (lu,*) (terms(i),i=1,nfour,ip)
      write (lu,*) (la(i),i=1,nfour,ip)
      write (lu,*) ((ah(i,j),j=1,nt),i=1,nfour,ip)
      write (lu,*) ((ap(i,j),j=1,nt),i=1,nfour,ip)
      write (lu,*) ((bh(i,j),j=1,nt),i=1,nfour,ip)
      write (lu,*) ((bp(i,j),j=1,nt),i=1,nfour,ip)
      write (lu,*) ((an(i,j),j=1,nt),i=1,nfour,ip)
      write (lu,*) ((bn(i,j),j=1,nt),i=1,nfour,ip)
      close (lu,status='keep')
      return
      end
c     ******** EOF ********
```

B.2 Re-calculation of stiffness terms

step ( )	**Update Stiffness Terms for a Stepped CAGE**
dtheta	the linear displacement of rotor
sraz	stiffness terms of CAGE
thao	period for periodicity on left/right limits
nfour	number of terms of the Fourier expansion
sum	sum of the Fourier terms
terms	the six terms contained in Fourier expansion
nrs	number of nodes on the lower CAGE boundary
nt	number of nodes on the top CAGE boundary

```
      subroutine step(dtheta,sraz,nfour,terms,an,bn,nrs,nt,
     &  ah,ap,bh,bp,la,thao)
      implicit double precision (a-h,o-z)
      double precision thao,sum,dtheta,ah,ap,bh,bp,dth,thdiv2
      integer nrs,nt,i,j,nfour,n
      double precision sraz(481,481),terms(481),la(481)
      dimension ah(481,481),ap(481,481),bh(481,481),bp(481,481)
      dimension an(481,481),bn(481,481)
```

```
      thdiv2=thao/2.0d0
      do i=1,nrs
      do j=(nrs+1),nt
      sum=0.0d0
      do n=1,nfour,2
      if (i.ne.1) goto 10
      dth=-la(n)*dtheta
      an(n,j)=ah(n,j)*dcos(dth+ap(n,j))
      bn(n,j)=bh(n,j)*dcos(dth+bp(n,j))
10    sum=sum+terms(n)*(an(n,i)*an(n,j)+bn(n,i)*bn(n,j))
      end do
      sraz(i,j)=2.0d0*sum*thdiv2
      sraz(j,i)=sraz(i,j)
      end do
      end do
      return
      end
c     ******** EOF ********
```

B.3 Torque calculation using CAGE

torque ( )	**Calculate Torque Using CAGE Terms**
rrad	y-coordinate of CAGE low boundary
srad	y-coordinate of CAGE top boundary
ntot	total number of nodes of CAGE
nrr	number of nodes on the lower CAGE boundary
torq	overall torque of the machine

```
      subroutine torque(rrad,srad,torq,nfour,nrr,ntot,w,
     &  a,an,bn,razind,thao)
      implicit double precision (a-h,o-z)
      double precision lan,tij
      double precision an(481,481),bn(481,481)
      double precision fact(481,4)
      double precision a(4000)
      integer razind(481)
      pi=4.0d0*datan(1.d0)
      u0=4.0d0*pi*1.d-7
      aa=rrad
```

```
      bb=srad
      torq=0.0d0
      do nh=1,nfour,2
      lan=2.d0*pi*dfloat(nh)/thao
      x1n=dexp(lan*(aa-bb))-dexp(lan*(bb-aa))
      x2n=dexp(lan*(bb-aa))-dexp(lan*(aa-bb))
      x3n=dexp(lan*(aa-bb)/2.d0)+dexp(lan*(bb-aa)/2.d0)
      x4n=dexp(lan*(bb-aa)/2.d0)+dexp(lan*(aa-bb)/2.d0)
      x5n=dexp(lan*(aa-bb)/2.d0)-dexp(lan*(bb-aa)/2.d0)
      x6n=dexp(lan*(bb-aa)/2.d0)-dexp(lan*(aa-bb)/2.d0)
      fact(nh,1)=lan*lan*x3n*x5n/(x1n*x1n)
      fact(nh,2)=lan*lan*x3n*x6n/(x1n*x2n)
      fact(nh,3)=lan*lan*x4n*x5n/(x1n*x2n)
      fact(nh,4)=lan*lan*x4n*x6n/(x2n*x2n)
      end do
      do i=1,ntot
      do j=1,ntot
      if (i.gt.nrr.and.j.gt.nrr) then
      index=4
      else if (i.gt.nrr.and.j.le.nrr) then
      index=3
      else if (i.le.nrr.and.j.gt.nrr) then
      index=2
      else if (i.le.nrr.and.j.le.nrr) then
      index=1
      end if
      tij=0.0d0
      do nh=1,nfour,2
      tij=tij+fact(nh,index)*(an(nh,i)*bn(nh,j)-
     & bn(nh,i)*an(nh,j))
      end do
      torq=torq+a(razind(i))*a(razind(j))*tij
      end do
      end do
      torq=torq*thao/u0
      print*,'force = ',torq
      return
      end
c     ******** EOF ********
```

B.4 Magnetic stored energy calculation

energy ( )	**Calculate Stored Energy in a CAGE**
araz	vector potential on CAGE boundary
asa	$[a]^T[S][a]$
nnode	number of nodes
sraz	stiffness terms of the CAGE
storeE	magnetic stored energy in CAGE

```
      subroutine energy(x,y,a,nnode,ro_od,st_id,sraz,storeE)
      parameter (lu = 9)
      implicit integer (i-n)
      implicit double precision (a-h,o-z)
      dimension x(4000),y(4000),a(4000)
      dimension araz(481,1),araz1(1,481),sraz(481,481),sa(1,481)
      double precision ro_od,st_id,storeE,nnode
      integer nbpoint(481),ncpoint(481),nbcount,ndum,nbcount1
      pi=4.d0*datan(1.d0)
      u0=4.d0*pi*1.0d-7
      v0=1.d0/u0
      nbcount=0
      do  i=1,nnode
      if (dabs(y(i)-ro_od).lt.1.0d-7) then
      nbcount=nbcount+1
      nbpoint(nbcount)=i
      end if
      end do
      do j=1,nbcount
      do k=(1+j),nbcount
      if (x(nbpoint(j)).gt.x(nbpoint(k))) then
      ndum=nbpoint(j)
      nbpoint(j)=nbpoint(k)
      nbpoint(k)=ndum
      end if
      end do
      end do
      nbcount=nbcount-1
      do 20 i2=1,nbcount
      araz(i2,1)=a(nbpoint(i2))
   20 continue
```

```
      nbcount1=0
      do 30 i3=1,nnode
      if (dabs(y(i3)-st_id).lt.1.0d-7) then
      nbcount1=nbcount1+1
      ncpoint(nbcount1)=i3
      end if
   30 continue
      do 40 i4=1,nbcount1
      do 50 j4=(1+i4),nbcount1
      if (x(ncpoint(i4)).gt.x(ncpoint(j4))) then
      ndum=ncpoint(i4)
      ncpoint(i4)=ncpoint(j4)
      ncpoint(j4)=ndum
      end if
   50 continue
   40 continue
      nbcount1=nbcount1-1
      do 60 i6=1,nbcount1
      araz(i6+nbcount,1)=a(ncpoint(i6))
   60 continue
      nt=nbcount+nbcount1
      call mmult1(nt,sraz,araz,sa)
      do i=1,481
      araz1(1,i)=araz(i,1)
      end do
      call mmult2(nt,araz1,sa,asa)
      storeE = asa*v0/2.d0
      return
      end
c     ******** EOF: Main Program ********

      subroutine mmult1(ns,a,b,c)
c     mmult1( ) does [c]=[a][b]
c     [a] is a [ns x ns] matrix
c     [b] is taken as [1 x ns]
c     [c] is taken as [1 x ns]
      implicit double precision (a-h)
      implicit double precision (o-z)
      dimension a(481,481),b(481),c(481)
```

```
      integer i,j,ns
      do i=1,ns
      c(i)=0.d0
      do j=1,ns
      c(i)=c(i)+a(i,j)*b(j)
      end do
      end do
      return
      end
c     ******** EOF: mmult1 ( ) ********

      subroutine mmult2(ns,a,b,c)
c     mmult2 ( ) does [c]=[a][b]
c     [a] is a [1 x ns] matrix
c     [b] is taken as [ns x 1]
c     [c] is taken as [1 x 1]
      implicit double precision (a-h)
      implicit double precision (o-z)
      dimension a(1,481),b(481)
      integer j,ns
      c=0
      do j=1,ns
      c=c+a(1,j)*b(j)
      end do
      return
      end
c     ******** EOF: mmult2 ( ) ********
```

Appendix C

Thermofluid Model Computer Solution Algorithm

C.1 Program for air flow model

airflow ( )	**Calculate AFPM Machine's Volumetric Flowrate**
fr	pole-arc/pitch ratio
nh	number of air inlet holes
nb	number of blades (PM poles)
dh	diameter of air inlet holes
r1, r2	rotor inner, outer radius
omega	rotation speed of rotor disc
q	the determined volumetric flowrate

```
      subroutine airflow(r1,r2,l_a,l_r,l_s,nh,nb,fr,omega,hm,dh,q)
      double precision delta_p,delta_p1,delta_p2,pi,a1,a2,dh,l_r
      double precision q,q1,rho,step,ks,r1,r2,omega,hm,fr,l_a,l_s
      integer i,j,k,nb,nh
      rho = 1.177d0
      pi = 4.d0*atan(1.d0)
      a1 = 2.d0*pi*r1/dble(nb)*(1.d0-fr)*hm
      a2 = 2.d0*pi*r2/dble(nb)*(1.d0-fr)*hm
      ks = 1.d0 - 0.63d0*pi/dble(nb)
      step = 1.d-5
      do i = 1,210000
      q = 1.d-5+step*dble(i-1)
      delta_p1 = rho*(omega**2)*(ks*r2*r2-r1*r1)+
     &  rho/2.d0*(1.d0/(a1*a1)-1.d0/(a2*a2))*(q/dble(nb))**2
```

```
      call sysloss(dh,r1,r2,nh,nb,fr,hm,l_a,l_r,l_s,q,delta_p2)
      delta_p = delta_p1 - delta_p2
      if (delta_p.lt.0.0d0) then
      q1 = q
      goto 20
      endif
      end do
20    continue
      do j = 1,100
      q = q1
      do k = 1,(100*j)
      q = q - step/(dble(j)*100.d0)
      call sysloss(dh,r1,r2,nh,nb,fr,hm,l_a,l_r,l_s,q,delta_p2)
      delta_p1 = rho*omega**2.d0*(ks*r2*r2-r1*r1)+
     & rho/2.d0*(1.d0/(a1*a1)-1.d0/(a2*a2))*(q/dble(nb))**2
      delta_p = delta_p1 - delta_p2
      if (dabs(delta_p).le.1.d-5) then
      print*,'air flowrate=',q,' [m^3/s]'
      goto 30
      end if
      end do
      end do
30    continue
      return
      end
c     ******** EOF: airflow ( ) ********

      subroutine sysloss(dh,r1,r2,nh,nb,fr,hm,l_a,l_r,l_s,q,delta_p2)
      double precision k1,k2,k3,k4,k5,k6,k7,k8,k9,re2,re4,re5,re8
      double precision a,b,c,a1,a2,a3,a4,a5,a6,a7,a8,a9,pi,mu,l2,f2
      double precision p4,dh4,p5,dh5,l5,f5,dh8,p8,l8,f8,aa,bb,cc,dh
      double precision q,rho,d1,d2,delta,fr,hm,r1,r2,l_a,l_s,l_r
      integer nb,nh
      mu = 18.64d-6
      rho = 1.177d0
      pi = 4.d0*atan(1.d0)
      d1 = dh
      a1 = pi*(d1/2.d0)**2
      k1 = 0.25d0
```

```
d2 = d1
l2 = l_r
a2 = pi*(d2/2.d0)**2
re2 = rho*q*d2/(a2*dble(nh)*mu)
c = 1.d0/(7.d0/re2)**0.9d0
a = (2.457d0*log(c))**16
b = (37530.d0/re2)**16
f2 = 8.d0*((8.d0/re2)**12+1.d0/(a+b)**1.5d0)**(1.d0/12.d0)
k2 = f2*l2/d2
k3 = 0.5d0
a3 = a2
a4 = pi*r1*2.d0*0.005d0/dble(nb)
p4 = pi*r1*2.d0*2.d0/dble(nb)
dh4 = 4.d0*a4/p4
re4 = rho*q*dh4/(a4*dble(nb)*mu)
if (re4.ge.10.d0.and.re4.le.2000.d0) then
k4 = 58.36d0*re4**(-0.7175d0)
else if (re4.gt.2000.d0.and.re4.lt.100000.d0) then
k4 = 1.3417d0*re4**(-0.1633d0)
else
k4 = 58.36d0
endif
a5 = 0.000251d0
p5 = 0.16729d0
l5 = 0.005d0
dh5 = 4.d0*a5/p5
re5 = rho*q*dh5/(a5*dble(nb)*mu)
c = 1.d0/(7.d0/re5)**0.9d0
a = (2.457d0*log(c))**16.d0
b = (37530.d0/re5)**16.d0
f5 = 8.d0*((8.d0/re5)**12.d0+1.d0/(a+b)**1.5d0)**dble(1./12.)
k5 = f5*l5/dh5
a6 = r1*2.d0*pi*(hm/dble(nb)*(1.d0-fr)+(l_a-l_s)/dble(2*nb))
k6 = 1.5d0
a7 = a6
k7 = 0.5d0
a8 = (r1+r2)*pi*hm/dble(nb)
p8 = (r1+r2)*pi/dble(nb)
l8 = r2 - r1
```

```
      dh8 = 4.d0*a8/p8
      re8 = rho*q*dh8/(a8*dble(nb)*mu)
      cc = 1.d0/(7.d0/re8)**0.9d0
      aa = (2.457d0*log(cc))**16.d0
      bb = (37530.d0/re8)**16.d0
      f8 = 8.d0*((8.d0/re8)**12+1.d0/(aa+bb)**1.5d0)**dble(1./12.)
      k8 = f8*l8/dh8
      a9 = 2.d0*pi*r2*hm/(dble(nb))*(1.d0-fr)
      k9 = 0.66d0
      delta_p2 = rho*((q/dble(nb))**2)/2.d0*(25.d0*k1/a1**2+
     &  25.d0*k2/a2**2+k3/a3**2+k4/a4**2+k5/a5**2+k6/a6**2+
     &  k7/a7**2+k8/a8**2+k9/a9**2)
      print *,'total loss=',delta_p2
      return
      end
c     ******** EOF: sysloss ( ) ********
```

C.2 Program for heat transfer model

thermal ( )	**Calculate Machine's Steady-state Temperature**
h	airgap convective heat transfer coefficient
k3	thermal conductivity of permanent magnets
k4	thermal conductivity of epoxy layer
k5	thermal conductivity of rotor disc
lm	axial length of magnet
lr	axial length of rotor disc
ls	axial length of stator disc
la	axial length of airgap (PM to PM)
nb	number of blades, i.e. number of PM poles
nh	number of air inlet holes
v	kinematic viscosity
k	thermal conductivity
Nu	Nusselt number
D	outer diameter of the disc
Pr	Prandtl number
ReD	Rotational Reynolds number
Re	Rotational Reynolds number
rc	radius where transition between laminar& turbulent

```
      subroutine thermal(heat_file,T1,T2,T3,T4)
      character*25 heat_file
      parameter (is = 3)
      double precision T1,T2,T3,T4,Ta,Tai,K3,K4,del,dh
      double precision epsilon,epsilon1,epsilon3,epsilon4,d0,di,ds
      double precision qdot_cu,qdot_edy,qdot_bear,qdot_edym
      double precision c1,c2,c3,c4,l_r,l_m,l_s,l_a,m2
      double precision h1,h_ar,h_e,h_sa,v_air,qdot_c23
      double precision rho_cu,rho_epxy,rho_air,rho_fe,rho_pm
      double precision Rc12,Rc23,Rr13,Rg34,Rc4a,Rr4a,Rc4ea,Rr4ea
      double precision area,area_s,area1,area_e,area_se,fr,pi
      double precision T1a,T2a,T3a,T4a,r1,r2,rs,Q,speed,omega
      integer nb,nh
      open(unit=is, file=heat_file, form='formatted')
      rewind is
      read (is,22) r1
      read (is,22) r2
      read (is,22) speed
      read (is,22) l_m
      read (is,22) l_s
      read (is,22) l_r
      read (is,22) l_a
      read (is,22) qdot_cu
      read (is,22) qdot_edy
      read (is,22) qdot_bear
      read (is,22) qdot_edym
      read (is,*) nb
      read (is,*) nh
      read (is,22) rs
      read (is,22) fr
      close (is)
22    format (d15.6)
      pi = 4.d0*atan(1.d0)
      K3 = 9.d0
      K4 = 50.d0
      qdot_cu = qdot_cu
      qdot_edy = qdot_edy
      qdot_bear = qdot_bear
      qdot_edym = qdot_edym
```

```
      del = 5.67d-8
      epsilon1 = 0.9d0
      epsilon3 = 0.85d0*fr+0.3d0*(1.d0-fr)
      epsilon4 = 0.3d0
      epsilon  = 0.9d0
      d0 = r2*2.d0
      di = r1*2.d0
      area = pi*(d0*d0-di*di)/4.d0
      ds = 2.d0*rs
      dh = 0.04d0
c     (J/kg K )air-gap only
      c2 = 1005.d0
c     (J/kg K )rotor(mild steel)
      c4 = 434.d0
c     (kg/m^3) density of copper
      rho_cu = 7500.d0
c     (kg/m^3) density of epoxy/hardener
      rho_epxy = 1655.d0
c     (kg/m^3) (300k/1at) density of air
      rho_air = 1.177d0
c     (kg/m^3) density of mild steel
      rho_fe = 7711.d0
c     (kg/m^3) density of magnets
      rho_pm = 7880.d0
c     Gauss-Seidel Iteration
      omega = 2.d0*pi*speed/60.d0
      call airflow(r1,r2,l_a,l_r,l_s,nh,nb,fr,omega,l_m,dh,Q)
      call twodisc(Q,r2,h_sa)
      call freedisc(r2,omega,h1)
      call periphery(d0,omega,h_e)
      Ta = 25.d0
      Tai = Ta
      T1 = Ta
      T2 = Ta
      T3 = Ta
      T4 = Ta
      T1a = 0.0d0
      T2a = T1a
      T3a = T2a
```

```
      T4a = T3a
10    continue
c     Control volume 1: half stator
      area1 = pi*(d0*d0)/4.d0
      area_s = pi*((d0+2.d0*l_a)**2-(di-2.d0*l_a)**2)/4.d0
      area_se = area_s*1.1d0
      Rc12 = 1.d0/(h_sa*area_se)
      Rr13 =((1.d0 - epsilon1)/(epsilon1*area_s)+1.d0/area_s+
     & (1.0d0 - epsilon3)/(epsilon3*area_s))/(del*((T1+273.d0)+
     & (T3+273.d0))*((T1+273.d0)**2+(T3+273.d0)**2))
      T1 = 1.d0/(Rr13+Rc12)*(Rr13*T2+Rc12*T3+
     & Rc12*Rr13*(qdot_cu+qdot_edy))
c     Control volume 2: air-gap
      h_ar = h_sa
      v_air = 2.d0*Q/(pi*d0*(l_a+2.d0*l_m))
      m2 = rho_air*Q
      Rc23 = 1.d0/(h_ar*area_se)
      qdot_c23 = (T2-T3)/Rc23
      T2 = 1.d0/(Rc12+Rc23+2.d0*Rc12*Rc23*m2*c2)*(Rc23*T1+Rc12*T3+
     & 2.d0*Rc12*Rc23*m2*c2*Tai)
c     Control volume 3: magnet
      Rg34 = l_m/(2.d0*k3*area*0.8d0)+l_r/(2.d0*k4*area1)
      T3 = 1.d0/(Rc23+Rg34)*(Rc23*T4+Rg34*T2+Rc23*Rg34/Rr13*(T1-
     & T3)+Rc23*Rg34*qdot_edym)
c     Control volume 4: rotor
      ds = 2.d0*rs
      area1 =pi*(d0*d0-ds*ds)/4.d0
      Rc4a = 1.d0/(h1*area1)
      Rr4a = 1.d0/(epsilon4*area1*del*((T4+273.d0)+
     & (Ta+273.d0))*((T4+273.d0)**2+(Ta+273.d0)**2))
      area_e = d0*pi*l_r
c     Convection thermal resistance of rotor top edge
      Rc4ea = 1.d0/(h_e*area_e)
c     Rr4ea: radiation thermal resistance of rotor top edge
      Rr4ea = 1.d0/(epsilon4*area_e*del*((T4+273.d0)+
     & (Ta+273.d0))*((T4+273.d0)**2+(Ta+273.d0)**2))
      T4 = 1.d0/(Rr4a*Rc4a*Rc4ea*Rr4ea+Rr4a*Rg34*Rc4ea*Rr4ea+
     & Rr4ea*Rc4a*Rg34*Rc4ea+Rg34*Rr4a*Rc4a*Rr4ea+
     & Rg34*Rc4a*Rr4a*Rc4ea)*(Rc4a*Rr4a*Rc4ea*Rr4ea*T3+
```

```
     &  (Rg34*Rr4a*Rc4ea*Rr4ea+Rg34*Rc4a*Rc4ea*Rr4ea+
     &  Rg34*Rc4a*Rr4a*Rr4ea+Rg34*Rc4a*Rr4a*Rc4ea)*Ta+
     &  qdot_bear*Rc4a*Rr4a*Rg34*Rc4ea*Rr4ea)
        if (dabs(T1a-T1).lt.1.d-5.and.dabs(T2a-T2).lt.1.d-5
     &  .and.dabs(T3a-T3).lt.1.d-5.and.dabs(T4a-T4).lt.1.d-5) then
        goto 20
        else
        T1a = T1
        T2a = T2
        T3a = T3
        T4a = T4
        print *,T1,T2,T3,T4
        goto 10
        end if
20      continue
        T1 = T1 - Ta
        T2 = T2 - Ta
        T3 = T3 - Ta
        T4 = T4 - Ta
        print *,' '
        print 21
        print 23,T1
        print 24,T3
        print 26,Q
        print 25,h_sa
        print *,' '
21      format('-------- Thermal performance --------')
23      format('Winding temp. rise=',f10.5,' [degC]')
24      format('PMagnet temp. rise=',f10.5,' [degC]')
25      format('Heat transfer rate=',f10.5,' [W/m^2K]')
26      format('Volumetric airflow=',f10.5,' [m^3/s]')
        return
        end
c       ******** EOF: Main Program ********

c       Heat Transfer Rate of Rotor-Stator System
        subroutine twodisc(Q,R,h_sa)
        double precision k,Nu,R,v,Q,pi,h_sa
        pi = 4.d0*atan(1.d0)
```

```
      v = 1.566d-5
      k = 0.02624d0
      Nu = 0.333d0*Q/(v*R*pi)
      h_sa = k*Nu/R
      return
      end
c     ******** EOF: twodisc ( ) ********

c     Heat Transfer Rate of Rotation Cylinder
      subroutine periphery(D,omega,h_e)
      double precision k,Nu,D,v,h_e,omega,Pr,ReD
      v = 1.566d-5
      k = 0.02624d0
      Pr = 0.69d0
      ReD = omega*(D*D)/v
      Nu = 0.133d0*ReD**(2.d0/3.d0)*Pr**(1.d0/3.d0)
      h_e = (k/D)*Nu
      return
      end
c     ******** EOF: periphery ( ) ********

c     Heat Transfer Rate of a Free Disc
      subroutine freedisc(R,omega,h_e)
      double precision k,Nu,R,Re,rc,v,h_e,omega
      v = 1.566d-5
      k = 0.02624d0
      Re = omega*(R*R)/v
      rc = dsqrt(2.5d0*100000.d0*v/omega)
      Nu = 0.015d0*Re**(0.8d0)-100.d0*(rc/R)**2
      h_e = (k/R)*Nu
      return
      end
c     ******** EOF: freedisc ( ) ********
```

Appendix D

Thermal Properties

D.1 The heat transfer correlations for AFPM machines

Configuration	Correlations	Conditions
Free rotatin disc [108]	$\overline{Nu} = 0.015Re^{0.8} - 100(\frac{r_c}{R})^2$ where $r_c = (2.5 \times 10^5 \nu/\omega)^{0.5}$, $Re = \frac{\omega R^2}{\nu}$, $\overline{Nu} = \frac{hR}{k}$	Laminar flow: $0 \leq r \leq r_c$ Turbulent flow: $r_c \leq r \leq R$ $Pr = 0.72$
	$\overline{Nu} = 0.4(Re^2 + Gr)^{0.25}$ where $Gr = \frac{\beta g R^3 \pi^{1.5} \Delta T}{\nu^2}$	Combined effects of free convection & rotation in laminar flow
Parallel plates	$\overline{Nu} = 7.54 + \frac{0.03\frac{D_h}{L} Re_{D_h} Pr}{1+0.016[\frac{D_h}{L} Re_{D_h} Pr]^{\frac{2}{3}}}$	Laminar flow (fully developed)
Vertical plate [72]	$\overline{Nu} = 0.68 + 0.67(Ra\Psi)^{\frac{1}{4}}$ where $\Psi = [1 + (\frac{0.492}{Pr})^{\frac{9}{16}}]^{-\frac{16}{9}}$ $Ra = GrPr$, $Gr = \frac{\beta g x^3 \pi^{\frac{3}{2}} \Delta T}{\nu^2}$	Laminar nature-convection $Ra \leq 10^9$, $Pr \simeq 1$
	$\overline{Nu} = 0.68 + 0.67(Ra\Psi)^{\frac{1}{4}} \times$ $(1 + 1.6 \times 10^{-8} Ra\Psi)^{\frac{1}{12}}$	Turbulent nature-convection $10^9 \leq Ra < 10^{12}$
Rotating cylinder [72]	$\overline{Nu} = 0.133Re^{\frac{2}{3}} Pr^{\frac{1}{3}}$ where $Re = \Omega D^2/\nu$	$Re \leq 4.3 \times 10^5$ $0.7 \leq Pr \leq 670$

D.2 Thermal properties of materials used in the analysis

Table D.1: Selected emissivities relevant to AFPM machines.

Material	Surface condition	Emissivity, ε
Copper	Polished	0.025
Epoxy	Black	0.87
	White	0.85
Mild steel	-	0.2-0.3
Cast iron	Oxidized	0.57
Stainless steel	-	0.2-0.7
Permanent magnet, NdFeB	Uncoated	0.9

Table D.2: Selected thermal properties of materials.

Material	Grade	ρ	c_p	k
(300 K)		kg/m^3	J/kg K	W/m K
Air	-	1.177	1005	0.0267
Mica	-	3000	813	0.33
Epoxy resin	-	1400	1700	0.5
Copper	-	8950	380	360
Aluminum	Pure	2700	903	237
	Alloy (cast)	2790	883	168
Steel	1% Carbon	7850	450	52
	Silicon	7700	490	20-30
Permanent magnet	NdFeB	7400	420	9

Appendix E

Experimental Equipment

E.1 Photographs of experimental equipment

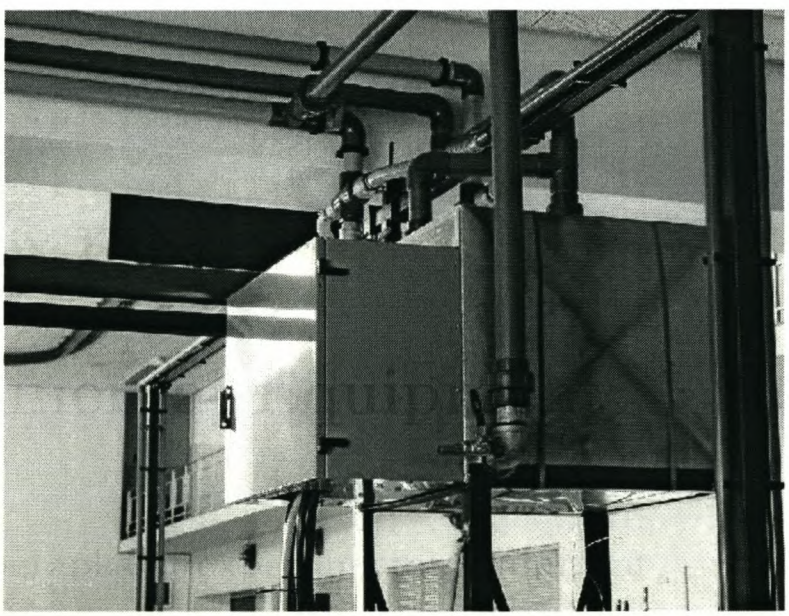

Figure E.1: Water-cooled electrical load system used in the testing of the AFPM generator.

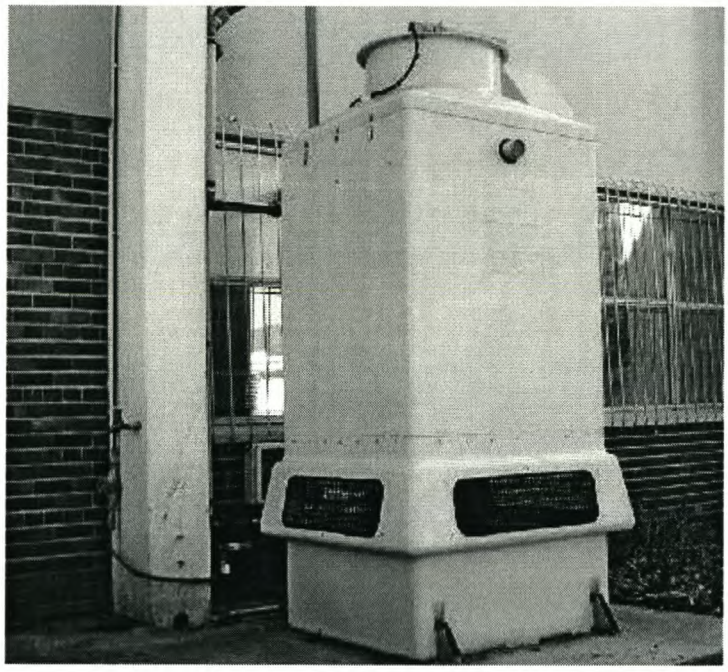

Figure E.2: Cooling tower

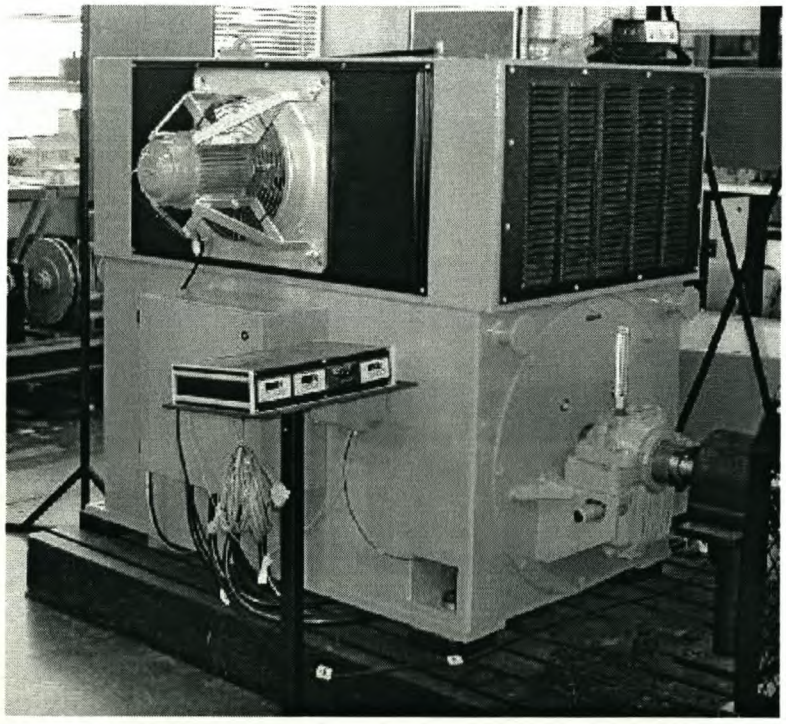

Figure E.3: 600 kW industrial induction machine used as prime mover for the testing of the AFPM generator.

University of Stellenbosch

Design Aspects and Optimisation of an Axial Field Permanent Magnet Machine with an Ironless Stator

Rong-Jie Wang

Thesis presented for the degree of
Doctor of Philosophy in Electrical Engineering at
the University of Stellenbosch

Supervisor:

Prof. M.J. Kamper, University of Stellenbosch

September 2002